POLYPUBLIE
Polytechnique Montréal

POLYTECHNIQUE MONTRÉAL
UNIVERSITÉ D'INGÉNIERIE

Titre: Title: A Viscoplastic Constitutive Model For Cyclic Clay Behavior

Auteur: Author: Mohammad Zarrabi

Date: 2021

Type: Mémoire ou thèse / Dissertation or Thesis

Référence: Citation: Zarrabi, M. (2021). A Viscoplastic Constitutive Model For Cyclic Clay Behavior [Thèse de doctorat, Polytechnique Montréal]. PolyPublie. https://publications.polymtl.ca/5583/

Document en libre accès dans PolyPublie
Open Access document in PolyPublie

URL de PolyPublie: PolyPublie URL: https://publications.polymtl.ca/5583/

Directeurs de recherche: Advisors: Samuel Yniesta

Programme: Program: Génie civil

Ce fichier a été téléchargé à partir de PolyPublie, le dépôt institutionnel de Polytechnique Montréal
This file has been downloaded from PolyPublie, the institutional repository of Polytechnique Montréal

https://publications.polymtl.ca

POLYTECHNIQUE MONTRÉAL

affiliée à l'Université de Montréal

A VISCOPLASTIC CONSTITUTIVE MODEL FOR CYCLIC CLAY BEHAVIOR

MOHAMMAD ZARRABI

Département des génies civil, géologique et des mines (CGM)

Thèse présentée en vue de l'obtention du diplôme de *Philosophiæ Doctor*

Génie civil

Décember 2020

© MOHAMMAD ZARRABI, 2020.

POLYTECHNIQUE MONTRÉAL

affiliée à l'Université de Montréal

Cette thèse intitulée :

A VISCOPLASTIC CONSTITUTIVE MODEL FOR CYCLIC CLAY BEHAVIOR

Présentée par **Mohammad ZARRABI**

en vue de l'obtention du diplôme de Philosophiæ Doctor

a été dûment acceptée par le jury d'examen constitué de :

COURCELLES Benoit, président

YNIESTA Samuel, membre et directeur de recherche

OVALLE Carlos, membre

LI Biao, membre externe

ACKNOWLEDGMENT

This work is a little step towards making the world a safer place to live. I hope this dissertation's outcome impacts the understanding of complicated geotechnical phenomena and mitigates earthquakes' unpleasant consequences on people’s lives.

I would like to thank all the people who helped, guided, and supported me academically and morally during my PhD study. Firstly, I would like to thank my PhD advisor, Prof. Samuel Yniesta, for defining such an exciting project and his continuous support towards the end of it.

Then, I would like to thank Prof. Guiseppe Buscarnera and Dr. Zhenhao Shi for their invaluable support and guidance during my visit to Northwestern University and all the resources they provided.

Spending four years of tough times far from family may not be possible without having great friends. I want to thank all the friends I had unforgettable memories and beautiful moments with; Many special thanks go to my colleagues in the office, with whom I have studied, had coffee, hanged out, improved my French, and built professional connections.

I would also like to thank all my Persian friends by whom we filled our family gap and celebrated many Persian festivals such as Nowruz, Yalda, Sizdah Bedar, etc.

Special thanks to my sisters and my parents, who have always been encouraging and supportive in the toughest moments in my life.

Finally, many thanks to Quebecers for their friendly attitudes and generous hospitality that made my study life in a new country enjoyable. I will never forget my Montreal's living experience, especially the joyful memories of “cabane à sucre” in snowy winters and multicultural festivals in summers.

RÉSUMÉ

Les séismes peuvent avoir des conséquences désastreuses en termes de pertes humaines et matérielles. Parmi les phénomènes géotechniques qui peuvent mener à des pertes pendant un tremblement de terre, la liquéfaction des sols granulaires a été le plus étudié, bien que l'amollissement cyclique des argiles puisse générer des dommages significatifs. Par exemple, le tremblement de 1964 en Alaska a déclenché un glissement de terrain majeur le long de la 4ième avenue à Anchorage, dont la cause principale était l'amollissement cyclique.

Pour étudier l'impact de tels phénomènes, des simulations numériques dynamiques non linéaires peuvent être utilisées. Ces simulations s'appuient sur des modèles constitutifs qui sont formulés pour capturer le déclenchement de la liquéfaction ou de l'amollissement cyclique. L'utilisation de ces modèles nécessite une connaissance de leur formulation et des essais et erreurs fastidieux pour calibrer leurs nombreux paramètres d'entrée. La calibration difficile a rendu difficile l'utilisation de modèles constitutifs avancés pour les applications géotechniques sismiques. En conséquence, les modèles constitutifs avancés n'ont pas été largement adoptés dans la pratique malgré l'attention significative qu'ils ont reçue ces dernières années.

Parmi les modèles constitutifs développés pour les applications géotechniques sismiques, la plupart ont été créés pour simuler le comportement de sols granulaires liquéfiables, et prédire le déclenchement de la liquéfaction. En revanche, peu de travaux ont été réalisés concernant la modélisation de l'amollissement cyclique des sols cohésifs. De plus, les quelques modèles constitutifs développés pour modéliser le comportement des argiles sous chargement cyclique, aucun ne considère une dépendance au taux de chargement du fait de la complexité des lois de comportement nécessaires pour développer un modèle viscoplastique.

Le premier objectif de cette étude est d'évaluer l'utilisation des techniques d'optimisation pour calibrer les modèles constitutifs du sol et de les améliorer pour les applications de chargement cyclique. Le deuxième objectif est de développer un modèle constitutif dépendant du taux qui peut simuler le comportement de sols cohésifs sous chargement cyclique.

Dans cette thèse, deux algorithmes d'optimisation sont étudiés, les algorithmes Gauss-Newton (GN) et Particle Swarm Optimization (PSO), et appliqués pour calibrer plusieurs modèles

constitutifs formulés pour des applications cycliques. Des ajustements aux algorithmes sont présentés pour améliorer leur efficacité et les rendre plus adaptés à l'application présentée. Plusieurs exemples de validation sont utilisés sur une variété de modèles constitutifs, et la conclusion est que ces algorithmes peuvent faciliter la procédure d'étalonnage et peuvent être considérés comme des alternatives efficaces et précieuses aux étalonnages par essais et erreurs.

Dans la deuxième partie de cette thèse, un modèle viscoplastique est introduit. Le modèle est d'abord formulé dans l'espace triaxial, et généralisé pour un espace multiaxial. Les lois de comportement du modèle proposé sont dérivées en modifiant des modèles de comportement avancés récents pour capturer le comportement dépendant du taux de déformation présenté dans la littérature par divers auteurs. Le modèle développé est validé en comparant les résultats à quelques études et tests cycliques en laboratoire réalisés sur une argile de plasticité moyenne prélevée au Québec. Le modèle proposé montre la capacité de capturer les principales caractéristiques du comportement cyclique du sol, telles que la dégradation cyclique, la réduction du module et le comportement d'amortissement, et la dépendance à la vitesse de déformation de la résistance au cisaillement présentée dans la littérature.

Cette thèse fournit aux praticiens et aux chercheurs un moyen de calibrer des modèles constitutifs avancés de manière avancée et un modèle constitutif qui peut être utilisé dans des simulations numériques non linéaires où les argiles devraient subir une perte de résistance.

ABSTRACT

Earthquakes can have dire consequences both in terms of loss of human lives and properties. Among the geotechnical phenomena that can induce losses during an earthquake, liquefaction of granular soils is the most well-studied but cyclic softening of clays is also capable of producing significant damages. For instance, the 1964 Alaska earthquake triggered a major landslide along the 4th avenue in Anchorage, attributed to cyclic softening.

To study the impact of such phenomena, numerical dynamic nonlinear simulations can be used. These simulations rely on constitutive models that are formulated to capture the triggering of liquefaction or cyclic softening. The use of these models requires knowledge of their formulation, and time-consuming trial and error efforts to calibrate their numerous input parameters. The arduous calibration has rendered the use of advanced constitutive models for earthquake geotechnical applications in practice challenging. As a results advanced constitutive models have not been widely adopted in practice despite the significant attention they have received in recent years.

Among the constitutive models developed for earthquake geotechnical applications, most of them have been created to simulate the behavior of liquefiable granular soils, and predict the triggering of liquefaction. In contrast, little work has been done regarding the modeling of cyclic softening of cohesive soils. In addition, the few constitutive models developed to model the behavior of clays under cyclic loading, none consider a dependency on the loading rate due to the complexity of the constitutive laws required to develop a viscoplastic model.

This study's first objective is to evaluate the use of optimization techniques to calibrate soil constitutive models, and improve them for cyclic loading applications. The second objective is to develop a rate-dependent constitutive model that can simulate the behavior of cohesive soils under cyclic loading.

In this dissertation, two optimization algorithms are studied, the Gauss-Newton (GN) and the Particle Swarm Optimization (PSO) algorithms, and applied to calibrate several constitutive models formulated for cyclic applications. Adjustments to the algorithms are presented to improve their efficiency and make them more suitable for the presented application. Several validation

examples are used on a variety of constitutive models, and the conclusion is that these algorithms can ease the calibration procedure and may be considered as efficient, and valuable alternatives to trial and error calibrations.

In the second part of this dissertation, a viscoplastic model is introduced. The model is first formulated in the triaxial space, and generalized for a multiaxial space. The proposed model's constitutive laws are derived by modifying recent advanced constitutive models to capture the strain-rate dependent behavior presented in the literature by various authors. The developed model is validated by comparing the results with a few studies and laboratory cyclic tests performed on a medium plasticity clay sampled in Québec. The proposed model shows the ability to capture the salient features of the soil cyclic behavior, such as cyclic degradation, modulus reduction and damping behavior, and the strain-rate dependency of shear strength presented in the literature.

This dissertation provides practitioners and researchers a means to calibrate advanced constitutive models in an advanced manner and a constitutive model that can be used in nonlinear numerical simulations where clays are expected to undergo strength loss.

TABLE OF CONTENTS

ACKNOWLEDGMENT III

RÉSUMÉ IV

ABSTRACT VI

TABLE OF CONTENTS VIII

LIST OF TABLES XIII

LIST OF FIGURES XV

LIST OF SYMBOLS AND ABBREVIATIONS XXI

LIST OF APPENDICES XXIII

CHAPTER 1 INTRODUCTION 1

CHAPTER 2 CYCLIC RESPONSE OF FINE-GRAINED SOILS 5

2.1 Introduction 5

2.2 Liquefaction and Cyclic Softening 5

2.3 Loading Rate Effects 12

2.4 Effect of Soil Plasticity (*PI*) 13

2.5 Loading Rate Effects on Modus Reduction and Damping Ratios 14

2.6 Cyclic Stiffness Degradation 15

2.7 Anisotropic Consolidation Effects 16

2.8 Cyclic Threshold 17

CHAPTER 3 LITERATURE REVIEW OF SOIL CONSTITUTIVE MODELING 20

3.1 Introduction 20

3.2 Introduction to Constitutive Modeling 20

3.2.1 Stress States 20

3.2.2 Classic Plasticity Theory 22

3.2.3 Critical State Concept 27

3.3 Rate-independent Constitutive Models 28

3.3.1 Modified Cam-Clay (*MCC*) 28

3.3.2 *SANICLAY*- Simple Anisotropic Clay Model 31

3.3.3 SANICLAY-D: *SANICLAY* with Destructuration 34

3.3.4 SANICLAY-B: Bounding Surface *SANICLAY* Model 38

3.3.5 SANICLAY-H: SANICLAY with a Hybrid Flow Rule 42

3.3.6 Dafalias and Manzari (2004) (*DM04*): 46

3.3.7 *PM4SAND*: Plasticity Model for Sands 50

3.3.8 *PM4SILT*: Plasticity Model for Silts 54

3.4 Rate-dependent Constitutive Models 55

3.4.1 A Visco-plastic *SANICLAY* Model 57

3.4.2 *TVP UH*: Thermo-Viscoplastic Unified Hardening Model 59

3.4.3 *AVISA*: an Anisotropic Visco-*ISA* Model 64

CHAPTER 4 CALIBRATION IN CONSTITUTIVE MODELING 69

4.1 Introduction 69

4.2 Gauss-Newton Optimization (*GNO*) 70

4.2.1 Formulation of the *GNO* 70

4.2.2 Cyclic Applications of the *GNO* 74

4.3 Particle Swarm Optimization (*PSO*) 86

4.3.1 Cyclic Applications of *PSO* to Calibrate Three Models Against the Low Plasticity Silt Mixtures 88

4.4 Comparing *PSO* and *GNO* 97

4.5 Summary and Conclusions 102

CHAPTER 5 FORMULATION OF A VISCOPLASTIC CONSTITUTIVE MODEL FOR CLAY CYCLIC BEHAVIOR 104

5.1 Introduction 104

5.2 Model Formulation in Triaxial Space 105

5.2.1 Stress-Strain Definition in Triaxial Space 105

5.2.2 Elastic Response 106

5.2.3 Bounding and Viscoplastic Potential Surfaces 106

5.2.4 Image Stress and Projection Center 109

5.2.5 Viscoplastic Hybrid Flow Rule 111

5.2.6 Relocation of the Static Loading Surface 113

5.2.7 Hardening Variables 114

5.2.8 Plastic Modulus and Damage Variable 115

5.3 Model Generalization in Multiaxial Space 117

5.3.1 Elastic Response 118

5.3.2 Bounding and Viscoplastic Potential Surfaces 118

5.3.3 Image Stress and Projection Center 119

5.3.4 The Viscoplastic Hybrid Flow Rule 121

5.3.5 Hardening Variables 122

5.3.6 Plastic Modulus and Damage Variable 123

5.4 Summary and Conclusions 125

CHAPTER 6 MODEL CALIBRATION AND VALIDATION 126

6.1 Introduction 126

6.2 Calibration of Model Parameters 126

6.2.1 Elasticity Parameters $\boldsymbol{\kappa}$ and $\boldsymbol{\nu}$ 127

6.2.2 Critical State Parameters $\boldsymbol{\lambda}$, $\boldsymbol{Mc}$, and $\boldsymbol{Me}$ 127

6.2.3 Bounding Surface Parameters $\boldsymbol{Nc}$ and $\boldsymbol{Ne}$ 128

6.2.4 Rotational Hardening Parameters $\boldsymbol{\chi}$ and $\boldsymbol{C}$ 128

6.2.5 Plastic Modulus Parameters $\boldsymbol{hc}$ and $\boldsymbol{he}$ and $\boldsymbol{cd}$ 130

6.2.6 Hybrid Flow Rule Parameters $\boldsymbol{\omega}$ and $\boldsymbol{mg}$ 131

6.2.7 Viscos Parameters $\boldsymbol{\mu 1}$ and $\boldsymbol{\mu 2}$ 132

6.3 Model's Performance, Calibration, and Validation 133

6.3.1 Model's monotonic and Cyclic performance 133

6.3.2 Simulation of the Glacio-Lacustrine Clay Cyclic Behavior 139

6.3.3 Simulation of Rate-Dependent Undrained Shear Behavior of Saturated Boston Blue Clay 145

6.3.4 Simulation of Rate Effects on Undrained Shear Strength of Sensitive Grande-Baleine Clay (Lefebvre and LeBoeuf, 1987) 153

6.3.5 Simulation of Rate Effects on Damping and Modulus Reduction of Normally Consolidated Kaolin Clay (Shibuya et al., 1995) 157

6.3.6 Simulation of Cyclic Behavior of Sensitive Saint-Adelphe Clay at Different Loading Frequencies (Abdellaziz et al., 2017) 161

6.4 Summary and Conclusions 164

CHAPTER 7 SUMMARY, CONCLUSIONS, AND FUTURE RESEARCH RECOMMENDATIONS 165

7.1 Summary and Conclusions 165

7.2 Recommendations for Future Research 167

7.2.1 Model Implementation into *FLAC* 167

7.2.2 Model Validation Against an Experimental Program 167

7.2.3 Pre-calibrating the Model 168

7.2.4 Application of the Model to a Case History 168

REFERENCES 169

APPENDICES 180

LIST OF TABLES

Table 3.1: Constants of the *SANICLAY* (Dafalias et al., 2006) 34

Table 3.2: Constants of the *SANICLAY* with destructuration (Taiebat et al., 2010) 37

Table 3.3: Constants of the *SANICLAY-B* (Seidalinov and Taiebat, 2014) 41

Table 3.4: Parameters of the model (Shi et al., 2018) 45

Table 3.5: Summary of the Dafalias and Manzari model's equations (Dafalias and Manzari, 2004) 48

Table 3.6: Summary of the model constants (Dafalias and Manzari, 2004) 49

Table 3.7: Input parameters of the visco-plastic *SANICLAY* (Rezania et al., 2006) 59

Table 3.8: Input parameters of the *UH TVP* (Kong et al., 2020) 63

Table 3.9: Summary of *AVISA* input parameters (Tafili and Triantafyllidis, 2020) 67

Table 4.1: *SANICLAY-B* input parameters used in numerical simulations. 76

Table 4.2 The *DM04* model parameters used in numerical simulations. 78

Table 4.3 *SANICLAY-H* parameters used in numerical simulations. 83

Table 4.4: Properties of the mixture tested in the laboratory (Eslami, 2017) 88

Table 4.5: Model parameters calibrated by *PSO* 93

Table 4.6: Model parameters calibrated by *GNO* 98

Table 6.1. Initial conditions 134

Table 6.2. Model input parameters 134

Table 6.3 Model input parameters for Glacio-Lacustrine Clay 141

Table 6.4: Summary of $CK0UC$ tests on normally consolidated *BBC* (Sheahan et al., 1996) 145

Table 6.5 Summary of $CK0UC$ tests on over-consolidated *BBC* (Sheahan et al., 1996) 146

Table 6.6 Model input parameters for *BBC* 147

Table 6.7 Model input parameters for Grande-Baleine clay 154

Table 6.8 Model input parameters for normally consolidated Kaoling clay.....159

Table 6.9 Model input parameters for Saint-Adelphe clay 162

LIST OF FIGURES

Figure 2.1 Monotonic normalized stress-strain behavior as a function of *OCR* (Boulanger and Idriss, 2006; Ladd and Foott, 1974) for clay-like fine-grained soils.....6

Figure 2.2 Cyclic normalized strength versus plasticity index (Boulanger and Idriss, 2007) 7

Figure 2.3 Cyclic stress ratio versus the number of cycles to reach 3% shear strain for different clays, mainly normally consolidated or slightly overconsolidated (OCR=2), (Boulanger and Idriss, 2007).....8

Figure 2.4 Cyclic stress ratio versus the number of cycles to reach (a) initial liquefaction (b) 5% shear strain for clean sands (Ziotopoulou and Boulanger, 2012).....8

Figure 2.5 Stress-strain response and effective stress paths of Sacramento River sand under cyclic loading (Boulanger and Truman, 1996). 9

Figure 2.6 Stress-strain response and effective stress paths of Cloverdale clay under cyclic loading (Zergoun and Vaid, 1994). 9

Figure 2.7 Stress-strain response and effective stress paths of normally consolidated silt mixtures *#1* (a) and *#3* (b) under cyclic loading (Boulanger and Idriss, 2006; Romero, 1995) 10

Figure 2.8 Comparisons of the critical state (*CSL*), isotropic consolidation (*ICL*), and quasisteady state lines (*QSSL*) of soils with sand-like and clay-like behavior (Romero, 1995) 11

Figure 2.9 The critical state line (*CSL*) and isotropic consolidation lines (*ICL*) for Toyoura sand in loose and dense states (Verdugo and Ishihara, 1996) 12

Figure 2.10 Normalized (a) shear strength and (b) shear-induced pore pressure versus axial strain rate (Sheahan et al., 1996).....13

Figure 2.11 Shear modulus reduction (a) and equivalent damping ratio (b) versus shear strain for clays (Vucetic and Dobry, 1989).....13

Figure 2.12 Strain rate effects on (a) shear modulus (Lo Presti et al., 1996) and (b) damping ratio (Lo Presti et al., 1997).....15

Figure 2.13 Shear modulus of San Francisco Bay Mud at various strain rates (Isenhower and Stokoe, 1981) 15

Figure 2.14 Degradation index versus the number of cycles for different *OCR* values (Vucetic and Dobry, 1988) 16

Figure 2.15 Cyclic shear stress (a) and total undrained shear stress (b) as a function of the number of cycles for initial static shear stress range of 0 to 0.8 Cu (Lefebvre and Pfendler, 1996) ..17

Figure 2.16 Stress path of a normally consolidated clay under cyclic loading followed by monotonic loading after stabilization (Lefebvre et al., 1989) 18

Figure 2.17 Stability threshold versus frequency (Lefebvre et al., 1989). 18

Figure 2.18 Threshold shear strains for (a) cyclic degradation and (b) pore water pressure (Mortezaie and Vucetic, 2016). 19

Figure 3.1: Schematic of the yield surface and the elastic region (Wood, 2014) 24

Figure 3.2: *CSL* in *p-q* (a) and *p-v* (b) space (Wood, 1990).....27

Figure 3.3: The original and modified Cam-Clay in *p-q* space (Eslami, 2017).....29

Figure 3.4: Simulations of the *MCC* with different *OCRs* (Yniesta, 2016). 31

Figure 3.5 *SANICLAY* Surfaces in triaxial stress space (Dafalias et al., 2006).....32

Figure 3.6 Comparison of data and simulations for undrained plane strain compression tests on a clay using the *SANICLAY* model (Dafalias et al., 2006).....34

Figure 3.7 Illustration of the effects of isotropic and frictional destructuration mechanism independently and in combination. (Taiebat et al., 2010).....38

Figure 3.8 Plastic potential, bounding, and loading surfaces of the *SANICLA-B* model in the *p-q* stress space (Seidalinov and Taiebat, 2014).....39

Figure 3.9 The SANICLAY-B model simulations (Seidalinov and Taiebat, 2014).....42

Figure 3.10 Schematic diagram of plastic flow vectors at the current stress (R_c) and image stress (R_i) (Shi et al., 2018). 43

Figure 3.11 Illustration of the bounding surface and the damage parameter effects in the simulation of undrained cyclic triaxial loading (Shi et al., 2018) 45

Figure 3.12: Schematic of the yield, critical, dilatancy, and bounding lines in *p-q* space (Dafalias and Manzari, 2004) 46

Figure 3.13: Numerical and experimental results of undrained compression tests on Toyoura sand at different effective confining pressures and initial void ratios (Dafalias and Manzari 2004). 49

Figure 3.14: Simulation and experiment results for Toyoura sand (Dafalias and Manzari 2004). 50

Figure 3.15: Schematic of the bounding, dilatancy, and yield surfaces on the stress-ratio plane Boulanger and Ziotopoulou (2017, version 3.1). 51

Figure 3.16: Undrained cyclic *DSS* loading response of *PM4SAND* for sands with three different relative densities Boulanger and Ziotopoulou (2017, version 3.1). 53

Figure 3.17: Undrained cyclic *DSS* loading response of *PM4SILT* for silt with three different normalized strength ratios Boulanger and Ziotopoulou (2018). 55

Figure 3.18: Schematic of the static and dynamic loading surfaces, elastic and viscoplastic regimes in Perzyna's model (Karim and Gnanendran, 2014) 57

Figure 3.19: Schematic illustration of the visco-plastic *SANICLAY* model (Rezania et al., 2006). 58

Figure 3.20: Undrained monotonic simulations of visco-plastic *SANICLAY* (Rezania et al., 2006) 59

Figure 3.21: Parallel line concepts for time and temperature (Kong et al., 2020). 60

Figure 3.22: The schematic illustration of the current and reference yield surface used in the *UH TVP* model (Kong et al., 2020). 61

Figure 3.23: Undrained triaxial and isotropic simulations with the *UH EVP* model (Kong et al., 2020) 63

Figure 3.24: Schematic of the yield and bounding surface of the extended *ISA* (*AVISA* model) (Tafili and Triantafyllidis, 2020).....65

Figure 3.25: *AVISA* predictive ability (in red) at different loading rates against experiments (in blue) (Tafili and Triantafyllidis, 2020). 67

Figure 3.26: *AVISA* predictive ability (in red) against experiments (in blue) in simulating the hysteresis loops at two different loading rates (Tafili and Triantafyllidis, 2020).....68

Figure 4.1: Flowchart of the *GNO* algorithm.....73

Figure 4.2: Comparison of the performance of the calibration of the *SANICLAY-B* model against Georgia Kaolin clay test data for the initial guess calibration (a, b, c, d), the calibration after 30 iterations (e, f, g, h), and after 60 iterations (i, j, k, l). 76

Figure 4.3: Stress-strain and stress-path responses for Ottawa *F65* sand at varying cyclic strain amplitudes: (a, b) ε_a = 0.21% (c, d) ε_a = 0.32%, and (e, f) ε_a = 0.42%.....79

Figure 4.4: Deviatoric stress and excess pore pressure ratio versus number of uniform loading cycles for Ottawa *F65* sand at various cyclic strain amplitudes: (a, b) ε_a = 0.21% (c, d) ε_a = 0.32%, and (e, f) ε_a = 0.42%. 80

Figure 4.5: Cyclic axial strain versus the number of uniform loading cycles for Ottawa *F65* sand. 81

Figure 4.6: Measured and predicted response of Young Bay Mud for Cyclic *DSS* loading and *SANICLAY-B* simulation when calibrated based on shear strain. 84

Figure 4.7: *CSR* versus the number of loading cycles for San Francisco Young Bay Mud from laboratory tests and simulations of the *SANICLAY-H* with varying modified calibration approaches.....86

Figure 4.8 Flowchart of the *PSO* algorithm 87

Figure 4.9 Results of a *DSS* laboratory cyclic shearing on *SBFW* (Eslami, 2017). 90

Figure 4.10 Comparison between models' simulations calibrated using *PSO* and results of *DSS* laboratory cyclic shearing (*CSR_0.120*).....95

Figure 4.11 Comparison between models' simulations calibrated using *PSO* and results of *DSS* laboratory cyclic shearing (*CSR_0.178*).....96

Figure 4.12 Comparison of *CSR vs. N* curves (*N*@γ=1%) from experimental results and model simulations calibrated using *PSO*.....97

Figure 4.13 Comparison of *CSR vs. N* curves (*N*@γ=5%) from experimental results and model simulations calibrated using *PSO*.....97

Figure 4.14 Comparison between *DM04* simulations and results of *DSS* laboratory cyclic shearing (*CSR_0.157*). 100

Figure 4.15 Comparison of *CSR vs. N* curves (*N*@γ=3%) from experimental results and model simulations (a) *SANICLAY-B* (b) *DM04* 101

Figure 5.1 Schematic of bounding, dynamic, and static loading surfaces of the *BS-EVP* model. 107

Figure 5.2 Schematic of the viscoplastic surface of the *BS-EVP* model.....109

Figure 5.3 Schematic of the hybrid flow rule applied to the *BS-EVP* model.....113

Figure 6.1 Effects of hc and he on the initial stiffness of the hysteresis loops 131

Figure 6.2 Model response at different cd values.....131

Figure 6.3 Influence of ω on the stress path and the excess pore water pressure generation.....132

Figure 6.4 Undrained monotonic triaxial compression tests simulated by the *BS-EVP* model at different *OCRs* and loading rates. 135

Figure 6.5 Effective stress path and the hysteresis loops of stress-controlled undrained cyclic triaxial tests simulated by the *BSVP* model.....137

Figure 6.6 Effective stress path and the hysteresis loops of strain-controlled undrained cyclic triaxial tests simulated by the *BSVP* model.....138

Figure 6.7 (a) One-dimensional compression test results and (b) effective stress path from undrained triaxial tests on Glacio-Lacustrine Clay (Bonin et al., 2019).....140

Figure 6.8 Simulation and experimental results of the Glacio-Lacustrine clay, *CSR=0.33*, (experimental data from Bonin et al. (2019)). 142

Figure 6.9 Simulation and experimental results of the Glacio-Lacustrine clay, *CSR=0.26*, (experimental data from Bonin et al. (2019)). 143

Figure 6.10 *CSR-N* cures from simulations and experiments for the Glacio-Lacustrine clay (experimental data from Bonin et al. (2019)). 144

Figure 6.11 Simulations and experimental results in terms of normalized shear stress versus Axial strain for $CK0UC$ tests on resedimented *BBC*. 149

Figure 6.12 Simulation and experimental results in terms of normalized effective stress paths of $CK0UC$ tests on resedimented *BBC*. 150

Figure 6.13 Simulation and experimental results in terms of normalized pore water pressure versus axial strain for $CK0UC$ tests on resedimented *BBC*. 151

Figure 6.14 Normalized shear strength versus the deviatoric shear strain at different strain rates for $CK0UC$ tests on resedimented *BBC* 152

Figure 6.15 Stress-deformation curves and Stress path of the Grande-Baleine clay (simulations versus experiments) 155

Figure 6.16 Simulation of strain rate effects on destructured and structured specimens of the Grande-Baleine 156

Figure 6.17 Hysteresis loops of strain-controlled cyclic loading tests at two different amplitudes (Shibuya et al., 1995) 157

Figure 6.18 Shear modulus and hysteretic damping curves the Kaolin clay: (a) experiments Shibuya et al. (1995) (b) simulations 160

Figure 6.19 Model simulations and cyclic test results (Abdellaziz et al., 2017) on the Saint-Adelphe clay: (a) *PWP* ratio versus *N* (b) *CSR* versus *N*. 163

Figure A.1 Comparison between models' simulations calibrated using *PSO* and results of *DSS* laboratory cyclic shearing on *SBFW* (*CSR_0.178*) 180

Figure A.2 Comparison between models' simulations calibrated using *PSO* and results of *DSS* laboratory cyclic shearing on *SBFW* (*CSR_0.161*) 181

Figure A.3 Comparison between models' simulations calibrated using *PSO* and results of *DSS* laboratory cyclic shearing on *SBFW* (*CSR_0.149*) 182

Figure A.4 Comparison between models' simulations calibrated using *PSO* and results of *DSS* laboratory cyclic shearing on *SBFW* (*CSR_0.137*) 183

Figure A.5 Comparison between models' simulations calibrated using *PSO* and results of *DSS* laboratory cyclic shearing on *SBFW* (*CSR_0.126*) 184

Figure A.6 Comparison between models' simulations calibrated using *PSO* and results of *DSS* laboratory cyclic shearing on *SBFW* (*CSR_0.161*) 185

Figure A.7 Comparison between models' simulations calibrated using *PSO* and results of *DSS* laboratory cyclic shearing on *SBFW* (*CSR_0.186*). 186

Figure A.8 Comparison between simulations of *DM04* and *SANICLAY-B* calibrated using GNO with results of *DSS* laboratory cyclic shearing (*CSR_0.149*).....187

Figure A.9 Comparison between simulations of *DM04* and *SANICLAY-B* calibrated using GNO with results of *DSS* laboratory cyclic shearing (*CSR_0.161*).....188

Figure A.10 Comparison between simulations of *DM04* and *SANICLAY*-B calibrated using GNO with results of *DSS* laboratory cyclic shearing (*CSR_0.180*).....189

Figure A.11 Comparison between simulations of *DM04* and *SANICLAY-B* calibrated using GNO with results of *DSS* laboratory cyclic shearing (*CSR*_0.*186*).....190

Figure A.12 Comparison between simulations of *DM04* and *SANICLAY-B* calibrated using GNO with results of *DSS* laboratory cyclic shearing (*CSR*_0.126).....191

Figure A.13 Comparison between simulations of *DM04* and *SANICLAY-B* calibrated using GNO with results of *DSS* laboratory cyclic shearing (*CSR*_0.155).....192

LIST OF SYMBOLS AND ABBREVIATIONS

AVISA	An anisotropic visco-ISA model
BBC	Boston blue clay
BSEVP	Bounding surface elasto-viscopastic
CLTST	Cyclic torsional shear tests
CSL	Critical state line
CSR	Cyclic stress ratio
DM04	Dafalias and Manzari model (2014)
DSS	Direct simple shear
GNO	Gauss-Newton optimization
ICL	Isotropic consolidation line
LL	Liquid limit
MCC	Modified Cam-Clay
OCR	Overconsolidatio ratio
PI	Plasticity index
PL	Plastic limit
PM4SAND	Plasticity model for sands
PM4SILT	Plasticity model for clays
PSO	Particle swarm optimization
PWP	Pore water pressure
QSSL	Quassi steady state line
RCT	Resonant column test
SANICLAY	Simple anisotropic clay model
SANICLAY-B	Bounding surface SANICLAY model

SANICLAY-D	SANICLAY with destructuration
SANICLAY-H	SANICLAY with a hybrid flow rule
SBFW	Silt Bentonite fresh water
UBCSAND	University of Biritsh Columbia sand model
USCS	Unified soil classification system
UHTVP	Unified hardening thermo-viscop plastic model

LIST OF APPENDICES

Appendix A – Model Calibrations against SBFW mixtures using *PSO* and *GNO*.....180

SELECTED PUBLICATIONS

Journal papers:

Zarrabi, M., Eslami, M.M., and Yniesta, S. "Cyclic application of an Advanced Calibration Algorithm to Three Cyclic Bounding Surface Soil Constitutive Models." (under review at ASCE's International Journal of Geomechanics).

Zarrabi, M., Eslami, M.M., and Yniesta, S. "Experimental and Numerical Investigations of Low Plasticity Soil Mixtures under Cyclic Loading using Three Constitutive Models." (to be submitted to the Canadian Geotechnical Journal).

Zarrabi**,** M., Shi, Z., Yniesta, S., and Buscarnera, G. "A Viscoplastic Bounding Surface Model for Cyclic Softening." (to be submitted to the International Journal for Numerical and Analytical Methods in Geomechanics).

Conference Papers:

Zarrabi, M., Shi, Z., Yniesta, S., and Buscarnera, G. (2020) "Simulation of the Cyclic Response of Anisotropic Clay through Bounding Surface Viscoplasticity". GeoVirtual, Canada.

Zarrabi, M., and Yniesta, S. (2019). "Recent Advanced Constitutive Models for Liquefaction and Cyclic Softening Analysis". Geo-St.John’s, Newfoundland, Canada.

Eslami, M.M., Zarrabi, M., and Yniesta, S. (2019). "Evaluation of Two Constitutive Models in Predicting Cyclic Behavior of a Natural Clay". 7th International Conference on Earthquake Geotechnical Engineering, Rome, Italy.

Eslami, M.M., Zarrabi, M., and Yniesta, S. (2019) "Performance of Bounding Surface Constitutive Models in Predicting Cyclic Behavior of Low-Plasticity Fine-Grained Soils". Geo-Congress, Phi

CHAPTER 1 INTRODUCTION

There can be several phenomena occurring in soils under earthquake loading, among which "liquefaction" is the most well-understood. Liquefaction is characterized as a loss of shear strength due to pore water pressure generation and can happen in granular soils (Jefferies and Been, 2015). However, cyclic softening of fine-grained soil can be as disastrous but studied to a lesser extent (Boulanger and Idriss, 2007). Albeit the mechanisms are similar, there exist fundamental differences between liquefaction and cyclic softening. In both cases, soils experience a loss of shear strength, usually accompanied by severe deformations.

For example, liquefaction-induced damages to human-made and natural earth structures followed by loss of human properties and lives reported in many major earthquakes such as the 1964 Niigata earthquake (Seed and Idriss, 1971) and the 2011 Christchurch earthquake (Bradley and Cubrinovski, 2011) to name a few). Similarly, the evidence of such strength loss in materials with clay-like behavior has been reported in a few case histories (such as the fourth avenue landslide during the 1964 Alaskan earthquake (Stark and Contreras, 1998)).

The study of the aforementioned phenomena, as well as other geotechnical problems, requires numerical simulations. However, the validity of the numerical simulations is positively related to the applied constitutive models. Therefore, several models have been emerged so far based on different assumptions to predict more realistically the behavior of soils for different problems.

The modified Cam-Clay model (Roscoe and Burland, 1968) is one of the earliest models that are still popular among practitioners due to its simplicity. Recently, a family of models called SANICLAY (Dafalias et al., 2006; Taiebat et al., 2010;) built upon the modified Cam-Clay to simulate more accurately the behavior of clays under monotonic loading. The SANICLAY model family has provided a powerful tool for capturing several key features of clays, such as anisotropy and destructuration, but their applications are limited to monotonic loading cases. To extend the SANICLAY model family for cyclic loading applications, Seidalinov and Taiebat (2014) and Shi et al. (2018) developed two models by recasting the SANICLAY framework into the bounding surface plasticity and provided valuable tools to investigate the potential of failure of clays under cyclic loading. However, compared to the significant amount of work done on the constitutive

modeling of granular soils with liquefaction susceptibility (e.g., Dafalias and Manzari, 2004; UBCSAND (Beaty and Byrne, 2011), PM4SAND (Boulanger and Ziotopoulou, 2017)), much less attention has been given to the modeling of clays under cyclic loading. In addition, none of the developed models for cyclic clay behavior takes into account the effect of loading time or loading rates in their formulation.

In addition, although advanced soil models could simulate soil response more accurately, the challenges associated with their calibration could prevent them from being widely used in practice. One of the common limitations of the constitutive models that renders their application challenging for practitioners is that they include numerous input parameters. The calibration of these input parameters requires field data and/or several laboratory tests under different loading and drainage conditions, which may often be unavailable. On the other hand, in cases where sufficient field and lab data are available, the calibration of the myriad of input parameters to match the soil behavior under different types of loading conditions is a challenging task (Yang and Elgamal, 2003), because of their combined effect on the volumetric and deviatoric behavior. Hence finding the optimal parameters using a trial and error procedure can be a time-consuming task. Therefore, a systematic, efficient, and convenient tool is required to calibrate a model based on a large body of literature and data to tackle the calibration difficulties, especially for sophisticated models developed for cyclic loading applications.

The general objective of this study is, firstly, to modify optimization techniques to be used as alternatives for trial and error efforts to calibrate models developed for cyclic loading applications, and secondly, to introduce a robust constitutive model to capture clays' behavior under cyclic loading while considering loading rate/frequency effects. Therefore, the specific objectives of this dissertation could be stated as:

1- Modify and adjust the optimization techniques to calibrate soil constitutive models for cyclic loading applications.

2- Evaluate the performance of the optimization techniques as alternations for trial and error calibrations.

3- Develop a viscoplastic constitutive model for clays under cyclic loading.

4- Provide guidance for the calibration of the input parameters of the developed model.

5- Calibrate the developed model using the provided guideline and the optimization techniques.

6- Validate the model against the experimental data published in the literature.

In addition to this introduction, this dissertation is composed of six chapters, the organization of which is as follows:

In the 2nd chapter, the underlying features of fine-grained soils' behavior, i.e., silts and clays, under seismic loading are reviewed so that the behavior necessary for the development of a constitutive model be adequately distinguished. This chapter's main topics could be summarized as liquefaction and cyclic softening, the difference between soils exhibiting clay-like and sand-like behavior, loading rate effects, and the effects of soil plasticity on modulus reduction and damping ratio curves.

Chapter 3 of this dissertation is divided into two main parts; In the first part, a short review of the following subjects needed to understand soil constitutive models are presented: the Cauchy stress and strain tensors along with their invariants, the critical state soil mechanics, and an introduction to classic elastoplasticity. In the second part of this chapter, a literature review on soil constitutive models is presented. The presented constitutive models in this part include rate-independent models for cyclic loading applications developed mainly for clays (mainly upon the MCC and SANICLAY framework), and less, for sands and silts. At the end of this chapter, some rate-dependent models are reviewed and discussed.

The 4th chapter of this dissertation mainly discusses the application of two sophisticated optimization techniques to calibrate advanced soil constitutive models. In the first part of this chapter, the Gauss-Newton Optimization (GNO) algorithm is discussed and applied to calibrate two soil constitutive models for cyclic loading applications (one for sands, namely the Dafalias and Manzari model, and one for clays, the SANICLAY bounding surface model) against different data sets. In the second part of this chapter, the Particle Swarm Optimization (PSO) algorithm is reviewed and applied to calibrate three soil models, the SANICLAY with a hybrid flow rule, and two models mentioned above. In both parts of this chapter, the predictive abilities of the models

are discussed and compared. In addition, the performance of the applied optimization algorithms in calibrating advanced soil constitutive models is compared in the final part of this chapter.

In the 5th chapter of the dissertation, the formulation of the proposed model is presented. The model developed in this study combines several underlying features and concepts such as the isotropic hardening rule to consider soil consolidation state, the rotational hardening rule for simulating soil anisotropy induced by stress history, the bounding surface with the proper relocation of the projection center, a decaying plastic modulus to capture the soil behavior under cyclic loading, a hybrid flow rule to improve the pore water pressure generation of the model in a cyclic event, and Perzyna's theory of viscoplasticity, to name a few, to allow the model to capture time or loading rate effects. The model formulation is first discussed regarding the triaxial space. Then, its formulation with respect to a generalized multiaxial space is presented.

The 6th chapter of this dissertation discusses the model calibration and validation. In the first part of this chapter, the calibration of the parameters of the developed model is presented by providing explanations for the physical meaning of the parameters and discussing the appropriate tests and closed-form solutions to obtain the parameters. In the second part of this chapter, first, the performance of the model in simulating the soil response under monotonic and seismic loading is presented, and then, the model is calibrated and validated against a series of experimental data.

The final chapter of this dissertation presents a summary, conclusions, and future research recommendations.

CHAPTER 2 CYCLIC RESPONSE OF FINE-GRAINED SOILS

2.1 Introduction

In this chapter, the main features of fine-grained soils' behavior, i.e., silts and clays, under seismic loading, are described. Overall, clayey material's cyclic behavior has been less studied than that of sandy soils, and a significant amount of work remains to be done. However, essential features have been clearly identified and defined, and these are sufficient for the development of a constitutive model.

2.2 Liquefaction and Cyclic Softening

Boulanger and Idriss (2006) suggested that the significant strength loss or strain development accompanied by a sharp increase in the excess pore water pressure be referred to as “liquefaction” for fine-grained-soils exhibiting sand-like behavior, while the same phenomenon be referred to as “cyclic softening” for those exhibiting clay-like behavior (Leboeuf et al., 2016). Either a soil is showing a clay-like or a sand-like behavior may be found out in different ways.

One key feature that differentiates the behavior of clay-like soils from that of the sand-like soils is the monotonic strength normalization. Soils exhibiting a clay-like behavior have a unique ratio of monotonic undrained shear stress over the consolidation pressure ratio $\left(\frac{s_u}{\sigma_{vc}}\right)$ which is highly dependent on the soil overconsolidation ratio (*OCR*) (Ladd, 1991; Ladd and Foott, 1974), as illustrated in Figure 2.1.

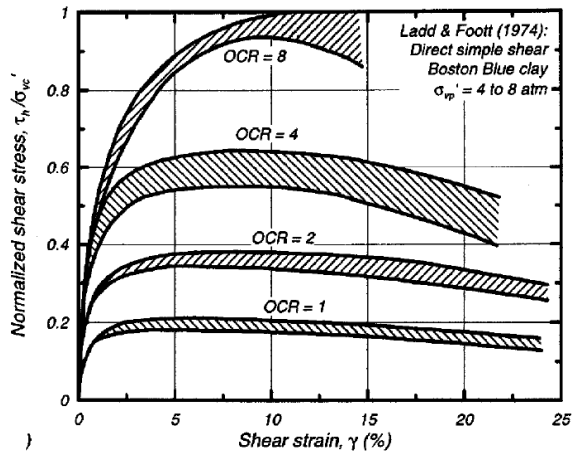

Figure 2.1 Monotonic normalized stress-strain behavior as a function of *OCR* (Boulanger and Idriss, 2006; Ladd and Foott, 1974) for clay-like fine-grained soils.

This figure shows the monotonic strength normalization $\left(\frac{\tau_h}{\sigma_{vc}}\right)$ versus the shear strain (γ) for various *OCR*. Ladd and Foott (1974) expressed the monotonic strength normalization relation with *OCR* as:

$$\frac{s_u}{\sigma_{vc}} = S \cdot OCR^m \tag{2.1}$$

Where *S* is the ratio $\left(\frac{s_u}{\sigma_{vc}}\right)$ at *OCR*=1 and *m* is the slope of the $\left(\frac{s_u}{\sigma_{vc}}\right)$ versus *OCR* relation in a log-log plot.

Similar to monotonic strength normalization, Boulanger and Idriss (2007) showed that, for soils exhibiting a clay-like behavior, the cyclic strength ratio ($\frac{\tau_{cyc}}{s_u}$) remains constant at different soil plasticity values (*PI*). The cyclic normalized strength versus the soil plasticity (*PI*) is shown in Figure 2.2 (a). Boulanger and Idriss (2007) stated that the cyclic strength ratio $\left(\frac{\tau_{cyc}}{s_u}\right)$ for *N*=30 cycles ($(\frac{\tau_{cyc}}{s_u})_{N=30}$) be taken as 0.83 for normally consolidated clays. The same trend has also reported for $\frac{\tau_{cyc}}{\sigma_{vc}}$ (Figure 2.2 (b)) in which $(\frac{\tau_{cyc}}{\sigma_{vc}})_{N=30}$ of 0.183 is suggested for normally consolidated specimens.

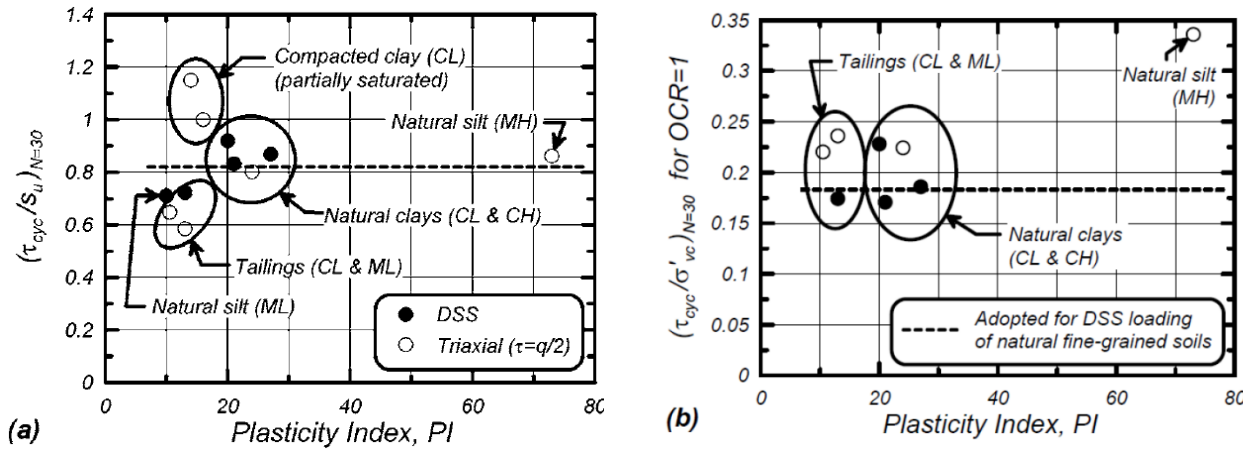

Figure 2.2 Cyclic normalized strength versus plasticity index (Boulanger and Idriss, 2007)

Whether a soil exhibits a clay-like or a sand-like behavior could also be understood from the cyclic stress ratio (*CSR*) versus the number of loading cycles to reach large deformations (3% shear strain, for example). *CSR-N* for soils with clay-like behavior is illustrated in Figure 2.3. For clay-like soils, $\frac{q_{cyc}(=\sigma_1-\sigma_3)}{2S_u}$ or $\tau_{cyc}/\ S_u$ falls within a narrow range for normally consolidated clays. However, such a narrow range in terms of the cyclic strength (or stress) ratio is not reported for sands; As illustrated in Figure 2.4, the *CSR-N* for sand-like soils, which is expressed in the form of $CSR = a \cdot N^b$, where *N* is the number of cycles and *a* and *b* are fitting parameters, is highly dependent on the relative density and is not limited to a narrow range (Boulanger and Idriss, 2007).

The behavior of a sand-like soil under cyclic loading is shown by Boulanger and Truman (1996) in Figure 2.5. In a cyclic event, sands tend to have sharp stress-strain loops and reach zero stiffness (the stress-strain loops becomes almost flat) during cyclic loading once the soil has liquefied. More importantly, their mean effective stress can reach zero due to the excess pore water pressure ratio (r_u), reaching 100%.

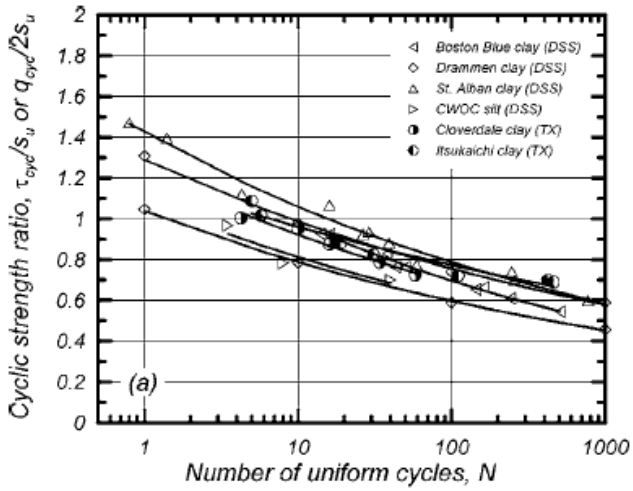

Figure 2.3 Cyclic stress ratio versus the number of cycles to reach 3% shear strain for different clays, mainly normally consolidated or slightly overconsolidated (OCR=2), (Boulanger and Idriss, 2007).

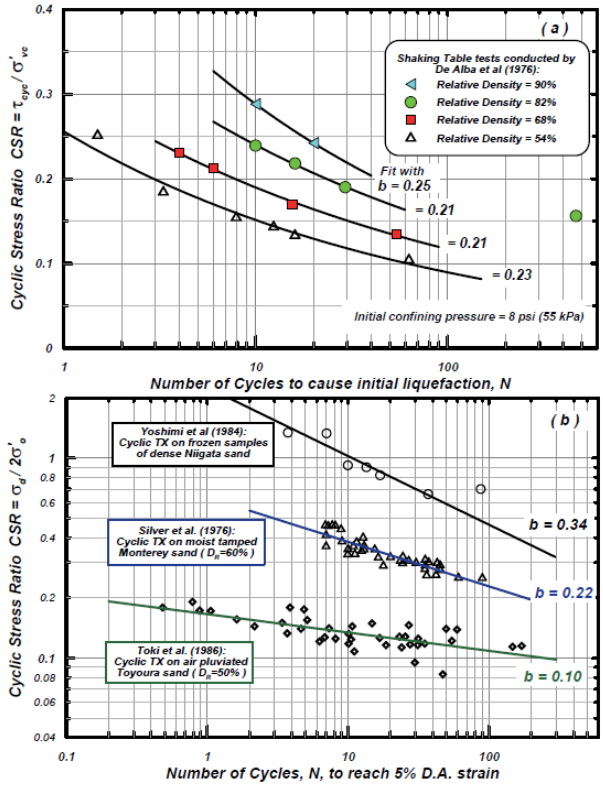

Figure 2.4 Cyclic stress ratio versus the number of cycles to reach (a) initial liquefaction (b) 5% shear strain for clean sands (Ziotopoulou and Boulanger, 2012).

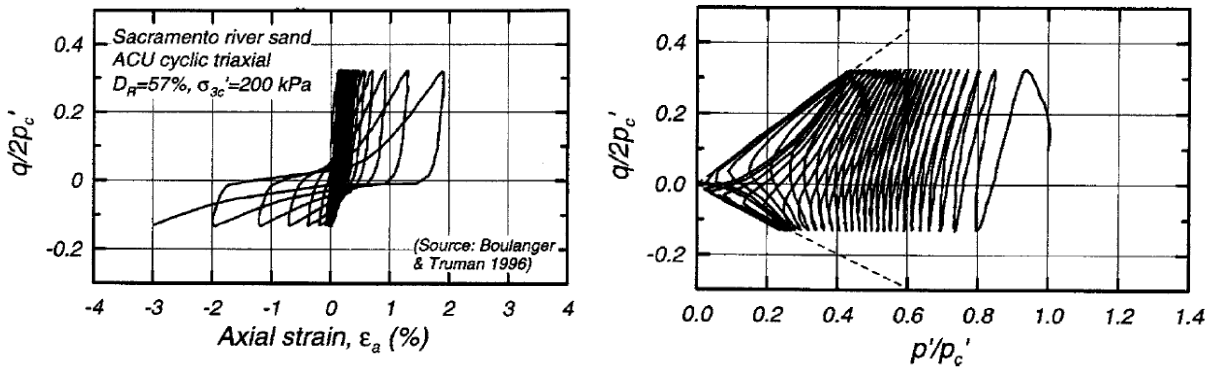

Figure 2.5 Stress-strain response and effective stress paths of Sacramento River sand under cyclic loading (Boulanger and Truman, 1996).

However, soils with clay-like behavior have a slightly different response to cyclic loading. For example, the response of Cloverdale clay under cyclic loading, presented by Zergoun and Vaid (1994), is shown in Figure 2.6. As opposed to sands, hysteretic loops are thicker for clays, and their stiffness does not reduce to zero as loops do not become flat when the cycles reach zero after the softening. Moreover, the cyclic loading generates pore water pressure and reduces the mean effective stress but not to a level sufficient to cancel the mean effective stress completely.

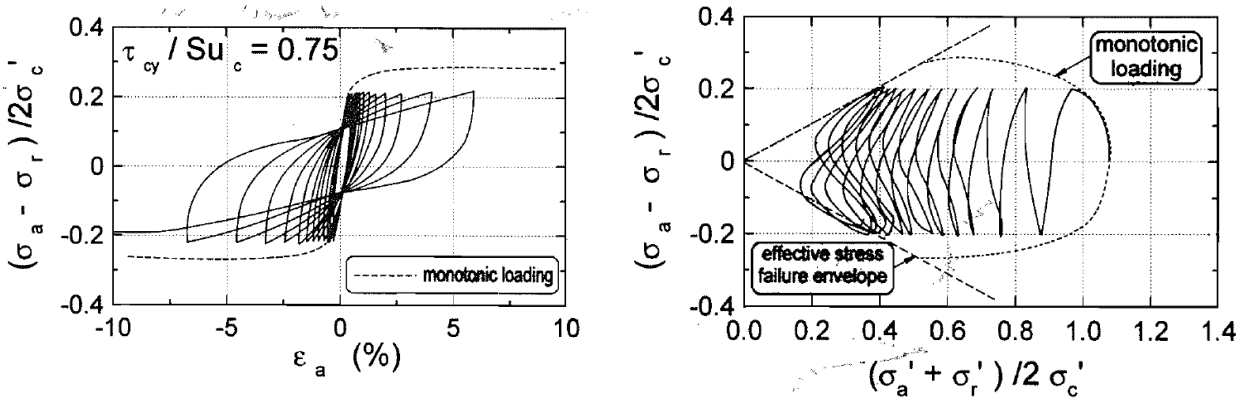

Figure 2.6 Stress-strain response and effective stress paths of Cloverdale clay under cyclic loading (Zergoun and Vaid, 1994).

As discussed, both liquefaction and cyclic softening are susceptible to occur in soils depending on whether they are showing a clay-like behavior or a sand-like behavior (Boulanger and Idriss, 2006). Boulanger and Idriss (2006) discussed cyclic tests' results on three blended silt mixtures tested in

undrained triaxial tests by Romero (1995). The three silt mixtures *#1*, *#2*, and *#3* were classified as *ML* and had Plasticity Indexes of *PI=0, 4, 10.5*, respectively. The undrained cyclic stress-strain paths of the normally consolidated specimens of silt 1 and 3 are plotted in Figure 2.7.

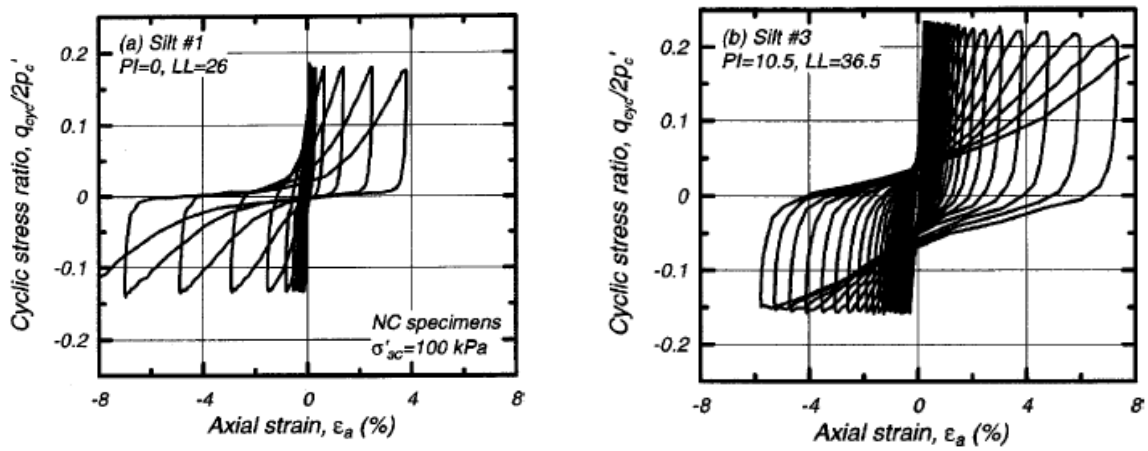

Figure 2.7 Stress-strain response and effective stress paths of normally consolidated silt mixtures *#1* (a) and *#3* (b) under cyclic loading (Boulanger and Idriss, 2006; Romero, 1995)

From this figure, it can be clearly observed that silt #1, with zero plasticity, exhibited sharp stress-strain loops with almost zero-stiffness intervals while silt #3 exhibited the opposite behavior, i.e., broader hysteretic loops without developing stiffness equal or near to zero. These cyclic responses are those that can be observed for sands and clays, respectively. It is worth mentioning that Silt #2, not shown in the figure, has been reported to have intermediate hysteretic behavior.

Boulanger and Idriss (2006) illustrated the transition behavior of these silt mixtures from clay-like behavior to a sand-like one in terms of the critical state line (*CSL*) and the isotropic consolidation line (*ICL*) (Figure 2.8). As shown in this figure, Silt #3 has a *CSL* parallel to *ICL*, and a phase transformation tendency did not exhibit (i.e. there is no quasi-steady state line (*QSSL*)), which is typical of a clay-like behavior, especially for normally consolidated clays. In silt #1, the critical state and the isotropic consolidated lines are not parallel. Also, it exhibited a *QSSL*, indicating a tendency for a phase transformation from contraction to dilation before reaching the critical state line, which is below the isotropic consolidated line. Silt #2 showed an intermediate behavior in a way that the *ICL* and *CSL* are almost parallel, and at the same time, a phase transformation tendency is exhibited (with *QSSL* being located below the *CSL*).

It should be mentioned that the goal of this comparison was to compare a transition behavior, from clay-like to sand-like, in a cyclic loading as the plasticity index decreases. In fact, other factors could influence the position of *CSL* and *ICL*, especially in sands. As shown in Figure 2.10 for Toyoura sand, the isotropic consolidation line could be either below or above the critical state line depending on the initial state of the soil (Verdugo and Ishihara, 1996; Been et al., 1991; Biarez and Hicher, 1994). Also, as can be seen in this figure, the *ICL* may be either parallel to the *CSL*, for loose states, or unparallel, for dense states.

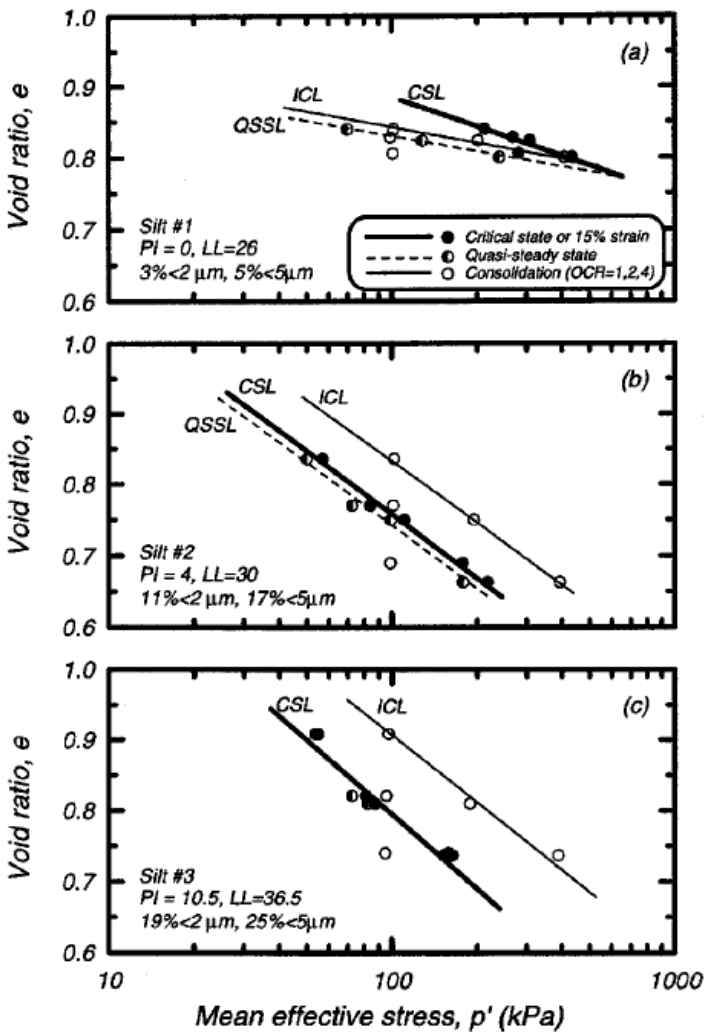

Figure 2.8 Comparisons of the critical state (*CSL*), isotropic consolidation (*ICL*), and quasisteady state lines (*QSSL*) of soils with sand-like and clay-like behavior (Romero, 1995)

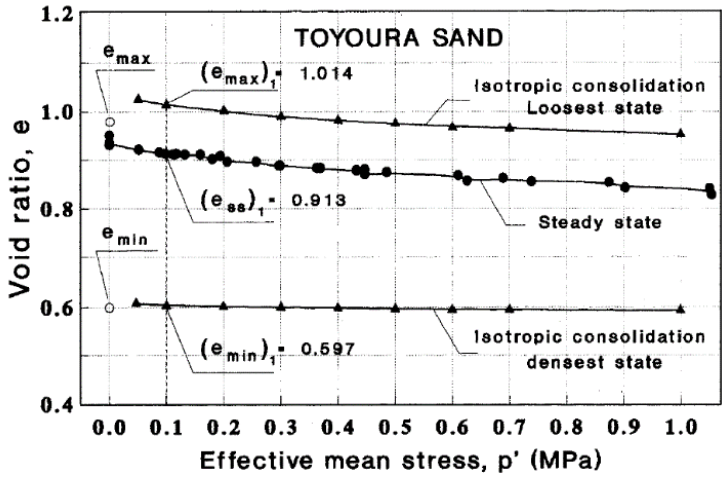

Figure 2.9 The critical state line (*CSL*) and isotropic consolidation lines (*ICL*) for Toyoura sand in loose and dense states (Verdugo and Ishihara, 1996)

2.3 Loading Rate Effects

Sheahan et al. (1996) investigated the combined effects of soil stress history (*OCR*) and loading rate on clay's cyclic strength. For this purpose, they performed twenty-five constant strain rate CK_0UC (K_0-consolidated undrained triaxial compression) tests on resedimented Boston blue clay (*BCC*) at four different axial strain rates ($\dot{\varepsilon_a} = 0.05, 0.5, 5, and\ 50\ \%/h$) consolidated under four different over consolidation ratios (*OCR*= 1, 2, 4, and 8). This study's results in terms of the normalized shear strength and shear-induced pore pressure are presented in Figure 2.10. The slope of the lines between the points are indicated in parentheses as a percentage of S_u/σ'_{vm} at $\dot{\varepsilon_a}$=0.5%/h. The results show that the effect of strain rate on the normalized undrained strength increase is more pronounced for lower *OCR* values (*OCR* = 1 and 2), and as *OCR* increases, the rate sensitivity decreases. For normally consolidated specimens, a constant increase in normalized undrained strength of about 6.5% has been observed, and as the *OCR* increases, this value reduces. However, regardless of the *OCR* level, all specimens showed an average increase of 9.5% when subjected to fast axial strain rate (i.e., $\dot{\varepsilon_a}$=50%/h). The induced pore water pressure seems to be rate-independent for high *OCR* values (*OCR*=4 and 8) and decreases sharply for lower *OCR* values (*OCR*=1 and 2). However, like the normalized strength, all specimens showed a decrease in pore water pressure at high strain rates ($\dot{\varepsilon_a}$=0.5%/h.) regardless of the *OCR* values.

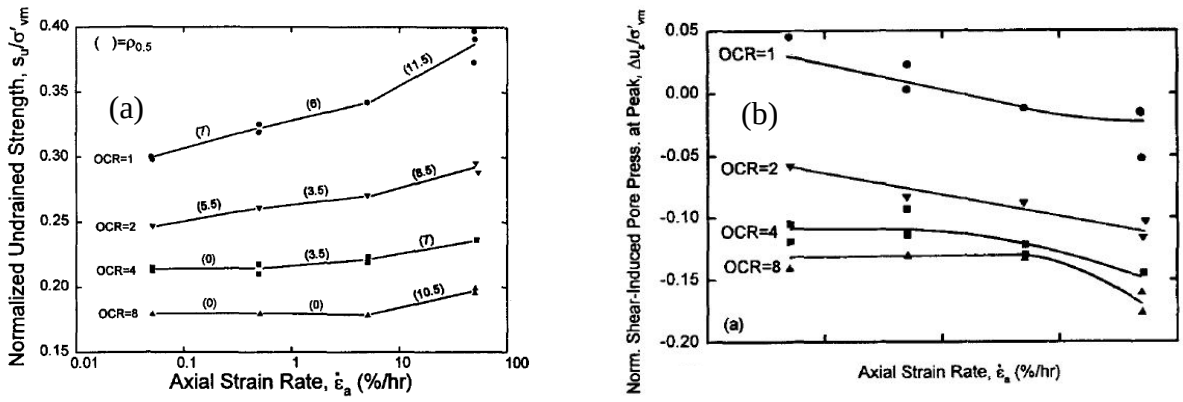

Figure 2.10 Normalized (a) shear strength and (b) shear-induced pore pressure versus axial strain rate (Sheahan et al., 1996)

2.4 Effect of Soil Plasticity (*PI*)

Vucetic and Dobry (1989) conducted a comprehensive study to investigate the effects of soil plasticity (*PI*) on the soil shear modulus *G* and damping ratios λ under undrained cyclic loading. They compiled a database composed of various undrained cyclic tests (e.g., triaxial, simple shear, resonant column, etc.) on normally and overconsolidated clays (*OCR*=1-15) published in 16 different publications. The results of this study are shown in Figure 2.11 as ready-to-use shear modulus reduction G/G_{max} and damping ratio λ versus cyclic shear strain (γ_c) charts.

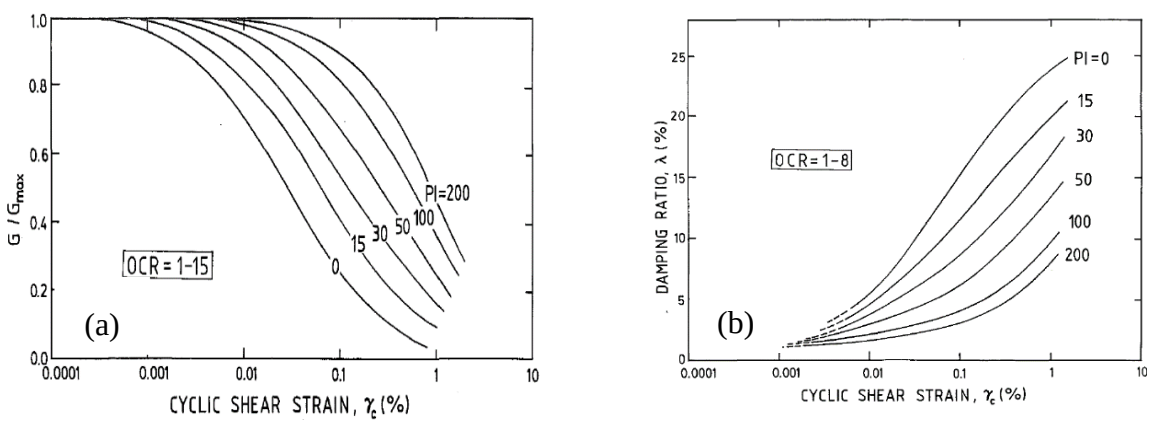

Figure 2.11 Shear modulus reduction (a) and equivalent damping ratio (b) versus shear strain for clays (Vucetic and Dobry, 1989)

As can be seen, as the plasticity index increases, the reduction in modulus becomes less important, the modulus reduction values increase, and the damping ratio decreases.

2.5 Loading Rate Effects on Modus Reduction and Damping Ratios

To study the effect of strain rate on the shear modulus and damping of clays, Lo Presti et al. (1996) and Lo Presti et al. (1997) performed a series of cyclic torsional shear tests (*CLTST*) and resonant column tests (*RCT*) on the Pisa and Augusta clays, which are two types of undisturbed Italian clays. The tests were performed in a stepwise manner using a sinusoidal wave pattern with an applied frequency ranging between 30 and 200 *Hz* for *RCTs* and 0.1 and 1 *Hz* for *CLTSTs*. Figure 2.12 shows the damping and shear modulus ratios obtained from the cyclic torsional shear tests as well as rotational column tests on samples of the Pisa clay with the *OCR* and *PI* in the range of 1.5-2 and 22-55, respectively. According to this figure, shear modulus and damping ratios obtained by *RCT* and *CLTST* are different. Lo Presti et al. (1996) and Lo Presti et al. (1997) believed that this difference originated from the fact that *RCT* and *CLTST* were performed at different loading rates, and thus, concluded that the shear modulus and damping curves are rate dependent.

A similar study was performed by Isenhower and Stokoe (1981) to assess the effect of rate and shear strain amplitude on the shear modulus of the San Francisco Bay mud using a torsional shear/resonant column apparatus. Figure 2.13 shows the variation of shear modulus corresponding to the applied constant shear strain amplitudes at different shear strain rates. Findings from these measurements indicate that the shear modulus increases about 4% per log cycle with the increase of shear strain rates, and that, this increase is independent of the shear strain amplitudes and the mean effective stress.

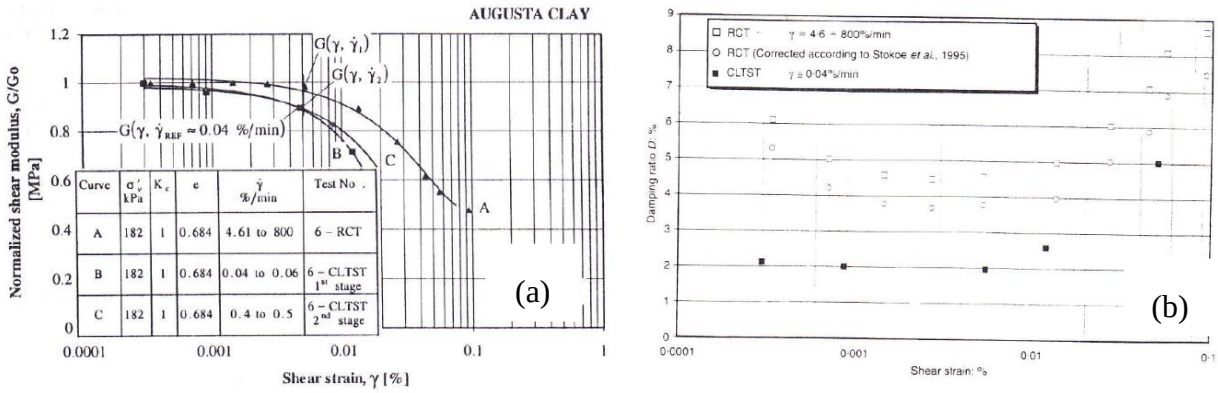

Figure 2.12 Strain rate effects on (a) shear modulus (Lo Presti et al., 1996) and (b) damping ratio (Lo Presti et al., 1997)

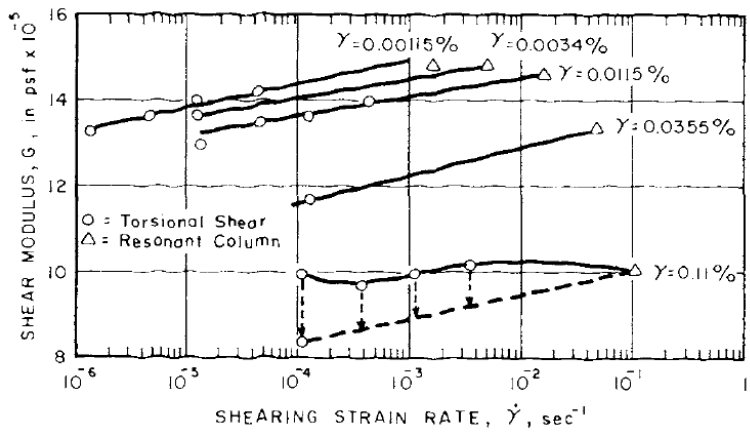

Figure 2.13 Shear modulus of San Francisco Bay Mud at various strain rates (Isenhower and Stokoe, 1981)

2.6 Cyclic Stiffness Degradation

Several studies have shown that cohesive soils exhibit stiffness degradation (Vucetic and Dobry, 1989; Idriss et al., 1978; Zhou and Gong, 2001; Vucetic, 1989). Stiffness degradation is usually measured using the "degradation index", which is expressed as:

$$\delta = \frac{G_{SN}}{G_{S1}} = \frac{\frac{\sigma_d}{\varepsilon_{CN}}}{\frac{\sigma_d}{\varepsilon_{C1}}} = \frac{\varepsilon_{C1}}{\varepsilon_{CN}} \tag{2.2}$$

Where ε_{C1} and ε_{CN} are the cyclic axial strains at the 1st and the Nth cycles, respectively; Correspondingly, G_{S1} and G_{SN} are the secant moduli at the 1st and the Nth cycles, respectively.

The cyclic stiffness degradation is highly related to the cyclic amplitude applied to the soil in a way that higher cyclically induced strains will cause higher stiffness degradation. Figure 2.14 shows the degradation index with the number of cycles for different OCR values. The stiffness degradation decreases with the increase of the number of cycles for all *OCR* values. However, at lower *OCR* values, the stiffness degradation is more pronounced, meaning that the shear modulus degrades more and faster than when the soil is over-consolidated.

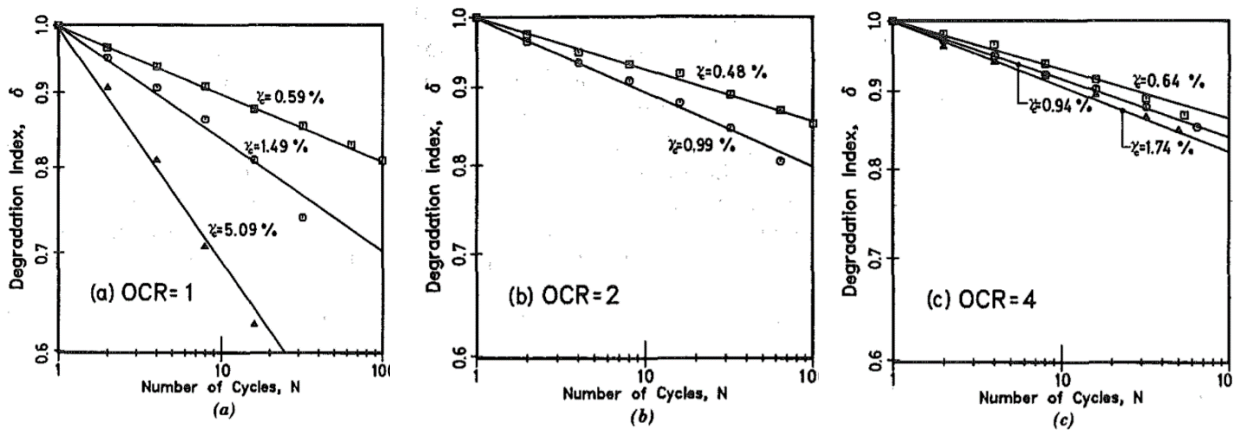

Figure 2.14 Degradation index versus the number of cycles for different *OCR* values (Vucetic and Dobry, 1988)

2.7 Anisotropic Consolidation Effects

Lefebvre and Pfendler (1996) recommended that cyclic tests for clays be carried out with initial static shear stress to simulate end-of construction conditions. The main reason is that seismic analyses for clays are mostly involved with anisotropic consolidation (e.g., the existence of an embankment or a structure, the lateral earth pressure other than one, etc.). Therefore, they performed a set of constant volume direct and simple shear tests under undrained conditions to study the initial static shear stress effects on clays' cyclic resistance. The specimens of the study were intact sensitive clay obtained from the St. Lawrence valley. All specimens were reconsolidated in the laboratory to achieve an *OCR* of 2.2. They reported that the applied initial

shear stress decreased the cyclic resistance, but it also decreased the cyclic degradation rate (Figure 2.12 (a)) tremendously. Moreover, the main result of the study was that any combination of static and cyclic shear stress (τ_{st} and τ_c) increased the total resistance of the soil (i.e., $\tau_{st} + \tau_c$) at the 12th cycle by 30% provided that the applied static shear stress falls between $0.3C_u < \tau_{st} < 0.8C_u$ (Figure 2.15 (b)). The main reason for this increase is referred to as an elimination of the stress reversal (the direction changes of the cyclic shear stress from positive to negative) that the initial static shear stress causes.

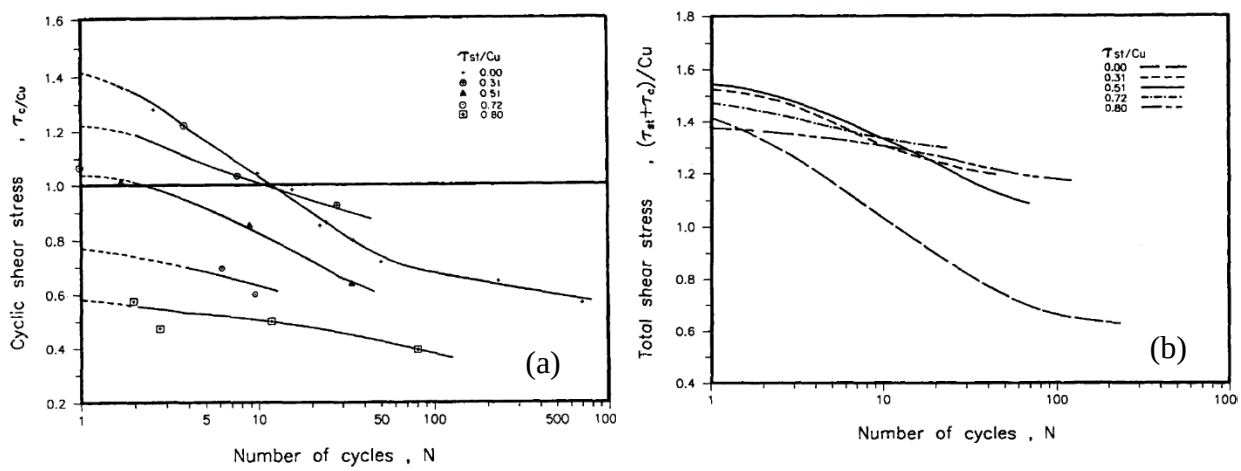

Figure 2.15 Cyclic shear stress (a) and total undrained shear stress (b) as a function of the number of cycles for initial static shear stress range of 0 to 0.8 C_u (Lefebvre and Pfendler, 1996)

2.8 Cyclic Threshold

Lefebvre et al. (1989) studied a stability threshold for a saturated sensitive clay under slow and rapid cyclic loading. They defined the cyclic stability threshold as the highest *CSR* at which soil does not exhibit damage or alteration to the peak failure envelope, under an infinite number of loading cycles. They reported a normalized stability threshold of 60-65% of the monotonic undrained shear strength for both structured and normally consolidated specimens under repeated cyclic loading. Both the axial strain and pore water pressure has been observed to be stabilized and constant under further cyclic loading below the normalized stability threshold (Figure 2.16). They also reported that this normalized threshold is independent of the consolidation pressure and

structure effects but can be increased up to 33% by increasing the strain rate from 0.01 to 2.0 *Hz* (Figure 2.17).

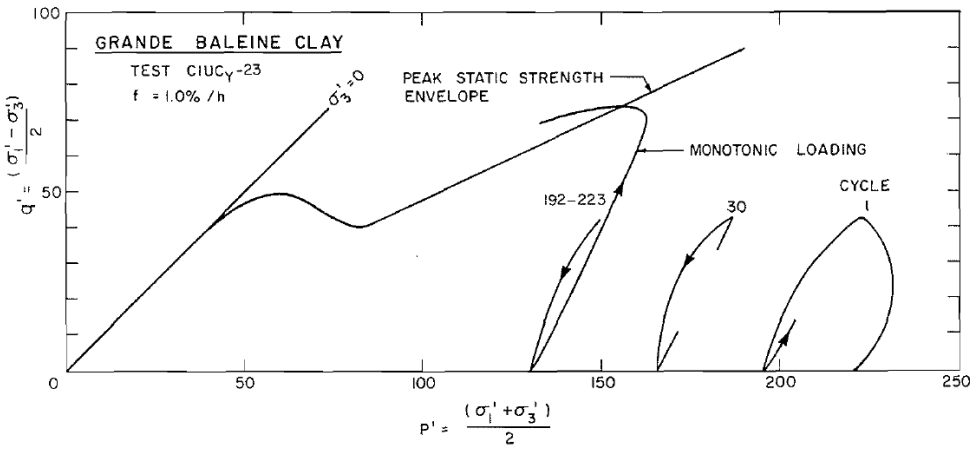

Figure 2.16 Stress path of a normally consolidated clay under cyclic loading followed by monotonic loading after stabilization (Lefebvre et al., 1989)

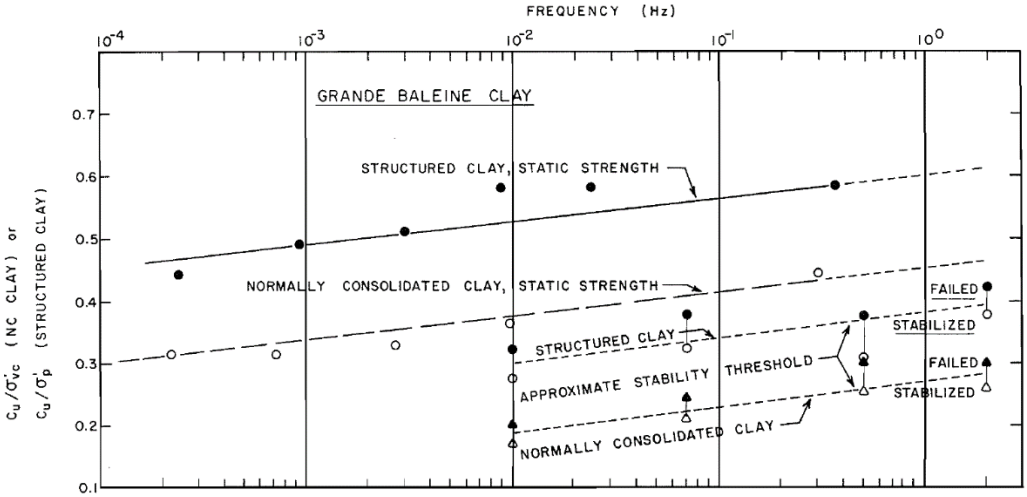

Figure 2.17 Stability threshold versus frequency (Lefebvre et al., 1989).

In another study, Mortezaie and Vucetic (2016) performed a series of multistage strain-controlled tests using direct shear tests on laboratory-made clays, kaolinite, and kaolinite bentonite, with different *PIs* of 28 and 55, respectively, to find the threshold shear strains bellow which cyclic degradation and pore water pressure is negligible. The tests were performed with various vertical consolidation stress, σ'_{vc}, (113 *kPa*, 216 *kPa*, and 674 *kPa*), overconsolidation ratios, *OCR*, (1, 4, and 7.8), and loading frequencies (0.01 and 0.1 *Hz*). The study's findings along with investigations

performed by other studies are plotted in Figure 2.18 (a) and (b) in terms of the threshold shear strains for cyclic degradation, γ_{td}, and pore water pressure generation, γ_{tp}. The findings of Mortezaie and Vucetic (2016) show that γ_{td} and γ_{tp} fall into the range of 0.006-0.05% and 0.01-0.1%, respectively, and increase with soil plasticity. Also, they observed no apparent effects of σ'_{vc}, *OCR*, and frequencis on γ_{td} and γ_{tp}.

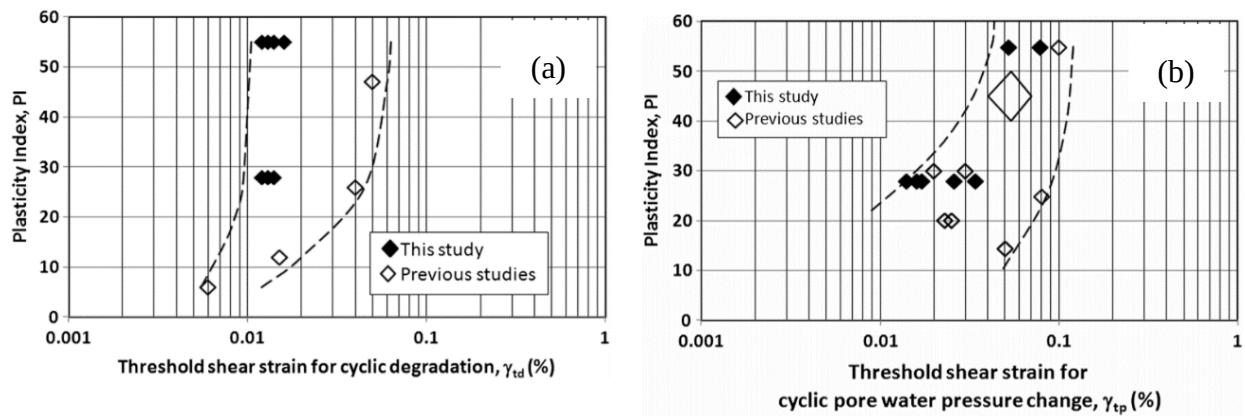

Figure 2.18 Threshold shear strains for (a) cyclic degradation and (b) pore water pressure (Mortezaie and Vucetic, 2016).

CHAPTER 3 LITERATURE REVIEW OF SOIL CONSTITUTIVE MODELING

3.1 Introduction

The first part of this chapter consists of the principles of constitutive modeling in geotechnical engineering. The main topics in this part are the stress state of soils, the critical state concept (which constitutes the main framework for most soil constitutive models), and an introduction to elastoplasticity. In the second part of the chapter, the developments of clay's models from the well known *MCC* for monotonic applications up to the recent complex, sophisticated models for cyclic softening and liquefaction are discussed. At the end of the chapter, some rate-dependent models will be and reviewed.

3.2 Introduction to Constitutive Modeling

3.2.1 Stress States

Constitutive models are usually formulated in the general stress space. However, in soil mechanics, models are typically presented in terms of deviatoric and mean effective stress (*p*-*q* space) for simplicity.

3.2.1.1 Full Stress Space

The stress state at a point can be represented with a stress tensor. In geotechnical engineering, the Cauchy stress tensor is typically used to represent the stress state of a soil element. The Cauchy stress tensor is a three-dimensional full stress tensor ($\boldsymbol{\sigma}$) which is defined as (note that a bold font denotes a second-order tensor):

$$\boldsymbol{\sigma} = \begin{bmatrix} \sigma_{xx} & \tau_{xy} & \tau_{xz} \\ \tau_{yx} & \sigma_{yy} & \tau_{yz} \\ \tau_{zx} & \tau_{zy} & \sigma_{zz} \end{bmatrix} \tag{3.1}$$

In which $\sigma_{xx}, \sigma_{yy}, \sigma_{zz}$ are normal stresses components having normals parallel to the axis of *x*, *y*, and *z*, respectively, and $\tau_{xy} = \tau_{yx}, \tau_{xz} = \tau_{zx}, \tau_{yz} = \tau_{zy}$ are shear stresses.

$\boldsymbol{\sigma}$ is usually divided into two separate components: volumetric (p') and deviatoric ($\boldsymbol{s}$). The apostrophe indicates an effective stress quantity. For simplicity, and as in the convention in geotechnical engineering, the apostrophe is dropped in the rest of this dissertation. The scalar quantity volumetric component (p), which is also called mean effective stress, is related to the first stress invariant I_1:

$$p = \frac{I_1}{3} = \frac{tr(\boldsymbol{\sigma})}{3} = \frac{\sigma_{xx} + \sigma_{yy} + \sigma_{zz}}{3} \tag{3.2}$$

$$\boldsymbol{s} = \boldsymbol{\sigma} - p \cdot \boldsymbol{I} = \begin{bmatrix} \sigma_{xx} - p & \tau_{xy} & \tau_{xz} \\ \tau_{xy} & \sigma_{yy} - p & \tau_{yz} \\ \tau_{xz} & \tau_{yz} & \sigma_{zz} - p \end{bmatrix} \tag{3.3}$$

Where "$tr(\boldsymbol{\sigma})$" is the trace of $\boldsymbol{\sigma}$, and $\boldsymbol{I}$ is a 3×3 identity matrix.

Similarly, the full strain tensor $\boldsymbol{\varepsilon}$ can be written in general stress/strain space as:

$$\boldsymbol{\varepsilon} = \begin{bmatrix} \varepsilon_{xx} & \varepsilon_{xy} & \varepsilon_{xz} \\ \varepsilon_{xy} & \varepsilon_{yy} & \varepsilon_{yz} \\ \varepsilon_{xz} & \varepsilon_{yz} & \varepsilon_{zz} \end{bmatrix} = \begin{bmatrix} \varepsilon_{xx} & \frac{\gamma_{xy}}{2} & \frac{\gamma_{xz}}{2} \\ \frac{\gamma_{yx}}{2} & \varepsilon_{yy} & \frac{\gamma_{yz}}{2} \\ \frac{\gamma_{zx}}{2} & \frac{\gamma_{zy}}{2} & \varepsilon_{zz} \end{bmatrix} \tag{3.4}$$

Where $\varepsilon_{xx}, \varepsilon_{yy}, \varepsilon_{zz}$ are normal strain components acting on planes that have a normal parallel to the axis of x, y, and z, respectively, and $\gamma_{xy} = \gamma_{yx}, \gamma_{xz} = \gamma_{zx}, \gamma_{yz} = \gamma_{zy}$ are engineering shear strains. $\boldsymbol{\varepsilon}$ may also be divided into two separate components: a volumetric strain part (ε_v) and a deviatoric one ($\boldsymbol{\varepsilon_d}$):

$$\varepsilon_v = tr(\boldsymbol{\varepsilon}) = \varepsilon_{xx} + \varepsilon_{yy} + \varepsilon_{zz} \tag{3.5}$$

$$\boldsymbol{\varepsilon_d} = \boldsymbol{\varepsilon} - \frac{1}{3}\varepsilon_v . \boldsymbol{I} = \begin{bmatrix} \varepsilon_{xx} - \frac{1}{3}tr(\boldsymbol{\varepsilon}) & \frac{\gamma_{xy}}{2} & \frac{\gamma_{xz}}{2} \\ \frac{\gamma_{xy}}{2} & \varepsilon_{yy} - \frac{1}{3}tr(\boldsymbol{\varepsilon}) & \frac{\gamma_{yz}}{2} \\ \frac{\gamma_{xz}}{2} & \gamma_{yz} & \varepsilon_{zz} - \frac{1}{3}tr(\boldsymbol{\varepsilon}) \end{bmatrix} \tag{3.6}$$

3.2.1.2 Deviatoric-mean effective stress (*p*-*q*) space

Stresses are also presented in *p*-*q* space, where q is the scalar deviatoric stress, which is calculated based on the second deviatoric stress invariant J_2:

$$q = \sqrt{3J_2} \tag{3.7}$$

$$J_2 = \frac{1}{2}\boldsymbol{s}:\boldsymbol{s} \tag{3.8}$$

":" denotes the inner products or dot products of two tensors, which is defined as $\boldsymbol{X}:\boldsymbol{Y} = \sum_i \sum_j X_{ij}Y_{ij}$. Therefore, based on equations (3.3) and (3.7), the scalar q can be calculated as:

$$q = \sqrt{\frac{3}{2}\boldsymbol{s}:\boldsymbol{s}} = \sqrt{\frac{1}{2}\left[(\sigma_{xx}-\sigma_{yy})^2 + (\sigma_{xx}-\sigma_{zz})^2 + (\sigma_{zz}-\sigma_{yy})^2\right] + 3({\tau_{xy}}^2 + {\tau_{xz}}^2 + {\tau_{yz}}^2)} \tag{3.9}$$

Like stresses, strains are also expressed in *p*-*q* space. Therefore, the scalar deviatoric strain (ε_q), which is the counterpart of the $\boldsymbol{\varepsilon_d}$, can be written as:

$$\varepsilon_q = \sqrt{\frac{2}{3}\boldsymbol{\varepsilon_d}:\boldsymbol{\varepsilon_d}} = \frac{1}{3}\sqrt{2\left[(\varepsilon_{xx}-\varepsilon_{yy})^2 + (\varepsilon_{xx}-\varepsilon_{zz})^2 + (\varepsilon_{zz}-\varepsilon_{yy})^2\right] + 3({\gamma_{xy}}^2 + {\gamma_{xz}}^2 + {\gamma_{yz}}^2)} \tag{3.10}$$

3.2.2 Classic Plasticity Theory

3.2.2.1 Elasto-plasticity Formulation

The main assumption in elastoplasticity is the decomposition of strain increments in elastic and plastic parts:

$$\dot{\boldsymbol{\varepsilon}} = \dot{\boldsymbol{\varepsilon}}^{\boldsymbol{e}} + \dot{\boldsymbol{\varepsilon}}^{\boldsymbol{p}} \tag{3.11}$$

It was also mentioned that the strain tensor decomposes into volumetric and deviatoric parts, and so does the increments of strain:

$$\dot{\boldsymbol{\varepsilon}} = \frac{1}{3}\dot{\varepsilon_v} \cdot \boldsymbol{I} + \dot{\boldsymbol{\varepsilon}}_{\boldsymbol{d}} \tag{3.12}$$

Therefore, volumetric and deviatoric components are each decomposed into elastic and plastic parts:

$$\dot{\varepsilon_v} = \dot{\varepsilon}_v^e + \dot{\varepsilon}_v^p \tag{3.13}$$

$$\dot{\boldsymbol{\varepsilon}}_{\boldsymbol{d}} = \dot{\boldsymbol{\varepsilon}}_{\boldsymbol{d}}^{\boldsymbol{e}} + \dot{\boldsymbol{\varepsilon}}_{\boldsymbol{d}}^{\boldsymbol{p}} \tag{3.14}$$

$$\dot{\varepsilon_q} = \dot{\varepsilon}_q^e + \dot{\varepsilon}_q^p \tag{3.15}$$

The increments of the elastic strain rate are given by:

$$\dot{\varepsilon}_v^e = \frac{\dot{p}}{K} \tag{3.16}$$

$$\dot{\boldsymbol{\varepsilon}}_{\boldsymbol{d}}^{\boldsymbol{e}} = \frac{\dot{\boldsymbol{s}}}{2G} \tag{3.17}$$

$$\dot{\varepsilon}_q^e = \frac{\dot{q}}{3G} \tag{3.18}$$

Rearrangement of the Equations (3.16), (3.17), and (3.18) will lead to:

$$\dot{p} = K \cdot \dot{\varepsilon}_v^e = K(\dot{\varepsilon}_v - \dot{\varepsilon}_v^p) \tag{3.19}$$

$$\dot{s} = 2G \cdot \dot{\varepsilon}_d^e = 2G(\dot{\varepsilon}_d - \dot{\varepsilon}_d^p) \tag{3.20}$$

$$\dot{q} = 3G \cdot \dot{\varepsilon}_q^e = 3G(\dot{\varepsilon}_q - \dot{\varepsilon}_q^p) \tag{3.21}$$

Where K and G are defined as the bulk and shear modulus, respectively, which are typically considered in critical state soil mechanics as:

$$K = \frac{p \cdot v_0}{\kappa} \tag{3.22}$$

$$G = \frac{3(1-2v)}{2(1+v)}K \tag{3.23}$$

Where v is the Poison's ratio, $v_0 = 1 + e_0$ is the initial specific volume, and e_0 is the initial void ratio. Note that other equations for bulk and shear modulus are sometimes used.

3.2.2.2 Formulation of Classical Plasticity

3.2.2.2.1 Yield Surface and Hardening Variables

In classical elastoplasticity, a yield surface (f) limits the region in the stress space where the behavior of the material is perfectly elastic, and only elastic strains can develop (Figure 3.1). Plastic strains start developing when the stress state goes beyond the yield surface, which then moves so that the stress state is on the yield surface. As a result, the stress state can either be inside the yield surface or on the yield surface.

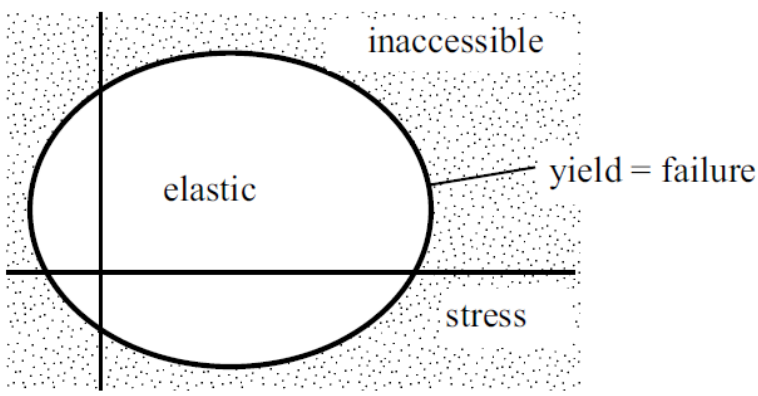

Figure 3.1: Schematic of the yield surface and the elastic region (Wood, 2014)

Mathematically, the general form of the yield surface can be written as:

$$f(\boldsymbol{\sigma}, \boldsymbol{q_n}) = 0 \tag{3.24}$$

The yield surface is a function of a stress state ($\boldsymbol{\sigma}$), and internal hardening variables ($\boldsymbol{q_n} = (q_1, q_2, \dots, q_n)$), that define the position and the size of the yield surface. Note that the previously defined scalar-valued deviatoric stress q should not be mistaken with the vector $\boldsymbol{q_n}$ consisting of different internal hardening variables. Internal hardening variables control how the yield surface

changes in shape, size, and position as plastic strains develop. There are three existing hardening rules that are typically used in constitutive models upon plastic straining:

- Isotropic hardening rule, in which the yield surface increases in size but without a change of position of its center.
- Kinematic hardening rule, in which the center of yield surface translates without a change of size.
- Rotational and/or distortional hardening rule, in which the yield surface rotates and/or distorts.

3.2.2.2.2 Consistency Condition

The consistency condition is one of the main requirements of elastoplasticity based on which every single stress point should always be either inside or on the yield surface. Once the material has yielded, internal hardening variables are updated to increase the size and/or adjust the yield surface's position so that the new stress point is on the yield surface. As a result, the yield function is constant (zero) upon plastic loading. The consistency condition and Kuhn Tucker loading-unloading condition are usually used to solve equations in plasticity using the loading index or plastic multiplier $\dot{\gamma}$, which has also been referred to as (L) in some references (Dafalias and Manzari, 2004; Dafalias et al., 2006):

$$\dot{\gamma} = \frac{1}{K_P}(\boldsymbol{N}:\dot{\boldsymbol{\sigma}}) = \frac{1}{K_P}(\frac{\partial f}{\partial \boldsymbol{\sigma}}:\dot{\boldsymbol{\sigma}}) \tag{3.25}$$

Where $\boldsymbol{N} = \frac{\partial f}{\partial \boldsymbol{\sigma}}$ is the loading direction. $\dot{\gamma}$ can be re-written in triaxial space (p-q space) as:

$$\dot{\gamma} = \frac{1}{K_p}\left(\frac{\partial f}{\partial p}\dot{p} + \frac{\partial f}{\partial q}\dot{q}\right) \tag{3.26}$$

Where K_p is the plastic modulus, which is generally formulated as:

$$K_p = \frac{\dot{\sigma}}{\dot{\varepsilon^p}} \tag{3.27}$$

The plastic modulus is also shown by:

$$K_p = -\frac{\partial f}{\partial q_n} : \overline{q_n} \tag{3.28}$$

Finally, the Prager consistency condition can be expressed mathematically as:

$$\dot{\gamma}\dot{f}(\boldsymbol{\sigma}, \boldsymbol{q_n}) = 0 \tag{3.29}$$

This condition can be simplified as:

$$\dot{f} = \frac{\partial f}{\partial \boldsymbol{\sigma}} : \dot{\boldsymbol{\sigma}} + \frac{\partial f}{\partial \boldsymbol{q_n}} : \dot{\boldsymbol{q}}_{\boldsymbol{n}} = 0 \tag{3.30}$$

The Kuhn Tucker loading-unloading condition is also used to solve equations in plasticity and is given as:

$$\dot{\gamma} \geq 0,\ f(\boldsymbol{\sigma}, \boldsymbol{q_n}) \leq 0 \text{ and } \dot{\gamma} f(\boldsymbol{\sigma}, \boldsymbol{q_n}) = 0 \tag{3.31}$$

3.2.2.2.3 Associative and Non-Associative Flow Rules

Plastic strain increments are generally defined in plasticity with a flow rule as:

$$\dot{\boldsymbol{\varepsilon}} = \langle \dot{\gamma} \rangle \boldsymbol{R} \tag{3.32}$$

Where $\langle\ \rangle$ denotes the McCauley brackets, which returns only positive values (i.e., $\langle \dot{\gamma} \rangle = \max(0, \dot{\gamma})$). $\boldsymbol{R} = \frac{\partial g}{\partial \boldsymbol{\sigma}}$ is the normal to the plastic potential surface, *g*, which controls the direction

of the plastic strains. If $g = f$ the flow rule is called an associated flow rule, meaning the plastic potential and the yield surface coincide, and their normals have the same direction.

3.2.3 Critical State Concept

Elasto-plasticity of soils is usually defined within the framework of critical state soil mechanics, which combines the consolidation response with the deviatoric response as a function of normal stress. The critical state is defined as a soil state in which the rate of change of deviatoric stress, mean effective stress, and the void ratio is zero upon further shearing:

$$\frac{\partial q}{\partial \varepsilon_q} = \frac{\partial p}{\partial \varepsilon_q} = \frac{\partial \upsilon}{\partial \varepsilon_q} = 0 \tag{3.33}$$

The stress states at which the critical state is reached define a critical state line (*CSL*) in $p - q$ and $\upsilon - p$ spaces ($\upsilon = 1 + e$ refers to the specific volume). This line is a property of soil that does not depend on the stress state of the soil. A schematic *CSL* of soil is illustrated in *p-q* space and *p-v* space in Figure 3.2. The final state of soil upon loading is on the *CSL* for every loading conditions. The soil stress path toward this line depends on drainage conditions (i.e., drained or undrained loading), types of loading (e.g., simple shear test or triaxial test), and the degree of soil consolidation (i.e., normally consolidated or overconsolidated).

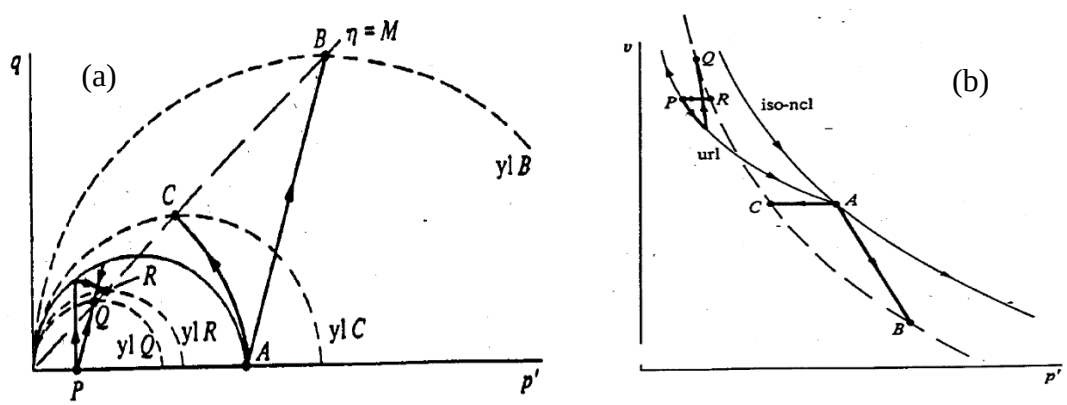

Figure 3.2: *CSL* in *p-q* (a) and *p-v* (b) space (Wood, 1990)

3.3 Rate-independent Constitutive Models

Up until now, there have been several soil constitutive models developed that are meant to capture the behavior of soils under specific conditions (e.g., static or cyclic loading, dry or saturated, etc.). Each model is based on different assumptions and, therefore, lead to precise results only if the model is being used in accordance with said assumptions. Most constitutive soil models use the critical state framework to predict the stress-strain behavior of soils under monotonic and/or cyclic loading. In the following subsection, some of the rate-independent constitutive models and their implementation are discussed.

3.3.1 Modified Cam-Clay (*MCC*)

This model is a modified version of the original Cam-Clay formulated by Roscoe and Schofield in 1963. Cam-Clay can be considered as the platform of many advanced constitutive models in that most of them are developed based on the *MCC*`s framework. The main modification from the original Cam-Clay was made by Roscoe and Burland in 1968, in which the logarithmic curve of the yield surface was substituted for an elliptical one.

MCC is an elastoplastic model with an elliptical yield surface defined in the triaxial space with the following function:

$$f = \frac{q^2}{M^2} + p^2 + p_0 p = 0 \tag{3.34}$$

While in the multiaxial space, the yield surface is given by:

$$f = \frac{3}{2M^2}\boldsymbol{s}:\boldsymbol{s} + (p - \frac{p_0}{2})^2 - (\frac{p_0}{2})^2 = 0 \tag{3.35}$$

Where p_0 is a hardening variable that controls the size and the position of the yield surface, and *M* is the stress ratio at the critical state line (critical stress ratio). The yield surface of the *MCC* and the original Cam-clay, as well as the critical state line, are shown in *p*-*q* space in Figure 3.3. It is worth mentioning that the yield surface always has its apex on the critical state line, defined in *p*-*q* space as a line with a slope of *M*.

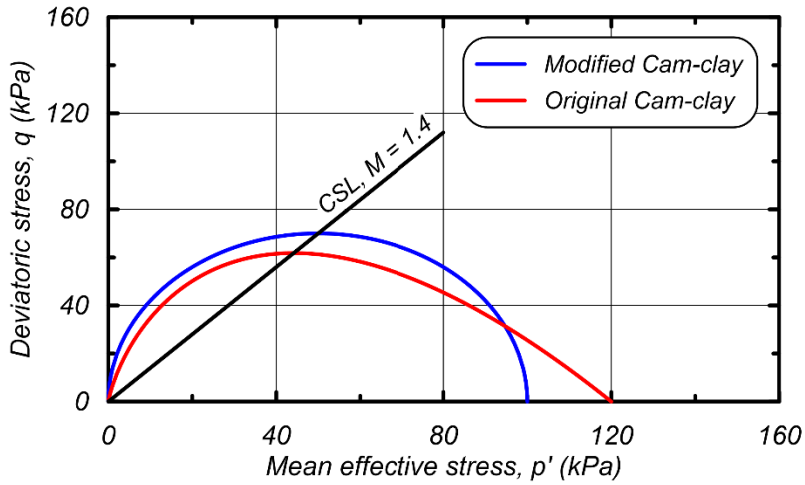

Figure 3.3: The original and modified Cam-Clay in *p*-*q* space (Eslami, 2017)

The *MCC* uses an associative flow rule, which means that the plastic potential surface is similar to the yield surface. Plastic volumetric and deviatoric strains are calculated according to the flow rule as:

$$\varepsilon_v^p = \dot{\gamma}\frac{\partial f}{\partial p} = \dot{\gamma}(2p - p_0) \tag{3.36}$$

$$\varepsilon_q^p = \dot{\gamma}\frac{\partial f}{\partial q} = \dot{\gamma}\frac{2q}{M^2} \tag{3.37}$$

This model follows both isotropic and kinematic hardening rules, which respectively means that the size and the center of the yield center change upon yielding. These changes are associated with a change in p_0 which is given in this model by:

$$\dot{p}_0 = \frac{\vartheta \cdot p_0 \cdot \dot{\varepsilon}_v^p}{\lambda - \kappa} \tag{3.38}$$

This model is one of the most often used constitutive models in geotechnical engineering because of both its simplicity and its ability to simulate the behavior of clays accurately under monotonic loading. Figure 3.4 shows examples of undrained simulations using different *OCRs*. One of the drawbacks of this model is its unrealistic large elastic range. Also, at *OCR*=2, the model shows an unrealistic elasto perfectly plastic behavior due to the vertical stress path crossing the yield surface

at its apex. In addition, the post-peak strain softening that is typical of overconsolidated and/or sensitive clays could not be simulated using *MCC*.

One of the big merits of the *MCC* is that it works with only 5 model parameters that all have a physical meaning:

- The slope of the critical state line (*M*) which is related to the friction angle (ϕ') as:

$$M = \frac{6\sin(\phi')}{3 - \sin(\phi')} \tag{3.39}$$

- The slope of the isotropic normal consolidation line (*NCL*) in e-ln p'plane related to the compression index (C_c):

$$\lambda = \frac{C_c}{ln\,10} \tag{3.40}$$

- The slope of the unloading-reloading line in *e-ln* p'plane related to the recompression index (C_r):

$$\kappa = \frac{C_r}{ln\,10} \tag{3.41}$$

- Γ or the specific volume of the *CSL* at $p_0 = 1$.
- Poisson's ratio, ν.

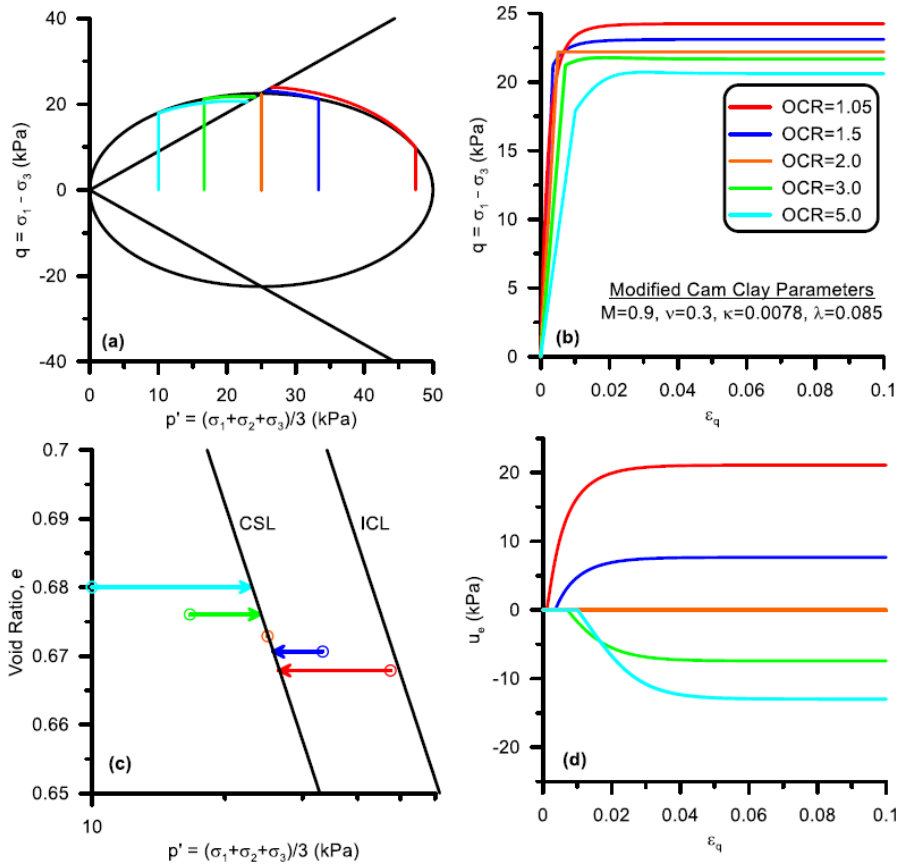

Figure 3.4: Simulations of the *MCC* with different *OCRs* (Yniesta, 2016).

3.3.2 *SANICLAY*- Simple Anisotropic Clay Model

SANICLAY is a plasticity model developed for the monotonic softening response of clays that considers the effect of soil anisotropy (Dafalias et al., 2006). The model uses a non-associative flow rule by defining a plastic potential surface other than the yield surface. As it was mentioned earlier, the normal to the plastic potential surface expresses plastic strains' direction. The yield and plastic potential surfaces evolve according to a distortional and rotational hardening rule in *p*-*q* space based on the following expressions:

$$f = (q - p \cdot \beta)^2 - (N^2 - \beta^2)p(p_0 - p) = 0 \tag{3.42}$$

$$g = (q - p \cdot \alpha)^2 - (M^2 - \alpha^2)p(p_\alpha - p) = 0 \tag{3.43}$$

The corresponding expressions for the volumetric and deviatoric plastic strain rates are obtained as follow using the flow rule:

$$\dot{\varepsilon}_v^p = \langle L \rangle \frac{\partial g}{\partial p} = \langle L \rangle p(M^2 - \eta^2) \tag{3.44}$$

$$\dot{\varepsilon}_q^p = \langle L \rangle \frac{\partial g}{\partial q} = \langle L \rangle 2p(\eta - \alpha) \tag{3.45}$$

Where $\eta = q/p$ is the stress ratio, and L is the loading index. The model surfaces in *p*-*q* space are illustrated in Figure 3.5.

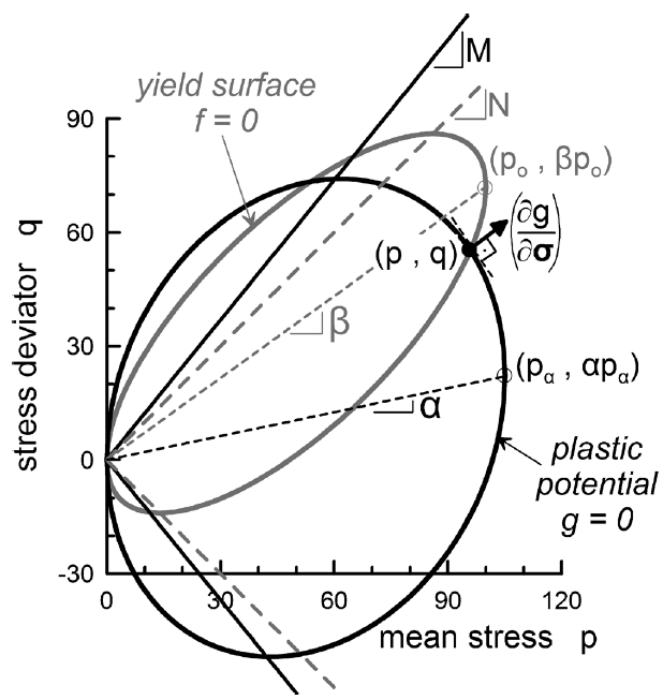

Figure 3.5 *SANICLAY* Surfaces in triaxial stress space (Dafalias et al., 2006)

α is a non-dimensional anisotropic variable controlling the degree of anisotropy, which is considered in the model by the rotation and distortion of the plastic potential surface. It also takes into account the coupling of deviatoric and volumetric plastic strain rates. β and p_0 are rotational and isotropic hardening variables of the yield surface, respectively. M is the critical stress ratio, and *N* is a limiting constant similar to *M*. Both *M* and *N* serve as bounds for α and β, respectively.

p_α adjust the size of the plastic potential surface. p_o, α, and β are functions of plastic volumetric strain evolving according to the following formulations.

$$\dot{p_0} = \langle L \rangle \overline{p_0} = \langle L \rangle (\frac{1+e_{in}}{\lambda - \kappa}) \overline{p_0} (\frac{\partial g}{\partial p}) \tag{3.46}$$

$$\dot{\alpha} = \langle L \rangle \bar{\alpha} = \langle L \rangle \left(\frac{1+e_{in}}{\lambda - \kappa}\right) C \left(\frac{p}{p_0}\right)^2 \left|\frac{\partial g}{\partial p}\right| |\eta - x \cdot \alpha| (\alpha^b - \alpha) \tag{3.47}$$

$$\dot{\beta} = \langle L \rangle \bar{\beta} = \langle L \rangle \left(\frac{1+e_{in}}{\lambda - \kappa}\right) C \left(\frac{p}{p_0}\right)^2 \left|\frac{\partial g}{\partial p}\right| |\eta - \beta| (\beta^b - \beta) \tag{3.48}$$

Finally, the loading index (L) and plastic modulus (K_p) are calculated by applying the consistency condition as follows:

$$L = \frac{1}{K_p}\left(\frac{\partial f}{\partial p}\dot{p} + \frac{\partial f}{\partial q}\dot{q}\right) = \frac{1}{K_p} p[(N^2 - \eta^2)\dot{p} + 2(\eta - \beta)\dot{q}] \tag{3.49}$$

$$K_p = -\left(\frac{\partial f}{\partial p_0}\overline{p_0} + \frac{\partial f}{\partial \beta}\bar{\beta}\right) = p\left[(N^2 - \beta^2)\overline{p_0} + 2(q - p_0 \cdot \beta)\bar{\beta}\right] \tag{3.50}$$

Based on these equations, the inward local movement of the yield surface occurs if K_p is negative while an outward one occurs when K_p is positive. The *SANICLAY* requires the calibration of eight constants, five of which are those of the *MCC* model (Table 3.1).

Table 3.1: Constants of the *SANICLAY* (Dafalias et al., 2006)

Constant	Description of its role	Value
M_c	Value of stress ratio $\eta = q/p$ at critical state in compression	1.18
M_e	Value of stress ratio $\eta = q/p$ at critical state in extension	0.86
λ	Compressibility of normally consolidated NC clay	0.063
κ	Compressibility of overconsolidated OC clay	0.009
ν	Elastic Poisson's ratio	0.2
N	Shape of the yield surface	0.91
x	Saturation limit of anisotropy (under paths with $\eta = q/p =$ constant)	1.56
C	Rate of evolution of anisotropy	16

Figure 3.6 shows the predictive ability of the model. The results show that the model can simulate the response of soils with high and low *OCR* values (*OCR* = 1–4) successfully. However, the disadvantage of the model is the lack of accounting for softening that occurs in some clays (Dafalias et al., 2006).

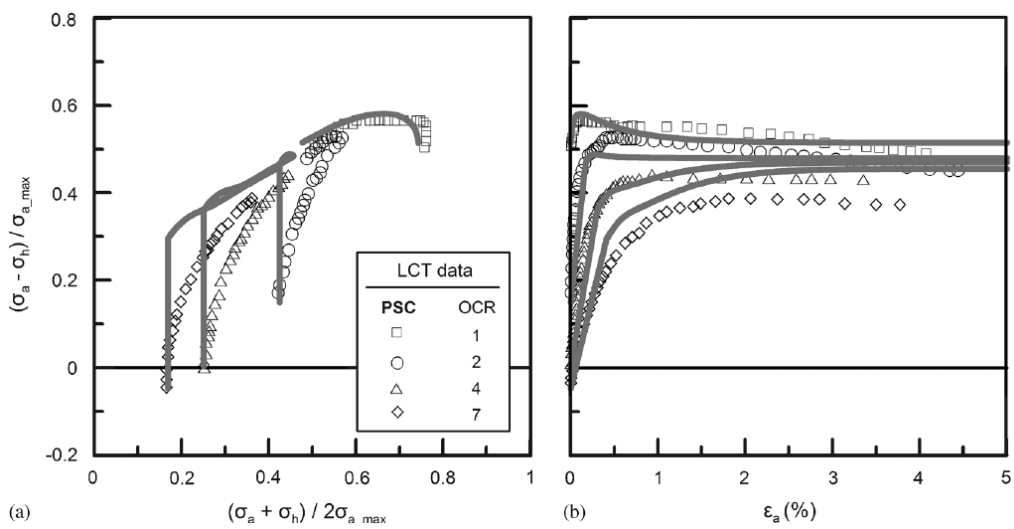

Figure 3.6 Comparison of data and simulations for undrained plane strain compression tests on a clay using the *SANICLAY* model (Dafalias et al., 2006)

3.3.3 SANICLAY-D: *SANICLAY* with Destructuration

This model is a developed version of the *SANICLAY* model that accounts for destructuration by including undisturbed and remolded shear strength of clays associated with softening (Taiebat et al., 2010). Destructuration is defined by the authors of the model as "a sudden post-yield increase

in compressibility, or a post-peak decrease in strength under shearing". In general, two types of destructuration are defined in this model: isotropic and frictional. Isotropic destructuration occurs due to the isotropic softening of the yield surface, and frictional destructuration is due to the reduction of the critical stress ratio. For incorporating the effect of destructuration, Taiebat et al. (2010) introduced the isotropic (S_i) and frictional (S_f) structuration factors. These factors and their rates of changes ($\dot{S}_i$, $\dot{S}_f$) are expressed as:

$$S_i = 1 + (S_{i0} - 1)\exp\left(\frac{-k_i(1+e)\varepsilon_d^p}{\lambda - \kappa}\right) \tag{3.51}$$

$$S_f = 1 + \left(S_{f0} - 1\right)\exp\left(\frac{-k_f(1+e)\varepsilon_d^p}{\lambda - \kappa}\right) \tag{3.52}$$

$$\dot{S}_i = -k_i\left(\frac{1+e}{\lambda - \kappa}\right)(S_i - 1)\dot{\varepsilon}_d^p \tag{3.53}$$

$$\dot{S}_f = -k_f\left(\frac{1+e}{\lambda - \kappa}\right)\left(S_f - 1\right)\dot{\varepsilon}_d^p \tag{3.54}$$

Where $\dot{\varepsilon}_d^p$ is a destructuration plastic strain rate which distributes the increments of volumetric ($\dot{\varepsilon}_v^p$) and deviatoric ($\dot{\varepsilon}_q^p$) plastic strain to destructuration rates ($\dot{S}_i$ and $\dot{S}_f$), since destructuration develop as plastic strains do:

$$\dot{\varepsilon}_d^p = \sqrt{(1-A)\dot{\varepsilon}_v^{p\,2} + A\dot{\varepsilon}_q^p} \tag{3.55}$$

In which A is a distributing material constant. In this constitutive model, the effect of destructuration is expressed by changing p_0, M, and N of the *SANICLAY* model to p_o^*, M^*, and N^* by means of the two isotropic (S_i) and frictional destructuration (S_f) factors.

$$p_o^* = S_i \cdot p_0 \tag{3.56}$$

$$N^* = S_f \cdot N \tag{3.57}$$

$$M^* = S_f \cdot M \tag{3.58}$$

The evolution rates of these variables are as follow:

$$\dot{p_o^*} = \dot{S}_i \cdot p_0 + S_i \cdot \dot{p_0} = \langle L \rangle \left(\dot{S}_i \cdot p_0 + S_i \cdot \overline{p_0} \right) = \langle L \rangle \overline{p_o^*} \tag{3.59}$$

$$\dot{N}^* = \dot{S_f} \cdot N = \langle L \rangle \left(\overline{S_f} \cdot N \right) = \langle L \rangle \overline{N^*} \tag{3.60}$$

$$\dot{M}^* = \dot{S_f} \cdot M = \langle L \rangle \left(\overline{S_f} \cdot M \right) = \langle L \rangle \overline{M^*} \tag{3.61}$$

It is worth mentioning that assigning 1 for each of the S_i or S_f makes the corresponding destructuration mechanism inactive and turns the model to the *SANICLAY* model. Therefore, the model's yield and plastic potential surfaces are similar to the *SANICLAY's* with the difference that the destructuration mechanism is included by substitution of *M*, *N*, and p_0 with M^*, N^*, and p_o^*, respectively:

$$f = (q - p \cdot \beta)^2 - ({N^*}^2 - \beta^2) p (\overline{p_o^*} - p) = 0 \tag{3.62}$$

$$g = (q - p \cdot \alpha)^2 - ({M^*}^2 - \beta^2) p (p_\alpha - p) = 0 \tag{3.63}$$

In addition, $\dot{p_0}$, $\dot{\alpha}$, and $\dot{\beta}$ are calculated accordingly to incorporate the effect of destructuration:

$$\dot{p_0} = \langle L \rangle \left(\frac{1+e}{\lambda - \kappa} \right) p_0 \frac{\partial g}{\partial p} = \langle L \rangle \left(\frac{1+e}{\lambda - \kappa} \right) p_0 \cdot p ({M^*}^2 - \eta^2) = \langle L \rangle \overline{p_0} \tag{3.64}$$

$$\dot{\alpha} = \langle L \rangle \left(\bar{\alpha} + \bar{\alpha}_f \right) = \langle L \rangle {\bar{\alpha}_f}^* = \langle L \rangle \left[\left(\frac{1+e}{\lambda - \kappa} \right) C \left(\frac{p}{{p_0}^*} \right)^2 \left| \frac{\partial g}{\partial p} \right| |\eta - x_\alpha \cdot \alpha| \left(\alpha^b - \alpha \right) + \frac{\bar{S}_f}{S_f} \alpha \right] \tag{3.65}$$

$$\dot{\beta} = \langle L \rangle \left(\bar{\beta} + \bar{\beta}_f \right) = \langle L \rangle {\bar{\beta}_f}^* = \langle L \rangle \left[\left(\frac{1+e}{\lambda - \kappa} \right) C \left(\frac{p}{{p_0}^*} \right)^2 \left| \frac{\partial g}{\partial p} \right| |\eta - x_\beta \cdot \beta| \left(\beta^b - \beta \right) + \frac{\bar{S}_f}{S_f} \beta \right] \tag{3.66}$$

The model uses the same concept for obtaining loading index and plastic modulus, but comparing to SANICLAY, $\overline{N}^*$ is a new term which is added to the plastic modulus formulation:

$$K_p = -\left(\frac{\partial f}{\partial {p_0}^*}\bar{p}_0{}^* + \frac{\partial f}{\partial N^*}\bar{N}^* + \frac{\partial f}{\partial \beta}\bar{\beta}^*\right) \tag{3.67}$$

Model constants are presented in Table 3.2. Except for the *SANICLAY* constants, three new constants are added to this model. k_i and k_f describe the rate of isotropic and frictional destructuration, and *A* is a parameter that distributes the effect of destructuration to volumetric and deviatoric plastic strain.

Table 3.2: Constants of the *SANICLAY* with destructuration (Taiebat et al., 2010)

Parameter	Description	Value
$M_c(N_c)$	Slope of the CSL on the compression side of $p-q$ plane (shape of the yield surface)	1.4 (1.2)
$m(n)$	Ratio of the slope of the CSL on the extension and on the compression side of $p-q$ plane (shape of the yield surface)	0.75 (1)
ν	Poisson's ratio	0.2
λ	Total volume change due to a change in mean stress	0.255
κ	Elastic volume change due to a change in mean stress	0.03
$x_\alpha(x_\beta)$	Saturation limit of anisotropy under paths with $\eta=$ const.	3.14 (1)
C	Rate of evolution of anisotropy	12
k_i	Parameter describing the rate of isotropic destructuration	0.9
k_f	Parameter describing the rate of frictional destructuration	1.3
A	Parameter describing coupling between volumetric and frictional destructuration	0.2

One could activate isotropic and/or frictional destructuration alone or in combination depending on the expected intensity of the softening response of the soil. Figure 3.7 shows the performance of the model for a combination of different destructuration patterns. Sudden softening response after the peak shear resistance, which is expected from the model, is clear in this figure. Authors believe that when a unique bound for α and β is used, i.e., *N*=*M*, or when an associative flow rule is used, i.e., *f*=*g*, the model shows fair response while the best performance of the model may be achieved when it is used as a two-surface model with *N* different than *M*. One of the drawbacks of the model is that the calibration of the model for a structured clay is not an easy task, especially as a truly intact sample may be impossible to obtain (Taiebat et al., 2010).

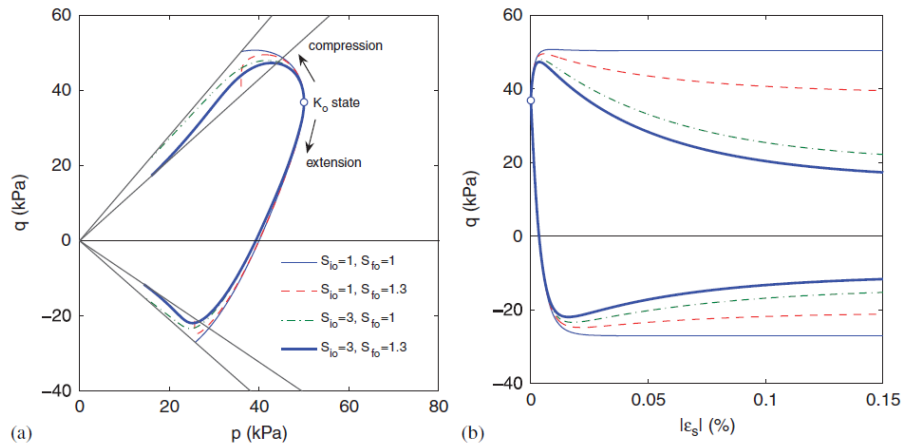

Figure 3.7 Illustration of the effects of isotropic and frictional destructuration mechanism independently and in combination. (Taiebat et al., 2010)

3.3.4 SANICLAY-B: Bounding Surface *SANICLAY* Model

The bounding surface *SANICLAY* model (*SANICLAY-B*) was specifically developed to simulate the response of clays under cyclic loading. To do so, this model uses the yield surface of the *SANICLAY* models (Dafalias et al., 2006; Taiebat et al., 2010) as its bounding surface (Seidalinov and Taiebat, 2014). Using the bounding surface concept allows plastic strains to develop under both monotonic and/or cyclic loadings for all the stress states inside the bounding surface. In particular, such an algorithm allows for nonlinearities to develop at low strains. The model uses a radial mapping rule to project the stress point inside the bounding surface (q, p) to the corresponding image point on it ($\bar{p}$, $\bar{q}$) from the projection center (p_c, q_c). According to the radial mapping rule, the image stress is found by:

$$\bar{p} = p_c + b(p - p_c) \tag{3.68}$$

$$\bar{q} = q_c + b(q - q_c) \tag{3.69}$$

Where b is a similarity ratio representing the distance between the loading surface $f=0$ and the bounding surface F=0. The loading surface, which is not explicitly defined, is a surface that has a center located at the projection center (PC = (p_c, q_c)) that expands and shrinks in a way that the actual stress point ($\bar{p}$, $\bar{q}$) always stays on it. The bounding surface, which represents the locus of

the ‘image’ stress $(\bar{p}, \bar{q})$, is a rotated and distorted ellipse, like previous versions of the model (Figure 3.8).

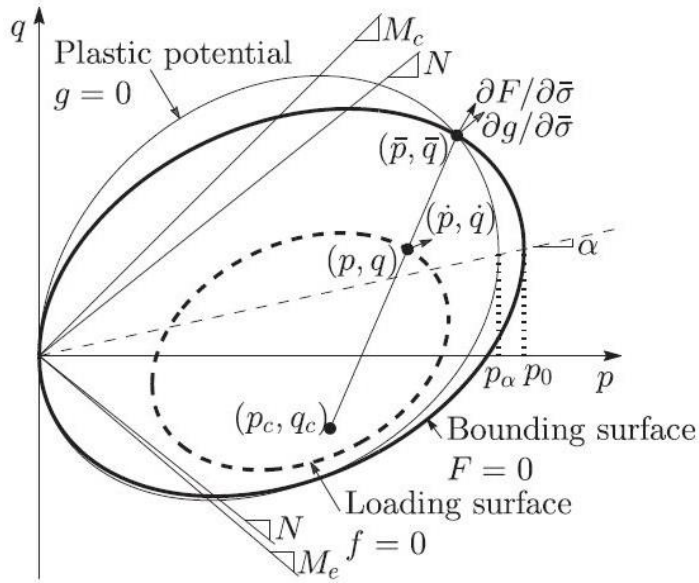

Figure 3.8 Plastic potential, bounding, and loading surfaces of the *SANICLA-B* model in the *p-q* stress space (Seidalinov and Taiebat, 2014).

The model follows a non-associative flow rule, where the plastic strain increment direction is parallel to the gradient of the plastic potential surface at the image stress point. The bounding and plastic potential surfaces are mathematically given in the triaxial stress space as:

$$f = (\bar{q} - \bar{p} \cdot \alpha)^2 - (N^2 - \alpha^2)\bar{p}(p_0 - \bar{p}) = 0 \tag{3.70}$$

$$g = (\bar{q} - \bar{p} \cdot \alpha)^2 - (M^2 - \alpha^2)\bar{p}(p_\alpha - \bar{p}) = 0 \tag{3.71}$$

Where p_0, and α are isotropic, related to density change, and rotational, related to anisotropy, hardening variables, respectively. The former accounts for the size, and the latter for the rotation (and/or distortion) of the bounding surface. They are obtained from the hardening rules mentioned for the *SANICLAY* with the destructuration model. *M* and *N* are the critical stress ratio and the stress ratio at the peak of the bounding surface, respectively. They also serve as bounds for the evolution of α of the bounding surface and plastic potential, respectively. It means that the bounding surface

F=0 and the plastic potential surface g =0 use an identical rotational variable (α), but with different limiting bounds of M, and N respectively.

The implicitly defined loading surface in Figure 3.8 is similar to the bounding surface with the similarity ratio of b and a homology center at PC (p_c, q_c). This ratio (b) varies from 1 to ∞ that corresponds to when the current stress reaches the bounding surface ($p = \bar{p},\ q = \bar{q}$) or the projection center ($p = p_c$, $q = q_c$), respectively.

Using a fixed PC does not ensure that the PC is always inside the bounding surface. Therefore, the authors adopted a moving PC to ensure that it is positioned inside the bounding surface. It guarantees to have unique image stress ($\bar{p}, \bar{q}$) and solves the problem of having overdamping associated with using a fixed projection canter (Seidalinov, 2012). It is also required that the projection center be updated to the current stress (p, q) upon any stress reversal. A stress reversal is defined as when the loading index L becomes lower than 0. This allows the model to predict plastic strains even at the very early stages of cyclic loading. The proposed evolution rule aiming to maintain a constant relative location of the projection center with the bounding surface is mathematically expressed by:

$$\dot{p_c} = \frac{p_c}{p_0}\dot{p_0} \tag{3.72}$$

$$\dot{q_c} = \frac{q_c}{p_0}\dot{p_0} + \left[p_c - X\frac{p_c(p_0 - p_c)\alpha}{[(N^2 - \alpha^2)p_c(p_0 - p_c)]^{1/2}}\right]\dot{\alpha} \tag{3.73}$$

$$X = (q_c - q_a)/(q_b - q_a) \tag{3.74}$$

In the bounding surface concept, in order to have plastic strains even if the stress point is inside the bounding surface, the plastic modulus K_p at the actual stress state (p, q) is set proportional to a bounding plastic modulus $\bar{K}_p$ at the corresponding image stress ($\bar{p}, \bar{q}$) and the Euclidian distance δ between ($\bar{p}, \bar{q}$) and (p, q) and r (between ($\bar{p}, \bar{q}$) and (p_c, q_c)):

$$K_p = \bar{K}_p + \frac{h \cdot p_0^3 \cdot \delta}{\langle r - s \cdot \delta \rangle} = \bar{K}_p + \frac{h \cdot p_0^3}{\langle \frac{b}{b-1} - s \rangle} \tag{3.75}$$

$$\bar{K}_p = -\left(\frac{\partial F}{\partial p_0}\bar{p}_0 + \frac{\partial F}{\partial \alpha}\bar{\alpha}\right) \tag{3.76}$$

$$h = \frac{h_0}{1+d};\ \dot{d} = a_d\left|\dot{\varepsilon}_d^p\right| \tag{3.77}$$

Where h and d are positive shape hardening and damage parameters, respectively. h_0 is the initial value of h, and a_d is a material constant. Also, $s \geq 1$ indirectly defines the size of the elastic region as a surface similar to the bounding surface with the *PC* its center of similarity. Overall, the model requires 11 model constants (Table 3.3), 2 of which are those related to the bounding surface formulation (h_0 and a_d).

Table 3.3: Constants of the *SANICLAY-B* (Seidalinov and Taiebat, 2014)

Model constant category	**Designation**	**Set 1**
Elasticity	κ	0.03
	ν	0.2
Critical state	λ	0.15
	M_c	1
	M_e	1
Bounding surface	N	1
	h_0	varied
	a_d	varied
Rotational hardening	C	5
	x	1.7
Destructuration	k_i	0

The model only employs the isotropic destructuration mechanism, out of two mechanisms introduced by Taiebat et al. (2010), meaning that the frictional destructuration mechanism is not included in this version of the model. An example of simulations of the model is illustrated in Figure 3.9. The model renders a realistic cyclic stress-strain response; however, the model shows an unrealistic effective stress lock-up that occurs after a few cycles of loading. This hinders the model's ability to realistically predict the pore water pressure build-up of a cyclically loaded soil.

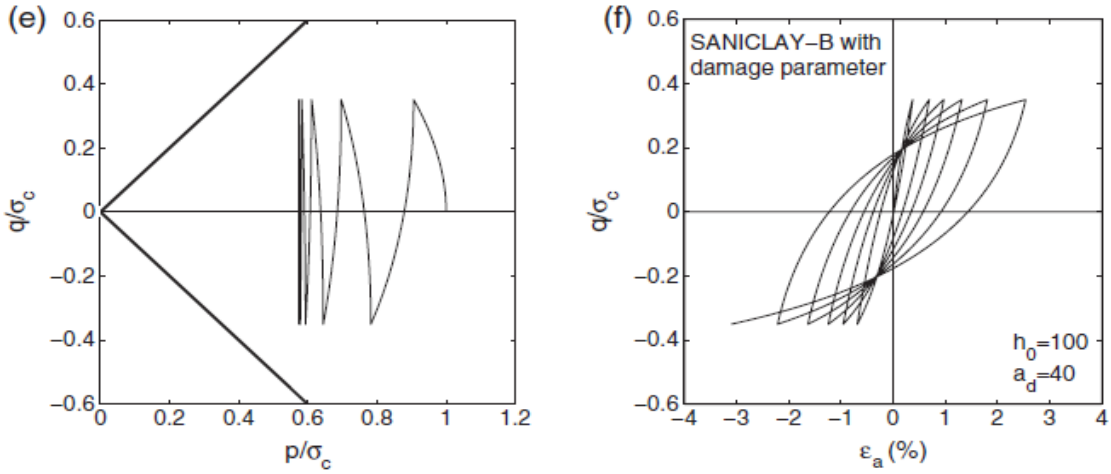

Figure 3.9 The SANICLAY-B model simulations (Seidalinov and Taiebat, 2014)

3.3.5 SANICLAY-H: SANICLAY with a Hybrid Flow Rule

The radial mapping rule that is used to find the image stress by projecting the current stress point on the bounding surface from a projection surface is referred to as the image stress flow rule by Shi (2016) and Shi et al. (2018). In their work, the use of an image stress flow rule is substituted by a hybrid flow rule to improve the model's ability to simulate the excess pore water pressure build-up. The new hybrid flow rule is using a plastic strain operator (flow rule) that depends not only on flow characteristics of the image stress, but also on those of the current stress:

$$R = R_i + R_c \tag{3.78}$$

Where R is the direction of plastic strains which is decomposed into R_i and R_c that are plastic directions at the image ($\bar{p}$, $\bar{q}$) and current stress (p, q) point, respectively, as shown in Figure 3.10 schematically.

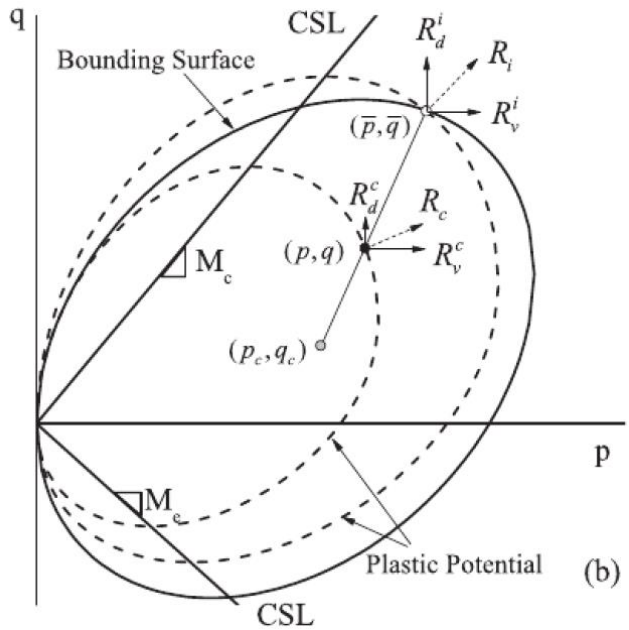

Figure 3.10 Schematic diagram of plastic flow vectors at the current stress (R_c) and image stress (R_i) (Shi et al., 2018).

The new hybrid flow rule proposes that the image and the current stress point gradients of the volumetric plastic flow direction (R_v^i and R_v^c) as well as the image stress point gradient of the deviatoric plastic flow direction (R_d^i) be used to find the plastic strains as follows:

$$R_v = R_v^i \cdot g_i + R_v^c(1 - g_i) \tag{3.79}$$

$$R_d = R_d^i \tag{3.80}$$

Where g_i is a distribution variable which is given by:

$$g_i = (\frac{1}{b})^w \tag{3.81}$$

Where w is a material constant coupling the relative contribution of R_v^i and R_v^c. The special case of the model, which is the image stress flow rule of Seidalinov and Taiebat (2014), is obtained when $w = 0$. b is the same similarity ratio introduced by Seidalinov and Taiebat (2014). As it was mentioned in the previous section, the two limits of this ratio (b) are 1 and ∞ that happens when the current stress is on the bounding surface ($p = \bar{p}$, $q = \bar{q}$) and on the projection center ($p = p_c$,

$q = q_c$), respectively. In addition, the projection center is updated to the current stress point at every stress reversal. Therefore, it means that at stress reversals, b takes a large value, g_i tends to be zero, and as a result, the current stress component of the volumetric plastic flow direction (R_v^c) plays a key role in developing plastic strains. The opposite occurs when b=1, where the current stress and the image stress coincide. In this case, the effect of the image stress component of the volumetric plastic flow direction (R_v^i) to develop plastic strains is more pronounced.

Building upon SANICLAY-B, the plastic potential of that is also used for this model. The volumetric (R_v^i) and deviatoric (R_d^i) components of the plastic flow direction at image stress as well as the volumetric component of the plastic flow direction at the current stress (R_v^c) are given as:

$$R_v^i = \frac{\partial g}{\partial \bar{p}} = \bar{p}(M^2 - \bar{\eta}^2) \tag{3.82}$$

$$R_d^i = \frac{\partial g}{\partial \bar{q}} = 2\bar{p}(\bar{\eta} - \alpha) \tag{3.83}$$

$$R_v^c = p(M^2 - s_l \cdot \eta^2) \tag{3.84}$$

where $\bar{\eta}$ is the image stress ratio ($\bar{\eta} = \frac{\bar{q}}{\bar{p}}$), and s_l a variable that alternates between 1 and -1 depending on the loading direction and the stress ratio. Besides the applied hybrid plastic flow rule, the model benefits from the new evolution rule for the projection center update, which is worth describing. In the *SANICLAY* bounding surface model, the evolution rule is based on the assumption that p_0 or α changes separately. To modify that, the model proposes substitutions for the projection center (p_c, a_c) update that may consider the simultaneous change of p_0 or α:

$$\dot{p_c} = \frac{p_c}{p_0}\dot{p_0} \tag{3.85}$$

$$\dot{q_c} = \frac{q_c}{p_0}\dot{p_0} + \frac{N_c^2 \cdot p_c - \alpha \cdot q_c}{N_c^2 - \alpha^2}\dot{\alpha} \tag{3.86}$$

The performance of the model is shown in Figure 3.11. As it is clear from this figure, the modifications of this model have resulted in capturing well the butterfly shape of the stress path, and as a result, the excess pore water pressure build-up.

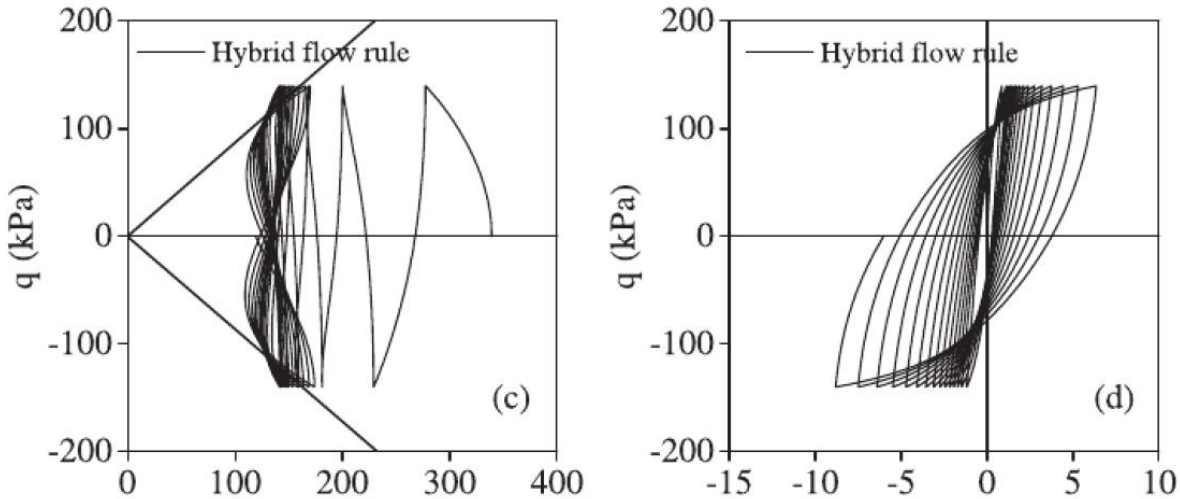

Figure 3.11 Illustration of the bounding surface and the damage parameter effects in the simulation of undrained cyclic triaxial loading (Shi et al., 2018)

Although the model has improved the SANICLAY model family's predictive capability, it lacks some of the main features for clays described in the literature. One of the model's underlying limitations is that it does not consider time rate effects crucial to simulate clay's behavior under monotonic and cyclic loadings.This model uses 17 model constants, which are summarised along with definitions in Table 3.4.

Table 3.4: Parameters of the model (Shi et al., 2018)

Model parameter	Description
λ,κ	Slopes of the virgin compression line and rebound line in the $e-ln(p)$ plane
ν	Poisson's ratio
M_o,M_e	Stress ratio at critical state
N_o,N_e	Shape of the bounding surface
χ	Upper-bound rotation during constant stress ratio loading
C	Rate of rotational hardening
A_g,e_g,n_g	Fitting parameters for G_0 function
$\gamma_{0.7}$	Rate of elastic stiffness degradation with shear strain
w	Cyclic pore pressure accumulation
c_d	Cyclic ratcheting/shakedown
h_o,h_e	Magnitude of plastic modulus in compression and extension

3.3.6 Dafalias and Manzari (2004) (*DM04*):

This model is a modified and improved version of the model proposed by Manzari and Dafalias (1997). This model is formulated in *p*-*q* and full stress spaces for simulations of both monotonic and cyclic responses of sands. The most interesting feature of the model is that it considers the effect of fabric changes upon the dilation. The model is formulated in terms of the stress ratio ($\eta = \frac{q}{p}$) and uses 4 different surfaces, which are lines (i.e., stress ratios) in *p*-*q* space: yield, critical, dilatancy, and bounding lines, which are illustrated in Figure 3.12. The main framework of this model is made such that only a change of stress ratio can cause plastic strains, and a loading condition resulting in no change in stress ratio will only develop elastic strains.

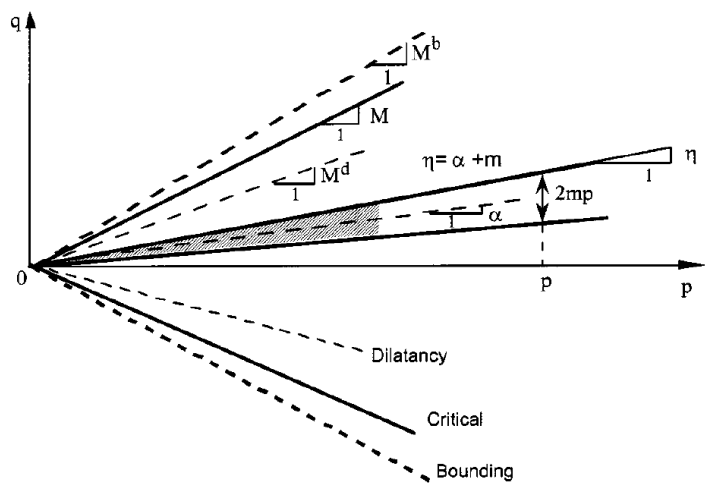

Figure 3.12: Schematic of the yield, critical, dilatancy, and bounding lines in *p*-*q* space (Dafalias and Manzari, 2004)

The yield surface of the model in *p*-*q* space is given by:

$$f = |\eta - \alpha| - m = 0 \tag{3.87}$$

The yield surface geometrically represents a wedge in *p*-*q* space inside which only elastic strains occur. α is the center of the yield surface or slope of the middle line of the elastic wedge, and m represents the width of the elastic wedge.

The model uses a non-associative flow rule. The deviatoric and volumetric plastic strain increments formulation are postulated as:

$$\dot{\varepsilon}_q^p = \frac{\dot{\eta}}{H} \tag{3.88}$$

$$\dot{\varepsilon}_v^p = d\left|\dot{\varepsilon}_q^p\right| \tag{3.89}$$

Based on these equations, the plastic deviatoric strain increment ($\dot{\varepsilon}_q^p$) depends on the increment of stress ratio ($\dot{\eta}$) and the plastic modulus (H). The increment of plastic volumetric strain ($\dot{\varepsilon}_v^p$) is associated directly with the plastic deviatoric strain increment ($\dot{\varepsilon}_q^p$) via the dilatancy parameter (d). H and d are proportional to the distance of the stress ratio (η) with bounding (M^b) and dilatancy (M^d) stress ratios in the contraction and dilation phase of loading, respectively:

$$H = h(M^b - \eta) \tag{3.90}$$

$$d = A_d(M^d - \eta) \tag{3.91}$$

The values of M^b and M^d are controlled by the state parameter, which is defined as the distance between the void ratio at the current stress point (e) and that at the critical state line (e_c) in the e-p space:

$$\psi = e - e_c \tag{3.92}$$

Which gives M^b and M^d as:

$$M^b = M \cdot exp(-n^b \cdot \psi) \tag{3.93}$$

$$M^d = M \cdot exp(n^d \cdot \psi) \tag{3.94}$$

Where n^b and $n^d$are positive model constants and h and A_d are functions of the state parameter. The summary of all model equations is provided in Table 3.5. Also, the model uses 15 different constants that are shown in Table 3.6.

In Figure 3.13, the results of monotonic simulations of the model are compared with those obtained from undrained compression tests on Toyoura sand at different effective stress levels and void ratios. As it can be observed, the contractive and dilative behavior of the soil, as well as the peak shear strength, is reasonably well predicted by this model.

Table 3.5: Summary of the Dafalias and Manzari model's equations (Dafalias and Manzari, 2004)

Triaxial equations	Multiaxial equations
Critical state line	
—	$e_c = e_0 - \lambda_c (p_c / p_{at})^{\xi}$
Elastic deviatoric strain increment	
$d\varepsilon_q^e = dq/3G$	$d\mathbf{e}^e = d\mathbf{s}/2G$
—	$G = G_0 p_{at}[(2.97-e)^2/(1+e)](p/p_{at})^{1/2}$
Elastic volumetric strain increment	
—	$d\varepsilon_v^e = dp/K$
	$K = 2(1+\nu)G/3(1-2\nu)$
Yield surface	
$f = \lvert\eta - \alpha\rvert - m = 0$	$f = [(\mathbf{s} - p\boldsymbol{\alpha}):(\mathbf{s} - p\boldsymbol{\alpha})]^{1/2} - \sqrt{2/3}pm = 0$
Plastic deviatoric strain increment	
$d\varepsilon_q^p = d\eta/H$	$d\mathbf{e}^p = \langle L \rangle \mathbf{R}'$
$H = h(M^b - \eta)$	$K_p = (2/3)ph(\boldsymbol{\alpha}_\theta^b - \boldsymbol{\alpha}):\mathbf{n}$
$M^b = M \exp(-n^b \Psi)$	$\boldsymbol{\alpha}_\theta^b = \sqrt{2/3}[g(\theta, c)M \exp(-n^b \Psi) - m]\mathbf{n}$
$h = b_0 / \lvert\eta - \eta_{in}\rvert$	$h = b_0 / (\boldsymbol{\alpha} - \boldsymbol{\alpha}_{in}):\mathbf{n}$
—	$b_0 = G_0 h_0 (1 - c_h e)(p/p_{at})^{-1/2}$
Plastic volumetric strain increment	
$d\varepsilon_v^p = d\lvert\varepsilon_q^p\rvert$	$d\varepsilon_v^p = \langle L \rangle D$
$d = A_d(M^d - \eta)$	$D = A_d(\boldsymbol{\alpha}_\theta^d - \boldsymbol{\alpha}):\mathbf{n}$
$M^d = M \exp(n^d \Psi)$	$\boldsymbol{\alpha}_\theta^d = \sqrt{2/3}[g(\theta, c)M \exp(n^d \Psi) - m]\mathbf{n}$
$A_d = A_0(1 + \langle sz \rangle)$	$A_d = A_0(1 + \langle \mathbf{z}:\mathbf{n} \rangle)$
Fabric-dilatancy tensor update	
$dz = -c_z \langle -d\varepsilon_v^p \rangle (s z_{max} + z)$	$d\mathbf{z} = -c_z \langle -d\varepsilon_v^p \rangle (z_{max}\mathbf{n} + \mathbf{z})$
Back-stress ratio tensor update	
$d\alpha = d\eta$	$d\boldsymbol{\alpha} = \langle L \rangle (2/3)h(\boldsymbol{\alpha}_\theta^b - \boldsymbol{\alpha})$

Table 3.6: Summary of the model constants (Dafalias and Manzari, 2004)

Constant	Variable	Value
Elasticity	G_0	125
	ν	0.05
Critical state	M	1.25
	c	0.712
	λ_c	0.019
	e_0	0.934
	ξ	0.7
Yield surface	m	0.01
Plastic modulus	h_0	7.05
	c_h	0.968
	n^b	1.1
Dilatancy	A_0	0.704
	n^d	3.5
Fabric-dilatancy tensor	z_{max}	4
	c_z	600

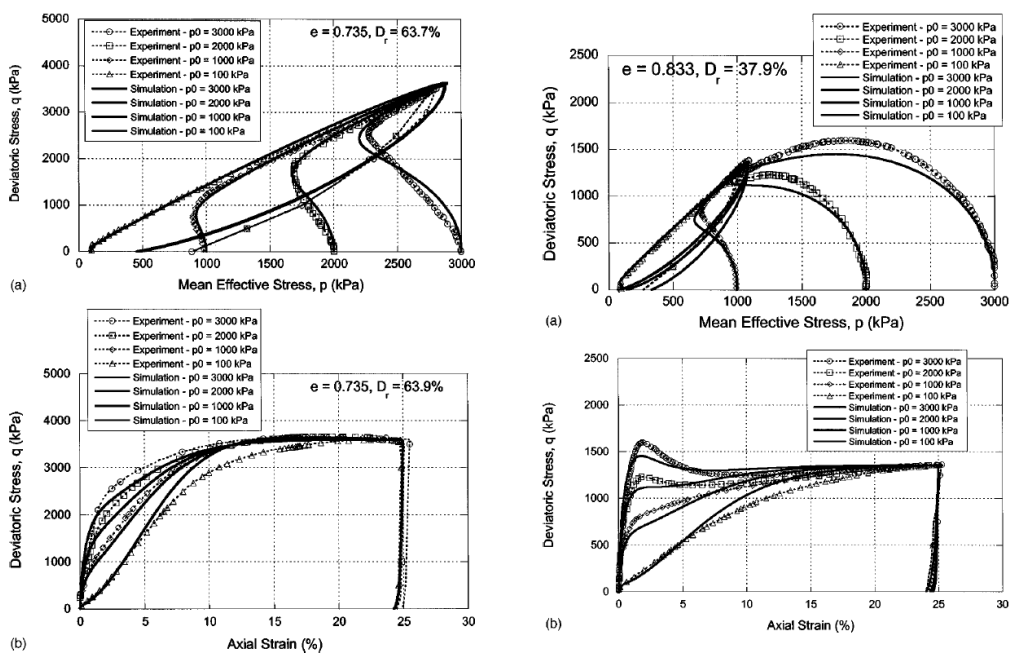

Figure 3.13: Numerical and experimental results of undrained compression tests on Toyoura sand at different effective confining pressures and initial void ratios (Dafalias and Manzari 2004).

In Figure 3.14, the model performance in simulating a cyclic triaxial test is compared with experimental data. Although this simulation is not as accurate as the monotonic counterparts, the model has been shown to capture the general trend of sands behavior well in terms of stress reversal and associated changes from dilation to contraction and vice versa.

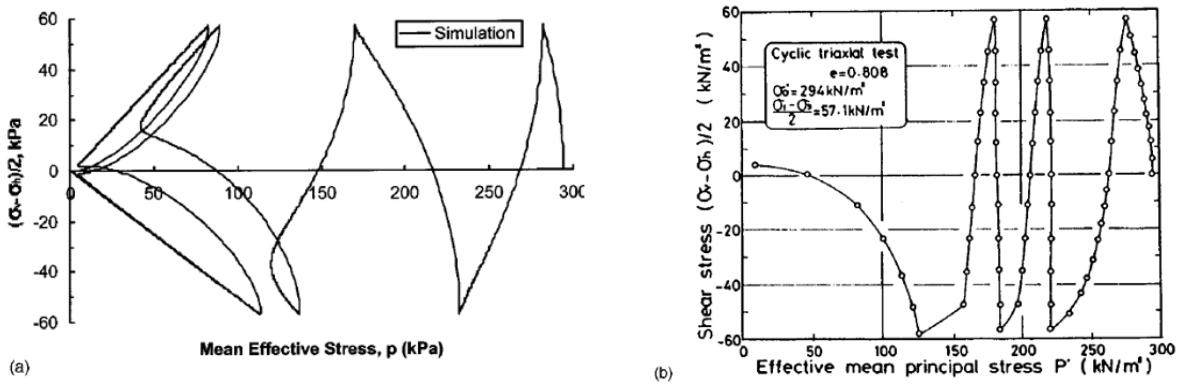

Figure 3.14: Simulation and experiment results for Toyoura sand (Dafalias and Manzari 2004).

3.3.7 *PM4SAND*: Plasticity Model for Sands

Boulanger (2010) published the first version of the plasticity model for sand (*PM4SAND*) in 2010. This model is based on the Dafalias and Manzari model, and similarly, it is a stress ratio-based model cast within the critical state framework and the bounding surface plasticity. Since the earlier version of the model, it has been modified several times to improve the model's ability to predict sands' cyclic response under cyclic loadings. One of the emphases in this model is that in its simplest application, the model only requires three input parameters, which are soil relative density, the shear modulus coefficient, and the contraction rate parameter. In this section, the last version of the model published by Boulanger and Ziotopoulou (2017, version 3.1) will be briefly discussed.

The *PM4SAND* model is developed to be only in terms of the in-plane stresses to simplify the model and reduce the computations and corresponding time required for solving complex engineering problems. The yield surface of the *PM4SAND* model is expressed in terms of the back-stress ratio, α:

$$\mathrm{f} = \sqrt{(r-\alpha):(r-\alpha)} - \sqrt{1/2m} \qquad (3.95)$$

This expression implies that the yield surface is a cone in the stress space where the back-stress ratio and elastic parameter, m, defines the center and radius of the cone, respectively, as shown in Figure 3.15.

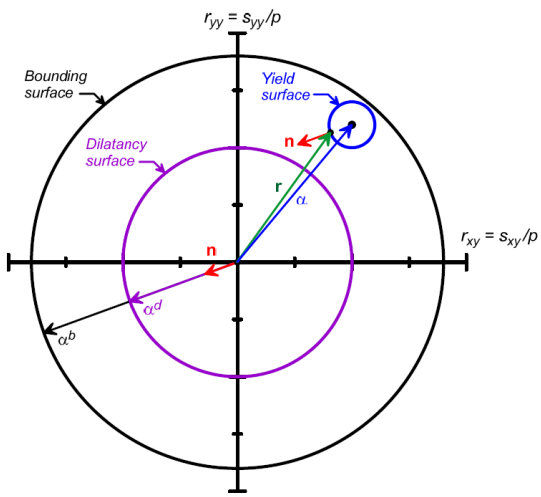

Figure 3.15: Schematic of the bounding, dilatancy, and yield surfaces on the stress-ratio plane Boulanger and Ziotopoulou (2017, version 3.1).

The volumetric ($\dot{\boldsymbol{\varepsilon}}_v^p$) and deviatoric ($\dot{\boldsymbol{\varepsilon}}_d^p$) increments of the plastic strains are expressed as:

$$\dot{\boldsymbol{\varepsilon}}_d^p = < L > \boldsymbol{R}' \tag{3.96}$$

$$\dot{\varepsilon}_v^p = < L > D \tag{3.97}$$

Where D is the dilatancy and $\boldsymbol{R}'$ is the deviatoric component of the plastic strain direction, $\boldsymbol{R}$, which is expressed as:

$$\boldsymbol{R} = \boldsymbol{n} + \frac{1}{3} D \cdot \boldsymbol{I} \tag{3.98}$$

Where $\boldsymbol{I}$ is the identity tensor, and $\boldsymbol{n}$ is the unit normal to the yield surface. It should be noted that one of the applied changes to this model compared to the *DM04* is the exclusion of the Lode angle dependency, meaning that the same friction angles are used in compressive and extension loading. Employing a no Lode angle dependency assumption in this model implies that $\boldsymbol{R}' = \boldsymbol{n}$. Although

the Lode angle independency has simplified the model and its implementation, it brings the responsibility of selecting a representative friction angle to the user

Similar to the yield surface, bounding and dilatancy surfaces are also conical-shape surfaces in the stress space, which are mathematically shown in terms of back stress ratios as:

$$\alpha^b = \sqrt{1/2}\,[M^b - m]n \tag{3.99}$$

$$\alpha^d = \sqrt{1/2}\,[M^d - m]n \tag{3.100}$$

Where $M^b$and M^d are bounding and dilatancy ratios which are related to the critical state, M .

The bounding and dilatancy ratios are associated with the critical state line via the relative state parameter index, ξ_R, which is defined in the model using the empirical Bolton's dilatancy relationship (Bolton, 1986). Based on this relationship $D_{R,cs}$, which is the relative density at the critical state, is calculated using Bolton parameters, Q and R as:

$$D_{R,cs} = \frac{R}{Q - \ln\left(100\,\frac{p}{P_A}\right)} \tag{3.101}$$

Where P_A is the atmospheric pressure. One of the improvements of the *PM4SAND* compared to the *DM04* is the modification of the shear modulus formulation to be only dependent on one constant, i.e. G_0, but not both G_0 and void ratio, e, that was the case in the *DM04* model. In fact, the authors of the model believe that confining stress has more effect on G than the void ratio does. In addition, removing e eases calibration purposes. Instead, two other factors are added to the shear modulus formulation to better predict the soil hysteretic stress-strain response at large shear strains where liquefaction happens. The model performance on simulating a cyclic direct simple shear test on sands with three different relative densities of 0.35, 055, and 0.75% is shown in Figure 3.16.

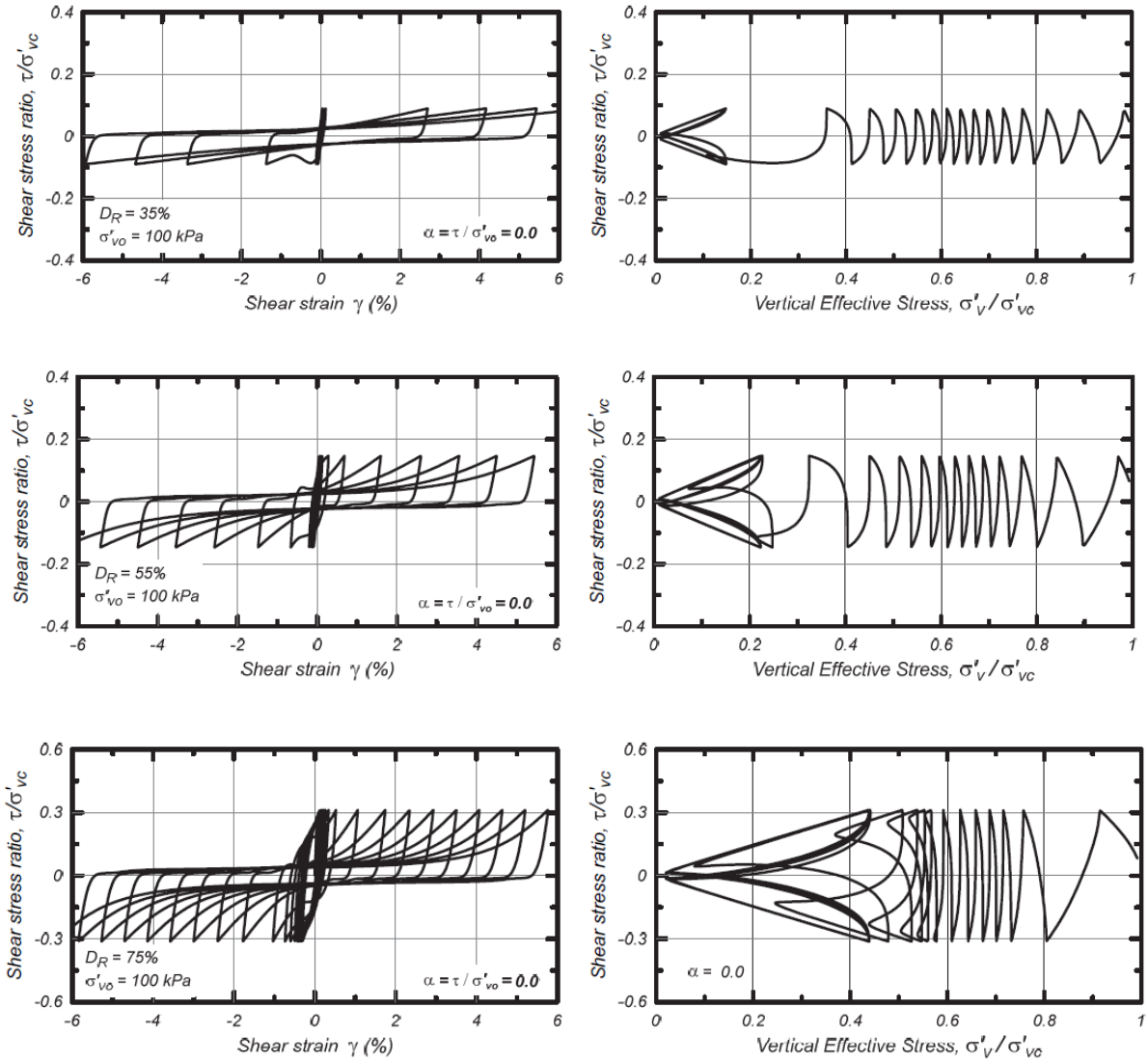

Figure 3.16: Undrained cyclic *DSS* loading response of *PM4SAND* for sands with three different relative densities Boulanger and Ziotopoulou (2017, version 3.1).

This figure shows that the hysteresis loops and the stress path response can be simulated closely to what is expected for sands (shown in the literature review). The sharp hysteresis loops, the ability to predict the butterfly loops when reaching the critical state line, and the contractive and dilative behavior under cyclic loading are the main features that the model could predict very well.

3.3.8 *PM4SILT*: Plasticity Model for Silts

The *PM4Silt* model has been developed by Boulanger and Ziotopoulou (2018) for geotechnical cyclic applications of low plasticity silts and clays. The model is cast in the same framework as the *PM4Sand* model (version 3), and therefore, shares several features with that model. Like the *PM4SAND*, the *PM4SILT* is a stress-ratio controlled model that has been framed in a bounding surface plasticity and critical state concept. Improvements to the model have been made such that the model predicts the undrained cyclic and monotonic response of low to non-plastic silts with high precision. One of the main emphases in the model that also holds for the *PM4SAND* is that the model is pre-calibrated so that the practitioners may use the model by only providing three input parameters that are: the undrained shear strength ratio (or undrained shear strength), the shear modulus coefficient, and the contraction rate parameter. However, assigning different values other than default values to the model's internal or secondary parameters is possible if desired by the user.

PM4SILT shares the same yield, bounding, and dilatancy surfaces as well as the same expressions for the volumetric and deviatoric plastic strain increments with *PM4SAND*. The main difference between this model with *PM4SAND* is the way by which the critical state is employed. The state parameter, which calculates the difference between the current void ratio (e) and the void ratio at the critical state line (e_{cs}) is adopted in this model from the work of Been and Jefferies (1985) in which (e_{cs}) is calculated by the following expression:

$$e_{cs} = \Gamma - \lambda \cdot ln\left(\frac{p}{1kPa}\right) \tag{3.102}$$

This expression implies a linear critical state line in void ratio versus the natural logarithm of mean effective stress space with a slope of λ and an intercept of Γ when $p' = 1\ kPa$.

The model uses the same bounding, M^b, dilatancy, M^d, and critical stress, M , surfaces that are incorporated in the *PM4SAND* model. Similar to the *PM4SAND* model, reaching the critical state causes the bounding and dilatancy surfaces to collapse onto the critical stress surface.

The performance of the model to simulate cyclic direct simple shear tests on specimens with different normalized strength ratios ($S_{u,cs}/\sigma'_{vc}$) of 0.25, 0.5, and 0.75 are plotted in Figure 3.17.

The model's simulations show that it could fairly simulate the cyclic response of low plasticity silts and clays.

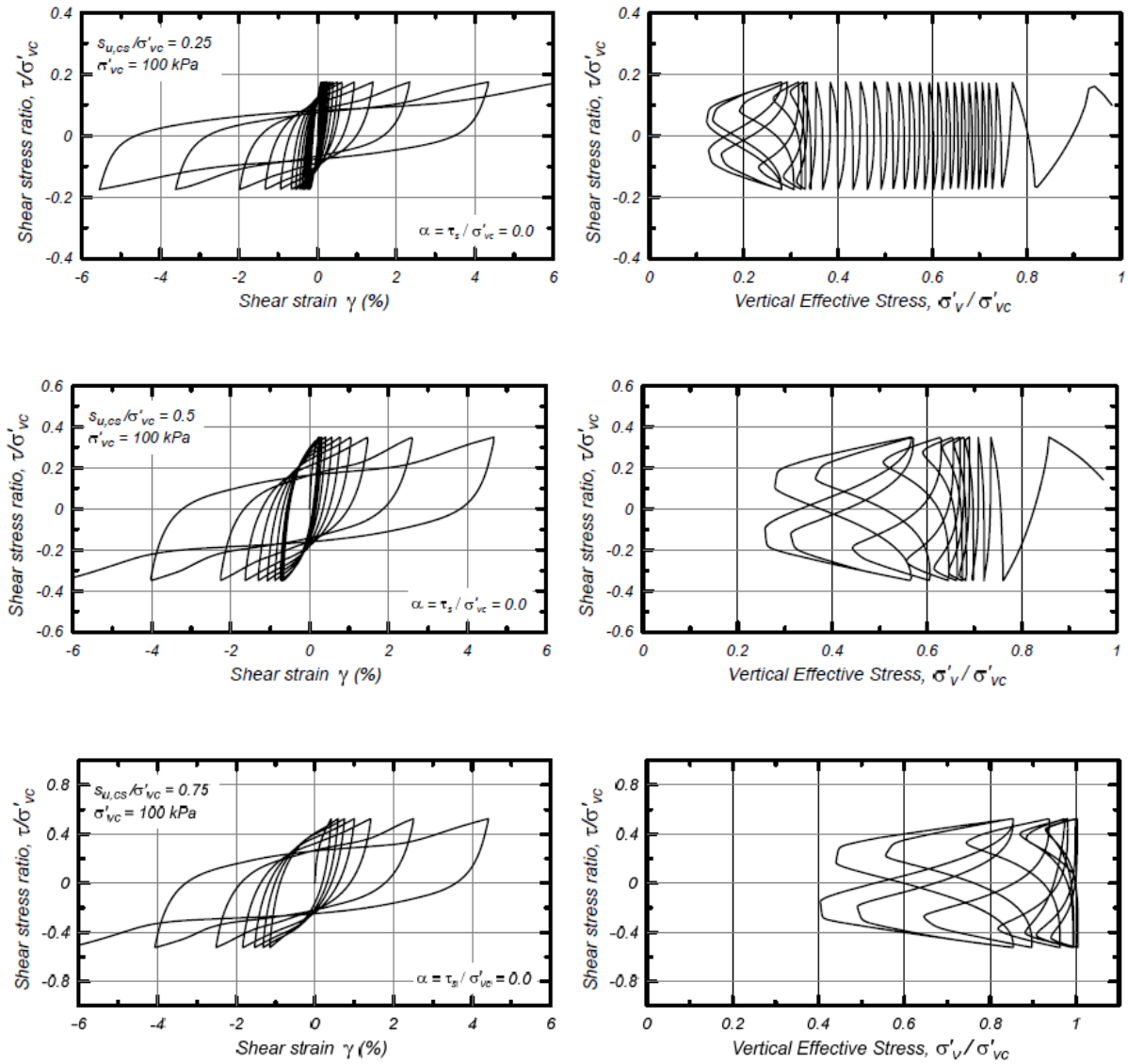

Figure 3.17: Undrained cyclic *DSS* loading response of *PM4SILT* for silt with three different normalized strength ratios Boulanger and Ziotopoulou (2018).

3.4 Rate-dependent Constitutive Models

All the discussed models in the previous section were rate-independent models. To consider the time-dependency of the soil, it is crucial to use a time-dependent constitutive model. Time and time

dependency are usually recognized as creep, stress relaxation, and strain-rate effects related to the soil skeleton's viscosity (Liingaard et al. 2004). A wide range of constitutive models has been developed so far to capture the time dependency of soils, among which the general stress-strain-time models have received the most attention. These models are mostly given in terms of the incremental forms and include a wide range of time-dependent and viscoelastic-viscoplastic models (Karim and Gnanendran, 2014).

Perzyna's (1963) theory of viscoplasticity is one of the most popular propositions used for incorporating time or rate effects in soil plasticity. According to this theory, the total strain increments $\dot{\boldsymbol{\varepsilon}}$ is decomposed into a time-independent elastic $\dot{\boldsymbol{\varepsilon}}^{\boldsymbol{e}}$ part and an irreversible and time-dependent (viscoplastic) $\dot{\boldsymbol{\varepsilon}}^{\boldsymbol{vp}}$ part:

$$\dot{\boldsymbol{\varepsilon}} = \dot{\boldsymbol{\varepsilon}}^{\boldsymbol{e}} + \dot{\boldsymbol{\varepsilon}}^{\boldsymbol{vp}} \tag{3.103}$$

A static loading surface (f_s) as well as a dynamic loading surface (f_d) are used in Perzyna's theory to calculate elastic and viscoplastic strain increments. The static loading surface represents the soil's time-independent behavior, while the dynamic loading surface represents that of the time-dependent. In other words, elastic strains occur inside the static loading surface (SLS) while viscoplastic strains may develop anywhere inside, on, or outside the static loading surface with the following expression:

$$\dot{\boldsymbol{\varepsilon}}^{\boldsymbol{vp}} = \mu.\langle\varphi(f)\rangle.\frac{\partial g}{\partial \boldsymbol{\sigma}} \tag{3.104}$$

Where μ is the fluidity parameter, and g is the viscoplastic potential surface, which has the same direction as the dynamic loading surface (DLS), if an associate flow rule is used. $\varphi(f)$ is called the overstress or excess stress function, which is a distance between static and dynamic loading surfaces. In fact, the distance between static and dynamic loading surfaces, or the departure from the static loading surface, produces the viscoplastic increments. Different components of Perzyna's theory are schematically demonstrated in Figure 3.18. Most of the viscoplastic constitutive models use Perzyna's theory with different relationships for the overstress function $\varphi(f)$ (Adachi and Oka, 1982; Shahrour and Meimon, 1995; Rezania et al., 2016)

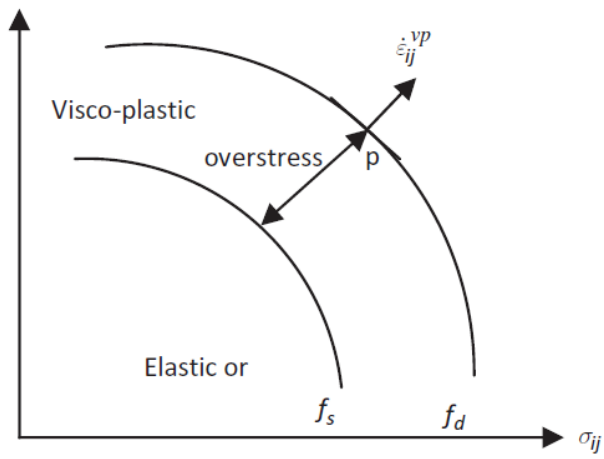

Figure 3.18: Schematic of the static and dynamic loading surfaces, elastic and viscoplastic regimes in Perzyna's model (Karim and Gnanendran, 2014)

According to Perzyna's theory, the overstress function, $\varphi(f)$, produces viscoplastic strains only if the elastic nucleus, f, is greater than zero. Therefore, the state of the soil inside the elastic nucleus does not develop viscoplastic deformation. This criterion can be expressed as:

$$\langle\varphi(f)\rangle = \begin{cases} \varphi(f) & if\ \varphi(f) \geq 0 \\ 0 & if\ \varphi(f) < 0 \end{cases} \tag{3.105}$$

In the rest of the section, some of the recent visco-plastic models are discussed by mainly focusing on capturing the stress or strain rate dependency, while creep is also covered as a by-product.

3.4.1 A Visco-plastic *SANICLAY* Model

Rezania et al. (2006) introduced a model for clays to account for rate dependency, soil anisotropy, consolidation state, and destructuration. For this purpose, Perzyna's theory of viscoplasticity is anchored to the *SANICLAY* framework. Therefore, the model employs a rotated elliptical surface in the stress space, similar to that of the *SANICLAY* model family, as the static loading surface. Due to the application of an associated flow rule, the dynamic loading surface, which shares the same shape as the static loading surface, functions as the visco-plastic potential function in this model. The static and dynamic loading surfaces are shown in Figure 3.19.

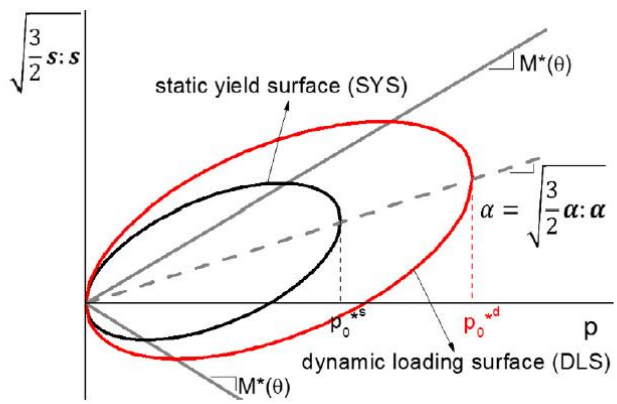

Figure 3.19: Schematic illustration of the visco-plastic *SANICLAY* model (Rezania et al., 2006).

In the multiaxial stress space, the static loading surface of the model is expressed as:

$$f = \frac{3}{2}(\boldsymbol{s} - p \cdot \boldsymbol{\alpha}):(\boldsymbol{s} - p \cdot \boldsymbol{\alpha}) - (M^*(\theta)^2 - \frac{3}{2}\boldsymbol{\alpha}:\boldsymbol{\alpha})p(p_o^{*s} - p) = 0 \qquad (3.106)$$

Where $\mathbf{s}$ and p are the deviatoric and volumetric components of the stress tensor, respectively (defined in Eq.(3.2)and Eq.(3.3)). $M^*(\theta)$ is the Lode angle , θ, dependent function that interpolates the slope of the critical state line in the stress space between its values in compression,M_c, and extension , M_e. p_o^{*s} and $\boldsymbol{\alpha}$ adjust the size and rotation of the structured static loading surface using isotropic and rotational hardening rules. The isotropic and rotational hardening rules discussed in this model are similar to those discussed for *SANICLAY* with destructuration; therefore, they are not repeated here.

As mentioned earlier, in Perzyna's theory, once the stress exits the static yield surface, the visco-plastic deformations occur, the magnitude of which corresponds to the departure of the stress from the static loading surface (the overstress). The overstress function required in Perzyna's theory to find the visco-plastic strains (refer to Eq. (3.104) are expressed in terms of the size of the static, p_0^s, and dynamic , p_0^d, loading surfaces, respectively, as:

$$\varphi(F) = \exp(F) - 1 = exp\left[N\left(\frac{p_0^d}{p_0^s} - 1\right)\right] - 1 \qquad (3.107)$$

Where N is a model viscosity parameter with which the model has a total of twelve input parameters, provided in Table 3.7

Table 3.7: Input parameters of the visco-plastic *SANICLAY* (Rezania et al., 2006)

Model constant		Kawasaki	Haney	St. Herblain	Batiscan
Elasticity	κ	0.021	0.05	0.022	0.037
	ν	0.2	0.25	0.3	0.3
Critical state	M_c (M_e)	1.65 (1.24)	1.28	1.25	0.98
	λ	0.16	0.32	0.41	0.41
Rotational hardening	C	12	12	10	12
	x	2.6	2.4	1.5	1.7
Destructuration	k_i	0	1.5	0	1.4
	k_f	0	1.4	0	1.3
	A	0	0.3	0	0.5
Viscosity	N	12	17	9	12
	μ [s^{-1}]	7×10^{-6}	5×10^{-11}	5×10^{-9}	2×10^{-9}

The model performance in predicting the soil's undrained monotonic response at different loading rates is shown in Figure 3.20. The model captures well the effects of the time on compression tests; however, less predictive accuracy could be observed for extension tests.

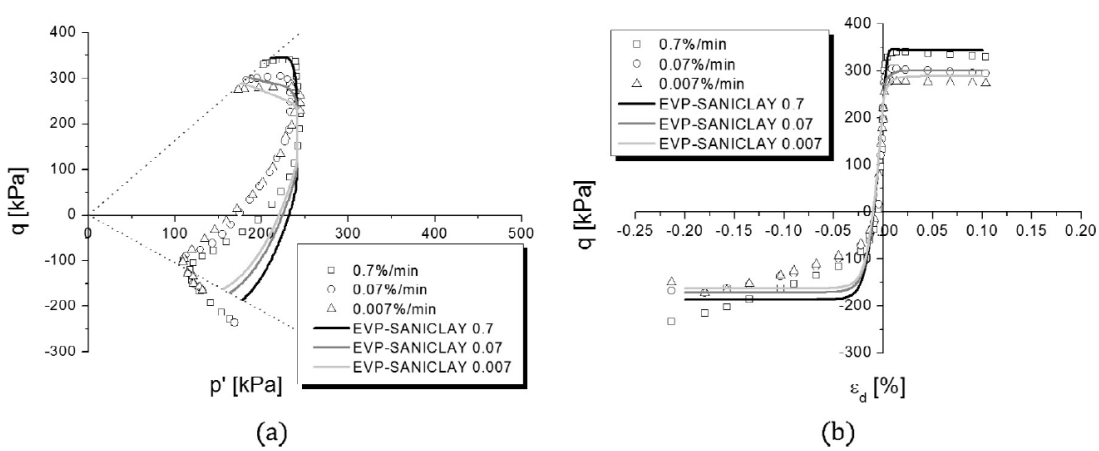

Fig. 2. Undrained triaxial test: (a) effective stress path; (b) deviator stress versus axial strain.

Figure 3.20: Undrained monotonic simulations of visco-plastic *SANICLAY* (Rezania et al., 2006)

3.4.2 *TVP UH*: Thermo-Viscoplastic Unified Hardening Model

Kong et al. (2020) developed a thermo-visco-plastic model upon the unified hardening model (developed by Yao et al. (2009), Yao et al. (2013), and Yao et al. (2014) to evaluate the combined

effects of time and temperature on monotonic soil behavior and their influence on the overconsolidation history of the soil. The following assumptions are made for the development of the *TVP UH* model:

1- A parallel-line concept, proposed by Bjerrum (1967), is adopted for the normally consolidation curves in the $e - lnp$ space, according to which the compression curves at different creep times are parallel to the normally consolidated line (the one at the farthest top is called the instant normally consolidate line (*INCS*)) and that the creep may consolidate the soil.

2- Like the above concept, the authors used the same parallel lines concept for the temperature effects. According to this concept, and supported based on Campanella and Mitchell's (1968) observations, the normally consolidated lines are supposed to be parallel to each other at different temperatures. However, the temperature does not over consolidate the soil. These two concepts are schematically shown in Figure 3.21.

3- The increase of the temperature could increase the slope of the critical state line, M, in the $p - q$ space while does not influence other parameters of the soil such as λ, κ, etc.

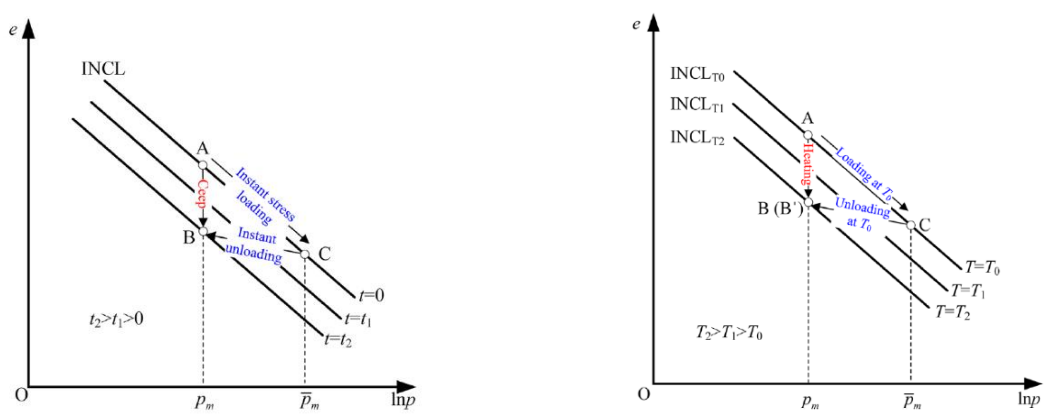

Figure 3.21: Parallel line concepts for time and temperature (Kong et al., 2020).

The model has two yield surfaces (similar to other unified hardening models); a current yield surface that indicates the overconsolidation state of the soil and a reference yield surface indicating the soil state at the corresponding normally consolidation. Similar to the *MCC*, elliptical surfaces in the $p - q$ space are adopted for these two surfaces (Figure 3.22).

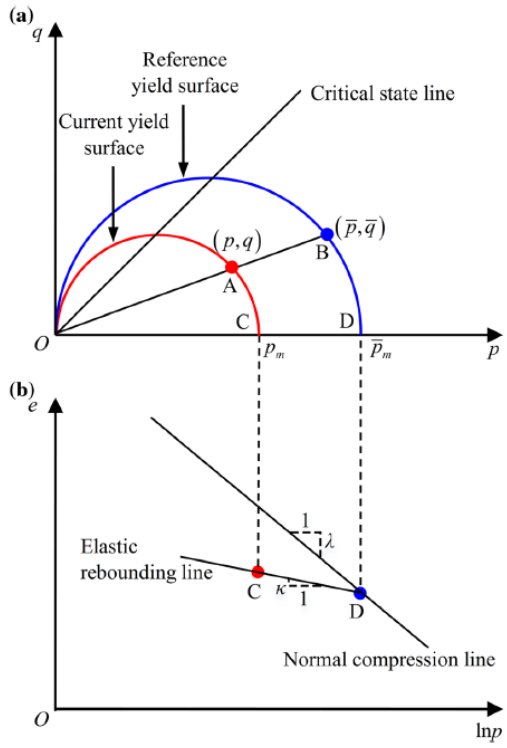

Figure 3.22: The schematic illustration of the current and reference yield surface used in the *UH TVP* model (Kong et al., 2020).

The current and the reference yield surfaces are expressed as:

$$p + \frac{q^2}{p \cdot M_T^2} - p_m = 0 \tag{3.108}$$

$$\bar{p} + \frac{\bar{q}^2}{\bar{p} \cdot M_T^2} - \bar{p}_m = 0 \tag{3.109}$$

where p_m and $\bar{p}_m$ are the cap pressures (their intersection with the effective stress axes) of the current and the reference surfaces, respectively, and $(p\,,q)$ and $(\bar{p}\,,\bar{q}\,)$ are the stress pairs on the current and reference surfaces, respectively. M_T is a strength parameter that adjusts the slope of the critical state according to the applied temperature, T, using the slope of the Hvorslev line, M_h, the slopes of the loading, λ_T, and reloading, κ_T, lines in the *p-ln(e)* space, and the reference temperature, T_0 (usually $20°C$).

$$M_T = (M - M_h)exp\left[\frac{\lambda_T - \kappa_T}{\lambda - \kappa}(1 + e_0)(T - T_0)\right] + M_h \tag{3.110}$$

Similar to other models developed under the unified hardening framework, the model employs different hardening rules for the current and reference surfaces.

$$p_m = p_{m0} \cdot exp\left[\frac{1 + e_0}{\lambda - \kappa}(H' - t' - T')\right] \tag{3.111}$$

$$\bar{p}_m = \bar{p}_{m0} \cdot exp\left[\frac{1 + e_0}{\lambda - \kappa}\left(\varepsilon_v^p - T'\right)\right] \tag{3.112}$$

H' is the unified hardening parameter, whereas t' and T' are time and temperature variables, respectively. Notice that only the temperature variable is included in the hardening law of the reference surface. This highlights the idea that only temperature affects the *INCL* and that this line is time-independent; therefore, creep does not influence it.

The *TVP UH* model has nine input parameters, provided in Table 3.8, among which four are shared with the *MCC*, one is related to the overconsolidation state, two are associated with the viscosity, and two are thermal parameters. The model's performance is shown in Figure 2.5, in which the effects of loading rates and temperature are compared with experiments using undrained triaxial and isotropic compression tests. The increasing effect of the loading time and temperature could be fairly captured with this model. Especially, it could be observed that the compression curves at different loading rates and temperatures are parallel. However, a sudden change in the soil structure could not be captured in this model due to the lack of a destructuration mechanism.

Table 3.8: Input parameters of the *UH TVP* (Kong et al., 2020)

Parameters	Boom clay	Champlain clay	Bangkok clay	HKMD	Kaolin	Illite
Parameter of MCC model						
λ	0.12	0.44	0.59	0.2	0.304	0.087
κ	0.02	0.0042	0.10	0.045	0.07	0.017
M	0.87	1.13	0.80	1.27	0.675	1.07
ν	0.3	0.3	–	0.2	0.3	0.3
Overconsolidated parameter						
M_h	0.6	0.2	0.2	0.5	0.35	0.75
Viscous parameter						
β	4.8×10^{-3}	0.04	–	0.008	0.01	–
t_0 (h)	24	1	–	1	1	–
Thermal parameter						
λ_T (°C^{-1})	2.4×10^{-4}	9.0×10^{-4}	5.6×10^{-4}	–	1.78×10^{-4}	3.0×10^{-4}
κ_T (°C^{-1})	-0.4×10^{-4}	-1×10^{-4}	-9.3×10^{-5}	–	-0.89×10^{-4}	-0.5×10^{-4}

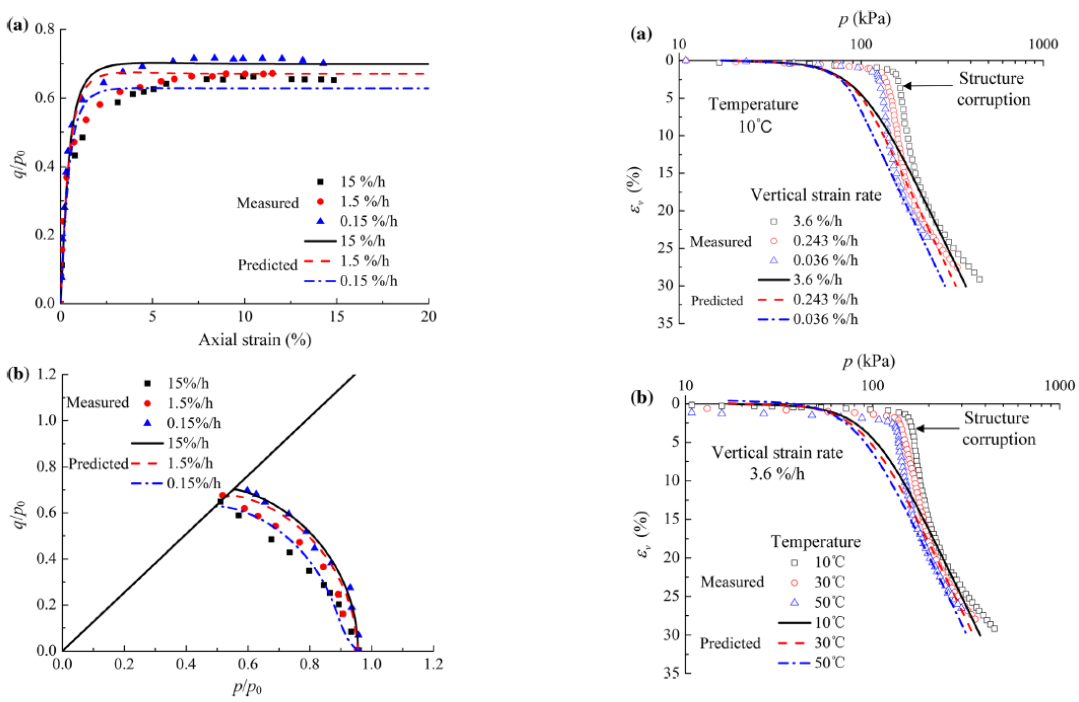

Figure 3.23: Undrained triaxial and isotropic simulations with the *UH EVP* model (Kong et al., 2020).

3.4.3 *AVISA*: an Anisotropic Visco-*ISA* Model

Tafili and Triantafyllidis (2020) introduced a constitutive model that could capture loading rates, anisotropy, and overconsolidation ratios for monotonic and cyclic loadings. The model which is called *AVISA* (an anisotropic visco-*ISA* model), is an updated version of the *ISA* model (Fuentes and Triantafyllidis, 2015) in which the intergranular strain (*IS*) concept (initially proposed by Niemunis and Herle (1997) for modulus reduction curves and small strain stiffness is reformulated.

In the *ISA* framework, a hypersphere moving yield surface with diameter $R/2$ is used in the strain space to define the locus of the elastic locus. The movement of the yield surface is governed by the tensors of the intergranular strain, $\boldsymbol{h}$, and the kinematic hardening, $\boldsymbol{c}$**.** In addition to the yield surface, A bounding surface is employed in this framework, with a diameter d time greater than that of the yield surface, limiting the movements of the yield surface. The yield and bounding surface, shown in Figure 3.24, may be expressed as:

$$F_H = \|\boldsymbol{h} - \boldsymbol{c}\| - \frac{R}{2} = 0 \tag{3.113}$$

$$F_H = \|\boldsymbol{h}\| - R = 0 \tag{3.114}$$

In the above equation, the intergranular strain tensor is evolved as the plastic condition satisfies, i.e., $F_H = 0$, according to:

$$\dot{\boldsymbol{h}} = \dot{\boldsymbol{\varepsilon}} - \dot{\lambda}_H \boldsymbol{N} \tag{3.115}$$

Where $\dot{\lambda}_H$ is the consistency parameter that may be obtained by satisfying the consistency condition.

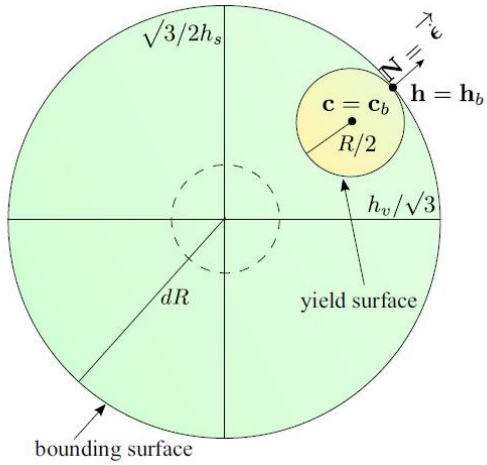

Figure 3.24: Schematic of the yield and bounding surface of the extended *ISA* (*AVISA* model) (Tafili and Triantafyllidis, 2020).

Once the yield surface is reached, the center of the yield surface evolves towards the image tenser, $\boldsymbol{c}_b$, according to a kinematic hardening rule:

$$\dot{\boldsymbol{c}} = \dot{\lambda}_H \bar{\boldsymbol{c}} \tag{3.116}$$

Where the hardening function, $\bar{\boldsymbol{c}}$, is suggested to have the following form:

$$\bar{\boldsymbol{c}} = \beta(\boldsymbol{c}_b - \boldsymbol{c})/(d \cdot R) \tag{3.117}$$

$$\boldsymbol{c}_b = R(d - 1/2)\, \dot{\boldsymbol{\varepsilon}} \tag{3.118}$$

This model's adopted *ISA* plasticity implies that the material state inside the yield surface induces a visco-plastic response, whereas reaching this surface causes visco-hypo-plastic deformations. The corresponding visco-elastic and fully mobilized visco-hypo-plastic constitution relations could be expressed as:

$$\dot{\boldsymbol{\sigma}} = m \cdot \boldsymbol{E} : (\dot{\boldsymbol{\varepsilon}} - \dot{\boldsymbol{\varepsilon}}^{vis}) \tag{3.119}$$

$$\dot{\boldsymbol{\sigma}} = m \cdot \boldsymbol{E} : (\dot{\boldsymbol{\varepsilon}} - y_h \cdot \dot{\boldsymbol{\varepsilon}}^{hp} - \dot{\boldsymbol{\varepsilon}}^{vis}) \tag{3.120}$$

Where the variables $1 \leq m \leq m_r$ and $0 \leq y_h \leq 1$, respectively, adjust the stiffness degradation and the reduction of the plastic strains upon stress reversal. In fact, these parameters ensure a smooth transition between the visco-plastic response and the fully mobilized visco-hypo-plastic response. In addition, $m_r > 1$ is a material constant that adjusts the strain stiffness at small amplitudes. The following interpreting functions, proposed by Fuentes and Triantafyllidis (2015), are adopted for m_r and y_h.

$$m = m_R + (1 - m_R) y_h \tag{3.121}$$

$$y_h = \rho^{\chi} \langle \boldsymbol{N} : \dot{\varepsilon} \rangle \tag{3.122}$$

The term ρ^{χ} in the formulation of y_h adjusted the model for cyclic loading applications in a way that the exponent χ increases from χ_0 when there are no cycles of loading to its max value, χ_{max}, (χ_0 and χ_{max} are model constants) after several loading cycles.

The increments of the hypoplastic and viscous strains in the above formulations are expressed as:

$$\dot{\boldsymbol{\varepsilon}}^{hp} = Y \cdot \boldsymbol{m} \cdot \|\dot{\boldsymbol{\varepsilon}}\| \tag{3.123}$$

$$\dot{\boldsymbol{\varepsilon}}^{vis} = I_v \cdot \lambda \cdot \boldsymbol{m} \cdot \left(\frac{1}{OCR}\right)^{1/I_v} \tag{3.124}$$

Where I_v, λ, and Y are the viscosity parameter, the slope of the critical state in the *p-ln(e)* space, and the degree of nonlinearity. In addition, it can be inferred from the above equations that the same direction, $\boldsymbol{m}$, is adopted for both plastic strains.

The model has sixteen input parameters listed in Table 3.9, along with their approximate range and their calibrated values against two types of clays. The model's performance is evaluated by simulating undrained triaxial tests at six different displacement rates of 0.01 to 0.5 mm/min under the deviatoric stress amplitude of 50 kPa and the initial mean effective stress of 200 kPa. The results of these simulations are shown in Figure 3.25 and Figure 3.26 in terms of the stress path and hysteresis loops versus the number of cycles. These tests show that the model's response in capturing the combined effects of cyclic loading and loading rates is promising in terms of the stress path and the pore water generation. Thus, the model is able to consider the effect of frequency

on cyclic loading. However, the model's response in terms of capturing the hysteresis loops is not satisfactory.

Table 3.9: Summary of *AVISA* input parameters (Tafili and Triantafyllidis, 2020)

Description		Approx. range	Kaolin	Lower Rhine clay
Transversal (hypo)elasticity				
λ	Compression index	$10^{-6} - 1$	0.13	0.26
κ	Swelling index	$10^{-7} - 0.6$	0.05	0.04
ν_h	Poisson ratio	$0 - 0.5$	0.3	0.2
α	Anisotropic coefficient	$0 - 5$	1.8	0.7
Intergranular strain (IS)				
m_R	Stiffness factor	$1 - 7$	3	5
R	IS yield surface radius	$10^{-6} - 10^{-2}$	2×10^{-4}	2×10^{-4}
d	IS bounding surface radius	$1 - 10$	3	4
β_0	IS hardening parameter	$0 - 2$	0.076	0.076
χ_0	Min IS exponent	$1 - 10$	7	7
$\chi_{\max}$	Max IS exponent	$20 - 50$	40	35
C_a	Accumulation rate factor	$0 - 0.2$	0.001	0.005
Critical and loading surface				
M_c	CS slope	$0.5 - 2$	1.0	0.95
e_{i0}	max void ratio at $p_{ref} = 1$ kPa	$0.5 - 5$	1.76	2.47
f_{b0}	Loading surface factor	$1 - 3$	1.5	1.45
Viscosity				
I_v	Viscosity index	$0 - 2$	0.015	0.025

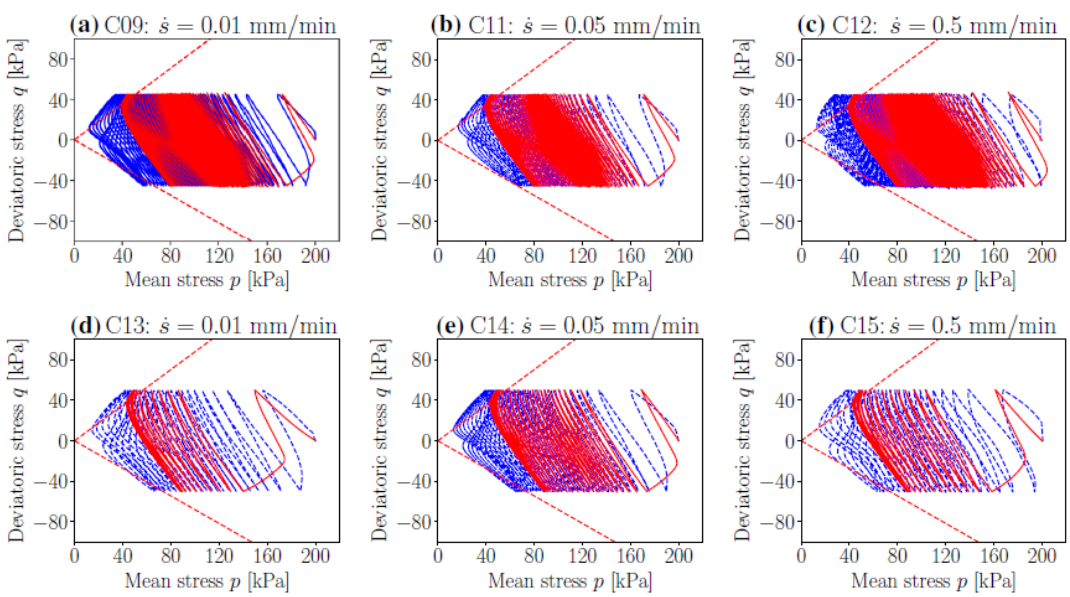

Figure 3.25: *AVISA* predictive ability (in red) at different loading rates against experiments (in blue) (Tafili and Triantafyllidis, 2020).

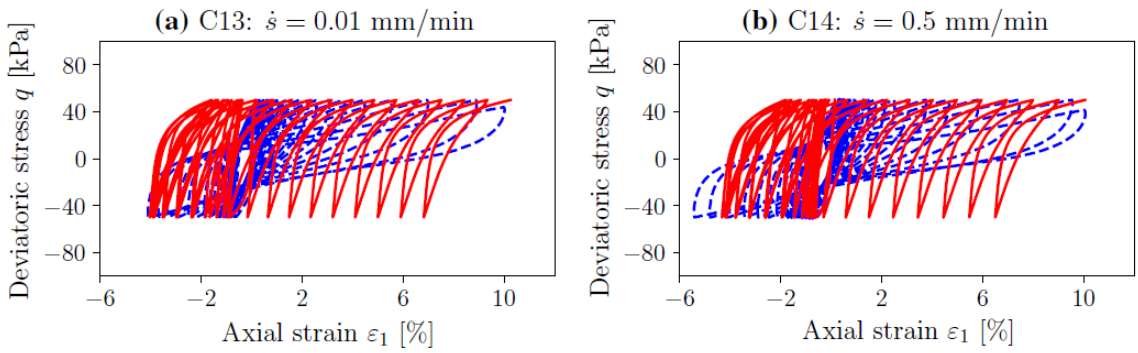

Figure 3.26: *AVISA* predictive ability (in red) against experiments (in blue) in simulating the hysteresis loops at two different loading rates (Tafili and Triantafyllidis, 2020).

CHAPTER 4 CALIBRATION IN CONSTITUTIVE MODELING

The information presented in this chapter is included in several publications:

Zarrabi, M., Eslami, M.M., and Yniesta, S. "Cyclic Application of an Advanced Calibration Algorithm to Three Cyclic Bounding Surface Soil Constitutive Models." (under review at ASCE's International Journal of Geomechanics).

Zarrabi, M., Eslami, M.M., and Yniesta, S. "Experimental and Numerical Investigations of Low Plasticity Soil Mixtures under Cyclic Loading using Three Constitutive Models." (to be submitted to the Canadian Geotechnical Journal).

Eslami, M., Zarrabi, M., and Yniesta, S. (2019). “Evaluation of Two Constitutive Models in Predicting Cyclic Behavior of a Natural Clay.” In Eighth International Conference on Case Histories in Geotechnical Engineering, Associazione Geotecnica Italiana, Rome, Italy, pp. 2275-2282.

Eslami, M., Zarrabi, M., and Yniesta, S. (2019). “Performance of Bounding Surface Constitutive Models in Predicting Cyclic Behavior of Low-Plasticity Fine-Grained Soils.” In Geo-Congress: Geotechnical Materials, Modeling, and Testing, Reston, American Society of Civil Engineers, pp. 57-66.

4.1 Introduction

MCC may be considered as one of the earlier well-known models that only requires five easy-to-calibrate physically meaningful parameters to work. However, modern constitutive models are complex, requiring multiple input parameters, and users need to be familiar with the mathematical laws that control the model, which renders the calibration task tedious. These shortcomings of complex models partially explain why simplified models such as the *MCC* model are still in use by practitioners, whereas many more advanced constitutive models have been developed in recent years.

Recent advanced developed constitutive models, such as *SANISAND* (Dafalias et al., 2010), and *SANICLAY* (Dafalias et al., 2006), require several parameters to work. These parameters are either physically meaningless or require numerous monotonic and/or cyclic tests to be calibrated, and

such a dataset is not often available in practice. In addition, when calibrating such models, practitioners usually rely on a time-consuming and ineffective trial and error procedure. To avoid such shortcomings, model developers are seeking alternates for trial and error calibration efforts. For instance, recently, the *PM4SAND* model (Boulanger and Ziotopoulou, 2017) was published with a pre-calibration that allows practitioners to use it easily by having to calibrate only three parameters (although it has secondary parameters that are set to default values but could be altered if desired by the users). The three parameters are easily obtained from field tests, which makes this model popular among practicing engineers. However, such a pre-calibrated model for clays does not exist, which is both reliable and easy to use.

To ease the challenges associated with finding the right model's input parameters, several studies have been focused on the development of efficient optimization algorithms to calibrate constitutive models against different types of soils and loading conditions (e.g., Mousa, 2017; Liu et al., 2016; Sadoghi Yazdi et al., 2012; Desai and Chen, 2006; Calvello, and Finno, 2004; Finno and Calvello, 2005; Yang and Elgamal, 2003).

In this chapter, two advanced optimization algorithms, namely the Gauss-Newton (*GNO*) optimization as well as the Particle Swarm Optimization (*PSO*) algorithms, are discussed, adjusted, and used to calibrate three advanced cyclic constitutive models for sands (Dafalias and Manzari, 2004) and clays [*SANICLAY* Bounding surface model (Seidalinov and Taiebat, 2014) and *SANICLAY* Bounding surface with a Hybrid flow rule (Shi, 2016)].

4.2 Gauss-Newton Optimization (*GNO*)

4.2.1 Formulation of the *GNO*

Liu et al. (2016) used an optimization algorithm to find the set of input parameters for the Dafalias and Manzari (2004) model that best fit a combination of laboratory tests and high-fidelity discrete element simulations of laboratory tests. This calibration process is formulated so that the input parameters are modified iteratively to diminish the discrepancies between model simulations and target data. The simulations and target data can be compared in terms of different soil response quantities such as axial or shear strains, stress ratio, void ratio, mean effective stress, excess pore pressure, etc. The following summarizes the relevant equations presented in Liu et al. (2016).

This optimization problem is solved using a Gauss-Newton algorithm (Conn et al., 2000), in which the set of parameters to be optimized are updated at every iteration as follows:

$$\boldsymbol{\theta}_i = \boldsymbol{\theta}_{i-1} - (\boldsymbol{J}_{i-1}^T \cdot \boldsymbol{W} \cdot \boldsymbol{J}_{i-1} + \lambda \cdot \boldsymbol{I}_\theta)^{-1} \boldsymbol{J}_{i-1}^T \cdot \boldsymbol{W} \cdot \boldsymbol{r}(\boldsymbol{\theta}_{i-1}) \tag{4.1}$$

Where i is the iteration number index, $\boldsymbol{\theta} \in R^{N\times 1}$ is a vector consisting of the constitutive model parameters to be calibrated, $\boldsymbol{r}(\boldsymbol{\theta}) \in R^{S\times 1}$ is the residual vector, $\boldsymbol{W} \in R^{S\times S}$ is the diagonal weight matrix, and $\boldsymbol{I}_\theta \in R^{N\times N}$ is an identity matrix. N and S are the total numbers of model parameters and data points, respectively. λ is the Levenberg-Marquardt (Marquardt, 1963) damping parameter, which defines the alternate between the Gauss-Newton and the gradient descent method (Aster et al., 2012). $\boldsymbol{r}(\boldsymbol{\theta})$ and $\boldsymbol{W}$ are mathematically defined as:

$$\boldsymbol{r}(\boldsymbol{\theta}) = (\boldsymbol{y}(\boldsymbol{\theta}) - \boldsymbol{y}_{exp}) \tag{4.2}$$

$$\boldsymbol{W} = \frac{\boldsymbol{w}'}{\boldsymbol{y_{exp}}^T \boldsymbol{y_{exp}}} \boldsymbol{I}_W \tag{4.3}$$

Where $\boldsymbol{w}' \in R^{S\times 1}$ is a vector containing the weight of each data point and $\boldsymbol{y_{exp}} \in R^{S\times 1}$ and $\boldsymbol{y}(\boldsymbol{\theta}) \in R^{S\times 1}$ are vectors containing the target data to be matched (a set of laboratory tests in the present case) and the predictions (calculated from a constitutive model), respectively. These two vectors can be chosen to include only one or a combination of several response quantities, such as shear strain (γ) or pore pressure (u). $\boldsymbol{I}_W \in R^{S\times S}$ is an identity matrix with different dimensions than $\boldsymbol{I}_\theta$.

$\boldsymbol{J} \in R^{S\times S}$ is the Jacobian matrix of $\boldsymbol{r}(\boldsymbol{\theta})$, composed of all first-order partial derivatives of $\boldsymbol{r}(\boldsymbol{\theta})$. Liu et al. (2016) used a central difference method to compute the components of the Jacobian matrix. According to this method, every column of the Jacobian matrix ($j = 1, 2, \dots N$) is approximated as follows (Wilmott et al., 1995):

$$J^j = \frac{\boldsymbol{r}\left(\theta_1, \dots, \theta_j + \delta\theta_j, \dots \theta_N\right) - \boldsymbol{r}\left(\theta_1, \dots, \theta_j - \delta\theta_j, \dots \theta_N\right)}{2\delta\theta_j} \tag{4.4}$$

Where $\boldsymbol{\delta}(\boldsymbol{\theta}) \in R^{N\times 1}$ is a small increment of $\boldsymbol{\theta} \in R^{N\times 1}$.

Note that the central difference method used by Liu et al. (2006) requires the residual vector to be calculated twice for each input parameter, once for $\theta_j + \delta\theta_j$ and once for $\theta_j - \delta\theta_j$. In the present study, a forward difference method is adopted since it only requires one computation of the residual vector, which reduces the computational time required to calculate the Jacobian matrix. The forward difference is expressed as follows:

$$J^j = \frac{\boldsymbol{r}\left(\theta_1, \dots, \theta_j + \delta\theta_j, \dots \theta_N\right) - \boldsymbol{r}\left(\theta_1, \dots, \theta_j, \dots \theta_N\right)}{\delta\theta_j} \tag{4.5}$$

Liu et al. (2016) focused on the calibration of the Dafalias and Manzari model against monotonic loading tests. However, they showed that for cyclic loading, their calibration algorithm is not satisfactory. The calibration process is adjusted in the present study to adapt it for cyclic applications. In this section, the main components of the Gauss-Newton algorithm are explained, and alternative options for Jacobian and weight matrices are provided to improve the algorithm performance for cyclic loading application in terms of time-efficiency and accuracy.

The increment $\boldsymbol{\delta\theta}$ used to compute the Jacobian matrix at every time step is set to be a small fraction of $\boldsymbol{\theta}$, to ensure smooth changes of the model parameters toward the optimal set through the calibration process. The parameter $\boldsymbol{\theta}$ is then updated at every iteration based on the Levenberg-Marquardt parameter, λ. Different methods have been proposed to compute λ such as Moré (1978) and Yamashita and Fukushima (2001). A variation of the simplified approach of Aster et al. (2012) is adopted in this study to update λ_i, as it proved efficient: (1) a large initial value for λ_0 is selected, (2) this value is increased by a constant factor (taken as 2 in the present study) following every unsuccessful step, and conversely decreased by that constant factor in every successful one. A successful step is defined as when the square sum of residuals of the current step becomes less than the one of the previous step (i.e $\sum(\boldsymbol{y}(\boldsymbol{\theta}_i) - \boldsymbol{y}_{exp})^2 < \sum(\boldsymbol{y}(\boldsymbol{\theta}_{i-1}) - \boldsymbol{y}_{exp})^2$. Note that selecting a large value for λ_0 improves the convergence of the algorithm because the initial guess of the parameters can be far from the final solution.

The computation, as well as inversion of the Jacobian matrix Eq.(4.6) at every iteration, are computationally expensive and control the computational speed of the algorithm. In order to decrease the calculation time, Broyden's method (Broyden, 1965) was applied in the present study.

In this method, the Jacobian matrix is only fully calculated at the first iteration and then updated at every subsequent iteration using rank-one updates. Hence the Jacobian matrix at every iteration J^j will be estimated using the Jacobian matrix J^{j-1} from the previous iteration:

$$J^j = J^{j-1} + \frac{(\boldsymbol{r}(\boldsymbol{\theta_1}) - \boldsymbol{r}(\boldsymbol{\theta}) - \boldsymbol{J} \cdot \Delta\theta_j)\Delta\theta_j^{\boldsymbol{T}}}{\sqrt{\sum|\Delta\theta_j^{\,2}|}} \tag{4.6}$$

Where $||$ denotes the L_2 norm of a vector. Using Broyden's method significantly reduces the calculation time of the calibration process because it only computes the full Jacobian matrix (Eq. (4.5) when convergence has not occurred. Otherwise, the previous Jacobian matrix is used to approximate the Jacobian matrix for the next iteration (Equation(4.6). The flowchart of the *GNO* algorithm is shown in Figure 4.1.

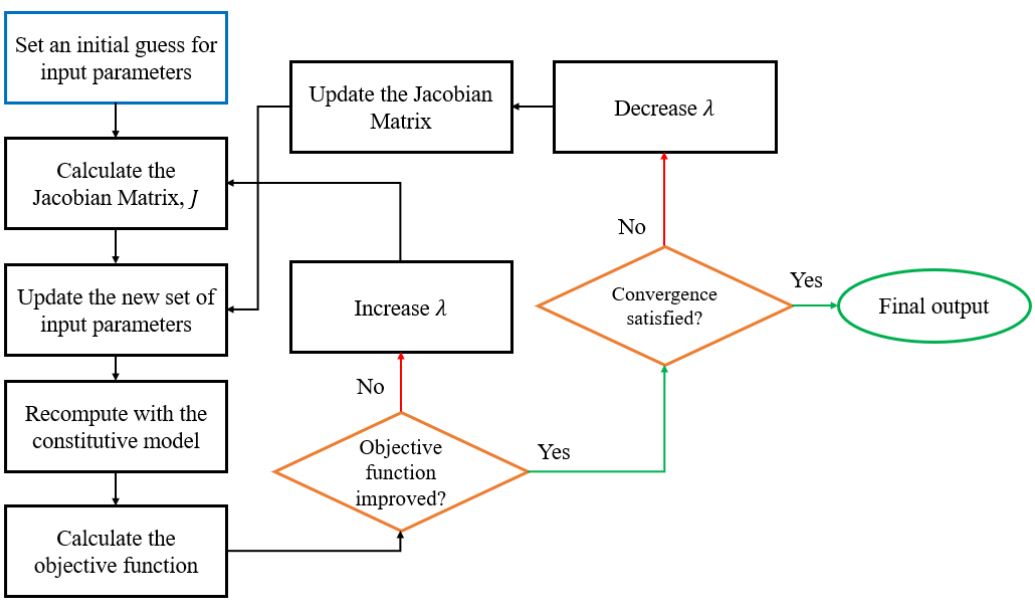

Figure 4.1: Flowchart of the *GNO* algorithm

The efficiency of the algorithm can be further improved by excluding parameters that have little influence on the performance of the constitutive model, i.e., parameters that do not substantially reduce the residual upon calibration. Each column of the Jacobian matrix corresponds to the change of the function based on one variable and computes the difference between $\boldsymbol{y}(\boldsymbol{\theta})$ and $\boldsymbol{y}(\boldsymbol{\theta}) + \boldsymbol{\delta\theta}$, in which the corresponding component of $\boldsymbol{\theta}$ is increased by a small increment while

other components are unchanged. As this difference is calculated for all the data points, the sum of the values in each column is an indication of the sensitivity of the function toward the corresponding variable, with low values indicating low influence.

Besides computational efficiency improvement, the accuracy of the calibration algorithm is increased by assigning different weights to all the data points. The weight of each observation is chosen to be proportional to the inverse of its variance ($\boldsymbol{W} = diag(\frac{1}{\sigma_1^2}, \frac{1}{\sigma_2^2}, \dots, \frac{1}{\sigma_s^2})$. This approach ensures that all the constant strain or stress amplitude cyclic tests have the same impact on the calibration while using equal weights (such as in Liu et al., 2016) would induce a bias toward high strain level cyclic tests. Assigning weights in such a manner has proven to improve the performance of the regression analysis (Calvello and Finno, 2004; Finno and Calvello, 2005).

4.2.2 Cyclic Applications of the *GNO*

In this part, the accuracy of the Gauss-Newton algorithm is illustrated through the calibration of bounding surface plasticity models formulated for cyclic loading applications, in three separate examples; 1- the *SANICLAY*-B model by Seidalinov and Taiebat (2014) for Georgia Kaolin clay, 2- the Dafalias and Mazari (2004) model for Ottawa 65 sand, and 3- the *SANICLAY*-H model for Young San Francisco Bay Mud.

4.2.2.1 Calibration of the *SANICLAY-B* based on the Simulated Data for Georgia Kaolin Clay

The *SANICLAY-B* model has 11 input parameters: κ, ν, λ, M_c, M_e, N, h_0, a_d, C, x, *and* k_i. Seidalinov and Taiebat (2014) calibrated κ, ν, λ, M_c, M_e, and N based on oedometer and undrained monotonic triaxial tests on Georgia Kaolin clay. The rest of the input parameters were calibrated by trial and error using an undrained cyclic triaxial test with a constant shear stress amplitude of q_{cy} = 140.7 *kPa*. Their simulations using the calibrated input parameters and using the *SANICLAY-B* model showed a good match with undrained cyclic triaxial tests for the Georgia Kaolin Clay.

Validation of the Gauss-Newton calibration algorithm is illustrated through a simple example, where the algorithm is used to back-calculate the input parameters of the *SANICLAY* bounding surface model (*SANICLAY-B*), developed by Seidalinov and Taiebat (2014). Seidalinov and

Taiebat (2014) calibrated their model for Georgia Kaolin clay against a large set of experimental data by trial and error. In the present study, the calibrated model by Seidalinov and Taiebat (2014) is used to generate a fictitious dataset composed of four undrained cyclic triaxial tests with cyclic deviatoric stress amplitudes of q_{cy} = 121.4, 136, 140.7, and 165.5 *kPa*. Then, the Gauss-Newton calibration algorithm is used to calibrate the model against the created data. To verify the performance of the algorithm in retrieving the exact values of the input parameters, the initial guess was selected significantly different than the exact values. In the calibration, the well-known physically meaningful input parameters, i.e., κ, ν, λ, M_c, M_e, *and* N, are left unchanged and picked directly from the work of Seidalinov and Taiebat (2014) since in practice, they should be evaluated accurately from the laboratory data. The remaining 3 input parameters h_0, a_d, and C, as well as the initial value for the initial isotropic structuration factor S_i, are calibrated to match the shear strain time series of the target data, using the Gauss-Newton algorithm. The two other input parameters, x and k_i, have a narrow range, and therefore, are set to their default and excluded from the calibration process. As a result, the vector of input parameters in the Gauss-Newton algorithm is composed of $\theta = \{h_0, a_d, C, S_i\}^{\mathrm{T}}$.

Table 4.1 compares the input parameters of the *SANICLAY-B* for initial guesses after 30, 60, and 90 iterations. The last column of this table includes the values reported by Seidalinov and Taiebat (2014). After 60 iterations, 2 of the 4 input parameters get close to their final value, while the values from Seidalinov and Taiebat are essentially retrieved after 90 iterations. No change in the values of the input parameters was found after further iterations.

Figure 4.2 shows the simulation results of the *SANICLAY-B* model at different iterations for various parameters; deviatoric stress (q), mean effective stress (p'), excess pore pressure ratio (r_u), and deviatoric strain (ε_q). The target data (i.e., the simulations with the reported input parameters) are also provided in each of these plots. The predictions are initially far from the target data in both stress-strain loops and stress path before slowly getting close to the target data after only 30 iterations and matching almost perfectly after 60 iterations. Before 90 iterations, simulation results are perfectly aligned with the target data, and therefore, are not presented.

Table 4.1: *SANICLAY-B* input parameters used in numerical simulations.

Input Parameters	Initial Guess	After 30 Iterations	After 60 Iterations	After 90 Iterations	Reported Values*
h_0	75	71.827	60.899	49.899	50
a_d	2	9.799	8.939	7.01	7
C	9	8.149	2.942	2.975	3
S_i	11	1.393	0.948	1.006	1

*Reported Values by Seidalinov and Taiebat (2014)

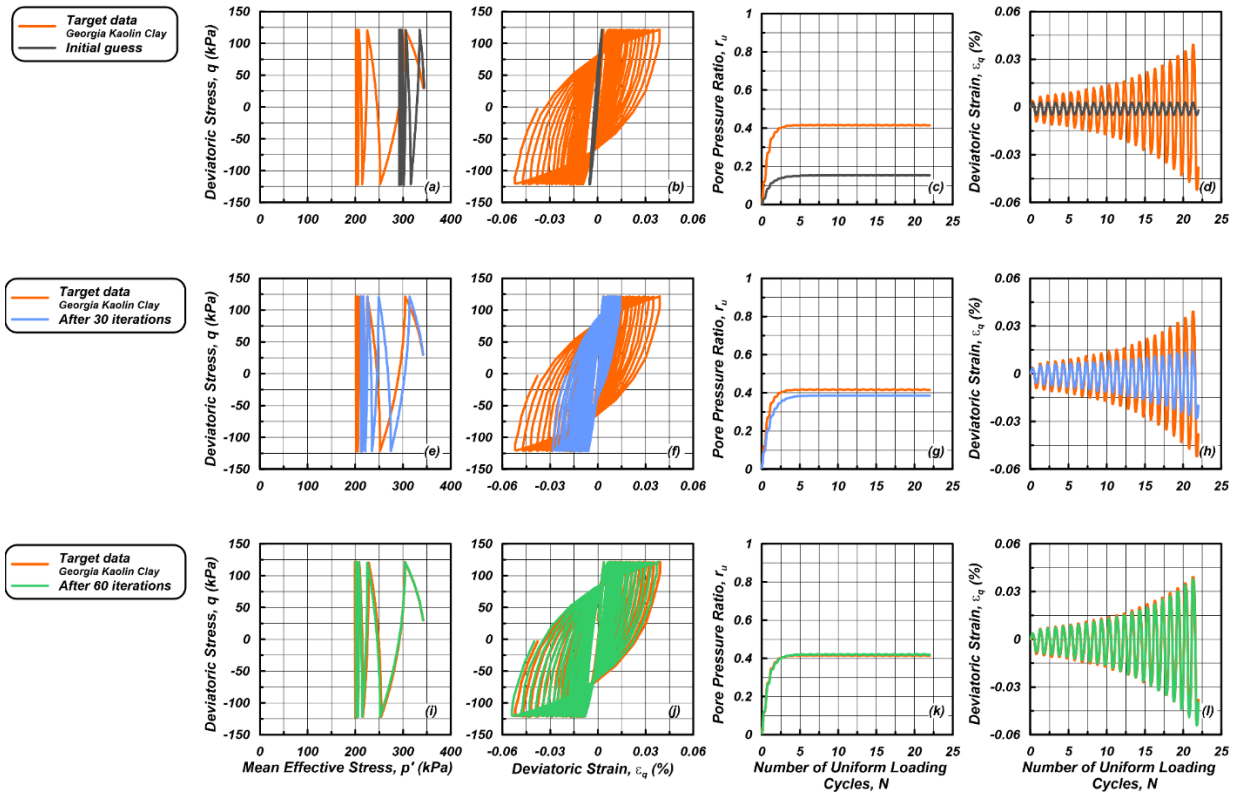

Figure 4.2: Comparison of the performance of the calibration of the *SANICLAY-B* model against Georgia Kaolin clay test data for the initial guess calibration (a, b, c, d), the calibration after 30 iterations (e, f, g, h), and after 60 iterations (i, j, k, l).

4.2.2.2 Calibration of the *DM04* for Ottawa *F65* Sand, based on Laboratory Tests

The Liquefaction Experiment and Analysis Project (*LEAP*) is an international research collaboration with the objective of evaluating the capabilities of existing numerical methods in

predicting soil liquefaction and lateral spreading of mildly sloping grounds, tested in different centrifuge facilities across the world (Kutter et al. 2014, Manzari et al. 2014, Tobita et al. 2014, Manzari et al. 2018). As part of the project, high-quality experimental data was provided to calibrate and validate the numerical models predicting liquefaction. The dataset includes a series of stress and strain-controlled monotonic and cyclic undrained triaxial tests as well as standard soil characterization tests (particle size distribution analysis, specific gravity, minimum and maximum densities, hydraulic conductivity) on Ottawa *F65* sand. In this example, the Dafalias and Manzari (2004) model is calibrated based on the cyclic triaxial tests provided by *LEAP* (Vasko et al., 2018) and compared to the calibration of the Dafalias and Manzari (2004) model performed by trial and error by Ghofrani and Arduino (2018) based on the same dataset, to assess the performance of the calibration algorithm.

In the current study, cyclic strain-controlled triaxial tests are used to calibrate the DM04 model against the deviatoric stress, q. All the tests, performed by Vesko et al. (2018), were done on specimens with an initial void ratio $e_0 = 0.604$ and initial confining stress of $p_0 = 200\ kPa$. The soil samples were tested at the following cyclic strain amplitudes ε_a = 0.058, 0.085, 0.11, 0.21, 0.32, and 0.42%. Table 4.2 includes the input parameters published by Ghofrani and Arduino (2018) as well as those calibrated using the Gauss-Newton algorithm.

Note that only input parameters without physical meaning, such as h_0, c_h, n^b, A_0, n^d, Z_{max}, *and* C_z were calibrated by the algorithm, while the parameters physically meaningful, such as G_0, ν, M, λ_c, e_0, and ξ along with the parameters c and m, were chosen from the work of Ghofrani and Arduino (2018). Figure 4.3 and Figure 4.4 compare simulation results of the two sets of calibrations of the *DM04* model (the current study, and those by Ghofrani and Arduino, 2018) and the results of laboratory cyclic triaxial tests at axial cyclic strain amplitudes of ε_a = 0.21, 0.32, and 0.42% on Ottawa sand with a relative density of about 55%. The Gauss-Newton calibration algorithm improves the simulations from various viewpoints; the cyclic degradation associated with the deviatoric behavior is better captured, along with the stress path, meaning that the volumetric response of the model is more accurate. Also, the calibrated model in this study shows an improved pore pressure response, as shown in Figure 4.3, especially in the dilative behavior of the model. The simulations provided by the calibration of Ghofrani and Arduino lack the dilative

behavior in which the stiffness increases temporarily as a consequence of an increase in mean effective stress, while the simulations provided in this study can reproduce part of the expected behavior. Further, Figure 4.4 demonstrates that both pore pressure and deviatoric stress as a function of the number of uniform loading cycles are better matched by the model calibrated by the current study's calibration algorithm. The cyclic axial strain versus the number of cycles to reach a zero mean effective stress from experimental data, as well as both studies, are plotted in Figure 4.5. As can be seen from this figure, the curve obtained using the DM04 calibration in the current study is closer to the experimental curve. The results presented in Figure 4.5 also shows that the number of cycles to reach liquefaction, i.e., $r_u = 1$, are fairly matched with experimental results, while the simulations using input parameters provided by Ghofrani and Arduino (2018) cause the model to overestimate the number of cycles required to reach $r_u = 1$.

Table 4.2 The *DM04* model parameters used in numerical simulations.

Category	Parameter	Current Study	Ghofrani and Arduino (2018)
Elasticity	G_0	82.35	82.35
	ν	0.01	0.01
Critical state	M	1.46	1.46
	c	0.47	0.47
	λ_c	0.055	0.055
	e_0	0.80	0.80
	ξ	0.50	0.50
Yield surface	m	0.02	0.02
Bounding surface	h_0*	15.18	15.114
	c_h*	0.207	0.996
	n^b*	0.438	0.64
Dilatancy	A_0*	1.299	0.45
	n^d*	0.616	0.50
Fabric tensor	z_{max}*	14.605	14.60
	c_z*	2000	2000

*Parameters included in the calibration process.

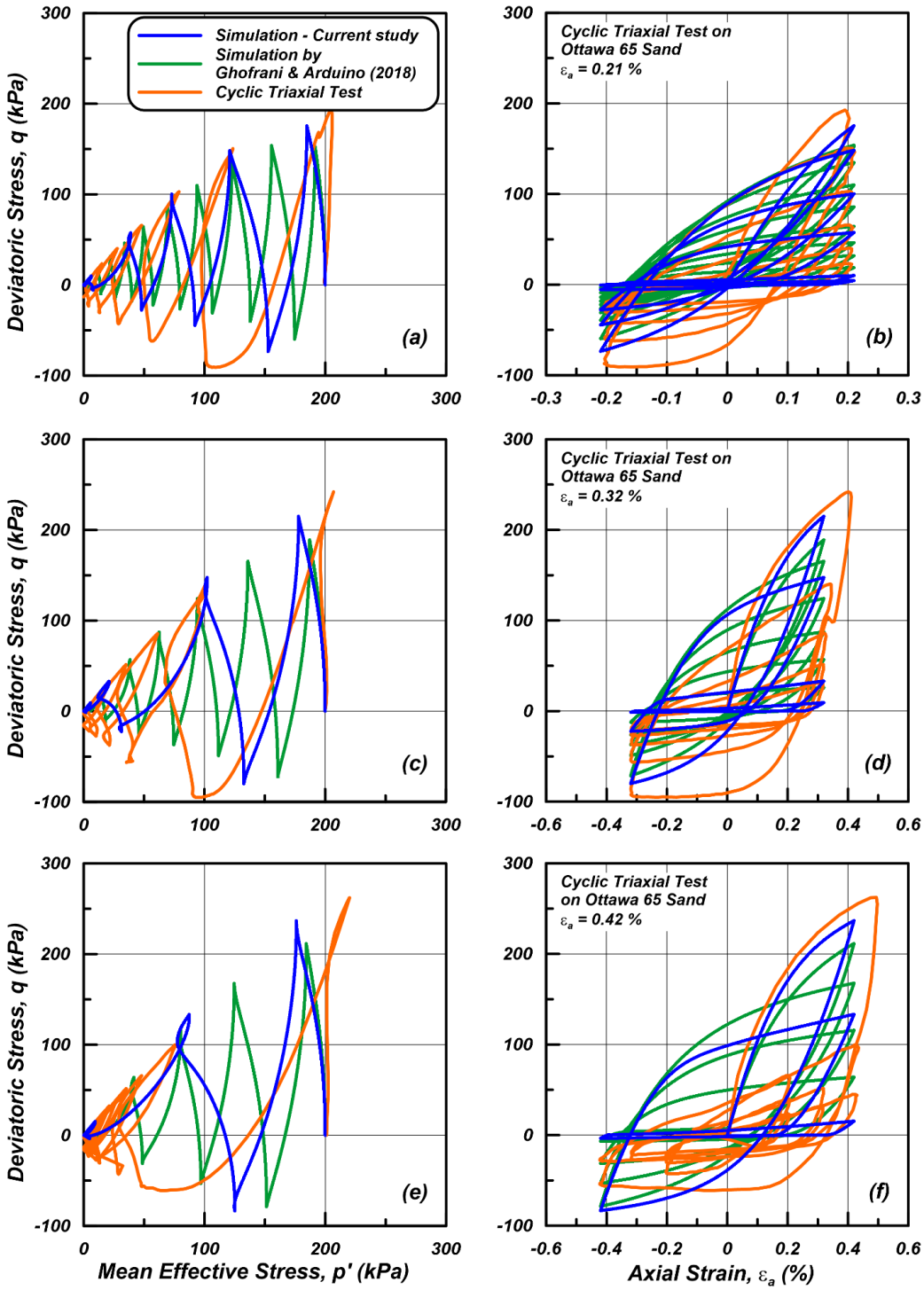

Figure 4.3: Stress-strain and stress-path responses for Ottawa *F65* sand at varying cyclic strain amplitudes: (a, b) ε_a = 0.21% (c, d) ε_a = 0.32%, and (e, f) ε_a = 0.42%.

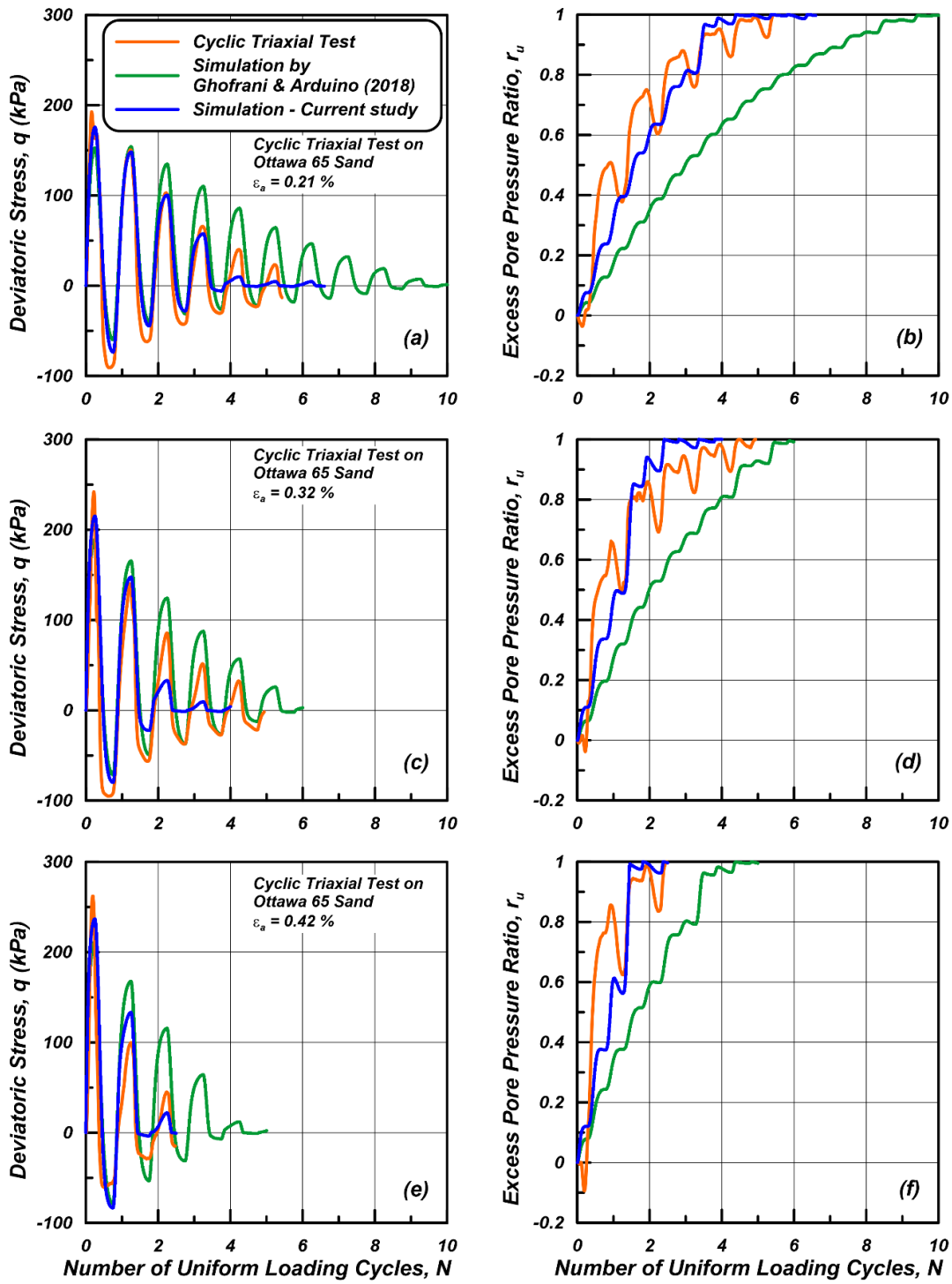

Figure 4.4: Deviatoric stress and excess pore pressure ratio versus number of uniform loading cycles for Ottawa *F65* sand at various cyclic strain amplitudes: (a, b) ε_a = 0.21% (c, d) ε_a = 0.32%, and (e, f) ε_a = 0.42%.

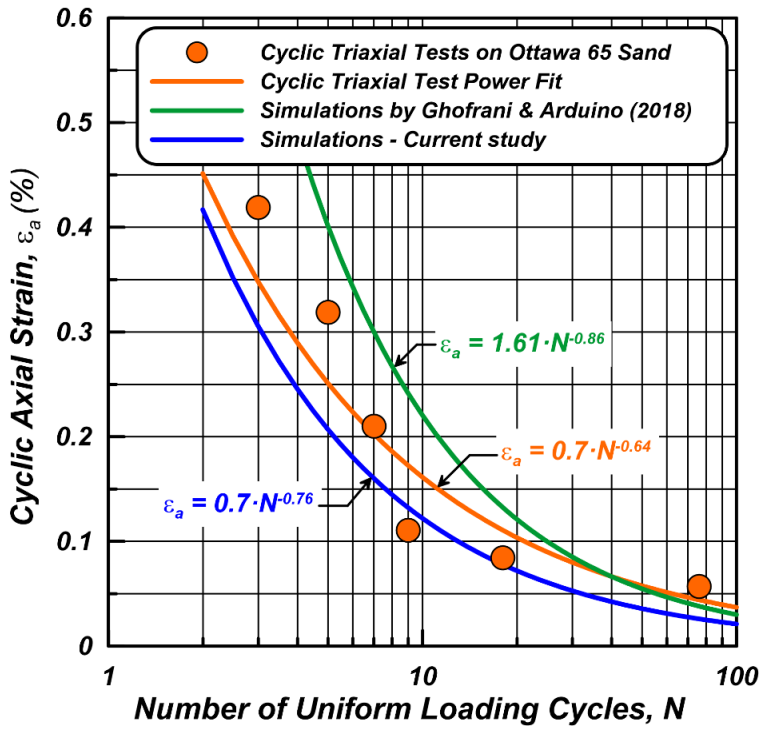

Figure 4.5: Cyclic axial strain versus the number of uniform loading cycles for Ottawa *F65* sand.

4.2.2.3 Calibration of *the SANICLAY-H* using Two Calibration Approaches

This example summarizes the efforts for calibrating the *SANICLAY* Bounding surface model with a hybrid flow rule (by Shi, 2016), referred to hereafter as *SANICLAY-H*, against experimental test results on San Francisco Young Bay Mud (*YBM*). Two various approaches are implemented to calibrate the model using the Gauss-Newton algorithm. In the first approach, the model is calibrated by trying to minimize the discrepancies in shear strains between the predictions and the data. In the second approach, the calibration is performed to minimize the distance between the cyclic strength ratio (*CSR*) versus the number of loading cycles to reach large deformations curves derived from the experiment and the model. The following sections summarize the laboratory testing results, the *SANICLAY-H* model, and present results of calibrations using the two approaches, as well as simulation results.

4.2.2.3.1 First Approach: Based on Shear Strain

The Gauss-Newton algorithm is used to calibrate the *SANICLAY-H* model against 3 cyclic direct, simple shear tests on normally consolidated San Francisco Bay Mud with *CSRs* ranging between

0.21 to 0.25. The *SANICLAY-H* model has 18 parameters, 5 of which reflect physical soil properties and are obtained from monotonic simple shear tests (i.e., $\theta = \{M_c, M_e, \lambda, \kappa, \nu\}^T$). Seven input parameters are calibrated using the Gauss-Newton algorithm: $\theta = \{h_c, h_e, N_c, N_e, c_d, C, x\}^T$, and four of the input parameters are set to their default values to capture small nonlinearities better (i.e., $\theta = \{e_g, A_g, n_g, \gamma_{0.7}\}^T$, and are not expected to control the large strain behavior that is the focus of the current study. The same reasoning is applied to the destructuration parameter, k_i, which also retains its default value of 1. Finally, the last parameter, ω, that controls the pore pressure accumulation, was set to 2, as this value proved to capture the butterfly loops of the experimental data. More information on the model parameters can be found in Seidalinov and Taiebat (2014) and Shi et al. (2018). The calibrated model parameters based on shear strains are presented in Table 4.3

Figure 4.6 shows the simulation results of the *SANICLAY-H* model for one of the cyclic direct shear tests after being calibrated using the Gauss-Newton algorithm. As can be seen, the calibrated *SANICLAY-H* model shows a fair response in terms of shear strain versus the number of cycles but is unable to capture the shape of the hysteresis loops and the volumetric response as illustrated by the stress-strain curve and the stress path. Moreover, the rate of pore pressure generation with respect to the number of loading cycles is much faster than observed in the laboratory tests, and as a result, the stress path is inaccurate.

Table 4.3 *SANICLAY-H* parameters used in numerical simulations.

Category	Parameter	Calibration No. 1**	Calibration No 2***
Elasticity	e_g	2.64	2.64
(small strain)	A_g	160	160
	n_g	0.635	0.635
	$\gamma_{0.7}$	0.00016	0.00016
Elasticity	κ	0.022	0.022
(large strain)	ν	0.24	0.24
Critical state	λ	0.271	0.271
	M_c	1.2	1.2
	M_e	0.86	0.86
Bounding	N_c	1.2	1.2
surface	N_e	0.86	0.86
	h_c*	98	104.76
	h_e*	100	100.02
	c_d*	4.72	8.08
	ω	2	2
Rotational	C*	0.06	3.47
Hardening	x*	9.6	4.45
Destructuration	k_i	1	1

**Parameters included in the calibration process.*

***Calibration based on the shear strains.*

****Calibration based on CSR versus N.*

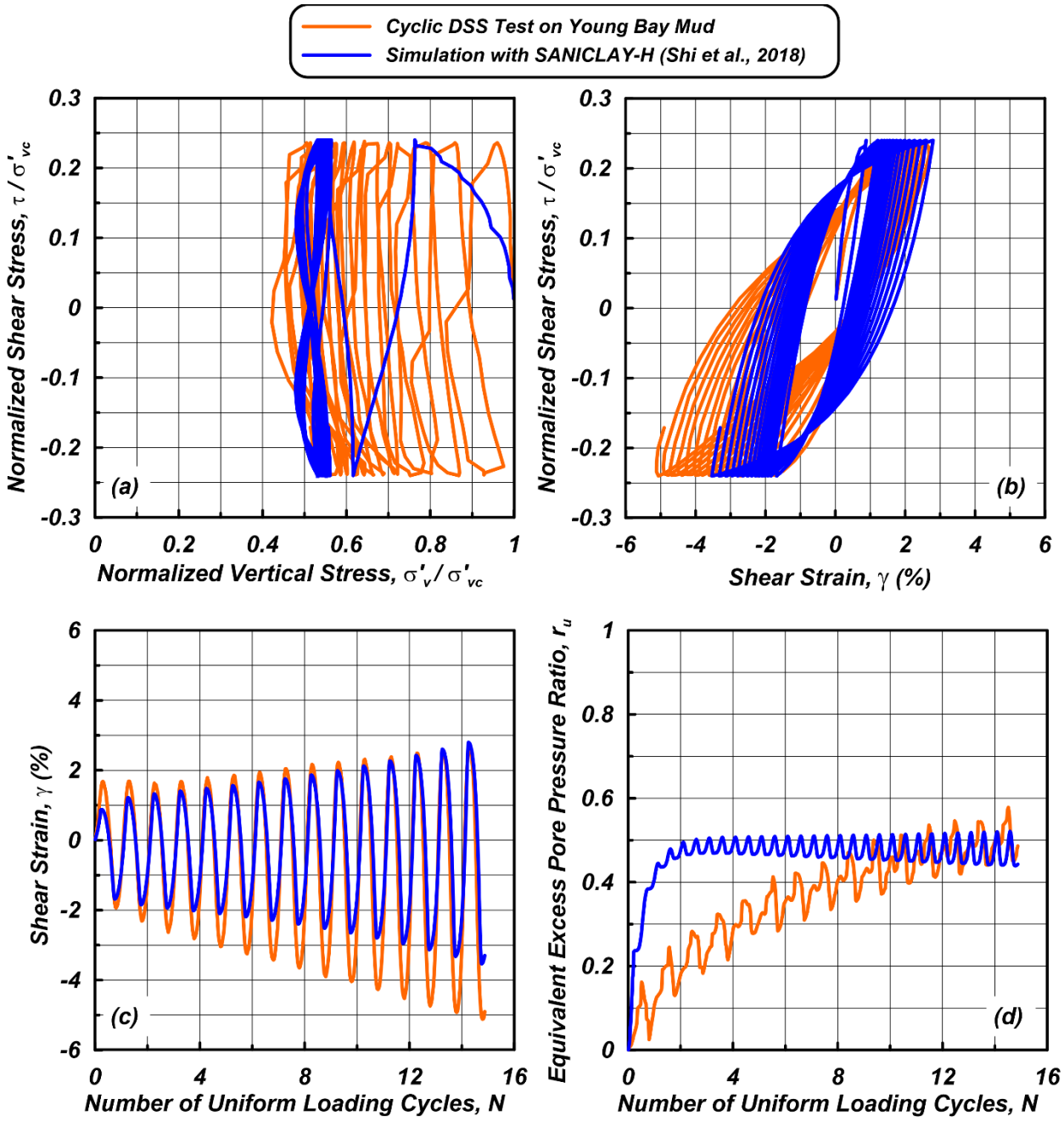

Figure 4.6: Measured and predicted response of Young Bay Mud for Cyclic *DSS* loading and *SANICLAY-B* simulation when calibrated based on shear strain.

4.2.2.3.2 Second Approach: Based on the CSR vs. N curve

In the second calibration approach, the algorithm aims to optimize the input parameters of the model to reduce the distance between the experimental *CSR* vs. *N* curve and the curve derived from simulations with the calibrated *SANICLAY-H* model. Therefore, in the alternative approach, the Gauss-Newton algorithm is used to minimize the difference between predicted and measured number of cycles to reach 3% shear strain for a given *CSR*. The target data consists of pairs of *CSR* vs. N points for *CSR* values ranging from 0.21 to 0.25, taken from the curve fitted to the laboratory test results (Figure 4.7) with the following relationship:

$$CSR = a \cdot N^{-b} \qquad 4.7$$

The last column of Table 4.3 presents the input parameters calibrated using this second approach, while Figure 4.7 presents *CSR* versus *N* curves for experimental data and both modified calibration approaches, along with regressed relationships of the form of equation 4.7. As can be seen from this figure, the modified calibration approach based on the *CSR-N* curve results in better capturing of the *CSR* versus the *N* curve compared to the calibration based on shear strain. Stress-strain curves, not presented here, showed a fair match, but without presenting an accumulation of shear strains observed in the previous calibration and the laboratory test. This can be explained by the fact that this second calibration approach does not consider the soil's response beyond 3% shear strain.

Moreover, it should be highlighted that the alternative calibration approach not only decreases the distance between the predicted and the observed *CSR* vs. *N* curves but also decreases the computational time significantly. The calibration using the *CSR-N* approach is done by using 17 data points defined from the *CSR* versus the number of cycles curve, while in the first calibration, approximately 200 data points of shear strain versus the number of cycles are used for the calibration. By reducing the number of data points, the size of the Jacobian matrix, and consequently, the time of calculation, are significantly reduced.

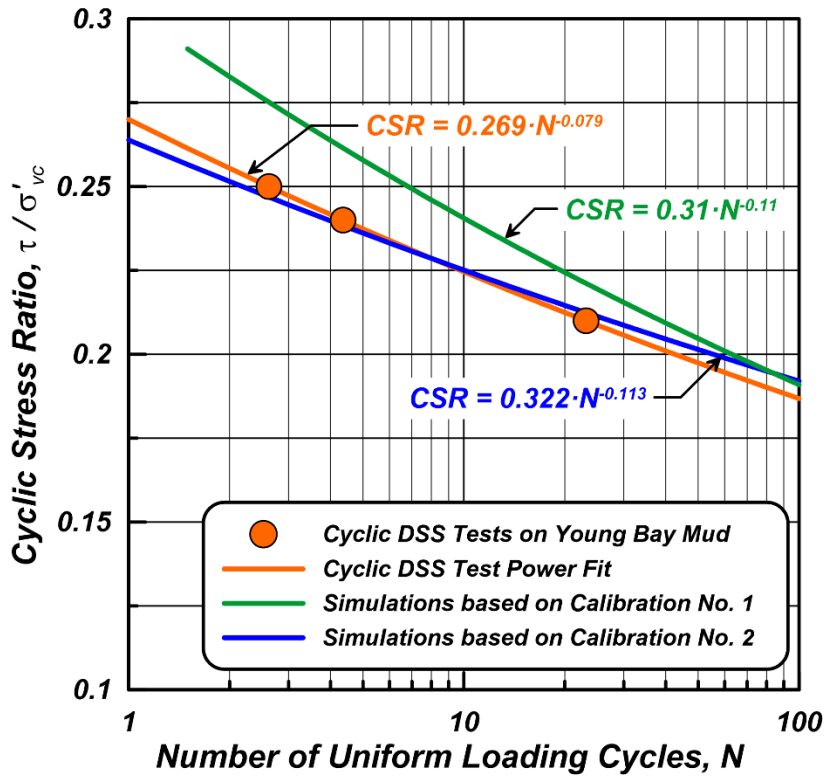

Figure 4.7: *CSR* versus the number of loading cycles for San Francisco Young Bay Mud from laboratory tests and simulations of the *SANICLAY-H* with varying modified calibration approaches.

4.3 Particle Swarm Optimization (*PSO*)

The particle swarm optimization (*PSO*) is another robust optimization technique to find a global optimum in a multi-dimensional searching space (Ramdya et al., 2017; Qi et al., 2018). The desired search space is initially defined by setting upper and lower bounds. Then, a swarm of particles is randomly generated within the desired search space. In each iteration, the best position of each particle is updated by comparing the current value of the objective function (the function that is subjected to optimization) with that of the previous one. Then, the best position of the swarm is updated to the newly best-found position of all the particles.

Swarms of particles proceed within the search space progressively toward the optimum position until either reaching the number of maximum iteration or the objective function criteria. The

algorithm of the *PSO* is shown in Figure 4.8. The position of particles is updated in each iteration according to the following formula (Bai, 2010):

$$\vec{V}_i^{t+1} = w \cdot \vec{V}_i^t + c_1 \cdot r_1(\vec{P}_i^t - \vec{X}_i^t) + c_2 \cdot r_2(\vec{G}^t - \vec{X}_i^t) \quad 4.8)$$

$$\vec{X}_i^{t+1} = \vec{X}_i^t + \vec{V}_i^{t+1} \quad 4.9)$$

where $\vec{V}_i^{t+1}$and $\vec{V}_i^t$ are the velocities of ith particle at iterations t and t + 1, respectively while $\vec{X}_i^{t+1}$ and $\vec{X}_i^t$ are the ith particle's position at iterations t and t + 1, respectively. w , c_1 and c_2 represent respectively the inertia parameter, the cognitive influence parameter, and the social influence parameter, which are selected as recommended by Vesterstrom and Thomsen (2004) and Karaboga and Akay (2009); r_1 and r_2 are random values between 0 and 1; $\vec{P}_i^t$ and $\vec{G}^t$ are the best position of the ith particle and the swarm best position, respectively. In the case of a soil constitutive model, $\vec{X}_i^t$, $\vec{P}_i^t$, and $\vec{G}^t$ are the vectors of input parameters being searched by the ith particle, the best input parameters found by the ith parameter, and the best input parameters found by the whole swarm, respectively. In each iteration, every particle's position, which is the vector of newly found/reached input parameters, is evaluated by the objective function, and the best input parameters found by each particle is stored to $\vec{P}_i^t$. Once this procedure is repeated for all the particles, the best input parameters found by the whole swarm is stored to $\vec{G}^t$,

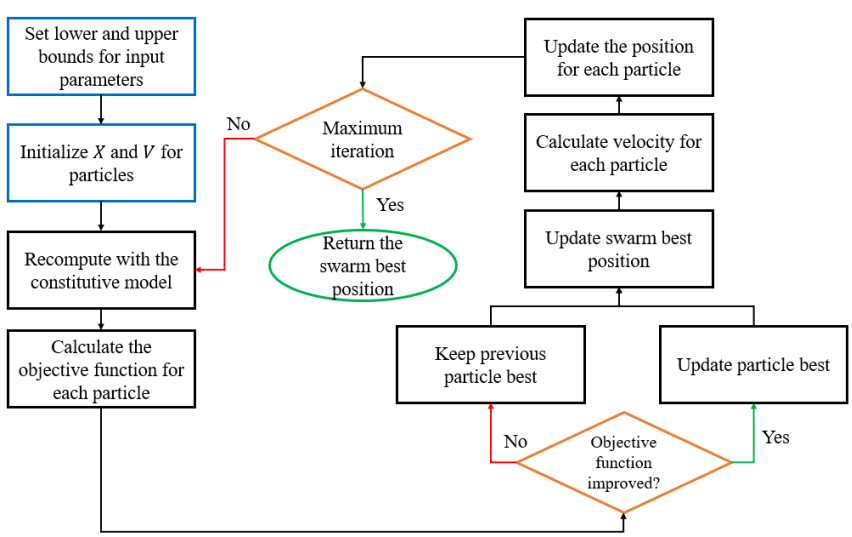

Figure 4.8 Flowchart of the *PSO* algorithm

4.3.1 Cyclic Applications of *PSO* to Calibrate Three Models Against the Low Plasticity Silt Mixtures

In this section, the monotonic and cyclic testing program of low plasticity silt mixtures performed by Eslami (2017) is first presented. Then, as there is no constitutive model for such low plasticity silts, two clay models, the *SANICLAY-B* model by Seidalinov and Taiebat (2014) and the *SANICLAY-H* model by Shi et al. (2018), as well as a sand model, the Dafalias and Manzari (2004), are used and calibrated by *PSO* to investigate the accuracy of *PSO* while evaluating how well these models could predict the cyclic loading behavior of these mixtures.

4.3.1.1 Monotonic and cyclic experiments of low plasticity silt mixtures

Commercially available non-plastic silt and bentonite clay minerals were mixed with deionized water and prepared to achieve Plasticity Index, $PI = 9$. Properties of the mixture, subsequently referred to as $SBFW$ (Silt Bentonite Fresh Water), as well as its constituent minerals, are summarized in Table 4.4. Atterberg limits were developed based on $ASTM$ 4318, and the mixture classifies as a low-plasticity clay (CL) per the Unified Soil Classification System ($USCS$).

The laboratory testing program consisted of oedometer consolidation testing and constant-height monotonic and cyclic Direct Simple Shear (*DSS*) experiments. Compression properties of the mixture are listed in Table 4.4, where C_C, C_r, and C_α are the virgin compression, recompression, and secondary compression indices, respectively.

Table 4.4: Properties of the mixture tested in the laboratory (Eslami, 2017)

ID	% silt[a]	% Bentonite[b]	G_s	LL	PL	PI	*USCS* Classification	C_C	C_r	C_α
SBFW	95	5	2.64	31.2	22.6	8.6	*CL*	0.14	0.014	0.011

[a] Sil-co-sil #45 ground silica, Non-plastic

[b] *LL* = 455.3, *PL* = 39.6, *PI* = 415.7

Mixtures were first made as a slurry at water contents higher than their liquid limit, then transferred to acrylic tubes with a diameter of 72.4 mm, slightly larger than the simple shear specimens. The slurries were consolidated inside the acrylic tubes to vertical consolidation stress of about 35 kPa and were subsequently extruded from the acrylic tubes and trimmed to a diameter of 66 mm and

height of 28 mm for cyclic or monotonic shearing. The specimens were then placed inside a wire-reinforced latex membrane and mounted in the simple shear device. They were then further consolidated to the desired vertical pressure and overconsolidation ratio before being sheared.

The *UCLA* Bi-directional Broadband Simple Shear (*BB-SS*) apparatus (Shafiee et al., 2017) was used for constant-height direct simple shear testing. The device is configured for both stress-controlled and strain-controlled constant height loading over a wide frequency range. Further details on the testing procedures can be found in Eslami (2017).

Constant-height undrained direct simple shear tests were performed on the *SBFW* mixture on normally consolidated (*OCR* = 1) specimens at an initial vertical effective stress of 50 *kPa*. Uniform sinusoidal cyclic stress loading with a frequency of 0.*1Hz* was applied to the specimens. The mixture produces relatively wide hysteresis loops that are typical of clay-like soil behavior (Figure 4.9). Also typical of such behavior is that the stress paths do not reach the origin, representing $r_u = 1.0$, or zero vertical effective stress at large applied strains. However, the material response indicates reaching high excess pore pressure ratios of about 0.85 at large shear strains, as well as developing large shear strains upon a low number of loading cycles, which is similar to sand-like soil behavior.

To evaluate the performance of *PSO*, *DM04*, *SANICLAY-B*, and *SANICLAY-H* are calibrated using this optimization technique. The input parameters of the three models calibrated using *PSO* is summarized in Table 4.5. To calibrate the models, the parameters with physical meaning are calibrated using lab tests data and conventional geotechnical relations (for example, λ and κ are obtained using the slopes of the loading, c_c, and reloading, c_r, lines in an isotropic consolidation test, respectively). Then, the rest of the input parameters, for which geotechnical relations do not exist or that cannot be directly obtained from lab data are calibrated using *PSO*.

The cyclic response of the three models in terms of the hysteresis loops, effective stress path, and excess pore water pressure and shear strains versus the equivalent number of cycles is plotted against the experimental data in Figure 4.10 and Figure 4.11. In figures correspond to two undrained cyclic direct shear tests with the same initial confining pressure of 50 *kPa* and cyclic stress ratios (*CSR*) of 0.120 and 0.178, respectively (the simulation results for all tests are provided in *APPENDIX A*). These tests are called hereafter *CSR*_0.*120* and *CSR_0.178*, respectively, and

selected so that the models' predicting ability to simulate the cyclic response of test data at two different *CSR* values be illustrated.

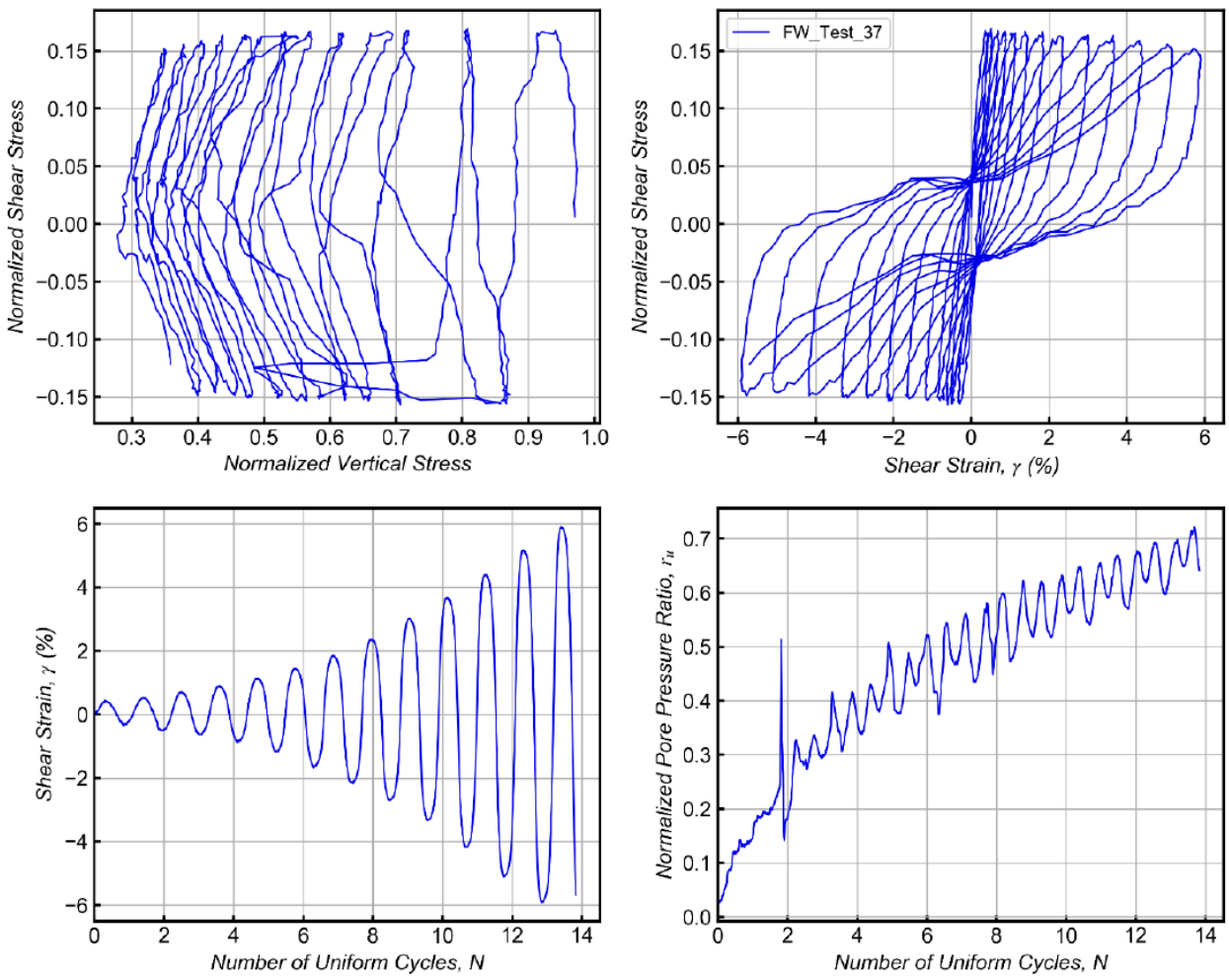

Figure 4.9 Results of a *DSS* laboratory cyclic shearing on *SBFW* (Eslami, 2017).

The comparison of the hysteresis loops of the clay models with those of laboratory tests shows that the formulation of models as well as the adoption of the bounding surface plasticity enables the models to develop plastic deformations as soon as the cyclic loading is applied. This allows the models to predict the shear strain accumulation of the test data fairly. However, despite a fair prediction of the shear strains, the shape of the hysteresis loops of the simulations are different than that of lab tests. In fact, the experimental data shows thin hysteresis loops regardless of the applied *CSR* while both clay models, as well as the sand model, tend to simulate broader hysteresis loops,

typical of clay materials, inducing a higher simulated hysteretic damping than that measured in experiments.

Comparing the stress path of the models with the experimental data, the stress path lock-up occurs in the *SANICLAY-B*. In fact, initially, the mean effective stress reduces due to the increase of the pore water pressure ratio and then remains unchanged after a few cycles. However, the stress path lock-up does not affect shear strain accumulations. This stress path lock-up and the consequent constant mean effective stress are attributed to the model's flow rule, where the plastic potential is defined according to the image stress point. This formulation causes the image stress to reach the critical state line, i.e. $\bar{\eta} = M$, far earlier than the current stress does. Consequently, the flow rule of the model, which is based on the image stress, does not accumulate further volumetric plastic strain, and as a result, the mean effective stress reduction no longer continues, recall that in an undrained test $\dot{p} = -K\dot{\varepsilon}_v^p$. Other than the pore water pressure ratio's underprediction, another limitation of the *SANICLAY-B* is the sharp increase in the pore water pressure generation, where the model reaches its final value within a few cycles.

One of the main improvements of the *SANICLAY-H* over *SANICLAY-B* is that the stress path lock-up does not occur in the stress path of the former model. This improvement is due to the use of a mixed flow rule in which the gradients of plastic potential surfaces at both the image and current stress are coupled to calculate the plastic deformations. With this modification, when the image stress reaches the critical state line, $\bar{\eta} = M$, although the gradient of the plastic potential at the image stress becomes zero, the model still produces volumetric strain as the gradient of the current stress has not reached the critical state line yet, since $\eta \neq M$. This improvement of the *SANICLAY-H* results in the mean effective stress path of the model to decrease further with the number of cycles until finally reaching the critical state line. In addition, using the hybrid flow rule enables the model to capture the butterfly loops in the effective stress path response as soon as the mean effective stress has reached the critical state line.

Another improvement of the *SANICLAY-H* is the ability of the model to predict a high pore water pressure generation in an undrained cyclic test. In this study, the model could predict up to more than 80% of the pore water pressure ratio while the stress path lock-up in *SANICLAY-B* causes the model to underpredict the pore water pressure severely; This underprediction of the pore water

pressure ratio in *SANICLAY-B* can be seen in Figure 4.10 and Figure 4.11 where the model could not predict more than 30% of this ratio. However, it should be mentioned that despite the improved performance in the effective stress path of the *SANICLAY-H*, the ability of the model to simulate a higher pore water pressure ratio is not realistic and has resulted in an overprediction of that feature compare to the experimental data. In addition, similar to *SANICLAY-B*, *SANICLAY-H* also shows an unrealistic sharp increase in generating the pore water pressure with the number of cycles.

Contrary to the clay models, *DM04* shows a realistic gradual increase in the pore water pressure ratio at both low and high *CSR*, resulting in a gradual decrease of the mean effective stress with the number of cycles. This is attributed to the dependency of the dilatancy and bounding lines to the state parameter via the critical state void ratio. In other words, the magnitude of the plastic deformations is set to be proportional to the distance of these lines to the critical state line. The gradual movements of these lines toward the *CSL* during plastic deformations ensures a gradual increase or decrease in the dilatancy parameter, d and the plastic modulus, H, and consequently, a gradual decrease in the mean effective stress. Therefore, these lines allow the model to reach the critical state line gradually as the soil state reaches the critical state, and thus, a realistic, effective stress path and pore water pressure be achieved.

Additionally, *DM04* is formulated to capture more realistically the dilative response of soils exhibiting sand-like behavior. For this purpose, as soon as the stress ratio passes the dilatancy line, the dilatancy variable, d, take negative values, as it is set to be a function of $(M^d - \eta)$. Therefore, by studying the rate of change of the mean effective stress in an undrained test, $\dot{p} = -d\left|\frac{\dot{\eta}}{H}\right| K$, obtained by setting $\dot{\varepsilon_v} = \dot{\varepsilon_v^p} + \dot{\varepsilon_v^e} = 0$, it can be understood that the negative values of d produces positive mean effective stress (dilation) in an undrained test. This dilative response predictability of the model evolves during the dilative phase of loading, i.e., when $\dot{\varepsilon_v^p} < 0$, and increases with the number of cycles. Contrary to *DM04*, both clay models lack such a dilative behavior that can be seen in experimental data. In fact, although the hybrid flow rule of the *SANICLAY-H* model induces butterfly-shaped loops that result from a dilative behavior, this feature is activated only when the model reaches the critical state line; Before reaching the critical state line, the model mostly shows contractive behavior.

In order to evaluate the performance of the *PSO* as well as the models' predictive ability to predict the number of cycles to reach a given shear strain, the *CSR-N* curves to reach shear strain values of 1% and 5% are compared for all models with those of the experimental data and shown in Figure 4.12 and Figure 4.13, respectively. According to these figures, the curve obtained for the Dafalias and Manzari model overpredict the number of cycles corresponding to the shear strain of 1% at higher *CSR* values and underpredict it for lower ones. Contrary to the sand model, the same curve obtained for clay models tend to be always underpredictive.

Table 4.5: Model parameters calibrated by *PSO*

	SANICLAY-B		SANICLAY-H		DM04	
Category	Parameter	SBFW	Parameter	SBFW	Parameter	SBFW
Elasticity	κ	6.08×10^{-3}	κ	6.08×10^{-3}	G_0	35
	ν	0.2	ν	0.2	ν	0.2
Critical state	λ	0.06	λ	0.06	M	1.22
	M_c	1.22	M_c	1.22	$c*$	1.683
	M_e	1.22	M_e	1.22	λ_c	2.593
					e_0	3.391
					ξ	0.016
Yield surface	*NA*	-	*NA*	-	m	0.01
Bounding surface	N	1.22	N_c (N_e)	1.22 (1.22)	h_0*	2.417
and plastic	h_0*	100	h_c $(h_e)*$	453.9 (37.6)	c_h*	0.096
modulus	a_d*	14	c_d*	32.244	n^{b*}	1.168
Rotational	$C*$	5.912	$C*$	0.09	*NA*	-
Hardening	$x*$	3.38	$x*$	1.088	*NA*	-
Destructuration	k_i*	0	k_i*	2.083	*NA*	-
Dilatancy	*NA*	-	*NA*	-	A_0*	0.015
					n^{d*}	7.948
Fabric-dilatancy	*NA*	-	*NA*	-	$z_{max}*$	2.572
tensor					c_z*	1100
Hybrid flow rule	*NA*	-	$\omega*$	5.396	*NA*	-

*Parameters included in the calibration process.

The *CSR-N* plotted for models and experiments at the shear strain of 5% shows that all models have a closer fit with experimental results indicating that the models' behavior is closer to that of the soil at higher shear strains. Among all models, the sand model and *SANICLAY-B* show the closer and the worst fit with experiments, respectively, while the performance of the *SANICLAY-H* may be considered to be intermediate of the other two models.

The closer fit, observed in all models, of the *CSR-N* curves corresponding to shear strain of 5%, compared at that of 3%, may be justifiable by the fact that higher shear strains could have more impact on the model's calibrations as all the models are calibrated based on the shear strain. As a result, the models might not be able to capture the cyclic behavior of soils at both low and high shear strains correctly. Therefore, the user must be aware that a calibration error bias might occur while using such kind of optimization algorithms for automatic calibrations.

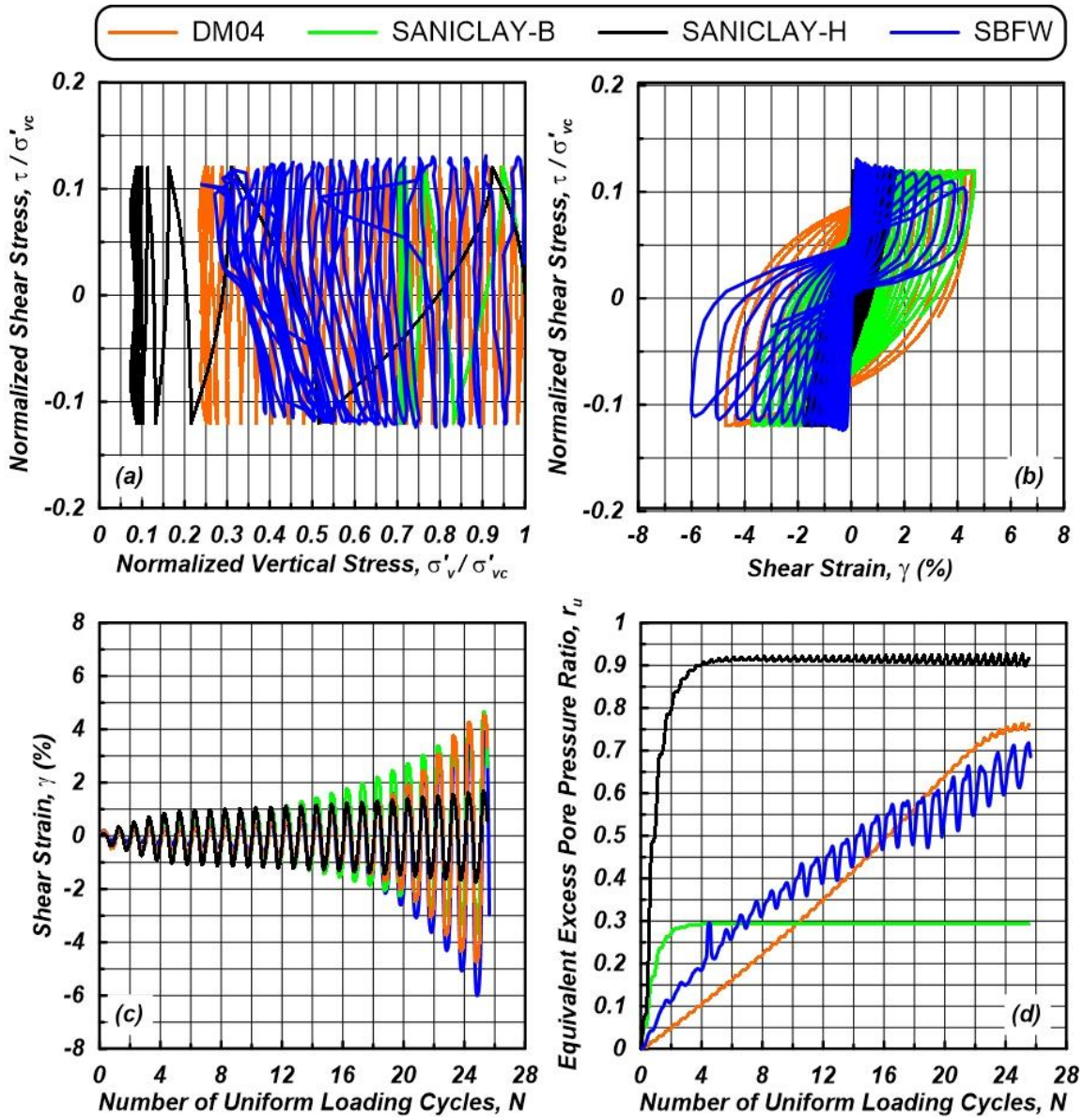

Figure 4.10 Comparison between models' simulations calibrated using *PSO* and results of *DSS* laboratory cyclic shearing (*CSR_0.120*).

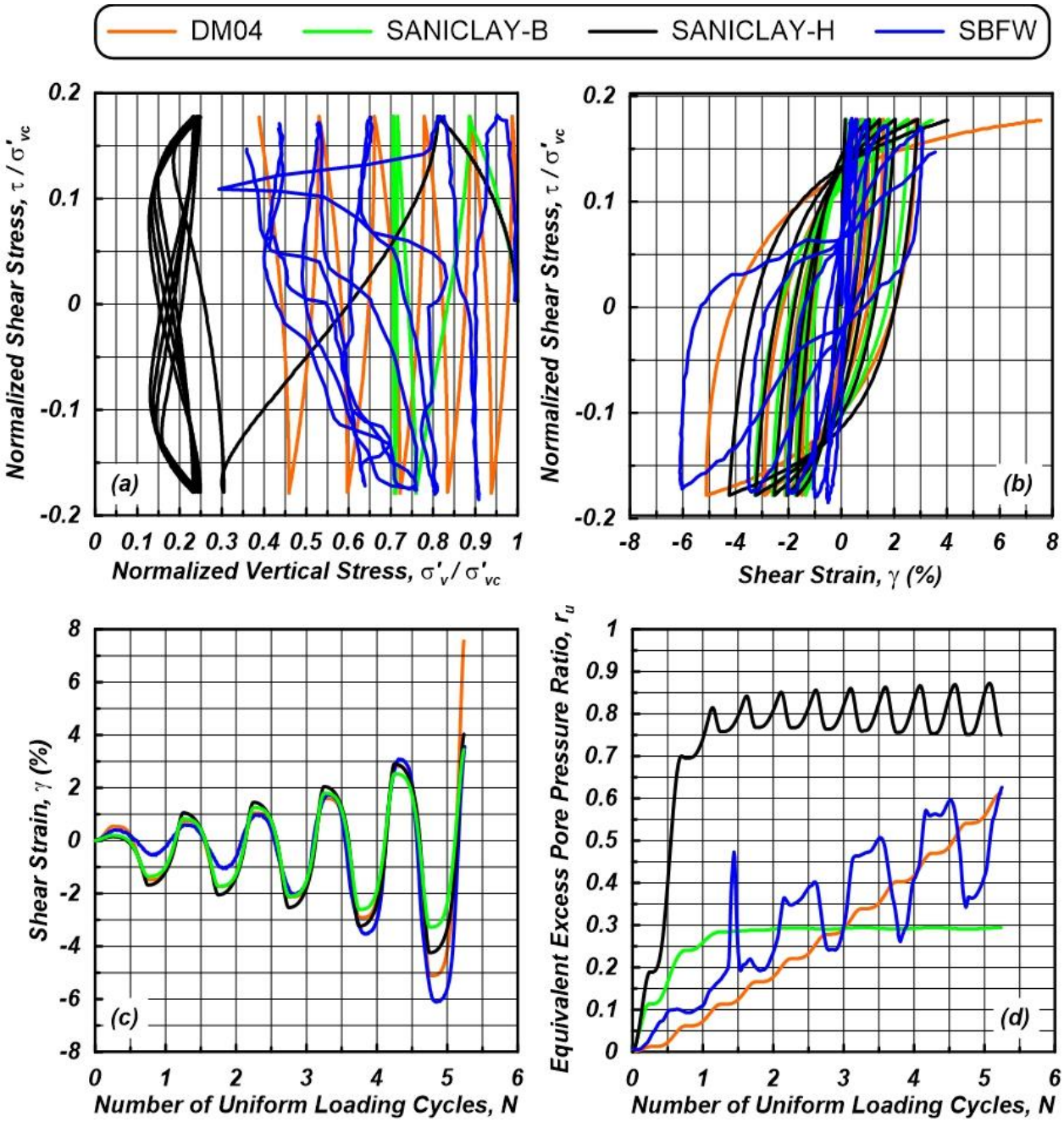

Figure 4.11 Comparison between models' simulations calibrated using *PSO* and results of *DSS* laboratory cyclic shearing (*CSR_0.178*).

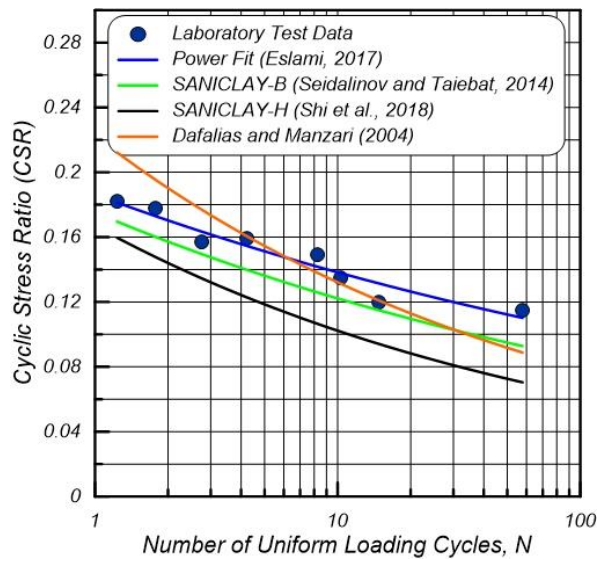

Figure 4.12 Comparison of *CSR vs. N* curves (*N*@γ=1%) from experimental results and model simulations calibrated using *PSO*

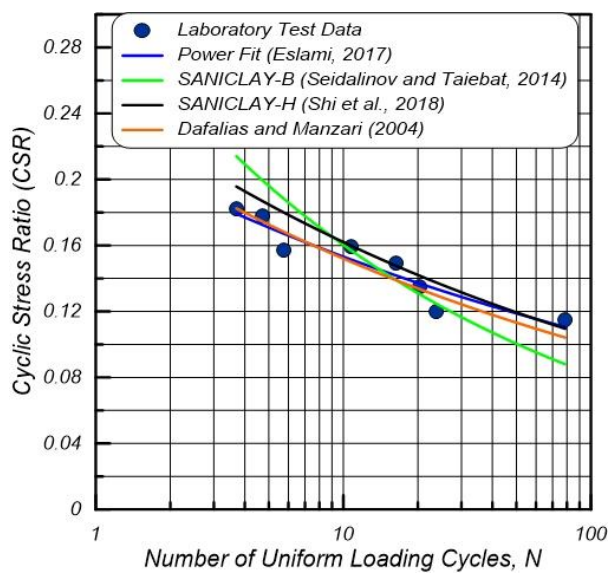

Figure 4.13 Comparison of *CSR vs. N* curves (*N*@γ=5%) from experimental results and model simulations calibrated using *PSO*

4.4 Comparing *PSO* and *GNO*

In this section, the performance of *PSO* and *GNO* are compared by applying both algorithms to a sand model, DM04, and a clay model, *SANICLAY-B*. For a fair comparison, the same model input

parameters are used in both calibrations using *GNO* and *PSO*. The input parameters of *DM04* and *SANICLAY-B* calibrated using *PSO* are summarized in Table 4.5, while those calibrated using GNO are provided in Table 4.6.

Table 4.6: Model parameters calibrated by *GNO*

	SANICLAY-B		DM04	
Category	Parameter	SBFW Mixture	Parameter	SBFW Mixture
Elasticity	κ	6.08×10^{-3}	G_0	35
	ν	0.2	ν	0.2
Critical state	λ	0.06	M	1.22
	M_c	1.22	$c*$	0.237
	M_e	1.22	λ_c	2.593
			e_0	3.391
			ξ	0.016
Yield surface			m	0.01
Bounding surface and plastic modulus	N	1.22	h_0*	6.56
	h_0*	104	c_h*	1.069
	a_d*	21	n^b*	2.81
Rotational Hardening	$C*$	1.8	*NA*	
	$x*$	0.9		
Destructuration	k_i*	0	*NA*	
Dilatancy	*NA*		A_0*	0.035
			n^d*	2.994
Fabric-dilatancy tensor	*NA*		$z_{max}*$	0
			c_z*	600

*Parameters included in the calibration process.

In Figure 4.14, the cyclic response of *DM04* calibrated with both optimization techniques is compared with that of the experimental data for a test with the cyclic stress ratio of 0.157 (*CSR_0.157*) in terms of stress-strain curves, strain vs. time, the effective stress path, and the ratio of pore water pressure built-up (other simulations with both *DM04* and *SANILCAY-B* at different *CSRs* are provided in *APPENDIX A*). As can be seen in this figure, the calibration using *PSO* has resulted in better capturing the cyclic response of the soil compared to the *GNO* calibration. In fact, calibration using *GNO* has caused the model to predict less shear strain accumulations with the number of cycles compared to the experimental data, while the calibration using *PSO* has resulted in a very close prediction of the shear strain accumulations. Additionally, the model simulations using the calibration with the *GNO* have shown a reduction of the mean effective stress with the number of cycles far less than that observed by the lab test. It should be mentioned that the same trends were observed when the model's simulations were compared with the lab tests at other *CSR* values.

In another comparison, the *CSR-N* curves for both *DM04* and *SANICLAY-B* models, calibrated with both algorithms, are shown in Figure 4.15. According to this figure, the model simulations calibrated using *PSO* have shown a closer fit with the experimental data. The difference is more pronounced for the *SANICLAY-B*. The reason for the better performance of the *PSO* over *GNO* can be explained by different search strategies each algorithm employs to find the optimum of the objective function. In the *GNO*, once the initial guess for input parameters are provided, the algorithm searches the vicinity of the provided input parameters to find the best set by which the objective function is optimum. In other words, the algorithm is dependent on the initial set of input parameters and could converge to the local minimum if the initial set of input parameters are far from the global minimum (Antoniou and Lu, 2007).

Contrary to *GNO*, the *PSO* search strategy is independent of the initial guess since it sets upper and lower bounds to ensure that the search space is fairly investigated. However, this optimization algorithm is dependent on the number of particles within the search space. Employing a low number of particles may not cover the search space completely and consequently could result in a poor calibration, while using a large number of particles requires more function evaluations per iteration and slows down the computation (Trelea, 2003). Trelea (2003) reported that using a medium number of particles (i.e., 30) yields the best results in performance and computation time.

However, it should be highlighted that the finding of Trelea (2003) is not a general recommendation of this study.

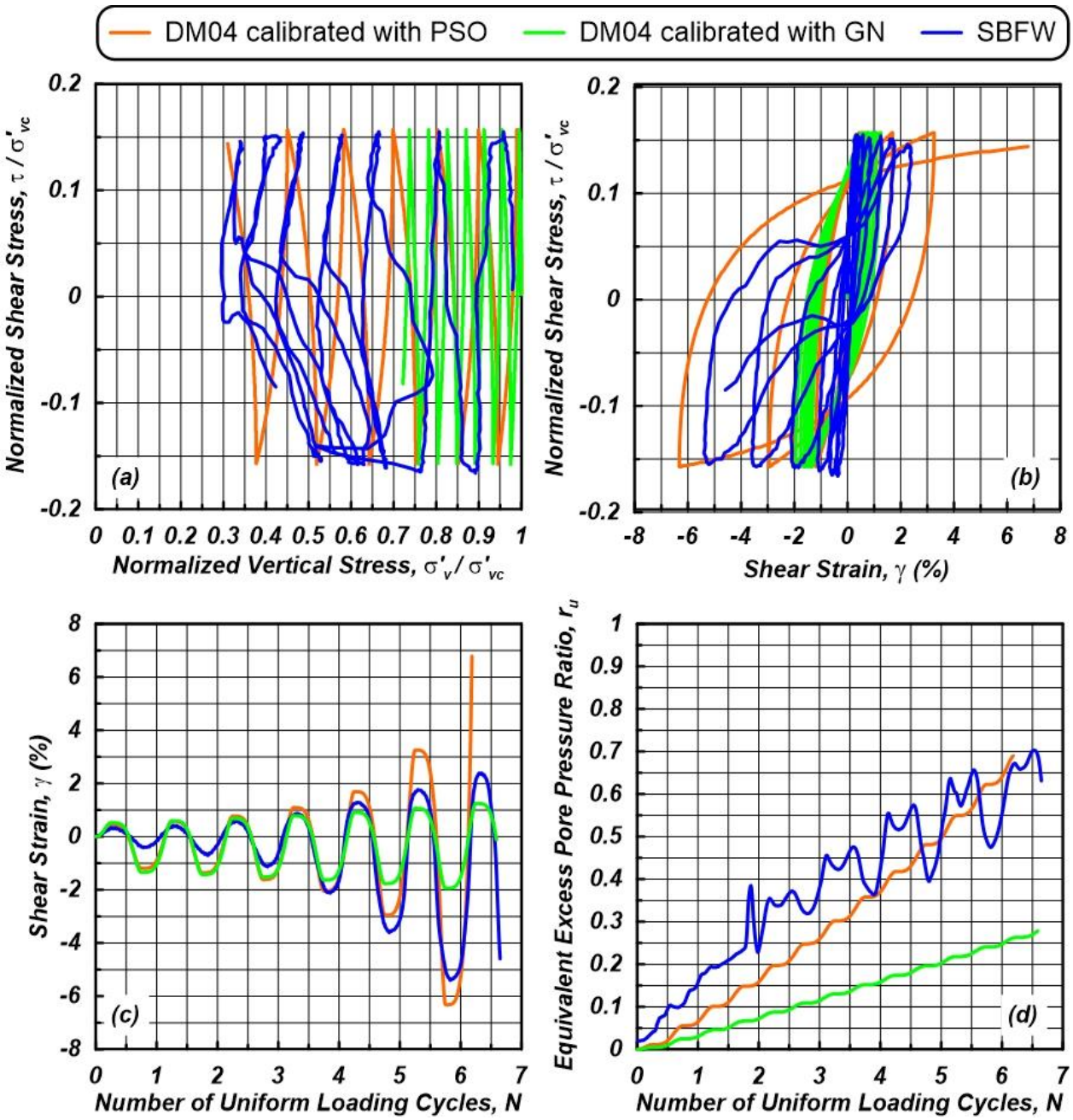

Figure 4.14 Comparison between *DM04* simulations and results of *DSS* laboratory cyclic shearing (*CSR_0.157*).

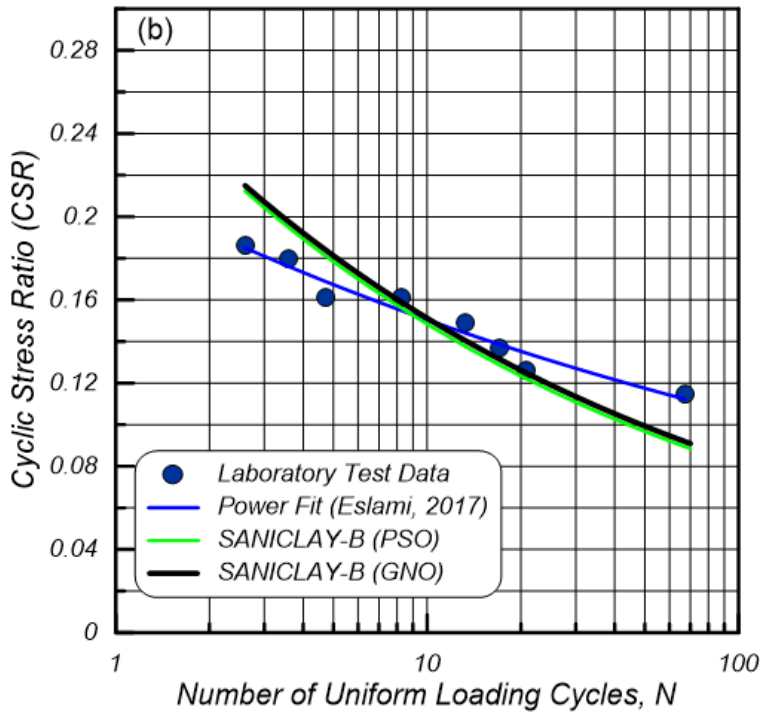

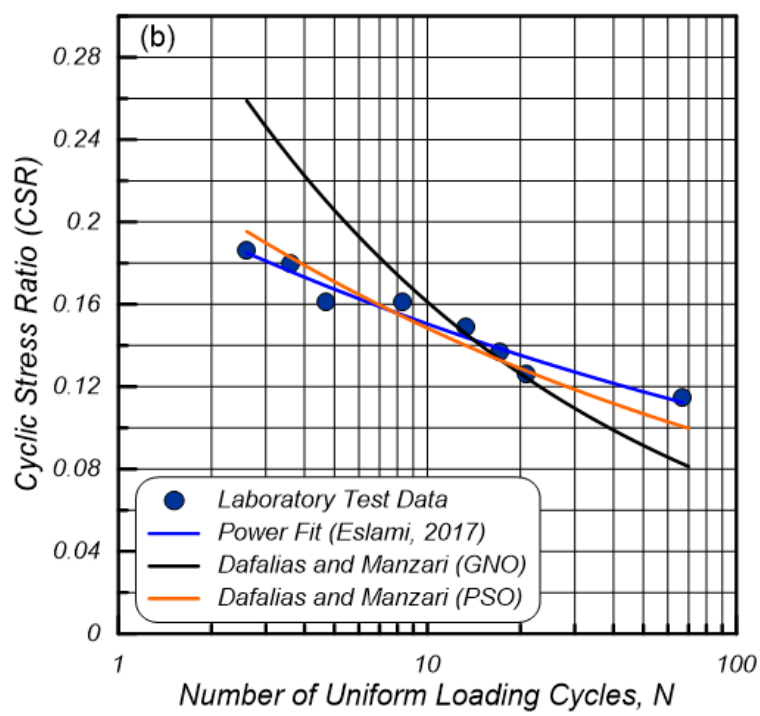

Figure 4.15 Comparison of *CSR vs. N* curves ($N@\gamma$=3%) from experimental results and model simulations (a) *SANICLAY-B* (b) *DM04*

4.5 Summary and Conclusions

In this chapter, two advanced optimization algorithms, namely the Gauss-Newton (*GNO*) optimization as well as the Particle Swarm Optimization (*PSO*) algorithms, were used to calibrate three advanced cyclic constitutive models for sands (Dafalias and Manzari, 2004) and clays [*SANICLAY* Bounding surface model (Seidalinov and Taiebat 2014) and *SANICLAY* Bounding surface with a Hybrid flow rule (Shi 2016)].

The *GNO* was adjusted to calibrate constitutive models developed for cyclic loading applications. The modifications applied to the *GNO* may be summarized as follows: 1- Applying a rank-one estimation of the Jacobian matrix using the Broyden's method (Broyden, 1965) instead of the full calculation at every iteration to reduce the computation time. 2- Employing the simplified approach of Aster et al. (2012) to find the Levenberg-Marquardt parameter, λ, to reduce the complications associated with finding this parameter. 3- Assigning weights proportional to the inverse of the variance of data points to ensure that all data have the same effect on the calibration results and reduce a bias that is induced at high strain levels. 4- Employing the forward difference method instead of the central difference method to reduce the number of calculations by half at each iteration and double the calibration speed. 5- Introducing a new approach to calibrate constitutive models developed for cyclic loading applications based on the *CSR-N* curves.

The application of the *GNO* to the *SANICLAY-B* model showed that it could retrieve the input parameters that were used to generate the target data. In addition, this algorithm was efficient in calibrating the Dafalias and Manzari (2004) model against laboratory test data provided within the *LEAP* project, and simulations using the model calibrated with the algorithm showed closer results to experimental data, compared to the model calibrated by trial and error by previous researchers. Furthermore, the application of the calibration algorithm to the *SANICLAY-H* model for San Francisco Young Bay Mud showed that calibrating in terms of the *CSR* versus the number of cycles to reach a given shear strain level is an efficient approach, compared to calibrating against shear strains, which in turn results in faster convergence of the calibration process, as well as the better agreement with the laboratory results.

Similar to *GNO*, the application of the *PSO* to calibrate three bounding surface constitutive models against the low plasticity silt mixtures showed that it could be a valuable substitute for the current trial and error calibration procedure to ease the challenges associated with calibrating advanced models. Among the two techniques, calibrations using the *PSO* yielded a closer fit for the *CSR-N* curve of the model's simulations compared with experimental data. The higher efficiency of this algorithm over the *GNO* was discussed to be attributed to its search strategy, faster convergence, and easier implementation due to its simplicity.

CHAPTER 5 FORMULATION OF A VISCOPLASTIC CONSTITUTIVE MODEL FOR CLAY CYCLIC BEHAVIOR

The information presented in this chapter is included in several publications:

Zarrabi, M., Shi, Z., Yniesta, S., and Buscarnera, G. "A Viscoplastic Bounding Surface Model for Cyclic Softening." (to be submitted to International Journal for Numerical and Analytical Methods in Geomechanics).

Zarrabi, M., Shi, Z., Yniesta, S., and Buscarnera, G. (2020). "Simulation of the Cyclic Response of Anisotropic Clay through Bounding Surface Viscoplasticity" *GeoVirtual*, Canada.

Zarrabi, M., and Yniesta, S. (2019). "Recent Advanced Constitutive Models for Liquefaction and Cyclic Softening Analysis" *Geo-St.John's*, Newfoundland, Canada.

5.1 Introduction

As was discussed in the 3rd chapter, two bounding surface plasticity models for cyclic loading applications have developed by Seidalinov and Taiebat (2014) and Shi et al. (2018) upon the framework of the *SANICLAY* family model (Dafalias et al. 2006; Taiebat et al. 2010). Although these constitutive laws are valuable tools to investigate the potential of failure of a system under cyclic loading, neither considers the effect of loading rate and/or soil viscosity in their formulation.

To include rate and time effects into bounding surface plasticity, an elasto-viscoplastic framework was proposed by Shi et al. (2019) by combining Perzyna's overstress theory with the bounding surface plasticity framework. Although the new framework has shown promising results in capturing rate effects in clay behavior under both monotonic and cyclic loading, it was applied to the modified Cam-Clay (Roscoe and Burland, 1968). Therefore, some features of clay behavior, mainly under the cyclic loading, cannot be realistically simulated using this model. For example, some limitations of the model could be highlighted as:

1- The model could not consider soil anisotropy due to the lack of a rotational hardening rule.

2- The model shows a big elastic response during cyclic loading.

3- The model could not predict realistic hysteresis loops under cyclic loading.

4- The model experiences a stress path lock-off after a few cycles of loading.

5- A realistic butterfly or 8-shaped loops in the stress path could not be captured in this model.

In this dissertation, the bounding surface elasto-viscoplasticity framework (*BS-EVP*) is used in the context of the *SANICLAY* model (Dafalias et al. 2006), thus using a rotational hardening rule, a procedure for the relocation of the projection center, and a hybrid flow rule. The model is able to capture the anisotropic properties and the cyclic loading response of clays, including pore water pressure built-up, hysteresis loops, and effective stress path at different loading rates and/or frequencies.

5.2 Model Formulation in Triaxial Space

This section describes the key components of the constitutive model with reference to the triaxial space, while the model generalization in multiaxial space will be discussed in the next section.

5.2.1 Stress-Strain Definition in Triaxial Space

This section describes the key components of the constitutive model with reference to the triaxial space. As a result, the model functions are given in terms of the mean effective stress p, deviatoric stress, q, volumetric strain, ε_v, and deviatoric strain, ε_q, defined as:

$$p = \frac{\sigma_a + 2\sigma_r}{3} \tag{5.1}$$

$$q = \sigma_a - \sigma_r \tag{5.2}$$

$$\varepsilon_v = \varepsilon_a + 2\varepsilon_r \tag{5.3}$$

$$\varepsilon_q = \frac{2}{3}(\varepsilon_a - \varepsilon_r) \tag{5.4}$$

Where σ_a and σ_r are axial and radial stresses, respectively and ε_a and ε_r are axial and radial strains, respectively.

5.2.2 Elastic Response

According to Perzyna's theory of viscoplasticity, the total strain rate is additively decomposed into an elastic part and a viscoplastic part:

$$\dot{\varepsilon} = \dot{\varepsilon}^{e} + \dot{\varepsilon}^{vp} \tag{5.5}$$

Where the superposed dot denotes a rate and superscripts e and vp stand for elastic and viscoplastic, respectively. The components of the elastic strain rate are commonly expressed based on an isotropic hypoplastic law:

$$\dot{\varepsilon}_{v}^{e} = \frac{\dot{p}}{K} \tag{5.6}$$

$$\dot{\varepsilon}_{q}^{e} = \frac{\dot{q}}{3G} \tag{5.7}$$

Where K and G are the elastic bulk and shear moduli, respectively, which are expressed as:

$$K = \frac{(1+e)p}{\kappa} \tag{5.8}$$

$$G = \frac{3(1-2v)}{2(1+v)}K \tag{5.9}$$

Where v and e are the Poisson's and void ratios, respectively, and κ is the slope of the isotropic unloading/recompression line in the *e-ln(p)* plot.

5.2.3 Bounding and Viscoplastic Potential Surfaces

To account for soil anisotropy, the *SANICLAY* model proposed by Dafalias et al. (2006) uses a distorted and rotated ellipse as a yield surface. In this study, this particular yield surface shape is used as a bounding surface, as previously done by Seidalinov and Taiebat (2014), Shi et al. (2018), etc. This bounding surface is schematically shown in Figure 5.1 and expressed as:

$$F = (\bar{q} - \bar{p} \cdot \alpha)^2 - (N^2 - \alpha^2)\bar{p}(p_0 - \bar{p}) = 0 \tag{5.10}$$

Where $(\bar{p}, \bar{q})$ is the image stress point obtained by mapping the current stress (p, q) on the bounding surface from a projection center PC (p_c, q_c) through a mapping rule, which will be detailed in the following sections. α and p_0 are rotational and isotropic hardening variables representing anisotropic states and soil consolidation, respectively, and N is a parameter controlling the distortion of the bounding surface which depends on the mode of shearing (i.e., $N = N_c$ for triaxial compression and $N = N_e$ for triaxial extension):.

$$N = \begin{cases} N_c & if \quad \bar{q} \geq \bar{p}\alpha \\ N_e & if \quad \bar{q} < \bar{p}\alpha \end{cases} \tag{5.11}$$

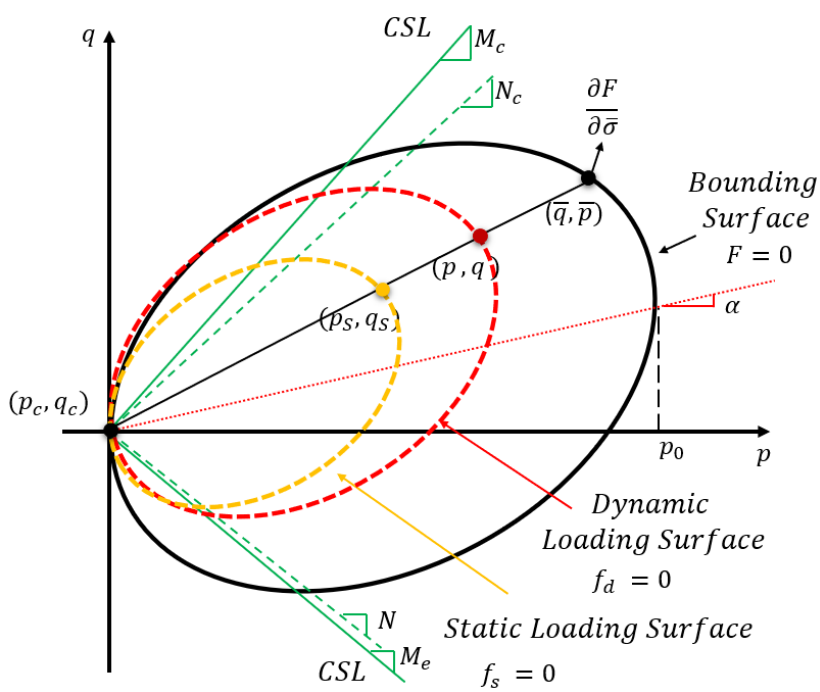

Figure 5.1 Schematic of bounding, dynamic, and static loading surfaces of the *BS-EVP* model.

In the rate-independent bounding surface plasticity, the image stress lies on the bounding surface, whereas the current stress lies on the implicitly defined loading surface. Extending Perzyna's theory of viscoplasticity (Perzyna, 1963) to a bounding surface framework requires the use of two distinct functional surfaces to compute the evolution of a modified overstress. Hereafter, such surfaces are defined as static and dynamic loading surfaces, which replace the role of the loading surface of rate-independent bounding surface models (Shi et al., 2019). As shown in Figure 5.1,

the static and dynamic loading surfaces always pass through the static (p_s, q_s) and current stress $(p\,, q\,)$, respectively. The use of the Perzyna's overstress concept implies that the state of stress can lay inside, on, or outside the static loading surface. However, the stress state inside the static loading surface can only cause elastic deformations, while states of stress outside of it cause viscoplastic strain with a magnitude dependent on the degree of violation of the static loading surface (here referred to as overstress).

The model uses a non-associated flow rule, therefore requiring the definition of a flow potential surface (shown in Figure 5.2 as the viscoplastic potential surface) different than the bounding surface to calculate the viscoplastic strain:

$$g = (\bar{q} - \bar{p} \cdot \alpha)^2 - (M^2 - \alpha^2)\bar{p}(p_\alpha - \bar{p}) = 0 \qquad (5.12)$$

Where p_α is the value of $\bar{p}$ at $\bar{q} = \alpha\bar{p}$ to adjust the viscoplastic potential for a given pair of the image stress on the bounding surface and M is the slope of the critical state line in the $p - q$ space:

$$M = \begin{cases} M_c & if \quad \bar{q} \geq \bar{p}\alpha \\ M_e & if \quad \bar{q} < \bar{p}\alpha \end{cases} \qquad (5.13)$$

Where M_c and M_e are the slope of the critical state line in triaxial compression and extension, respectively.

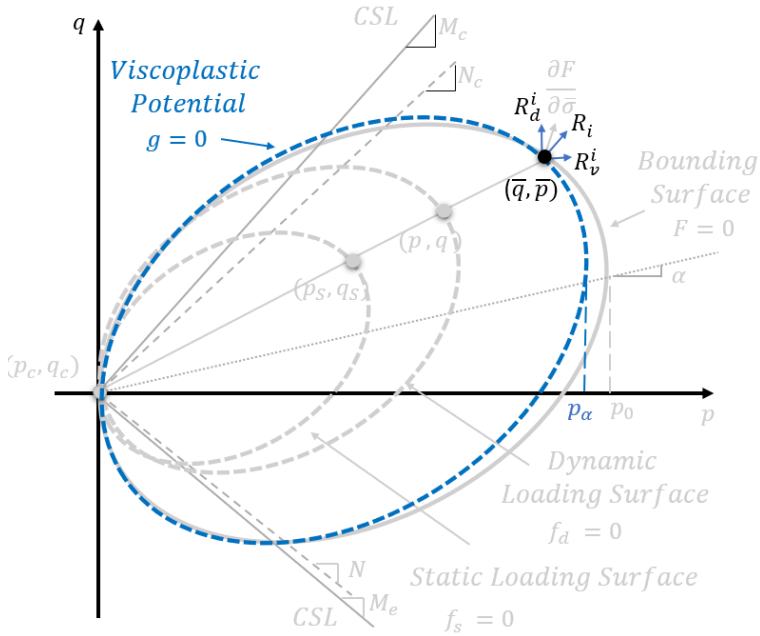

Figure 5.2 Schematic of the viscoplastic surface of the *BS-EVP* model.

5.2.4 Image Stress and Projection Center

In bounding surface plasticity, the current stress state is related to corresponding image stress on the bounding surface through a mapping rule. A usual choice is a radial mapping rule, which, similar to earlier propositions by Dafalias and Herrmann (1986), and can be expressed as:

$$\bar{p} = p_c + b_d(p - p_c) \tag{5.14}$$

$$\bar{q} = q_c + b_d(q - q_c) \tag{5.15}$$

Where $1 \leq b_d \leq \infty$ indicates the similarity ratio between the dynamic loading surface and the bounding surface, respectively, and the two extremes correspond to current stress coinciding with the image stress ($b_d = 1$) or the projection center ($b_d = \infty$). The exact value of b_d could be obtained by inserting the image stress, Eq.(5.14) and Eq.(5.15), into the bounding surface, Eq. (5.10), and solving the resulting quadratic equation for the positive root (Seidalinov, 2012; Seidalinov and Taiebat, 2014). Given the relationship between the static and current stress to the same image stress, it is possible to define a similarity ratio b_s for the static loading surface as well.

Knowledge of both b_s and b_d, allows the static stress to be expressed as a function of the current stress, as follows:

$$p_s = p_c + \frac{b_d}{b_s}(p - p_c) \tag{5.16}$$

$$q_s = q_c + \frac{b_d}{b_s}(q - q_c) \tag{5.17}$$

Contrary to the dynamic loading surface, the static loading surface moves according to its own evolution law, encapsulated in the rate of b_s. Such a viscoplastic hardening rule will be discussed in the next section.

In order to have unique image stress, the projection center should always be located inside the bounding surface. Seidalinov (2012) and Seidalinov and Taiebat (2014) suggested that updating the projection center at any stress reversal improves the predictive capability of the model for the cyclic response of clays. It can be shown that the stress reversal occurs whenever the loading index $L \leq 0$, where L can be obtained by satisfying the consistency condition, $\dot{F} = 0$:

$$L = \frac{\frac{\partial g}{\partial \bar{p}} \cdot \dot{p} + \frac{\partial g}{\partial \bar{q}} \cdot \dot{q}}{K_p} \tag{5.18}$$

Where K_p is the plastic modulus, to be defined later. If the projection center is unchanged till the next stress reversal, it might be located outside the bounding surface as the latter shrinks, expands, and/or rotates. Therefore, Seidalinov (2012) and Seidalinov and Taiebat (2014) proposed using a moving projection center to ensure that it always remains inside the bounding surface. In the current study, the evolution rule for the projection center proposed by Shi et al. (2018) is used in which the simultaneous changes of p_0 and α are considered:

$$\dot{p_c} = \frac{p_c}{p_0} \cdot \dot{p_0} \tag{5.19}$$

$$\dot{q_c} = \frac{q_c}{p_0} \cdot \dot{p_0} + \frac{N^2 \cdot p_c - \alpha \cdot q_c}{N^2 - \alpha^2} \cdot \dot{\alpha} \tag{5.20}$$

5.2.5 Viscoplastic Hybrid Flow Rule

In Perzyna's theory of Viscoplasticity, the viscoplastic strain rates are given as:

$$\dot{\varepsilon}_v^p = \mu \langle \phi(y) \rangle R_v \tag{5.21}$$

$$\dot{\varepsilon}_d^p = \mu \langle \phi(y) \rangle R_d \tag{5.22}$$

Where μ is the fluidity parameter, R_v and R_d are the volumetric and deviatoric gradients of the plastic flow potential function, g, respectively, and $\phi(y)$ is the overstress function. The latter is a normalized measure of the distance between the dynamic loading surface and the static loading surface. The use of Macauley brackets ensures that for stress states inside the elastic nucleus, y, the overstress function, $\phi(y)$, yields zero, resulting in no viscoplastic strain development:

$$\langle \phi(y) \rangle = \begin{cases} \phi(y) & if \quad y > 0 \\ 0 & if \quad y \leq 0 \end{cases} \tag{5.23}$$

Numerous overstress functions have been proposed in the literature (Kaliakin and Dafalias (1990); Martindale et al. (2013); Yin and Hicher (2008)). Here, an exponential form is adopted:

$$\phi = \mu_1 \cdot e^{\mu_2 \left(\langle \frac{b_s}{b_d} - 1 \rangle \right)} \tag{5.24}$$

In the following, it will be shown that the use of two distinct viscous parameters μ_1 and μ_2 in the overstress function leads to a more versatile viscoplastic formulation and an improved performance in capturing rate effects.

To find R_v and R_d, Seidalinov and Taiebat (2014) used the volumetric and deviatoric gradients of the plastic potential surface at the image stress as the flow rule of the rate-independent bounding surface model (i.e. $R_v = R_v^i$ and $R_d = R_d^i$). The main limitation of that flow rule, hereafter referred to as the image stress flow rule, was the occurrence of a lock-up in the effective stress path after a few cycles of loading in an undrained cyclic loading test. Shi et al. (2018) have shown that

employing a hybrid flow rule, i.e., using the gradients of the plastic potential at both image and current stress, may improve such stress path lock-up and add a so-called butterfly-shaped loop to the stress path of the model. In this work, the hybrid flow rule proposed by Shi et al. (2018), schematically shown in Figure 5.3, is applied for R_v while R_d is solely determined by the image stress flow rule:

$$R_v = R_v^i \cdot g_i + R_v^c(|m_g| - g_i) \tag{5.25}$$

$$R_d = R_d^i \tag{5.26}$$

Where m_g is a hybrid flow rule input parameter and g_i is the distribution variable. R_v^i and R_v^c are volumetric gradients of the viscoplastic potential surface at the image and current stress, respectively, and R_d^i is the deviatoric gradient of it at the image stress (refer to Figure 5.3). g_i is assumed to have the following expression:

$$g_i = \left(\frac{1}{b_s}\right)^{\omega} \tag{5.27}$$

Where ω is a material constant that along with m_g controls the contribution of R_v^c and R_v^c to the flow rule. It should be noted that the special case of $\omega = 0$ and $m_g = 1$ will result in an imaging stress flow rule. Consequently, R_v^i, R_v^c, and R_d^i are given as:

$$R_v^i = \frac{\partial g}{\partial \bar{p}} = \bar{p}(M^2 - \bar{\eta}^2) \tag{5.28}$$

$$R_d^i = \frac{\partial g}{\partial \bar{q}} = 2 \cdot \bar{p}(\bar{\eta} - \alpha) \tag{5.29}$$

$$R_v^c = p(M^2 - s_l \cdot \eta^2) \tag{5.30}$$

Where η and $\bar{\eta}$ are the current ($\eta = \frac{q}{\mathrm{p}}$) and image stress ratio ($\bar{\eta} = \frac{\bar{q}}{\bar{p}}$), respectively, and s_l is a variable that alternates between 1 and -1 depending on the loading direction and the stress ratio:

$$s_l = \begin{cases} 1 & if \quad (\bar{\eta} - \alpha)\eta \geq 0 \\ -1 & if \quad (\bar{\eta} - \alpha)\eta < 0 \end{cases} \tag{5.31}$$

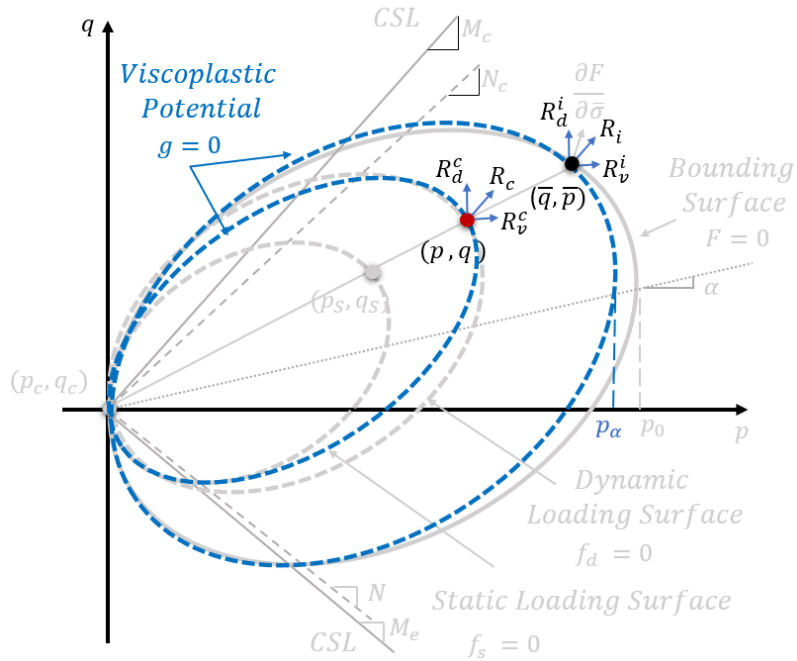

Figure 5.3 Schematic of the hybrid flow rule applied to the *BS-EVP* model.

5.2.6 Relocation of the Static Loading Surface

As mentioned previously, in Perzyna's viscoplasticity, any stress state inside the static loading surface will result in an elastic response. Therefore, under monotonic loading, once the stress state exits the static loading surface, the viscoplastic deformations start and continue to develop until the end of the loading path. However, under cyclic loading, a stress reversal brings the stress state back inside the static loading surface, and viscoplastic deformations stop until the stress state is such that the overstress is positive again. Since such abrupt changes of response after stress reversal do not occur in rate-independent bounding surface models, Shi et al. (2019) proposed to eliminate this inconvenience by relocating the static loading surface once two conditions occur simultaneously: (1) the current stress is inside the static loading surface and (2) the loading index attains a positive value. These conditions can be expressed as:

$$b_s = b_d \quad if\ (L > 0\ \ and\ \frac{b_s}{b_d} < 1\ ) \tag{5.32}$$

This relocation procedure mitigates the lack of visco-plastic effects upon stress reversal, in that it promotes the overstress growth as a result of a positive incremental loading index.

5.2.7 Hardening Variables

To complete all parts of the viscoplastic model, it is necessary to express the evolution laws for the hardening variables p_0, α, and b_s. As suggested by Seidalinov and Taiebat (2014), among the two distinct isotropic and frictional destructuration mechanisms that were suggested by Taiebat et al. (2010), only classical isotropic destructuration to capture the shear strength degradation is adopted in this model for the sake of simplicity. Therefore, p_0 is set to $p_{0d} \cdot S_i$ where $S_i \geq 0$ is the isotropic structuration factor and p_{0d} is the restructure value of p_0 (the value of p_0 when $S_\mathrm{i} = 1$). Therefore, the evolution law of p_0 may be expressed as follows:

$$\dot{p_0} = \langle \phi(y) \rangle \bar{p}_0 \tag{5.33}$$

$$\bar{p}_0 = S_i \cdot \bar{p}_{0d} + p_{0d} \cdot \bar{S}_i \tag{5.34}$$

$$\bar{p}_{0d} = \left(\frac{1+e}{\lambda - \kappa}\right) p_{0d}(R_v) \tag{5.35}$$

$$\bar{S}_i = k_i \left(\frac{1+e}{\lambda - \kappa}\right) (\, S_i - 1)(\bar{\varepsilon}_d^p) \tag{5.36}$$

Where λ and κ are the slopes of the isotropic loading and reloading curves in the $p - \ln\,(e)$ space, respectively, and k_i a material constant governing the rate of destructuration. It should be noted that the destructuration mechanism is active as long as $k_i > 0$. Therefore, setting $k_i = 0$ will switch off the destructuration mechanism. Also, $\bar{\varepsilon}_d^p$, the destructuration plastic strain rate, is an auxiliary internal variable which adjusts the degradation of $\bar{S}_i$:

$$\bar{\varepsilon}_d^p = \sqrt{(1-A)(R_v)^2 + (A)(R_d)^2} \tag{5.37}$$

Where A is a material constant that distributes the effects of the gradients of the volumetric and deviatoric plastic flows to $\bar{\varepsilon}_d^p$. A default value of 0.5 is set for this parameter.

For α, the rotational hardening rule proposed by Dafalias et al. (2006) is used:

$$\dot{\alpha} = \langle \phi(y) \rangle \bar{\alpha} \tag{5.38}$$

$$\bar{\alpha} = \langle \phi(y) \rangle \left(\frac{1+e}{\lambda - \kappa} \right) C \left(\frac{\bar{p}}{p_0} \right)^2 |R_v| |\bar{\eta} - x \cdot \alpha| (\alpha^b - \alpha) \tag{5.39}$$

C and x are input parameters governing the rotational rate of change of the bounding surface and the upper bound of α in a constant stress ratio loading, respectively. Also, α^b is the bounding value for α, determined as:

$$\alpha^b = \begin{cases} \min(M, N) & if \quad (\bar{\eta})/x \geq 0 \\ \max(-M, -N) & if \quad (\bar{\eta})/x < 0 \end{cases} \tag{5.40}$$

As mentioned previously, the static loading surface has its own evolution law:

$$\dot{b_s} = \langle \phi(y) \rangle \bar{b}_s \tag{5.41}$$

As suggested by Shi et al. (2019), $\dot{b_s}$ can be inferred from the consistency condition of the underlying rate-independent model used to construct the viscoplastic formulation:

$$\bar{b}_s = \frac{\left(-b_s \cdot K_p + \bar{K}_p - (1 - b_s)(R_v \cdot \bar{p}_c + R_d \cdot \bar{q}_c) \right)}{(p - \bar{p}_c)(R_v) + (q - \bar{q}_c)(R_d)} \tag{5.42}$$

Where K_p and $\bar{K}_p$ are the plastic modulus at the current and image stresses, respectively.

5.2.8 Plastic Modulus and Damage Variable

The core feature of the bounding surface framework is that the plastic modulus at the current stress, K_p, is associated with the plastic modulus, $\bar{K}_p$, at the image stress allowing the permanent strain to occur even if the stress state does not lie on the bounding surface. In this work, the expression of K_p proposed by Shi et al. (2018) is adopted:

$$K_p = \bar{K}_p + (b_s - 1)(1 + e) \cdot m_s \cdot p_0^3 \tag{5.43}$$

Where m_s is a shape hardening variable that controls the shape of the plastic modulus. Here, a decaying expression for m_s is used, in agreement with earlier propositions by Seidalinov and Taiebat (2014), who showed that to prevent hysteresis loop lock-up m_s should not be constant. As a result, the following expression is adopted:

$$m_s = \frac{h}{1 + d} \tag{5.44}$$

Where h is a variable which adjusts the plastic modulus magnitude and similar to M and N is dependent on the mode of shearing) (i.e., $N = N_c$ for triaxial compression and $N = N_e$ for triaxial extension) as suggested by Shi et al. (2018).

$$h = \begin{cases} h_c & if \quad \bar{q} \geq \bar{p}\alpha \\ h_e & if \quad \bar{q} < \bar{p}\alpha \end{cases} \tag{5.45}$$

d is the damage state variable, the rate of change of which is assumed to be linearly proportional to the deviatoric plastic strain increment:

$$\dot{d} = a_d \cdot \left|\dot{\varepsilon}_d^p\right| \tag{5.46}$$

Finally, $\bar{K}_p$ is obtained by satisfying the consistency condition, $\dot{F} = 0$:

$$\bar{K}_p = -\left(\frac{\partial F}{\partial p_0} \cdot \bar{p}_0 + \frac{\partial F}{\partial \alpha} \cdot \bar{\alpha}\right) \tag{5.47}$$

where $\frac{\partial F}{\partial p_0}$ and are $\frac{\partial F}{\partial \alpha}$ defined as:

$$\frac{\partial F}{\partial p_0} = -\bar{p} \cdot (N^2 - \alpha^2) \tag{5.48}$$

$$\frac{\partial F}{\partial \alpha} = -2 \cdot \bar{p} \cdot (\bar{q} - p_0 \cdot \alpha) \tag{5.49}$$

5.3 Model Generalization in Multiaxial Space

This section generalizes to a multiaxial space formulation all aspects of the viscoplastic model presented in the previous section, including the bounding surface, viscoplastic potential surface, viscoplastic flow rule, hardening rules of the internal variables, image stress, projection center evolution, and plastic modulus. The model generalization in this section is based on the approach proposed by Dafalias et al. (2006) for the original *SANICALY* model and the formulation provided by Seidalinov (2012) for the *SANICLAY* bounding surface and Shi (2016) for the *SANICLAY* with the hybrid flow rule.

In multiaxial space, with knowledge of the stress tensor, $\boldsymbol{\sigma}$, the deviatoric stress tensor, $\boldsymbol{s}$, and the hydrostatic pressure, p, may be expressed as:

$$\boldsymbol{s} = \boldsymbol{\sigma} - p \cdot \boldsymbol{I} \tag{5.50}$$

$$p = \frac{1}{3} tr(\boldsymbol{\sigma}) \tag{5.51}$$

Where $\boldsymbol{I}$ is the identity tensor, and *tr* indicates the trace of a tensor.

The deviatoric stress commonly used in triaxial space can be computed from the deviatoric stress tensor as:

$$q = [(3/2)\boldsymbol{s}:\boldsymbol{s}]^{1/2} \tag{5.52}$$

Where ":" symbolizes the inner product of two tensors. This equation indicates that s is the multiaxial counterpart of q. Similarly, the multiaxial counterpart of the triaxial α can be expressed in terms of the stress-ratio tensor $\boldsymbol{\alpha}$:

$$\alpha = [(3/2)\boldsymbol{\alpha}:\boldsymbol{\alpha}]^{1/2} \tag{5.53}$$

5.3.1 Elastic Response

Similar to the triaxial conditions, the tensor of the elastic strain increments, $\dot{\boldsymbol{\varepsilon}}^e$, may be expressed in terms of the volumetric strain increments, $\dot{\varepsilon}_v^e$, and the tensor of the deviatoric strain increments, $\dot{\boldsymbol{\varepsilon}}_d^e$:

$$\dot{\boldsymbol{\varepsilon}}^e = \dot{\boldsymbol{\varepsilon}}_d^e + \dot{\varepsilon}_v^e \boldsymbol{I} \tag{5.54}$$

Where the multiaxial generalization of the hypoelastic relations is expressed as:

$$\dot{\boldsymbol{\varepsilon}}^e = \frac{\dot{\boldsymbol{s}}}{2G} + \frac{\dot{p}}{3K}\boldsymbol{I} \tag{5.55}$$

Where K and G are the elastic bulk and shear moduli, respectively, which were defined previously.

5.3.2 Bounding and Viscoplastic Potential Surfaces

According to Eq.(5.52) and Eq.(5.53), the bounding and viscoplastic potential surfaces may be generalized to multiaxial space, respectively, as:

$$F = \frac{3}{2}(\bar{\boldsymbol{s}} - \bar{p}\cdot\boldsymbol{\alpha}):(\bar{\boldsymbol{s}} - \bar{p}\cdot\boldsymbol{\alpha}) - \left(N^2 - \frac{3}{2}\boldsymbol{\alpha}:\boldsymbol{\alpha}\right)\bar{p}(p_0 - \bar{p}) = 0 \tag{5.56}$$

$$g = \frac{3}{2}(\bar{\boldsymbol{s}} - \bar{p}\cdot\boldsymbol{\alpha}):(\bar{\boldsymbol{s}} - \bar{p}\cdot\boldsymbol{\alpha}) - (M^2 - \frac{3}{2}\boldsymbol{\alpha}:\boldsymbol{\alpha})\bar{p}(p_\alpha - \bar{p}) = 0 \tag{5.57}$$

Where $\bar{\boldsymbol{s}}$ and $\bar{p}$ are the deviatoric and hydrostatic components of the image stress, respectively. As was discussed previously, the slope of the critical state line, M, and the bounding line, N, varies in the triaxial stress space according to the sign of the $\alpha - \eta$. In the multiaxial stress space, M is interpolated between its values M_c and M_e using the Lode angle, θ, and an interpolation function as suggested by Argyris et al. (1974):

$$M = \theta(\bar{\theta}, c_M)M_c = \frac{2c_M}{(1 + c_M) - (1 - c_M)\cdot cos3\bar{\theta}}\cdot M_c \tag{5.58}$$

$$cos3\bar{\theta} = \sqrt{6}\cdot tr\bar{n}^3 \tag{5.59}$$

$$\bar{n} = \frac{\bar{s} - \bar{p} \cdot \boldsymbol{\alpha}}{\|\bar{s} - \bar{p} \cdot \boldsymbol{\alpha}\|} \tag{5.60}$$

Where $\|A\|$ denotes the Eulerian norm of a tensor, i.e., $\|A\| = \sqrt{A:A}$ and c_M equals to M_c/M_e. Similar to M, N may be interpolated using its values N_c and N_e:

$$N = \theta(\bar{\theta}, c_N) \cdot N_c = \frac{2 \cdot c_N}{(1 + c_N) - (1 - c_N)cos3\bar{\theta}} \cdot N_c \tag{5.61}$$

Where c_N equals to N_c/N_e.

5.3.3 Image Stress and Projection Center

In the multiaxial stress space, the radial mapping rule to project the current stress on the bounding surface using the dynamic stress ratio, b_d, may be generalized to:

$$\bar{p} = p_c + b_d(p - p_c) \tag{5.62}$$

$$\bar{\boldsymbol{s}} = \boldsymbol{s}_c + b_d(\boldsymbol{s} - \boldsymbol{s}_c) \tag{5.63}$$

Where $\boldsymbol{s}_c$ and p_c are the deviatoric and hydrostatic components of the projection center ($\boldsymbol{\sigma}_c$), respectively. Similar to the triaxial space, knowing both b_s and b_d allows calculating the static stress ($\boldsymbol{\sigma}_s$) in terms of the current stress:

$$p_s = p_c + \frac{b_d}{b_s}(p - p_c) \tag{5.64}$$

$$\boldsymbol{s}_s = \boldsymbol{s}_c + \frac{b_d}{b_s}(\boldsymbol{s} - \boldsymbol{s}_c) \tag{5.65}$$

Where $\boldsymbol{s}_s$ and p_s are the deviatoric and hydrostatic components of the projection center ($\boldsymbol{\sigma}_s$), respectively. It should be reminded that b_s is the hardening variable in the model, the variation of which will be discussed in sequence.

In agreement with the triaxial condition, to have unique image stress, the projection center should be updated to the current stress at any stress reversal so that it always remains inside the bounding

surface. As mentioned previously, the stress reversal occurs whenever the loading index $L \leq 0$, where L in the multiaxial space may be obtained by satisfying the consistency condition on the bounding surface, $\dot{F} = 0$:

$$L = \frac{1}{K_p}\frac{\partial F}{\partial \overline{\boldsymbol{\sigma}}} : \dot{\boldsymbol{\sigma}} \tag{5.66}$$

$\frac{\partial F}{\partial \overline{\boldsymbol{\sigma}}}$, called as $\boldsymbol{D}$ in this section, is the loading direction in the multiaxial stress space, which is defined as:

$$\frac{\partial F}{\partial \overline{\boldsymbol{\sigma}}} = \boldsymbol{D} = \boldsymbol{D}_d + 1/3\, D_v \cdot \boldsymbol{I} \tag{5.67}$$

Where L_v and $\boldsymbol{L}_d$ are the volumetric and deviatoric components of the loading direction in multiaxial space, respectively, which are given as:

$$D_v = tr\left(\frac{\partial F}{\partial \overline{\boldsymbol{\sigma}}}\right) = \bar{p}\left(N^2 - \frac{3}{2}\overline{\boldsymbol{r}} : \overline{\boldsymbol{r}}\right) + 3\left(\frac{\partial F}{\partial \bar{\theta}}\right)\frac{tr(\overline{\boldsymbol{n}}^2\boldsymbol{\alpha}) - tr\overline{\boldsymbol{n}}^3 tr(\overline{\boldsymbol{n}}\boldsymbol{\alpha})}{\|\overline{\boldsymbol{s}} - \bar{p}\boldsymbol{\alpha}\|\sqrt{(3/2)(1 - 6tr^2\overline{\boldsymbol{n}}^3)}} \tag{5.68}$$

$$\boldsymbol{D}_d = 3(\overline{\boldsymbol{s}} - \bar{p}\,\boldsymbol{\alpha}) + \sqrt{6}\left(\frac{\partial F}{\partial \bar{\theta}}\right)\frac{(tr\overline{\boldsymbol{n}}^3)\overline{\boldsymbol{n}} - \overline{\boldsymbol{n}}^2}{\|\overline{\boldsymbol{s}} - \bar{p}\boldsymbol{\alpha}\|\sqrt{(1 - 6tr^2\overline{\boldsymbol{n}}^3)}} \tag{5.69}$$

Where the term $\frac{\partial g}{\partial \bar{\theta}}$ may be expressed in the multiaxial stress space as:

$$\frac{\partial F}{\partial \bar{\theta}} = 6N^2 \cdot \bar{p} \cdot (p_0 - \bar{p})\left(\frac{1 - c_N}{2 \cdot c_N}\right)\theta(\bar{\theta}, c_N) sin3\bar{\theta} \tag{5.70}$$

To guarantee that the projection center is always inside the bounding surface, the generalization of the evolution rule of the moving projection center which considers the simultaneous changes of p_0 and α is expressed as:

$$\dot{p_c} = \frac{p_c}{p_0} \cdot \dot{p_0} \tag{5.71}$$

$$\dot{\boldsymbol{s}}_c = \frac{\boldsymbol{s}_c}{p_0} \cdot \dot{p}_0 + \left[\frac{p_c \cdot {N_c}^2 - [(3/2)\boldsymbol{\alpha}:\boldsymbol{\alpha}]^{1/2} \cdot [(3/2)\boldsymbol{s}_c:\boldsymbol{s}_c]^{1/2}}{{N_c}^2 - [(3/2)\boldsymbol{\alpha}:\boldsymbol{\alpha}]^{1/2}} \right] \cdot \dot{\alpha} \tag{5.72}$$

5.3.4 The Viscoplastic Hybrid Flow Rule

In Perzyna's theory of Viscoplasticity, the viscoplastic strain rates in the multiaxial space may be generalized to:

$$\dot{\boldsymbol{\varepsilon}}^p = \mu\langle\phi(y)\rangle \cdot \boldsymbol{R} \tag{5.73}$$

Where $\boldsymbol{R}$ is the gradient of the flow potential function, g, which is expressed in terms of the deviatoric, $\boldsymbol{R}_d$, and volumetric, $\boldsymbol{R}_v$, components as:

$$\boldsymbol{R} = \boldsymbol{R}_d + 1/3\, R_v \cdot \boldsymbol{I} \tag{5.74}$$

As discussed before, the hybrid flow rule is only applied to R_v while $\boldsymbol{R}_d$ is solely determined by the image stress flow rule (i.e., $\boldsymbol{R}_d = \boldsymbol{R}_d^i$). In multiaxial stress space, $\boldsymbol{R}_d^i$ is generalized to:

$$\boldsymbol{R}_d^i = \frac{\partial g}{\partial \bar{\boldsymbol{\sigma}}} - \frac{1}{3} tr\left(\frac{\partial g}{\partial \bar{\boldsymbol{\sigma}}}\right)\boldsymbol{I} = 3(\bar{\boldsymbol{s}} - \bar{p} \cdot \boldsymbol{\alpha}) + \sqrt{6}\left(\frac{\partial g}{\partial \bar{\theta}}\right)\frac{(tr\boldsymbol{n}^3)\bar{\boldsymbol{n}} - \bar{\boldsymbol{n}}^2}{\|\bar{\boldsymbol{s}} - \bar{p} \cdot \boldsymbol{\alpha}\|\sqrt{1 - 6tr^2 \cdot \bar{\boldsymbol{n}}^3}} \tag{5.75}$$

$$\frac{\partial g}{\partial \bar{\theta}} = 6M^2 \cdot \bar{p}(p_\alpha - \bar{p})(\frac{1 - c_M}{2c_M})\theta(\bar{\theta}, c_M) sin3\bar{\theta} \tag{5.76}$$

As mentioned earlier, applying a hybrid flow rule to the volumetric component of the plastic flow, R_v, indicates that it consists of those at the image stress, R_v^i, and the current stress, R_v^c.

$$R_v = R_v^i \cdot g_i + R_v^c(m_g - g_i) \tag{5.77}$$

Where the generalized form of the R_v^i and R_v^c in the multiaxial space may be shown as:

$$R_v^i = tr\left(\frac{\partial g}{\partial \bar{\boldsymbol{\sigma}}}\right) = \bar{p}\left(M^2 - \frac{3}{2}\bar{\boldsymbol{r}}:\bar{\boldsymbol{r}}\right) + 3\left(\frac{\partial g}{\partial \bar{\theta}}\right)\frac{tr(\bar{\boldsymbol{n}}^2\boldsymbol{\alpha}) - tr\bar{\boldsymbol{n}}^3 tr(\bar{\boldsymbol{n}}\boldsymbol{\alpha})}{\|\bar{\boldsymbol{s}} - \bar{p}\boldsymbol{\alpha}\|\sqrt{(3/2)(1 - 6tr^2\bar{\boldsymbol{n}}^3)}} \tag{5.78}$$

$$R_v^c = tr\left(\frac{\partial g}{\partial \boldsymbol{\sigma}}\right) = p\left(M^2 - \frac{3}{2}s_l \boldsymbol{r}:\boldsymbol{r}\right) + 3b\left(\frac{\partial g}{\partial \theta}\right)\frac{tr(\bar{\boldsymbol{n}}^2\boldsymbol{\alpha}) - tr\bar{\boldsymbol{n}}^3 tr(\bar{\boldsymbol{n}}\boldsymbol{\alpha})}{\|\bar{\boldsymbol{s}} - \bar{p}\boldsymbol{\alpha}\|\sqrt{(3/2)(1 - 6tr^2\bar{\boldsymbol{n}}^3)}} \tag{5.79}$$

Where the term $\frac{\partial g}{\partial \bar{\theta}}$ may be expressed in the multiaxial stress space as:

$$\frac{\partial g}{\partial \theta} = 6M^2 \cdot p(p_\alpha - p)(\frac{1 - c_M}{2c_M})\theta(\bar{\theta}, c_M)sin3\bar{\theta} \tag{5.80}$$

Where in the multiaxial stress space, s_l may be found according to the following rule:

$$s_l = \begin{cases} 1 & if \quad \bar{\boldsymbol{n}}\boldsymbol{n} \geq 0 \\ -1 & if \quad \bar{\boldsymbol{n}}\boldsymbol{n} < 0 \end{cases} \tag{5.81}$$

Where $\boldsymbol{n}$ and $\bar{\boldsymbol{n}}$ are unit tensors that point from the origin of the deviatoric plane to the current and image stress point, respectively, that are expressed as:

$$\boldsymbol{n} = \frac{\boldsymbol{s} - p \cdot \boldsymbol{\alpha}}{\|\boldsymbol{s} - p \cdot \boldsymbol{\alpha}\|} \tag{5.82}$$

$$\bar{\boldsymbol{n}} = \frac{\bar{\boldsymbol{s}} - p \cdot \bar{\boldsymbol{\alpha}}}{\|\bar{\boldsymbol{s}} - p \cdot \bar{\boldsymbol{\alpha}}\|} \tag{5.83}$$

5.3.5 Hardening Variables

In the following, the generalization of the hardening variables p_0, α, S_b and b_s in the multiaxial stress space is discussed separately. The evolution rule for the isotropic hardening variable, p_0, may be generalized as:

$$\dot{p_0} = \langle\phi(y)\rangle\bar{p}_0 = \langle\phi(y)\rangle\left(\frac{1+e}{\lambda - \kappa}\right)\bar{p}_0(R_v) \tag{5.84}$$

For $\boldsymbol{\alpha}$, the generalized rotational hardening rule proposed by Dafalias et al. (2006) is adopted:

$$\dot{\boldsymbol{\alpha}} = \langle\phi(y)\rangle\bar{\boldsymbol{\alpha}} = \sqrt{3/2}\left(\frac{1+e}{\lambda-\kappa}\right)C\left(\frac{\bar{p}}{p_0}\right)^2|R_v|\|\bar{\boldsymbol{r}} - x\cdot\boldsymbol{\alpha}\|(\boldsymbol{\alpha}^b - \boldsymbol{\alpha}) \tag{5.85}$$

Where:

$$\boldsymbol{\alpha}^b = \sqrt{3/2}\,M\cdot\bar{\boldsymbol{n}}_x \tag{5.86}$$

$$\bar{n}_x = \frac{(\bar{\boldsymbol{r}} - x\cdot\boldsymbol{\alpha})}{\|\bar{\boldsymbol{r}} - x\cdot\boldsymbol{\alpha}\|} \tag{5.87}$$

The generalization of the destructuration law for the internal variable S_b may be expressed as:

$$\dot{S_b} = \langle\phi(y)\rangle\bar{S}_b = -(k_i S_b)\sqrt{(1-A)(R_v)^2 + (A)(\frac{3}{2}\boldsymbol{R}_d:\boldsymbol{R}_d)} \tag{5.88}$$

Finally, the multiaxial generalization of the evolution of the static similarity ratio, b_s, is expressed as:

$$\dot{b_s} = \langle\phi(y)\rangle\bar{b}_s \tag{5.89}$$

Where $\dot{b_s}$ is generalized in the multiaxial stress space as:

$$\bar{b}_s = \frac{\left(-b_s\cdot K_p + \bar{K}_p - (1-b_s)\left(\frac{\partial F}{\partial\bar{p}}\cdot\bar{p}_c + \frac{\partial F}{\partial\bar{\boldsymbol{s}}}:\bar{\boldsymbol{s}}_c\right)\right)}{(p-\bar{p}_c)\left(\frac{\partial F}{\partial\bar{p}}\right) + (\boldsymbol{s}-\bar{\boldsymbol{s}}_c):\left(\frac{\partial F}{\partial\bar{\boldsymbol{s}}}\right)} \tag{5.90}$$

Where K_p and $\bar{K}_p$ are the plastic modulus at the current and image stresses, respectively, to be discussed in the following.

5.3.6 Plastic Modulus and Damage Variable

In multiaxial stress space, the plastic modulus shares the same expression with that of the triaxial space:

$$K_p = \bar{K}_p + (b_s - 1)(1 + e) \cdot m_s \cdot p_0^3 \tag{5.91}$$

Where $\bar{K}_p$ is obtained by satisfying the consistency condition on the bounding surface, $\dot{F} = 0$:

$$\bar{K}_p = -\left(\frac{\partial F}{\partial p_0}\bar{p}_0 + \frac{\partial F}{\partial \boldsymbol{\alpha}} : \bar{\boldsymbol{\alpha}}\right) \tag{5.92}$$

Where:

$$\frac{\partial F}{\partial \boldsymbol{\alpha}} = -3\bar{p}(\bar{\boldsymbol{s}} - p_0 \cdot \boldsymbol{\alpha}) \tag{5.93}$$

$$\frac{\partial F}{\partial p_0} = -\bar{p}(N^2 - \frac{3}{2}\boldsymbol{\alpha} : \boldsymbol{\alpha}) \tag{5.94}$$

Similar to the plastic modulus, in multiaxial space, the shape hardening variable, m_s, that controls the shape of the plastic modulus, shares the same expression with that of the triaxial space:

$$m_s = \frac{h}{1 + d} \tag{5.95}$$

Where similarly to M and N, h may be interpolated using the Lode angle between its values h_c and h_e :

$$h = \theta(\bar{\theta}, c_h)h_c = \frac{2c_h}{(1 + c_h) - (1 - c_h)cos3\bar{\theta}}h_c \tag{5.96}$$

Where c_h equals to h_c/h_e.

Finally, the damage state variable, d, which is assumed to be linearly proportional to the deviatoric plastic strain increment, is generalized to the multiaxial stress space as:

$$\dot{d} = a_d\left|(2/3)\dot{\boldsymbol{\varepsilon}}_d^p : \dot{\boldsymbol{\varepsilon}}_d^p\right|^{1/2} \tag{5.97}$$

5.4 Summary and Conclusions

In this chapter, the formulation of a rate-dependent SANICLAY model for simulations of clay behavior under monotonic and cyclic loading has been presented. Such formulations were based on isotropic and rotational hardening rules, a proper projection center update, a hybrid flow rule, and Pyerzyna's theory of viscoplasticity. Also, the model generalization in the multiaxial space was presented so that it could be implemented into numerical platforms for both two- and three-dimensional simulations under various types of loading (triaxial, torsional, shear, etc.). In the next chapter, the calibration of the model's input parameters, along with its performance and validation, is discussed.

CHAPTER 6 MODEL CALIBRATION AND VALIDATION

The information presented in this chapter is included in several publications:

Zarrabi**,** M., Shi, Z., Yniesta, S., and Buscarnera, G. "A Viscoplastic Bounding Surface Model for Cyclic Softening." (to be submitted to International Journal for Numerical and Analytical Methods in Geomechanics).

Zarrabi, M., Shi, Z., Yniesta, S., and Buscarnera, G. (2020). "Simulation of the Cyclic Response of Anisotropic Clay through Bounding Surface Viscoplasticity" *GeoVirtual*, Canada.

6.1 Introduction

The calibration efforts discussed in chapter 4 were mainly focused on automatic calibrations using two optimization algorithms so that some alternates for trial and error calibrations be covered. However, in this section, the calibration of input parameters of the developed model is discussed by explaining, in more detail, the physical meaning of parameters and reviewing the existing conventional geotechnical tests or relations for their calibrations offered by various researchers (Dafalias et al., 2006; Seidalinov, 2012; Shi, 2016). In the second part of the chapter, the model performance is illustrated by a series of monotonic and cyclic simulations performed at different loading rates. Then, its validation is investigated using experimental studies.

6.2 Calibration of Model Parameters

The developed model in its current form has 16 input parameters (κ, ν, λ, M_{c}, M_{e}, N_{c}, N_{e}, h_{c}, h_{e}, c_d, C, x, ω, m_g, μ_1, μ_2). Although one may criticize that having a large number of input parameters may be challenging to calibrate, it should be noted that the current model is developed and formulated upon the framework of previous existing models for clays (e.g., *MCC*, *SANICLAY*, *SANICLAY*-B, *SANICLAY*-H, etc.) and uses several well-established features and concepts (such as isotropic and rotational hardening rules, bounding surface plasticity, hybrid flow rule, Perzina's theory of viscoplasticity, etc.). Therefore, most of these parameters are not newly introduced input parameters; hence a fair amount of work could be found related to their discussions and calibrations.

6.2.1 Elasticity Parameters κ and ν

The parameter κ may be defined as the slope of the recompression (reloading or rebound) line in the $e - lnp$ space and may be found either by a *1D* compression test or an isotropic compression test (Dafalias et al., 2006). If such tests exist, κ may be estimated using the recompression index C_r:

$$\kappa = C_r / \ln(10) \tag{6.1}$$

However, Dafalias et al. (2006) stated that the estimation of κ using this method could be less reliable as K_0 could vary during a *1D* unloading.

6.2.2 Critical State Parameters λ, M_c, and M_e

The parameter λ is the slope of the virgin (normal) compression line, and similar to κ, may be estimated using the compression index C_c, obtained from a *1D* compression test or an isotropic compression test (Dafalias et al., 2006):

$$\lambda = C_c / ln(10) \tag{6.2}$$

Two input parameters M_c and M_e represent the slope of the critical state lines in triaxial compression and extension, respectively. M_c and M_e could be found using the effective stress path plotted from the CK_0TXC and TXE tests, respectively (Dafalias et al. 2006).

However, Dafalias et al. (2006) stated that in case one or both of the above tests are not available, for example, it is very common that an extension test is not performed, these slopes may be estimated using the expression between the critical state (or steady-state) friction angle, ϕ_{cs}:

$$M_c = \frac{6sin(\phi_{cs})}{3 - sin(\phi_{cs})} \tag{6.3}$$

$$M_e = \frac{6sin(\phi_{cs})}{3 + sin(\phi_{cs})} \tag{6.4}$$

$$\phi_{cs} = \arcsin\left(\frac{3M_c}{6 + M_c}\right) \tag{6.5}$$

6.2.3 Bounding Surface Parameters N_c and N_e

Two parameters N_c and N_e adjust the shape of the yield surface or/and the bounding surface (Dafalias et al., 2006). For the calibration of these parameters, three alternatives may be found in the literature. First, Dafalias et al. (2006) expressed an analytical solution in terms of the mean effective stress at the critical state, p_f, and that at the end of a K_0 consolidation, p_{k0}, obtained from a CK_0UTXC test on an *NC* clay (note that Dafalias et al. (2006) used a single *N* in their work, i.e., N_c and N_e were assumed to be the same):

$$\frac{p_f}{p_{k0}} = \left(\frac{N^2 - \eta_{k0}^2}{N^2 - 2\eta_{k0}\, M_c + M_c^2}\right)^{1-\left(\frac{\kappa}{\lambda}\right)} \tag{6.6}$$

Where η_{k0} represents the stress ratio at the end of a K_0 consolidation test and may be expressed using the earth coefficient at rest, $K_0, NC,$:

$$\eta_{k0} = 3(1 - K_0, NC)/(1 + 2K_0, NC) \tag{6.7}$$

Besides to above expression, Taiebat et al. (2010) suggested that N_c (and N_e) may be directly found by matching the bounding (or yield) surface of the model to the CK_0UTXC effective stress path on *NC* clay as the stress path of the soil in this test is similar to the shape of the yield (bounding surface). Finally, Shi (2016) suggested that in cases where neither of CK_0TXC (to find N_c) or TXE (to find N_e) tests have been conducted, N_C and N_e be initially set equal to M_c and M_e, respectively, and be adjusted to match the compressive and extensive post-cyclic undrained shear strength.

6.2.4 Rotational Hardening Parameters χ and C

According to Dafalias et al. (2006), the parameter χ is governing the anisotropy limit under stress paths in which η is constant (the characteristic of such a path is that the yield (or bounding) and plastic potential surfaces keep expanding while they are no longer distorting or rotating). In other

words, χ sets an upper limit for the internal variable α during a constant stress ratio loading. Dafalias et al. (2006) proposed the following analytical solution to find this parameter:

$$\chi = \frac{2\eta_k \varepsilon(1-\kappa/\lambda)}{B\varepsilon\eta_k^3 + \eta_k^2 + 2[(1-\kappa/\lambda) - BM_c^2]\varepsilon\eta_k - M_c^2} \tag{6.8}$$

Where $\varepsilon = \dot{\varepsilon}_v/\dot{\varepsilon}_q$ is the ratio of the total strain rates (i.e., the ratio of volumetric strain rate over the deviatoric strain rate), η_k a constant correspond to ε, and B expresses as:

$$B = -\frac{2(1+\nu)\kappa}{9(1-2\nu)\lambda} \tag{6.9}$$

Dafalias et al. (2006) stated that a K_0-loading path is among the most frequent paths in which η_k is constant. In such a test $\varepsilon = 3/2$ and $\eta_k = \eta_{k0}$ (that may be found using Eq.(6.7) in which K_0 may be found using experiments or estimated as $K_0 = 1 - sin\emptyset$ for normally consolidated clays). Finally, χ may be calculated once K_0 and other parameters in Eq. (6.8) and Eq. (6.9) (i.e., κ, λ, M_c, and ν) are known. However, in the absence of the aforementioned tests or data, a value between 1.75 t o 1.98 may be set for χ since a narrow range has been reported for this parameter for different types of clays (Shi, 2016; Seidalinov, 2012).

The parameter *C* governs the rate by which the bounding (or yield) and the plastic potential surfaces rotates and/or distorts (Dafalias et al. (2006); Taiebat et al. (2010)). Dafalias et al. (2006) suggested that tests in which the bounding (or yield) and the plastic potential surfaces rotates significantly (so that the stress ratio at the end of the loading, η_f, becomes far from the initial stress ratio, η_{in}) are the most suitable for calibrating this parameter. An example of such test is $CK_0U\ TXE$ on *NC* clay in which η_f and η_{in} are far different than the other due to the considerable surface rotation. In addition to the mentioned approach, Dafalias et al. (2006) stated that *C* falls in the range of 3 to 20 for different types of clays. Therefore, in the case of an absence of such data, a value from this range could be selected for *C*.

6.2.5 Plastic Modulus Parameters h_c and h_e and c_d

In the bounding surface plasticity proposed by Dafalias (Dafalias and Hermann, 1986), the plastic modulus, K_p, is related to the distance between the stress point and the image stress point (stress on the bounding surface) and a hardening variable, h. In this model, the plastic modulus parameters h_c and h_e are the initial values, in compression and extension, respectively, of the hardening variable, h, that adjust the plastic modulus, K_p, and hence, the soil stiffness at the very initiation of the loading (Seidalinov, 2012; Seidalinov and Taiebat, 2014). Therefore, in both monotonic and cyclic loading cases, higher values for these parameters will result in higher stiffness (less plasticity). In a monotonic loading, assigning high values for these parameters will cause the stress path to have a large elastic response. Similarly, in a cyclic event, high values of plastic modulus parameters make the initial cycles of hysteresis loops very stiff, as shown in Figure 6.1.

The damage parameter, c_d, is another parameter that affects the plastic modulus in cyclic loading. In fact, c_d governs the rate by which the hardening variable, h, and consequently plastic modulus, decays in cyclic loading. In other words, the damage parameter, the effects of which shown in Figure 6.2, governs the plastic strain developments during cyclic loading (as the decrease of the plastic modulus reduces the soil stiffness and increases the plasticity). Therefore, it should be highlighted that this parameter does not influence the monotonic behavior of the soil significantly.

To calibrate h_c, h_e, and c_d, Seidalinov (2012) proposed that h_c and h_e be calibrated against the first few hysteresis loops in a cyclic loading (where the soil is not softened yet) while the damage parameter is deactivated (i.e. c_d=0). Once h_c and h_e have been calibrated, c_d maybe found by matching the hysteresis loops at larger shear strains to capture the cyclic softening. For better performance and to avoid time-consuming trial-and-error efforts, the calibration of these parameters could be performed using optimization techniques, similar to calibrations performed and presented in chapter 4.

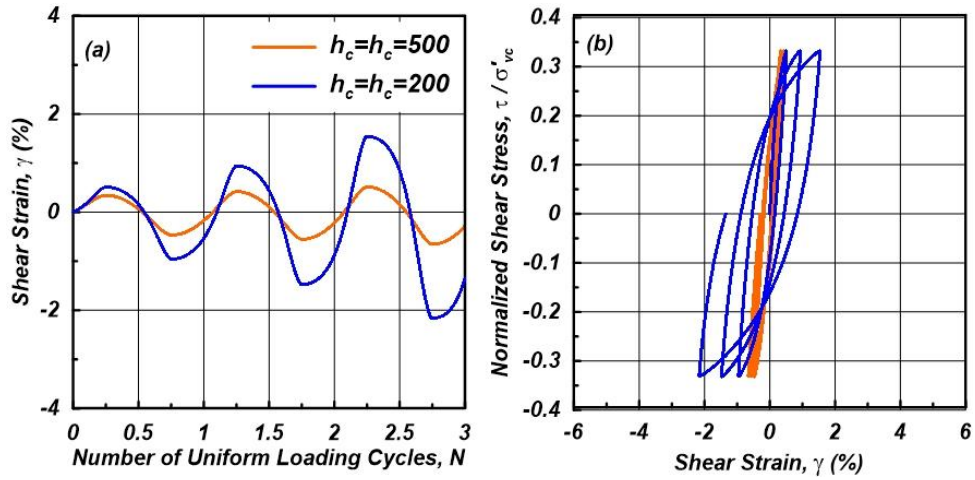

Figure 6.1 Effects of h_c and h_e on the initial stiffness of the hysteresis loops

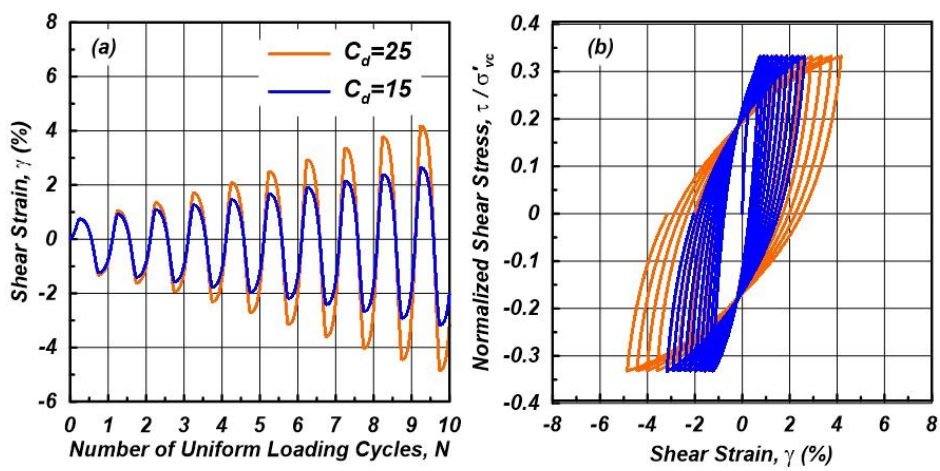

Figure 6.2 Model response at different c_d values

6.2.6 Hybrid Flow Rule Parameters ω and m_g

The parameter ω that is related to the hybrid flow rule proposed by Shi (2016) and Shi et al. (2018) governs the relative contribution of the viscoplastic gradient at the current stress and the image (on the bounding surface) stress points. It should be reminded that activating the hybrid flow rule (i.e., assigning a value other than 0 for ω) addresses the stress path lock-up, that occurs after a few cycles in cases where an image stress flow rule (i.e., $\omega = 0$) is activated, by simulating the so-called butterfly or eight-shaped loops which is typical of soil response under cyclic loading. The influence

of this parameter on model's respone is shown in Figure 6.3. Shi (2016) reported a range of 1 to 5 for different types of clays for this parameter.

The input parameter m_g governs the amount by which the pore water pressure builds-up or the mean effective stress decreases in an undrained cyclic loading test. The default value for this parameter is set to 1. Assigning a value lower than 1 avoids the sharp increase of the excess pore water pressure in a cyclic event, and consequently, ensures a gradual decrease of the mean effective stress.

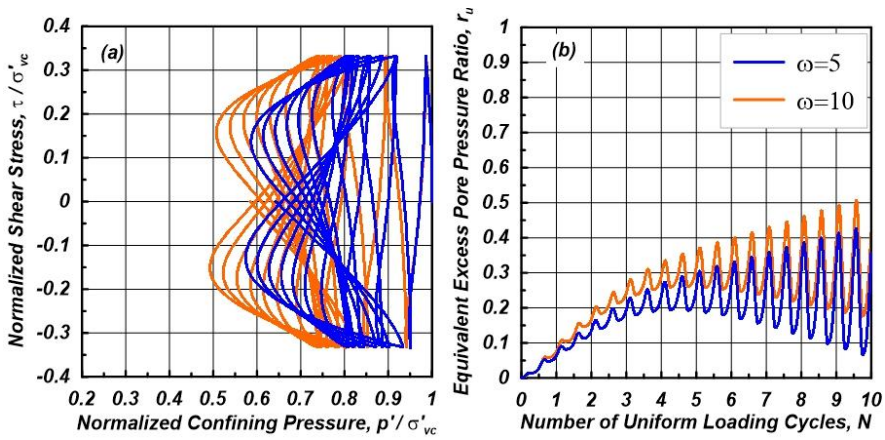

Figure 6.3 Influence of ω on the stress path and the excess pore water pressure generation

6.2.7 Viscos Parameters μ_1 and μ_2

Two viscous parameters μ_1 and μ_2 that governs the effects of time or loading rates could be calibrated independently (separately from rate-independent input parameters). To calibrate these parameters, a series of monotonic and/or cyclic loading tests with different loading rates or frequencies is needed. Once such tests are available, these parameters could be found by matching the stress path, hysteresis loops, load-displacement, etc., of the simulations to those of experiments. However, in the case where such data is not available, it is suggested that these parameters be set in a way that the model response matches with the experiments at conventional slow loading rates and produces a logical pattern at other loading rates/frequencies.

6.3 Model's Performance, Calibration, and Validation

In this section, the model's performance in simulating soil response under different loading conditions is presented. The model is first calibrated against the experimental studies of Bonin et al. (2019), on Glacio-Lacustrine clay, and Sheahan et al. (1996), on the effects of loading rate and consolidation state on the undrained shear strength of the Boston Blue Clay. Then, the model validation is discussed by applying the model to simulate further studies: 1- the Grande-Baleine clay behavior reported by Lefebvre and LeBoeuf (1987) at different loading rates, 2- the effects of strain rates on the modulus reduction and damping ratio curves studied by Shibuya et al. (1995), and 3- the combined effects of cyclic loading and loading rates on the Saint-Adelphe clay behavior reported by Abdellaziz et al. (2017).

6.3.1 Model's monotonic and Cyclic performance

Several simulations are performed to evaluate the model's performance in simulating soil response under monotonic and cyclic loading. The initial values for the model state variables for the example problems are summarized in Table 6.1, while the model's 16 input parameters are summarized in

Table 6.2. The performance of the model in simulating an undrained monotonic triaxial loading at four different *OCR* values of 1, 2, 4, 8, and two axial loading rates of 1%/*h* and 10%/*h* is shown in Figure 6.4. This figure shows that applying the *SANICLAY* bounding surface allows the model to consider the effect of consolidation history on the undrained monotonic loading. Also, as expected, as the axial loading strain rate increases, so does the monotonic strength. It should be mentioned that for these simulations, the use of an exponential-type overstress function and assigning low values for viscosity parameters (μ_1 and μ_2) have caused the increase of the soil strength with the loading rate to be modest. However, modifications of the overstress function or of the viscous parameters could result in a greater observed effect.

Table 6.1. Initial conditions

Category	Parameter	Value
Initial void ratio	e	0.7
Initial size of the bounding surface (kPa)	p_0	200
Initial orientation of the bounding surface	α	0
Initial value of the static similarity ratio	b_s	1

Table 6.2. Model input parameters

Category	Input Parameter	Value
Elasticity	κ	0.03
	ν	0.2
Critical state	λ	0.15
	M_{c}	1
	M_{e}	1
Bounding surface	N_{c}	1
	N_{e}	1
Plastic modulus	h_{c}	100
	h_{e}	100
	c_d	100
Rotational hardening	C	5
	x	1.7
Hybrid flow rule	ω	5
	m_g	0.3
Viscosity	μ_1	1e-8
	μ_2	50

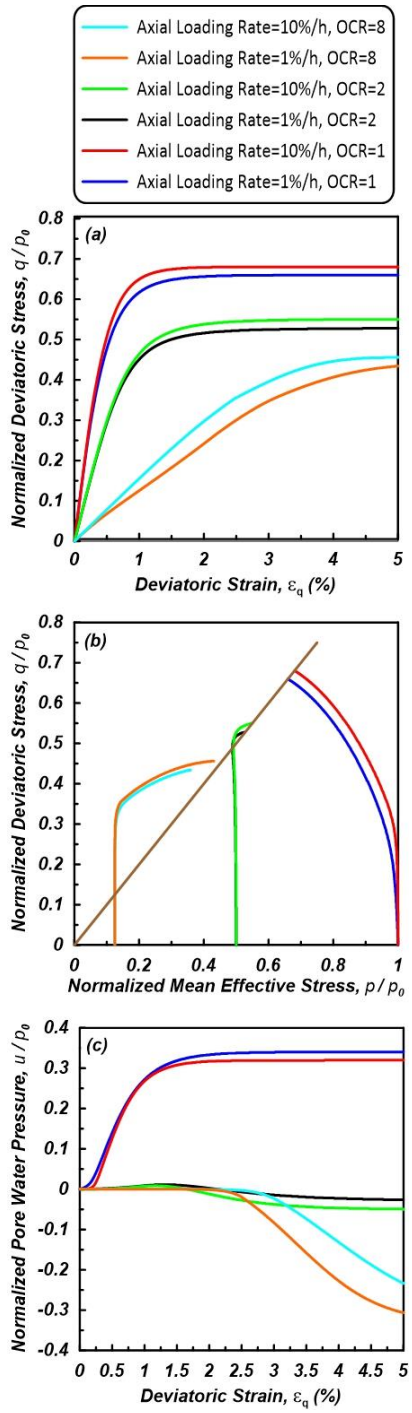

Figure 6.4 Undrained monotonic triaxial compression tests simulated by the *BS-EVP* model at different *OCRs* and loading rates.

Figure 6.5 and Figure 6.6 show the results of simulated undrained cyclic triaxial tests under stress- and strain-controlled conditions, respectively. The simulations are performed at two loading frequencies (i.e., 0.1 and 1 *Hz*). For the stress-controlled loading, a cyclic stress amplitude of $q_{cyc} = 70\ kPa$ is used, while for the strain-controlled tests, the applied cyclic strain amplitude is ε_{cyc}= 0.02. As can be seen in these figures, due to the use of the bounding surface concept with a proper relocation of the projection center, a large elastic response, which is typical of the *MCC*, does not occur in the mean effective stress path, indicating that the plastic response occurs at the very initiation of the cyclic loading.

Also, the use of a hybrid flow rule improves the mean effective stress path response by enabling the simulation of the so-called butterfly or eight-shaped loops. Finally, as the loading frequency increases, the accumulated deviatoric strain and the pore water pressure reduces. Such rate-dependent behavior is consistent with what has been reported in different studies (Li et al., 2011; Ni et al., 2014). In addition, the sharp increase in the excess pore water pressure of previous models (i.e., *SANICLAY-B* and *SANICLAY-H*) is not observed in this model, so that it shows a realistic gradual increase in the pore water pressure. This improvement is due to the adoption of the new input parameter, m_g, to the hybrid flow rule that renders a smooth transition of the initial soil state to the critical state in the course of cyclic loadings.

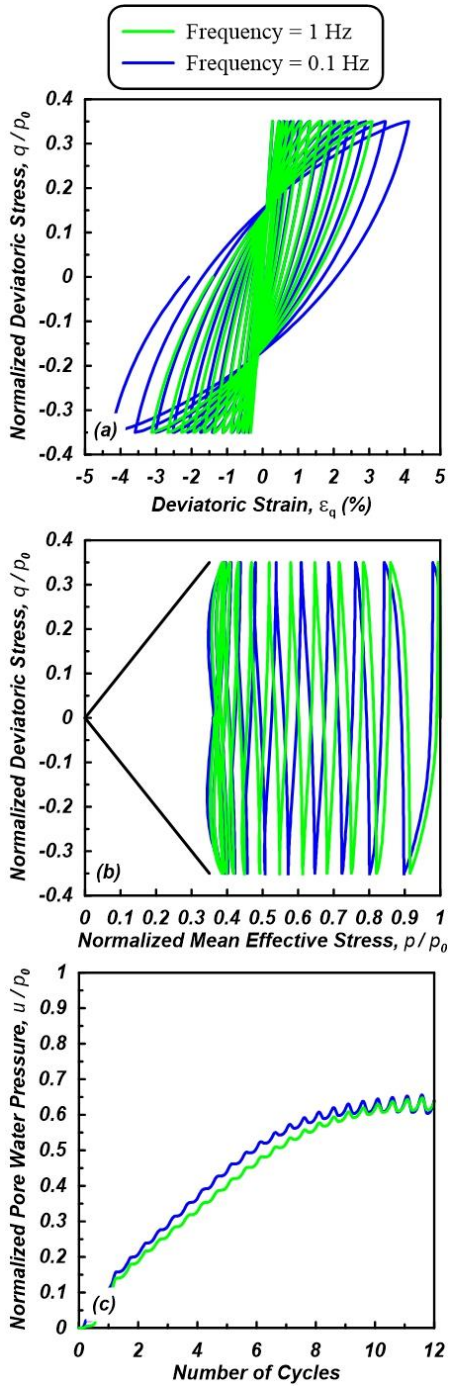

Figure 6.5 Effective stress path and the hysteresis loops of stress-controlled undrained cyclic triaxial tests simulated by the *BSVP* model.

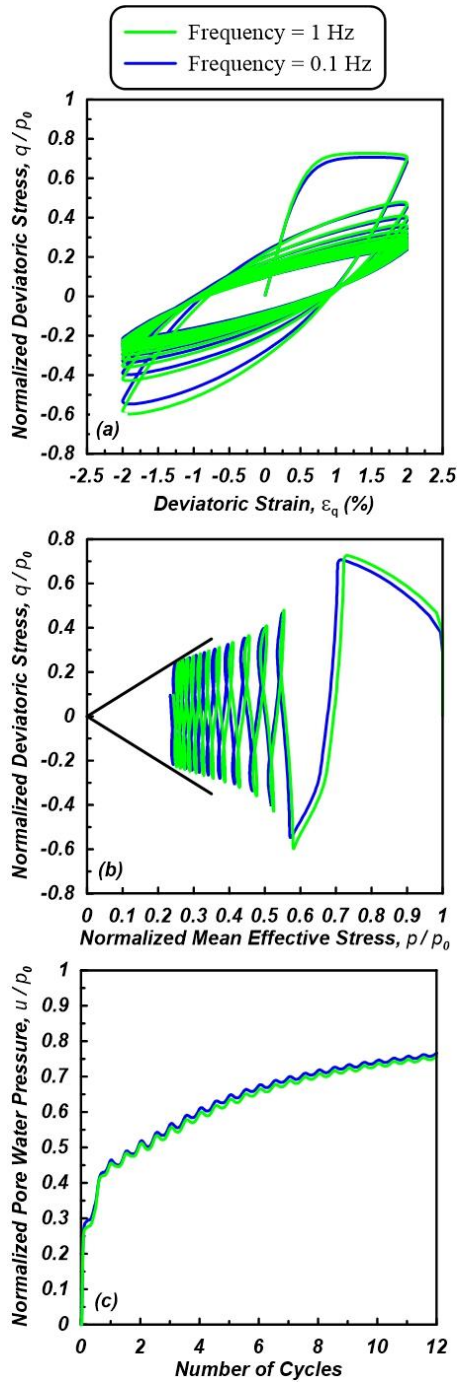

Figure 6.6 Effective stress path and the hysteresis loops of strain-controlled undrained cyclic triaxial tests simulated by the *BSVP* model.

6.3.2 Simulation of the Glacio-Lacustrine Clay Cyclic Behavior

Bonin et al. (2019) conducted a high-quality sampling program followed by comprehensive laboratory investigations on Glacio-Lacustrine varved clay deposits from a gold mine site in Abitibi, in the province of Quebec, to study the response of the clay under various loading conditions and consolidation states. The testing program of the study included one-dimensional compression tests, undrained triaxial compression and extension tests, and monotonic and cyclic direct simple shear tests.

The Atterberg limit tests conducted on varved samples showed that they consisted of clays and silts with different degrees of plasticity, from low to high plasticity clays (*CL*, *CI*, *CH*) to clayey silt and low plasticity silts (*CL-ML* and *ML*). The liquid limit (*LL*), plasticity limit (*PL*), plasticity index (*PI*), and water content (W_n) of the samples were measured to be in the range of (21% to 46)%, (17 to 24)%, (4 to 41)%, and (28 to 68)%, respectively, for the top 2 meters of the soil profile.

The compression tests are shown in Figure 6.7 (a) based on which the initial void ratio and the overconsolidation ratios of the samples were reported to fall in the range of 1.46 to 1.88 and 2.38 and 4.89, respectively, while the index of compression (C_c) and recompression (C_r) fell into the range of 0.026 to 0.08 and 0.83 to 1.77, respectively. According to the undrained triaxial test results, shown in Figure 6.7 (b), the sample's stress path could reach two different failure lines (i.e., two different critical stress ratios could be reached). The authors of the paper stated that this could be associated with the varved nature of the clay samples.

The cyclic loading test program consisted of constant-volume cyclic direct simple shear tests (*CDSS*) and conducted with a loading frequency of 0.1 on normally and moderately overconsolidated samples. In this study, the experimental results of three overconsolidated samples with *OCR* ratios of 3.46, 2.95, and 2.98 are compared with simulations performed with the developed model. The cyclic stress ratios ($CSR = \tau_{cyc}/\sigma'_{vc}$) of these simulated experiments are 0.19, 0.26, and 0.33, respectively, whereas their corresponding confining pressures (σ'_{vc}) reported as 45.6, 56.6, and 53 kPa, respectively.

Model input parameters calibrated for Glacio-Lacustrine clay are summarized in Table 6.3. In calibrating this model, the slope of the critical state lines in compression ($M_c = M_e$) is obtained

from the stress path (based on the two reported failure lines) as 0.62. λ and κ are obtained using the reported values for C_c and C_r, respectively. h_c and h_e are calibrated based on the initial loading cycles and c_d is selected to achieve the closest *CSR-N* fit. The calibrations of other input parameters are done either using the closed-form solutions or the optimization techniques, *PSO/GNO*, discussed in Chapter 4.

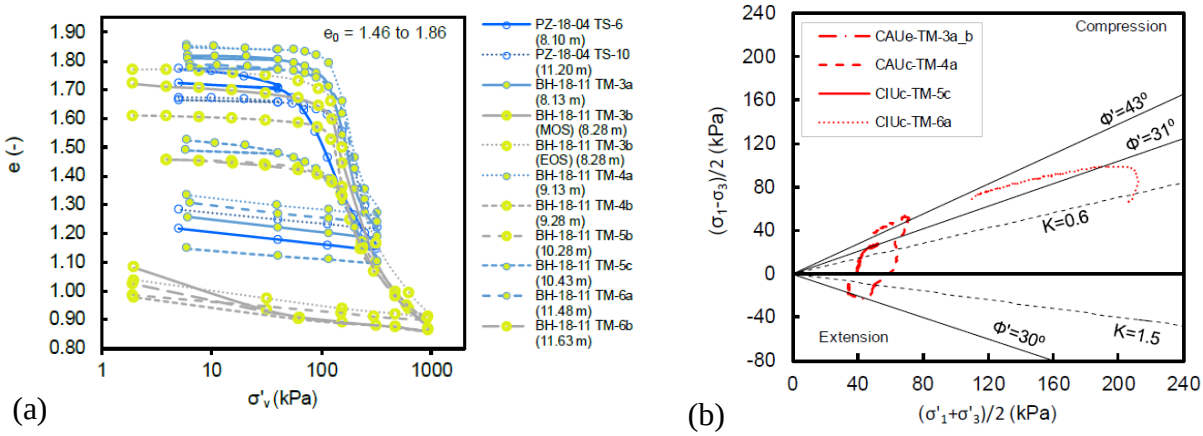

Figure 6.7 (a) One-dimensional compression test results and (b) effective stress path from undrained triaxial tests on Glacio-Lacustrine Clay (Bonin et al., 2019).

Simulation results for two of the tests, with cyclic stress ratios of 0.33 and 0.25, are plotted against the experimental data in Figure 6.8 and Figure 6.9, respectively, whereas the *CSR-N* curves from model simulations and experimental data are compared in Figure 6.10. It can be seen that the model shows a fair performance in capturing the cyclic behavior of the varved clay. Based on the *CSR-N* curves, it could be observed that the curve predicted by the model is closer to that of the varved clay at the medium level *CSRs* (around 0.25). Consequently, the model predictions are closer to the experimental data for the second test (*CSR=0.26*) that has a *CSR* closer to 0.25. However, it should be highlighted that either a constant stress or a constant strain loading is applied in numerical simulations. Therefore, the experimental testing condition of the varved clay in which the applied *CSR* is decreasing with the number of cycles could not be simulated.

Table 6.3 Model input parameters for Glacio-Lacustrine Clay

Category	Input Parameter	Value
Elasticity	κ	0.013
	ν	0.2
Critical state	λ	0.365
	M_c	0.62
	M_e	0.62
Bounding surface	N_c	0.5
	N_e	0.5
Plastic modulus	h_c	500
	h_e	500
	a_d	150
Rotational hardening	C	5
	x	1.7
Hybrid flow rule	ω	10
	m_g	1
Viscosity	μ_1	1e-10
	μ_2	75

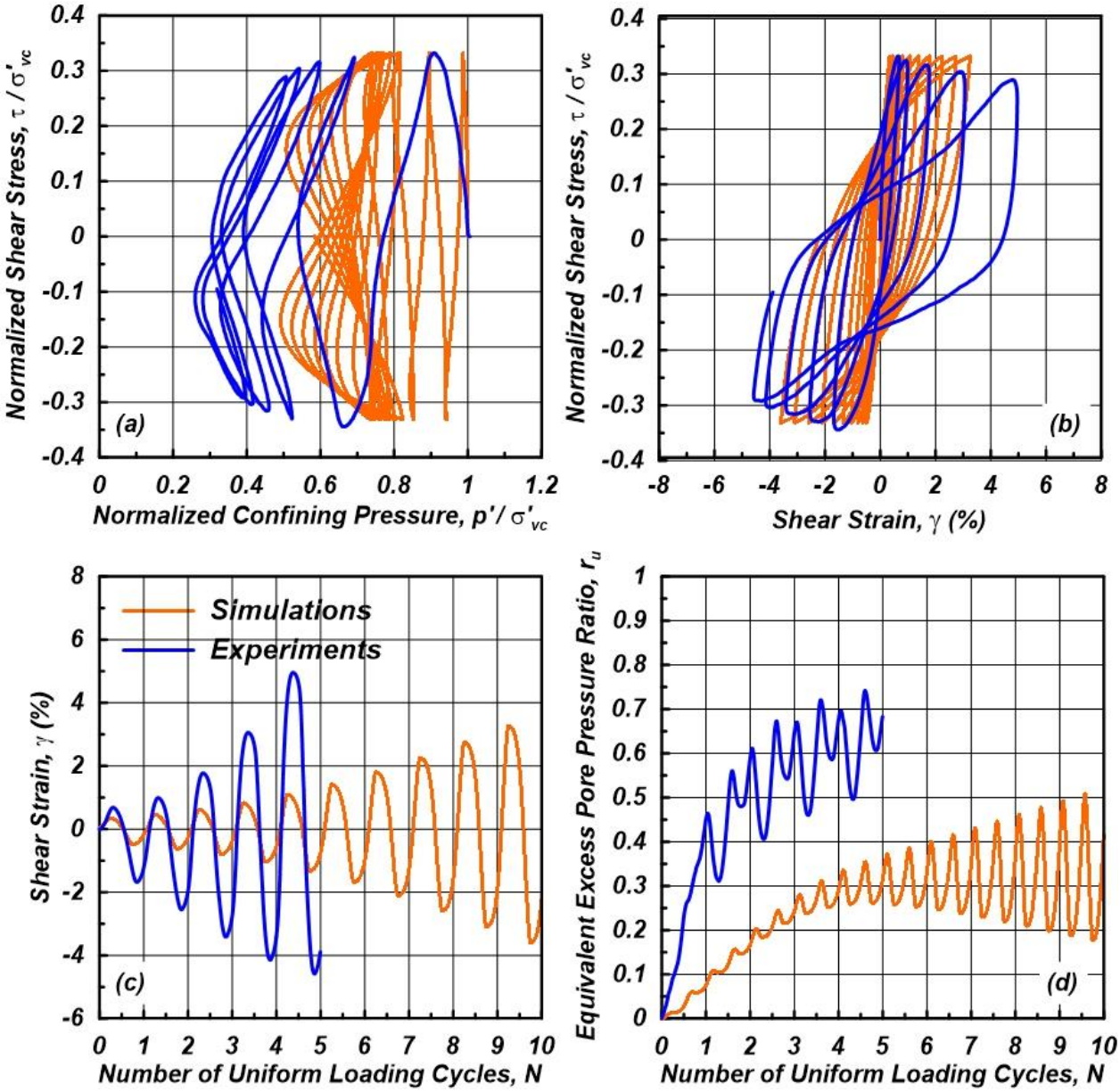

Figure 6.8 Simulation and experimental results of the Glacio-Lacustrine clay, *CSR=0.33*, (experimental data from Bonin et al. (2019)).

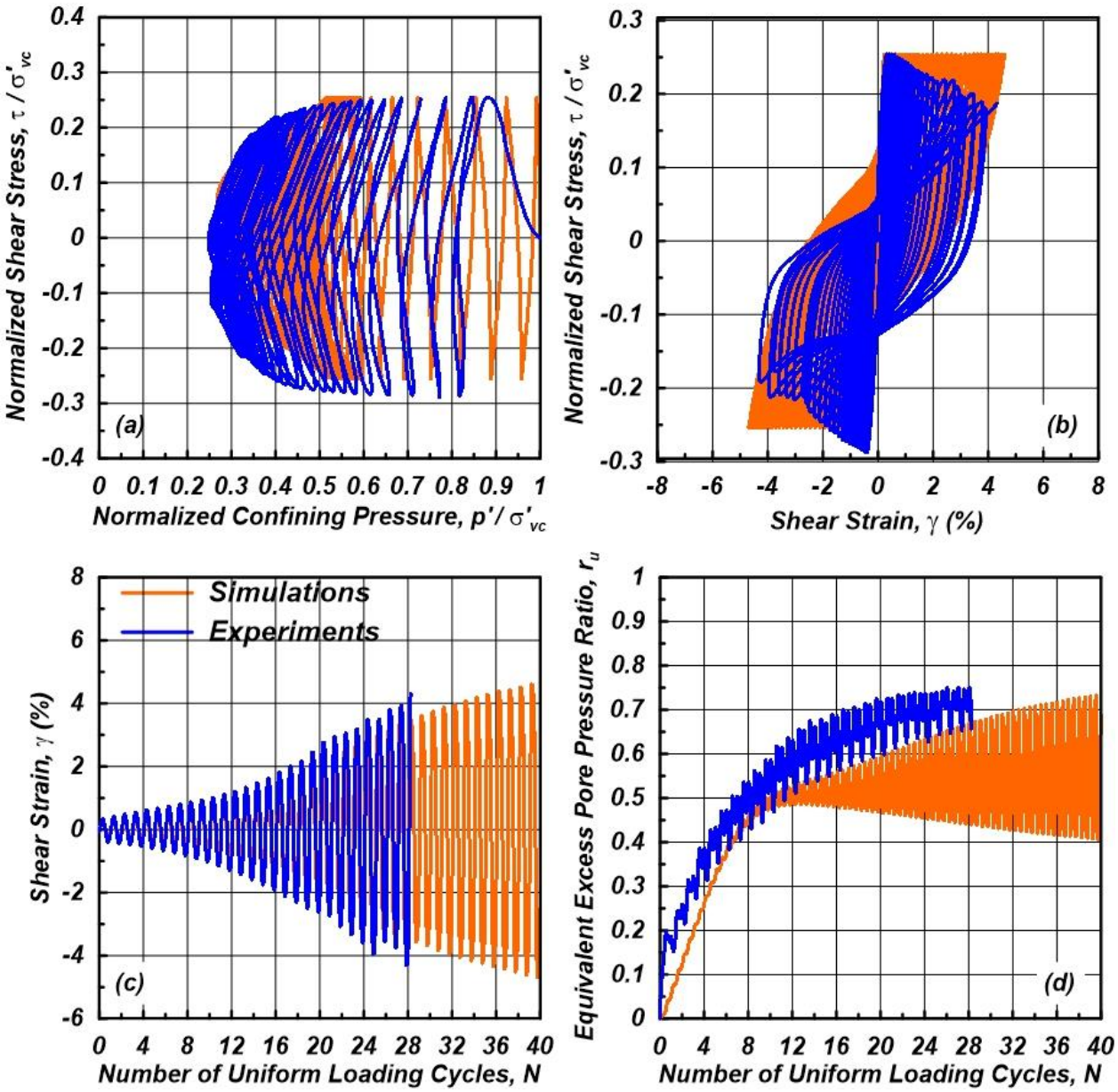

Figure 6.9 Simulation and experimental results of the Glacio-Lacustrine clay, *CSR=0.26*, (experimental data from Bonin et al. (2019)).

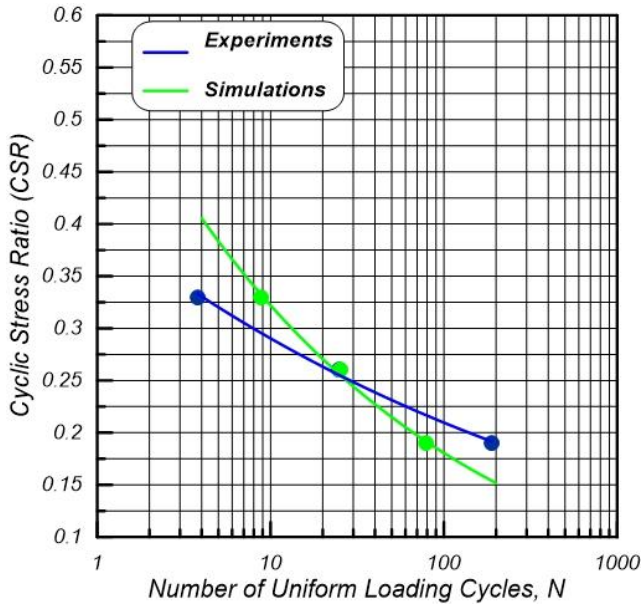

Figure 6.10 *CSR-N* cures from simulations and experiments for the Glacio-Lacustrine clay (experimental data from Bonin et al. (2019)).

6.3.3 Simulation of Rate-Dependent Undrained Shear Behavior of Saturated Boston Blue Clay

In this section, the developed viscoplastic model is used to simulate the laboratory tests, conducted by Sheahan et al. (1996), to simulate the effects of loading rates and consolidation history on the undrained shear strength of a saturated clay. As discussed in the literature review, Sheahan et al. (1996) performed a series of experiments consisting of twenty-five constant strain rate CK_0UC (K_0-consolidated undrained triaxial compression) tests to study the combined effects of soil stress history (*OCR*) and loading rates on the undrained strength of the resedimented Boston Blue Clay. In their study, they conducted the experiments at four different axial strain rates ($\dot{\varepsilon_a} = 0.05, 0.5, 5, and\ 50\ \%/h$) on specimens which were consolidated under four different over consolidation ratios (*OCR*= 1, 2, 4, and 8). The summary of CK_0UC tests on normally and overconsolidated program on *BBC* may be found in Table 6.4 and Table 6.5, respectively.

Table 6.4: Summary of CK_0UC tests on normally consolidated *BBC* (Sheahan et al., 1996)

Test no. (1)	σ'_{vc}, kPa (K_o)[a] (2)	OCR (3)	$\dot{\varepsilon}_a$[b] (%/h) (4)	At Peak Shear Stress: ε_a (%) (5)	q/σ'_{vc} (6)	p'/σ'_{vc} (7)	$\Delta u_s/\sigma'_{vc}$[c] (8)	ϕ' (9)	At Maximum Obliquity: ε_a (%) (10)	q/σ'_{vc} (11)	p'/σ'_{vc} (12)	ϕ' (13)	Comments (14)
CTX-21	284 (0.478)	1.00	0.051	0.22	0.298	0.734	0.018	23.9°	8.70	0.274	0.514	32.1°	Test stopped at ε_a = 8.8%
CTX-23	291 (0.490)	1.00	0.051	0.37	0.300	0.716	0.045	24.8°	9.87	0.277	0.503	33.4°	—
CTX-11	281 (0.472)	1.00	0.50	0.13	0.325	0.757	0.023	25.4°	10.97	0.252	0.450	34.0°	—
CTX-13	276 (0.489)	1.00	0.50	0.18	0.319	0.765	0.003	24.6°	12.18	0.247	0.455	32.9°	—
CTX-33	293 (0.518)	1.00	5.0	0.21	0.342	0.806	−0.012	25.1°	12.76	0.240	0.457	31.6°	Used base Δu measurements
CTX-17	276 (0.491)	1.05	50	0.39	0.379	0.816	−0.049	27.7°	7.84	0.315	0.564	34.0°	—[d]
CTX-18	280 (0.487)	1.05	49	0.41	0.374	0.774	−0.015	28.9°	8.17	0.298	0.547	33.1°	—[d]
CTX-52	292 (0.476)	1.00	49	0.33	0.373	0.806	−0.015	27.5°	7.71	0.295	0.559	31.8°	—

[a]Preshear K_o value.
[b]Axial strain rate based on ε_a-t linear regression.
[c]$\Delta u_s = \Delta u - \Delta\sigma_{oct} = \Delta u - 1/3(\Delta\sigma_v + 2\Delta\sigma_h)$.
[d]Some preshear unloading occurred; σ'_{vm} = 288 kPa and 280 kPa used to normalize CTX-17 and CTX-18 results, respectively.

Table 6.5 Summary of CK_0UC tests on over-consolidated *BBC* (Sheahan et al., 1996)

Test no. (1)	σ'_{vc}, kPa (K_o)[a] (2)	OCR (3)	$\dot{\varepsilon}_a$[b] (%/h) (4)	At Peak Shear Stress: ε_a (%) (5)	q/σ'_{vc} (6)	p'/σ'_{vc} (7)	$\Delta u_a/\sigma'_{vc}$[c] (8)	ϕ' or q/p'[d] (9)	At Maximum Obliquity: ε_a (%) (10)	q/σ'_{vc} (11)	p'/σ'_{vc} (12)	ϕ' or q/p'[d] (13)	Comments (14)
							(*a*) OCR = 2						
CTX-38	298 (0.638)	1.97	0.051	0.78	0.488	1.037	−0.115	28.1°	8.69	0.420	0.788	32.2°	Base Δu used; sh. plane at ε_a = 13%
CTX-40	297 (0.635)	1.98	0.50	0.69	0.518	1.093	−0.164	28.3°	8.52	0.445	0.859	31.2°	Base Δu used; sh. plane at ε_a = 13%
CTX-42	584 (0.641)	1.99	5.0	1.16	0.539	1.116	−0.176	28.9°	NR	NR	NR	NR	Sh. ended at ε_a = 5%
CTX-41	297 (0.632)	1.97	51	0.95	0.585	1.177	−0.229	29.8°	8.83	0.495	0.948	31.5°	—
CTX-60	291 (0.635)	1.98	54	0.99	0.573	1.153	−0.203	29.8°	5.54	0.514	0.987	31.4°	—
							(*b*) OCR = 4						
CTX-26	152 (0.836)	3.70	0.051	6.53	0.801	1.548	−0.389	0.517	5.79	0.796	1.485	0.536	—
CTX-35	148 (0.827)	3.95	0.051	4.68	0.851	1.651	−0.471	0.516	7.73	0.836	1.605	0.521	Sh. plane at ε_a = 13%
CTX-16	148 (1.054)	3.97	0.50	2.96	0.864	1.699	−0.370	0.508	13.30	0.782	1.479	0.529	High K_o = 1.054
CTX-29	146 (0.848)	4.02	0.50	3.17	0.843	1.638	−0.458	0.515	8.97	0.787	1.504	0.523	—
CTX-39	148 (0.845)	3.97	5.1	1.84	0.871	1.673	−0.484	0.521	0.70	0.762	1.444	0.528	—
CTX-49	147 (0.849)	4.00	5.0	3.01	0.893	1.717	−0.518	0.520	7.00	0.848	1.621	0.523	Sh. plane at ε_a = 14.8%
CTX-27	148 (0.804)	3.97	52	3.78	0.939	1.761	−0.576	0.533	0.75	0.768	1.416	0.542	—
							(*c*) OCR = 8						
CTX-44	75 (1.125)	7.89	0.051	5.94	1.419	2.675	−1.110	0.530	1.52	1.196	2.213	0.541	Sh. plane at ε_a = 7.5%
CTX-47	75 (1.120)	7.92	0.51	4.23	1.425	2.603	−1.035	0.548	1.39	1.223	2.188	0.559	—
CTX-46	74 (1.091)	7.93	5.1	6.45	1.418	2.584	−1.055	0.549	1.52	1.189	2.094	0.568	—
CTX-43	76 (1.092)	7.80	51	4.75	1.563	2.980	−1.382	0.524	1.51	1.363	2.395	0.569	Sh. plane at ε_a = 14%
CTX-45	75 (1.104)	7.82	50	4.51	1.537	2.848	−1.259	0.540	1.52	1.273	2.175	0.585	—

Note: NR = Not reached.
[a]Preshear K_o value.
[b]Axial strain rate based on ε_a-t linear regression.
[c]$\Delta u_a = \Delta u - \Delta\sigma_{oct} = \Delta u - 1/3(\Delta\sigma_v + 2\Delta\sigma_h)$.
[d]For OCR = 2, ϕ' based on $c' = 0$ is given; for OCR = 4 and 8, the ratio q/p' is given.

The results of this study show that all specimens, including normally consolidated and overconsolidated, have experienced an average increase in the normalized undrained strength when subjected to fast axial strain rate (i.e., $\dot{\varepsilon_a}$=50%/*h*). For other axial loading rates, the specimens were shown to be either rate-independent or slightly to moderately rate dependent, depending on the level of consolidation history.

To evaluate the performance of the developed viscoplastic model on capturing the loading rate effects, the model is used to simulate the experiments conducted by Sheahan et al. (1996). Table 6.6 summarizes the input parameters for the simulations. To calibrate the input parameters, the critical stress ratio in compression, M_c, and tension, M_e are set to the maximum ratio of deviatoric stress over the mean effective stress (i.e., *q/p*) that are provided in Table 6.5 and Table 6.6. Due to the lack of experiments to track the shape of the bounding surface, N_c and N_e are set initially to M_c

and M_e respectively, then altered slightly to obtain the best match. Three input parameters κ, ν, and λ, which are among the common geotechnical soil properties, are adopted from the experimental data for Boston Blue Clay reported by Papadimitriou et al. (2005).

Table 6.6 Model input parameters for *BBC*

Category	Input Parameter	Value
Elasticity	κ	0.03
	ν	0.2
Critical state	λ	0.15
	M_c	0.52
	M_e	0.52
Bounding surface	N_c	0.4
	N_e	0.4
Plastic modulus	h_c	varies
	h_e	varies
	a_d	50
Rotational hardening	C	20
	x	1.7
Hybrid flow rule	ω	0
	m_g	1
Viscosity	μ_1	1e-10
	μ_2	varies

Three input parameters h_c, h_e, and μ_2 have been selected according to the soil consolidation history (*OCR*); For clays with *OCRs* of 1, 2, 4, and 8, values of 50, 25, 12.5, and 7 has been selected for h_c ($h_e = h_c$). Similarly, for viscous parameter μ_2, values of 25, 50, 75, and 100 have been obtained for the *OCR* values of 1, 2, 4, and 8, respectively. Finally, the input parameters that could not be calibrated because of the lack of lab/field test or geotechnical relations were set to default values reported in other studies (e.g., Shi (2018), Shi et al. (2019), and Seidalinov and Taiebat (2014)),

such as x, or found using optimization algorithms (*PSO* or *GNO)* such as a_d and C.

Figure 6.11 compares the performance of the model in simulating the undrained shear strength versus the axial strains with that of the experiments. Also, the model's simulations and experimental data of the *BBC* are compared in terms of the stress path at four different stain rates and various states of consolidation history and presented in Figure 6.12. In these simulations, the vertical consolidation stress, σ_{vc}, is 280, 300, 150, and 75 for specimens with *OCR* values of 1, 2, 4, and 8, respectively. It should be mentioned that the accuracy of the calibration is dependent on whether the peak or the residual strength is targeted; As Sheahan et al. (1996) compared the test results using the peak shear strength, this strength was the calibrations' target in the current study.

In general, the model could capture fairly the final shear strength of the *BBC* at different loading rates, but the shape of the stress-strain curves and stress path could not be perfectly simulated. Especially, the post weak softening response, which is observed in specimens with *OCR>1* could not be captured. This shortcoming is due to the fact that the frictional destructuration, introduced by Taiebat et al. (2010), is not applied to the model for simplicity purposes.

The model's performance with experimental data in terms of the normalized pore water pressure versus the axial strain is plotted in Figure 6.13. Compared to previous quantities, it appears that the performance of the model in capturing the pore water pressure build-up is less satisfactory, at various loading rates and *OCR* values, in a way that the cap values of the normalized pore water pressure simulated by the model are different than that measured in the experiments.

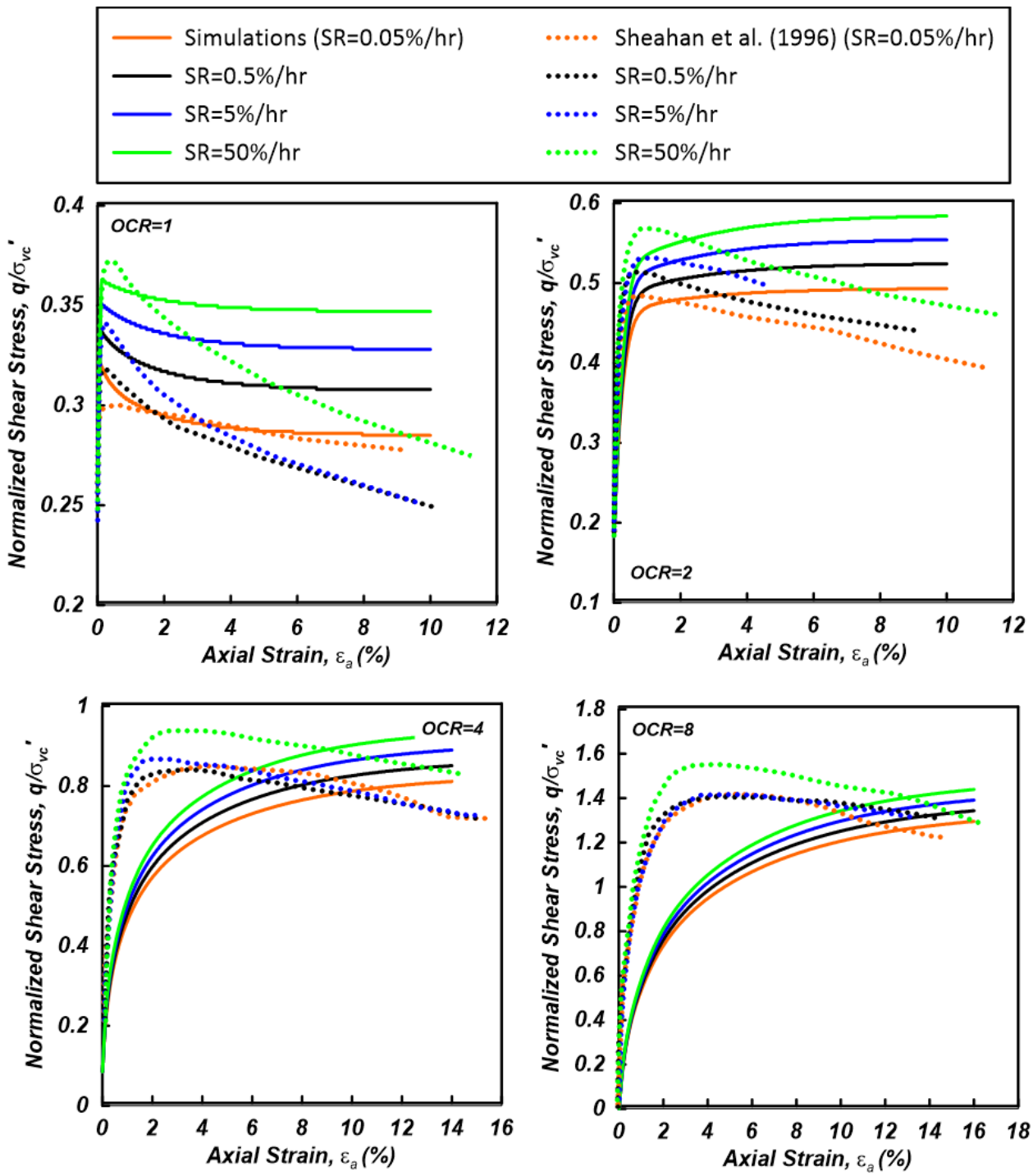

Figure 6.11 Simulations and experimental results in terms of normalized shear stress versus Axial strain for CK_0UC tests on resedimented *BBC*.

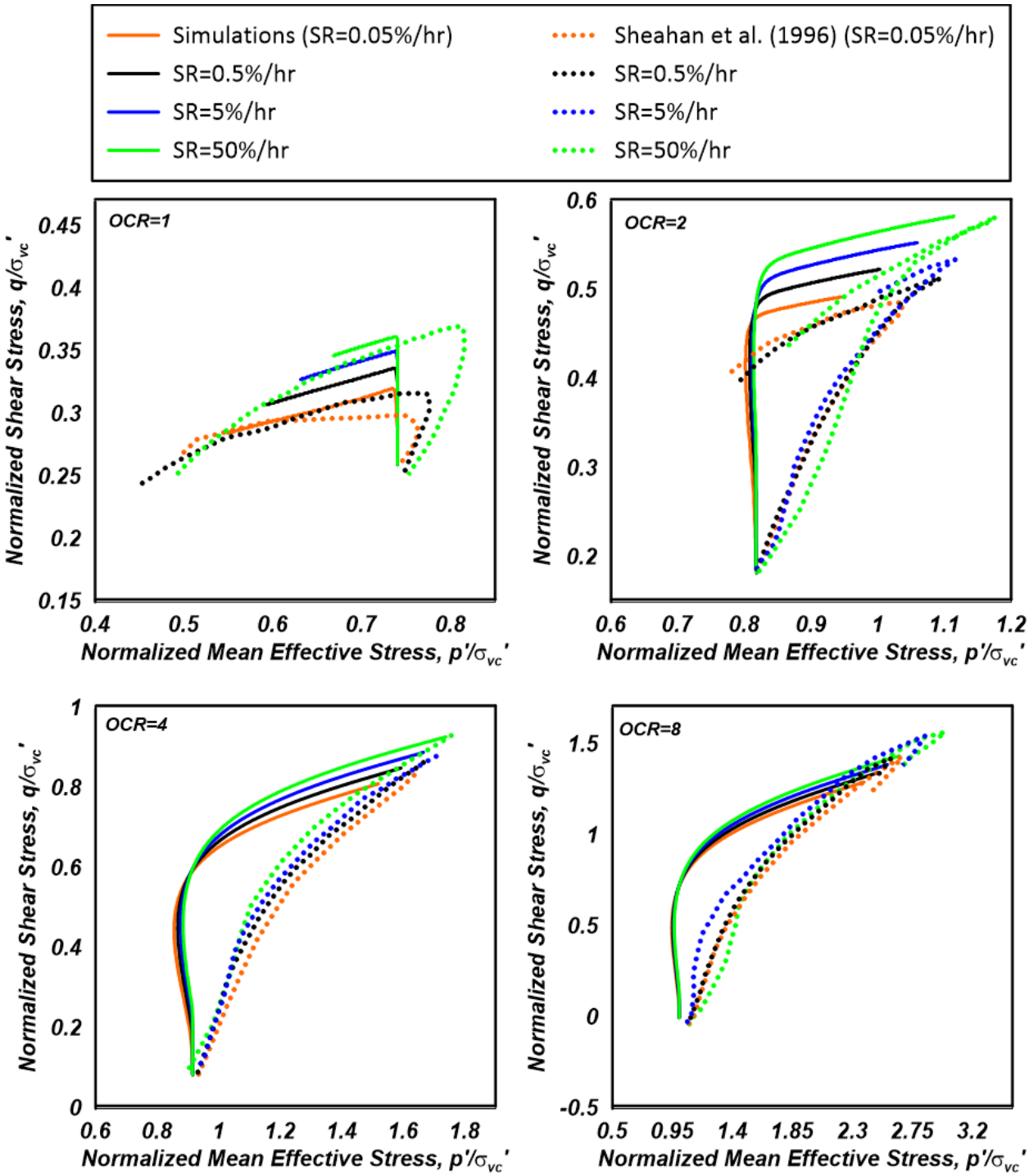

Figure 6.12 Simulation and experimental results in terms of normalized effective stress paths of CK_0UC tests on resedimented *BBC*.

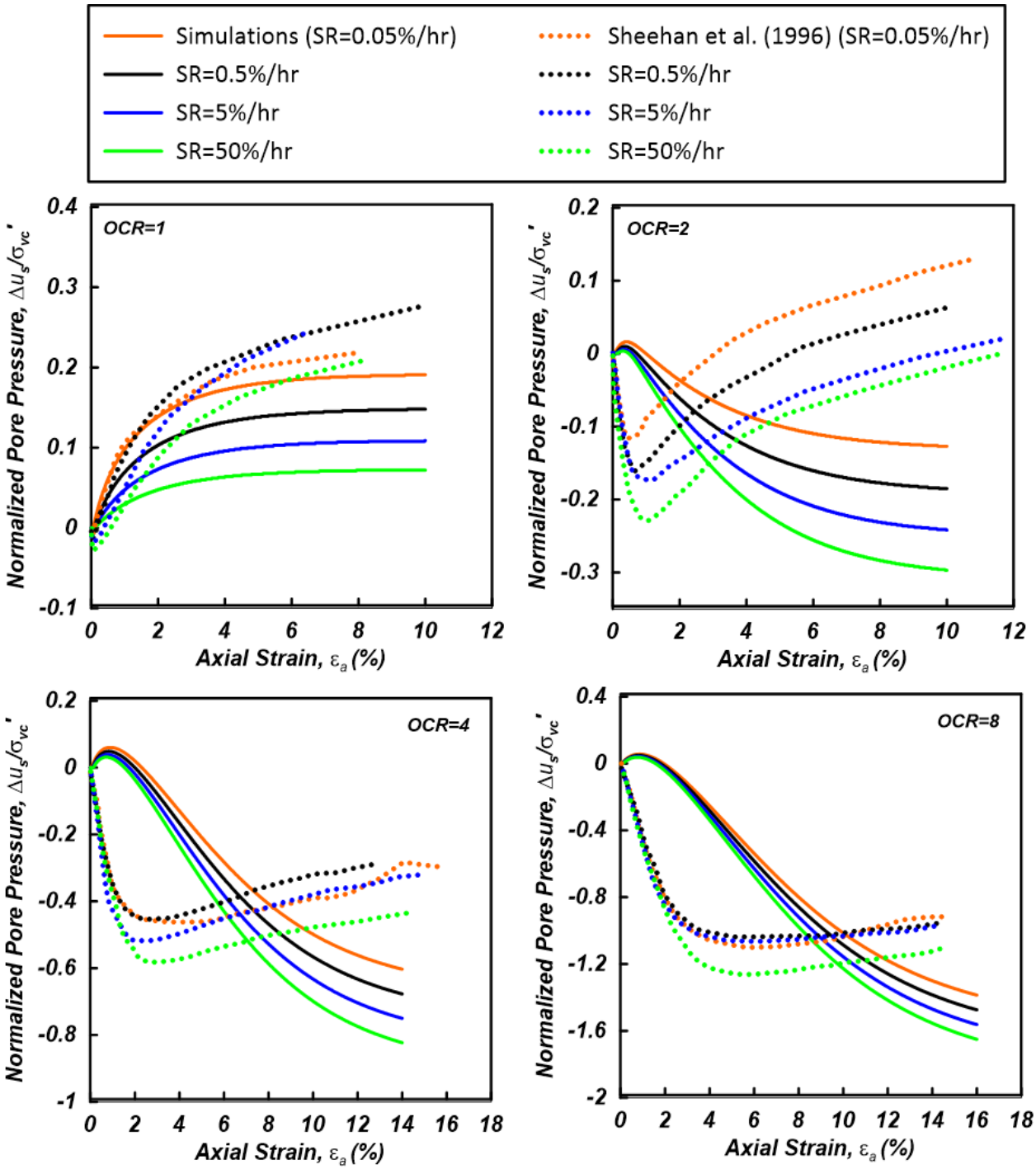

Figure 6.13 Simulation and experimental results in terms of normalized pore water pressure versus axial strain for CK_0UC tests on resedimented *BBC*.

A comparison between the model simulations and experimental results on the normalized undrained shear strength, $\frac{S_u}{\sigma_v}$, versus the strain rates are provided in Figure 6.14. It should be highlighted that the normalized stress used in Figure 6.14 is different than σ_{vc} used in Figure 6.11 to Figure 6.13. In Figure 6.14, the stress used to normalize the results is the maximum vertical stress, σ_v, which is 290 for normally consolidated and 585 for overconsolidated specimens. The curves' trend shows that the model can properly capture the loading rate effects at various *OCR* levels. However, the experiments show a very sharp increase at high strain rates (i.e., 50%/*hr*), especially for the normally consolidated soil specimens, that the model could not capture. Such a trend indicates that the undrained shear strength of the soil may be underestimated by the model at high strain rates for normally consolidated soils (i.e., greater than 100 %/hr).

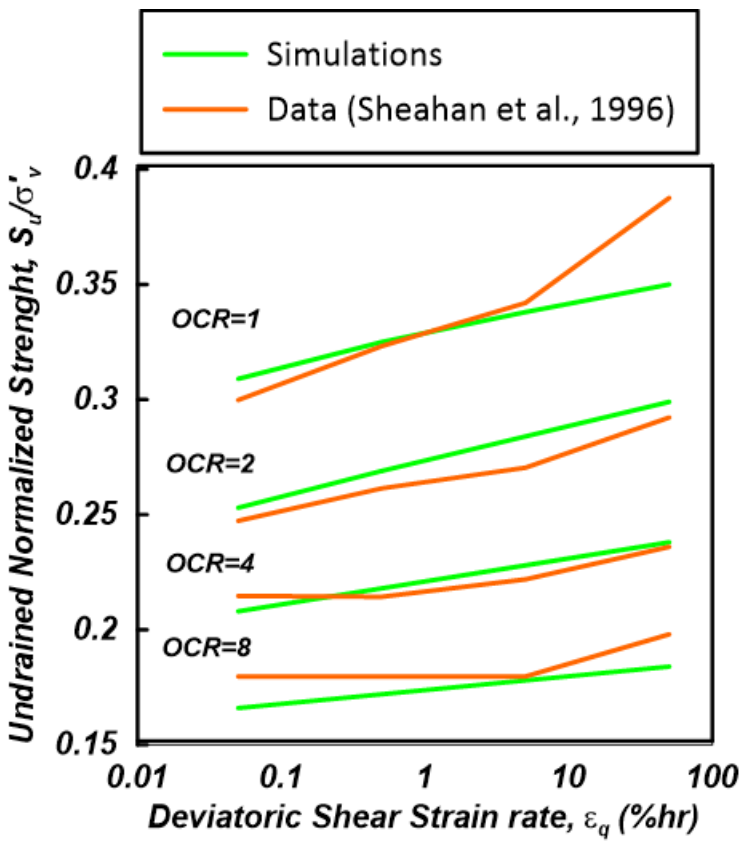

Figure 6.14 Normalized shear strength versus the deviatoric shear strain at different strain rates for CK_0UC tests on resedimented *BBC*

6.3.4 Simulation of Rate Effects on Undrained Shear Strength of Sensitive Grande-Baleine Clay (Lefebvre and LeBoeuf, 1987)

Lefebvre and LeBoeuf (1987) performed a series of monotonic tests to investigate the effect of strain rate on the undrained shear strength of sensitive clays found in Eastern Canada. This study's undisturbed soil samples were collected from four sites in Northwestern Quebec and were composed of soft and sensitive clays, including the highly sensitive (sensitivity greater than 300), Grande-Baleine clay with a marine origin.

Some part of the experimental program in this study was composed of undrained strain-controlled monotonic triaxial compression tests at strain rates ranging from 0.05 to 132.0 %/*hr*. To consider the influence of the consolidation state on the studied clays, the tests were conducted at consolidation stresses lower than the in-situ pre-consolidation stress, $\sigma'_p = 112\ kPa$, as well as at those higher than σ'_p. The clay samples corresponding to these pre-consolidation pressures were referred to as structured (overconsolidated) and destructured (normally consolidated), respectively. The vertical consolidation pressure, σ'_{vc}, applied to Grande-Baleine clay was set to be equal to the in-situ vertical effective stress, σ'_{vo}, for structured samples, and to $2 \cdot \sigma'_p$ for the destructured samples.

The developed visco-plastic model was first calibrated using the procedure previously discussed (refer to Table 6.7 for the summary of input parameters), and then used to simulate the undrained monotonic triaxial tests on structured, $\sigma'_{vc} = \sigma'_{vo} = 45\ kPa$, and destructured, $\sigma'_{vc} = 2 \cdot \sigma'_p = 224\ kPa$, samples at five different strain rates of 1, 3.6, 12.7, 42.2, and 132 *%/hr*. The comparison between simulations and experimental results of Lefebvre and LeBoeuf (1987) for structured and destructured samples are shown in Figure 6.15.

The simulated stress-deformation curves of the destructured samples show that the developed model could fairly capture the increase of the undrained strength with the increase of the loading strain rates. For structured samples, the increasing trend of the residual undrained strength with the loading rates could be captured, but as discussed before, the post-peak softening observed in experiments could not be simulated. In terms of the stress path, the model could fairly predict the

final values of the undrained strength, especially for destructured samples, but it could not simulate the initial dilative response observed in experiments, especially at higher loading rates.

To better evaluate the predictive ability of the model in capturing loading rate effects on undrained strength of Grande-Baleine clay, the peak values of the undrained strength, $c_u = \frac{q}{2} = \frac{\sigma_1 - \sigma_3}{2}$, obtained from simulations are compared with the results of the experiment presented by Lefebvre and LeBoeuf (1987) and plotted in Figure 6.16. In this figure, c_u is normalized by $\sigma'_{vc} = 224\ kPa$ for destructurated specimens and by $\sigma'_p = 112\ kPa$ for structured samples. Model simulations show that the loading rate effects simulated by the model are very close to the experiments for destructured samples. For structured samples, however, the model is not as precise as the destructured samples. The difference between simulations and experiments is mainly due to the model's inability to capture the peak and post-peak softening behavior.

Table 6.7 Model input parameters for Grande-Baleine clay

Category	Input Parameter	Value
Elasticity	κ	0.02
	ν	0.2
Critical state	λ	0.34
	M_c	0.54
	M_e	0.54
Bounding surface	N_c	0.52
	N_e	0.52
Plastic modulus	h_c	100
	h_e	100
	a_d	150
Rotational hardening	C	5
	x	1.7
Hybrid flow rule	ω	0
	m_g	1
Viscosity	μ_1	1e-10
	μ_2	17

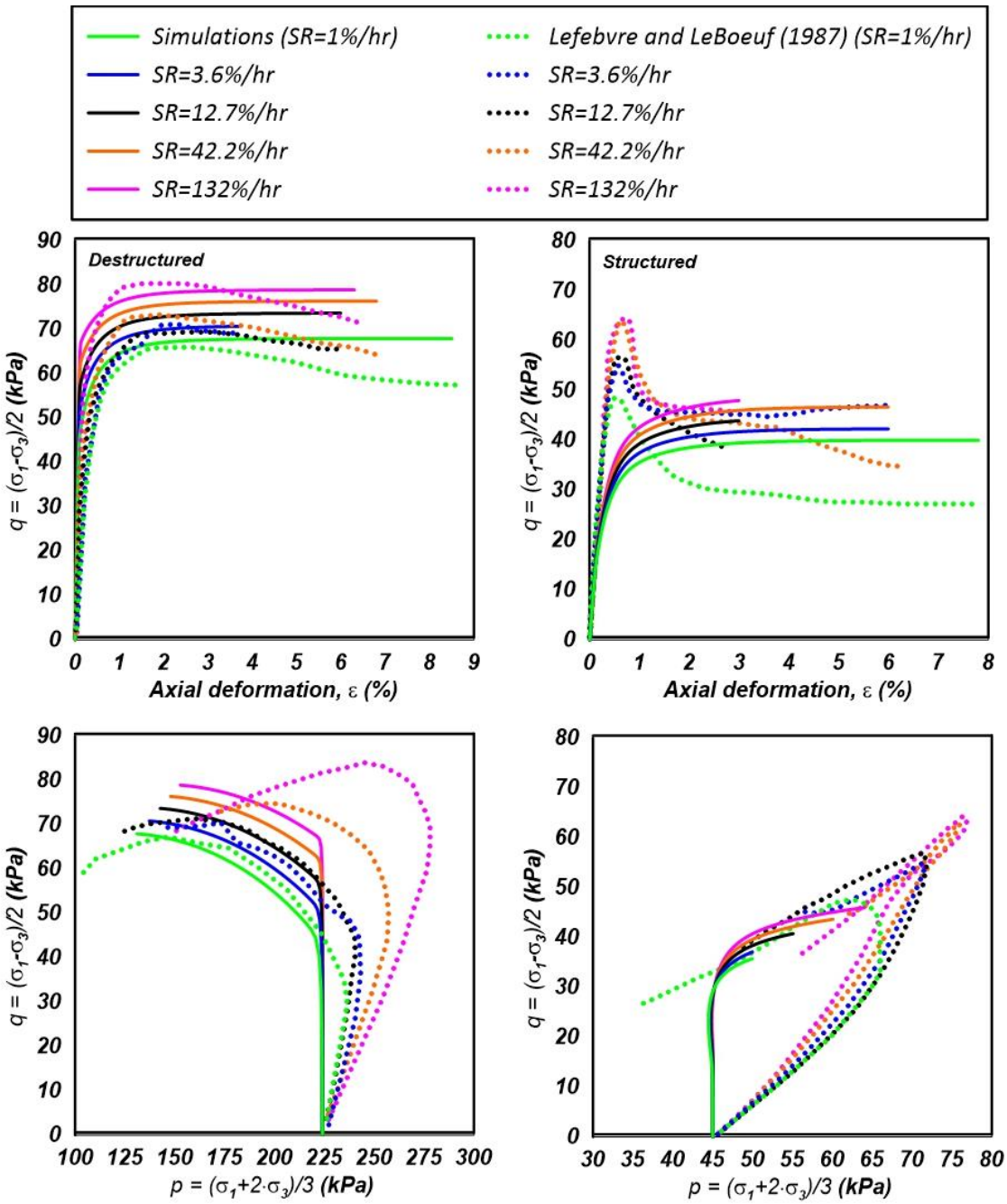

Figure 6.15 Stress-deformation curves and Stress path of the Grande-Baleine clay (simulations versus experiments)

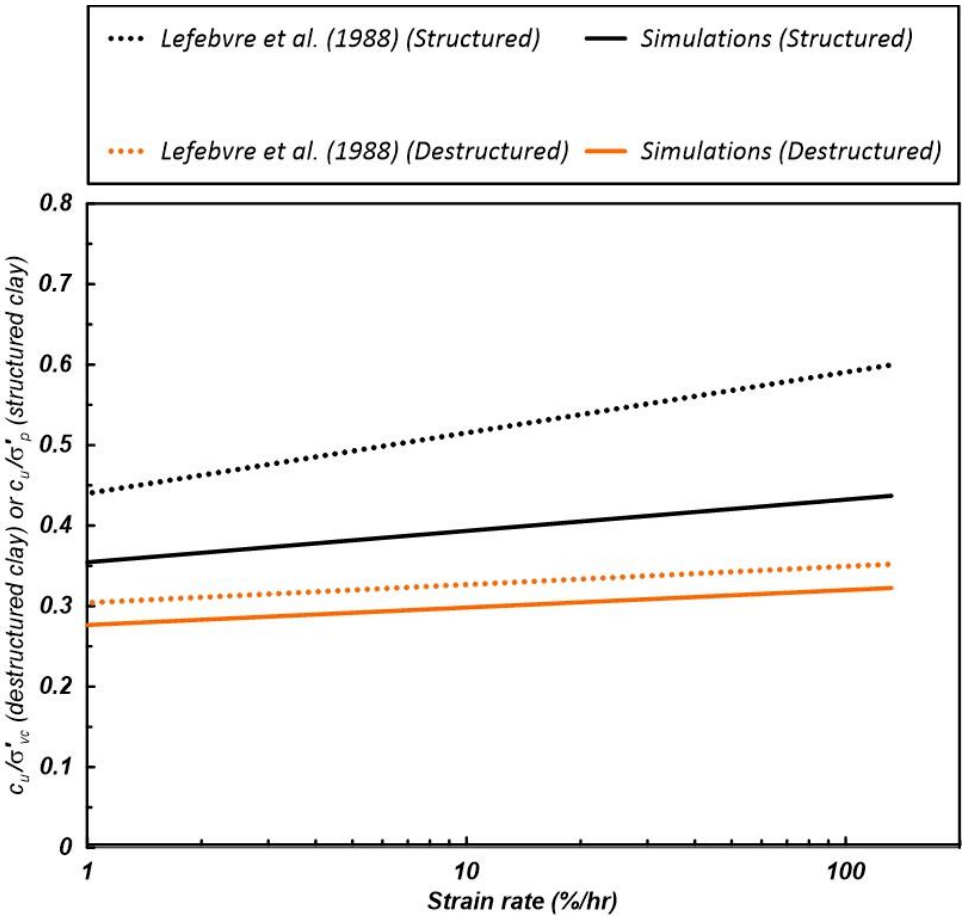

Figure 6.16 Simulation of strain rate effects on destructured and structured specimens of the Grande-Baleine

6.3.5 Simulation of Rate Effects on Damping and Modulus Reduction of Normally Consolidated Kaolin Clay (Shibuya et al., 1995)

Shibuya et al. (1995) performed a series of undrained strain-controlled cyclic torsion shear tests at different loading frequencies to study the effect of loading frequency on the hysteretic damping and modulus reduction curves. The Kaolin clay samples used in the experiment had an initial void ratio in the range of 1.320 to 1.336, and a plasticity index, PI, plasticity limit, PL, and liquid limit, LL, of 27, 29, and 56, respectively.

In experiments, the Kaolin clay samples were isotopically consolidated to an effective consolidation pressure, p'_c, of 200 kPa. Then, multistep strain-controlled cyclic loadings were applied to the specimens in a way that the single amplitude shear strain, γ_{SA}, was fixed during the whole stage and increased in a stepwise manner in the following steps. Figure 6.17 shows the cyclic loadings at two different shear strain amplitudes. The cyclic shear tests on the Kaolin clay were performed at shear strain amplitudes of 10^{-6} to 10^{-3} and loading frequencies of 0.005-0.1 Hz.

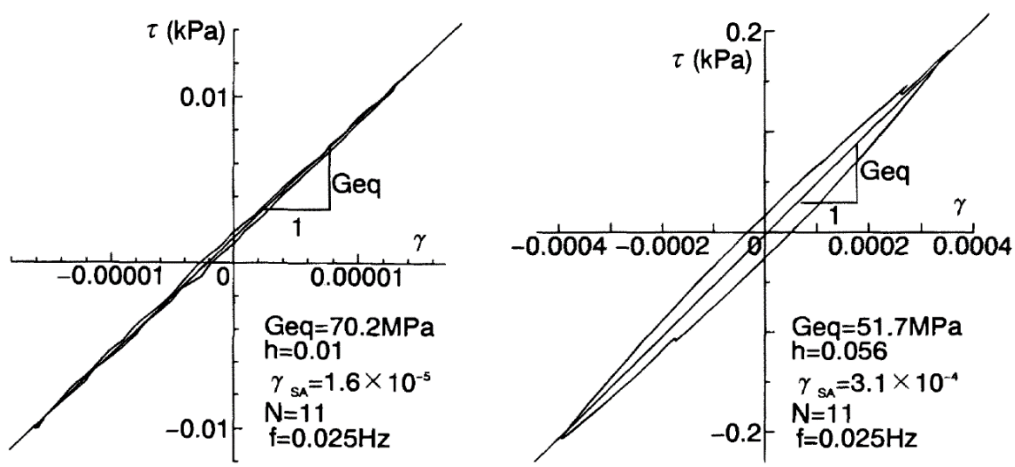

Figure 6.17 Hysteresis loops of strain-controlled cyclic loading tests at two different amplitudes (Shibuya et al., 1995)

The result of this cyclic loading program of Shibuya et al. (1995) on the Kaolin clay is shown in Figure 6.18 (a) as hysteretic damping, h, and modulus reduction curves. Each point corresponds to a cyclic test at a specific shear strain level and loading frequency in this figure. According to this figure, the equivalent shear modulus, G_{eq}, is hardly affected by the loading frequency, and the

modulus reduction exhibit a unique trend regardless of the applied frequency. However, the loading frequency influences the hysteretic damping so that the increase of loading frequency decreases the hysteretic damping.

To validate the model against the effect of loading frequency on the shear modulus reduction and hysteretic damping curves, several undrained cyclic strain-controlled tests at various shear strain amplitudes and loading frequencies were simulated (input parameters for these simulations are presented in Table 6.8). The modulus reduction and hysteretic damping calculated from the simulations are plotted in Figure 6.18 (b). In this plot, the black curves represent general trends of the modulus reduction and damping curves presented by Shibuya et al. (1995).

It should be noted that in all simulations, the developed damping or the shear modulus reduction is negligible at shear strain amplitudes lower than 0.015% regardless of the loading frequency. Therefore, the model could not be used to compare hysteretic damping or shear modulus curves with those of experiments at shear strain lower than 0.015%. However, it should be highlighted that, in numerical software such as FLAC, these small strains could be simulated by introducing viscous damping. For shear strain amplitudes greater than 0.015%, the model could capture the modulus reduction and damping curves' general trend relatively well. In addition, as the loading frequency increases, the hysteretic damping decreases, which is in good agreement with Shibuya et al. (1995) observations. However, the effect of loading frequency on the modulus reduction curves indicates that the modulus reduction curves increase with the increase of the loading frequency. Although this effect was not observed by Shibuya et al. (1995), it was reported by Lo Presti et al. (1996), Lo Presti et al. (1997), and Isenhower and Stokoe (1981) as discussed in the literature review.

Table 6.8 Model input parameters for normally consolidated Kaoling clay

Category	Input Parameter	Value
Elasticity	κ	0.015
	ν	0.2
Critical state	λ	0.34
	M_c	0.62
	M_e	0.62
Bounding surface	N_c	0.5
	N_e	0.5
Plastic modulus	h_c	500
	h_e	500
	a_d	150
Rotational hardening	C	5
	x	1.7
Hybrid flow rule	ω	10
	m_g	1
Viscosity	μ_1	1e-10
	μ_2	75

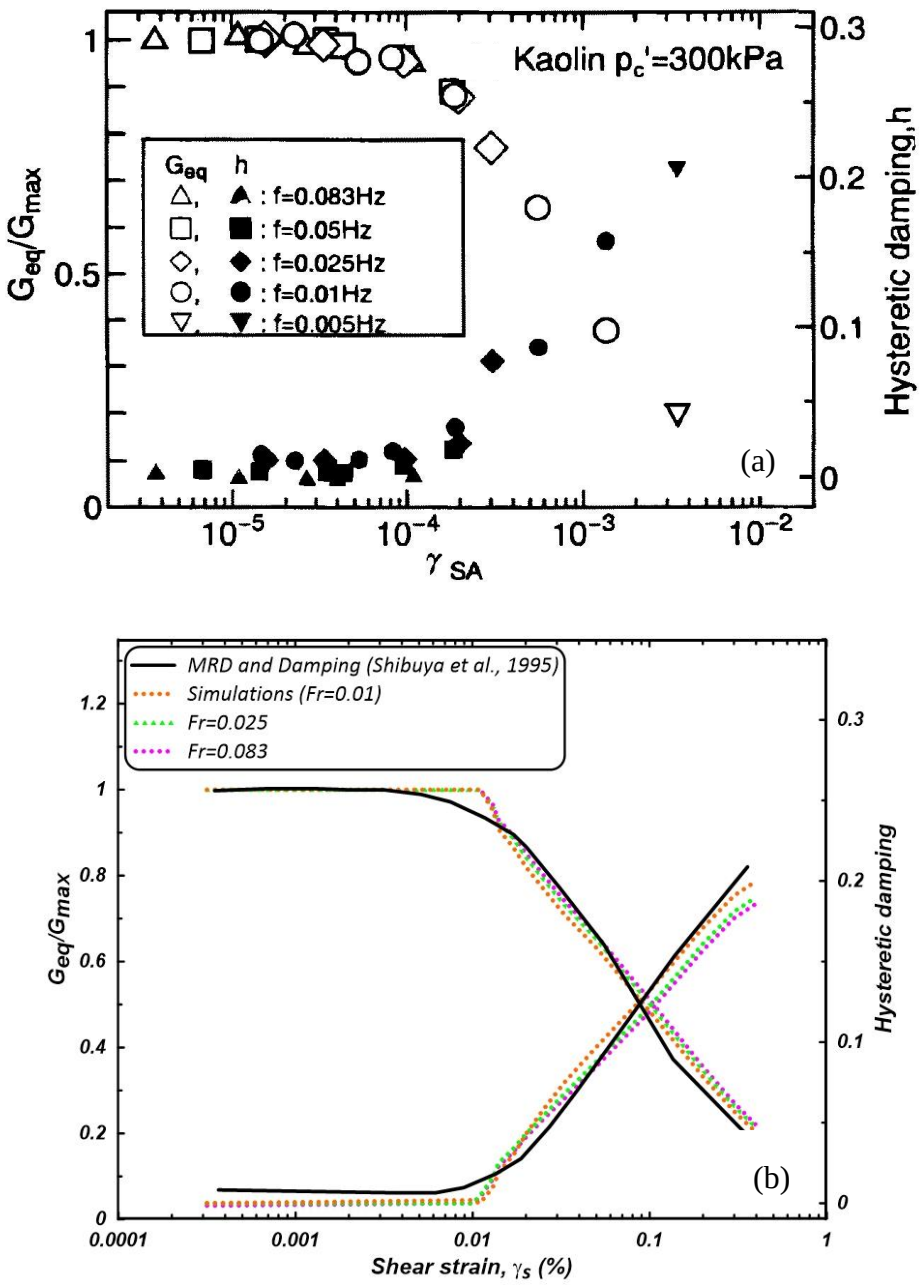

Figure 6.18 Shear modulus and hysteretic damping curves the Kaolin clay: (a) experiments Shibuya et al. (1995) (b) simulations

6.3.6 Simulation of Cyclic Behavior of Sensitive Saint-Adelphe Clay at Different Loading Frequencies (Abdellaziz et al., 2017)

Abdellaziz et al. (2017) conducted a set of undrained cyclic tests to study the effect of loading frequency on the cyclic behavior of Saint-Adelphe clay, a typical post-glacial sensitive marine clay found in eastern Canada. According to the geotechnical investigation of Lefebvre et al (1992), the Saint-Adelphe clay is of high sensitivity, S_t measured to be greater than 20 and up to 533, with the liquidity limit, plasticity limit, and plasticity index ranging from 20-22%, 30-47%, and 10-25%, respectively. The undrained shear strength, S_u, measured using the vane shear tests, and the pre-consolidation pressure, σ'_p, obtained by the oedometer tests, were to be in the range of 20-44 *kPa*, and 86-200 *kPa*, respectively. In addition, as reported by L'Ecuyer (1998), the ratio of undrained shear strength over the pre-consolidation pressure, $\frac{S_u}{\sigma'_p}$, falls to a constant value of 0.23.

A series of cyclic undrained tests performed by Abdellaziz et al. (2017) using the TxSS apparatus, developed by Chekired et al. (2015) at Sherbrooke University in collaboration with Hydro-Quebec. Abdellaziz et al. (2017) used the TxSS apparatus to conduct undrained strain-controlled cyclic tests at three various loading frequencies of 0.1, 1, and 5 *Hz*. In these tests, specimens were isotopically consolidated up to a consolidation pressure of $\sigma_3 = 75$ to slightly overconsolidated the soil (*OCR*=1.2). Then, undrained strain-controlled loading cycles with a shear strain amplitude of 1.5% were applied to the specimens.

To validate the performance of the developed viscoplastic model, it was first calibrated (model parameters are summarized in Table 6.9), then the simulations with loading conditions similar to the experiments of Abdellaziz et al. (2017) were performed. The results of these simulations compared to those of experiments are plotted in Figure 6.19 in terms of number of cycles, *N*, versus normalized pore water pressure and the peak $\frac{\tau_{cyc}}{S_u}$ ratio. In terms of the peak $(\frac{\tau_{cyc}}{S_u})$ versus *N*, the model could capture the decrease of the undrained shear strength with the loading cycles well, especially for higher loading frequencies, i.e., 1 and 5 *Hz*. However, regarding the pore water pressure response with the number of cycles, the model's performance is less satisfactory. The

model's performance is more pronounced for higher loading frequency, but it cannot accurately capture the excess pore water generation's general trend at lower frequencies.

Table 6.9 Model input parameters for Saint-Adelphe clay

Category	Input Parameter	Value
Elasticity	κ	0.013
	ν	0.2
Critical state	λ	0.365
	M_c	0.7
	M_e	0.7
Bounding surface	N_c	0.7
	N_e	0.7
Plastic modulus	h_c	100
	h_e	100
	a_d	0.5
Rotational hardening	C	5
	x	1.7
Hybrid flow rule	ω	3
	m_g	1
Viscosity	μ_1	1e-10
	μ_2	20

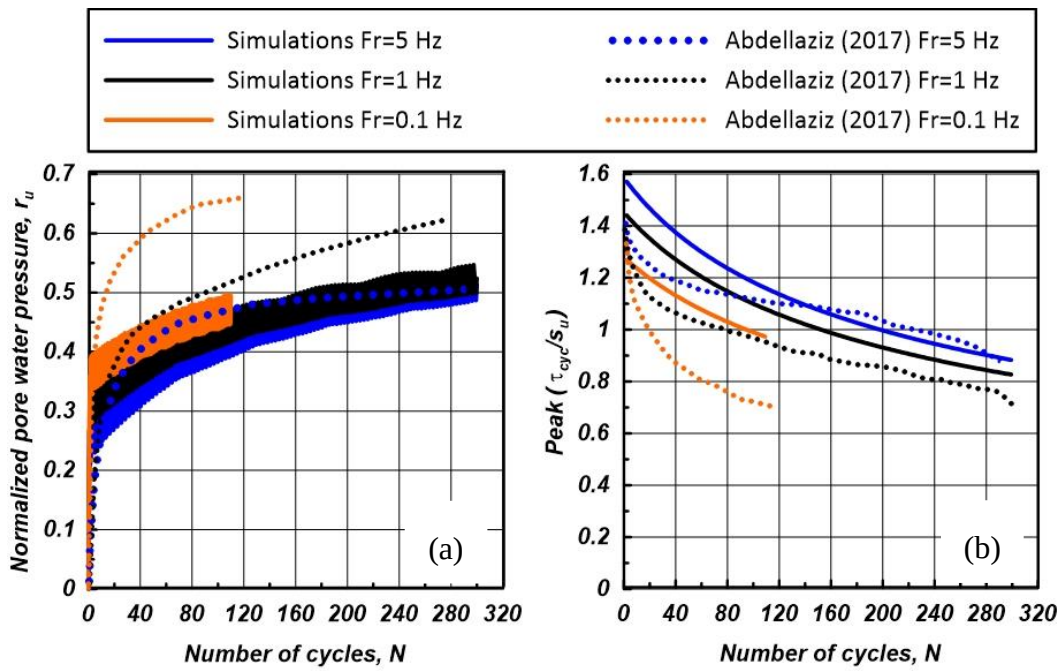

Figure 6.19 Model simulations and cyclic test results (Abdellaziz et al., 2017) on the Saint-Adelphe clay: (a) *PWP* ratio versus *N* (b) *CSR* versus *N*

6.4 Summary and Conclusions

In the first part of this chapter, the calibration of the model's parameters was presented. It was seen that as the model's parameters are mainly shared with the *SANICLAY* model family and that they are mostly supported by physical concepts, they could be obtained by either experimental tests, closed-form solutions, or conventional geotechnical relations. Also, the narrow ranges reported in the literature for some of the parameters makes their calibration a less challenging procedure

In the second part of the chapter, the model's performance, calibration, and validation were discussed. It was shown that the resulting model is characterized by improved capabilities in replicating the cyclic response of anisotropic clay at varying loading rates. In particular, it was shown that the model could capture changes in undrained strength caused by different monotonic loading rates, as well as changes in pore pressure build-up resulting from changes in the cyclic loading frequency, thus enabling more robust cyclic behavior simulations. In addition to these features, due to the use of an overstress viscoplastic formulation in a bounding surface context, the model could simulate rate effects for clays characterized by different degrees of consolidation.

The third part of this chapter discussed the model calibration against the Glacio-Lacustrine and Boston Blue clays using the guideline mentioned in the first part of this chapter and the optimization algorithms discussed in chapter 4. The calibrated model showed that it could reasonably simulate the cyclic behavior of the Glacio-Lacustrine clay at different stress amplitudes and capture well the increase of the undrained shear strength of the Boston Blue clay at different loading rates and degrees of consolidation.

Further simulations showed that the model could capture the effects of loading rates on the undrained shear strength accurately for destructured specimens and with less accuracy for structured specimens of the Grande-Baleine clay. Besides, the simulations of the modulus reduction and damping curves of the normally consolidated Kaolin clay indicated that the model could capture the general trend and the increasing effect of loading frequency on these curves. The model could also fairly simulate the effects of loading frequencies on the peak normalized cyclic strength and, with less accuracy, the excess pore water pressure of the sensitive Saint-Adelphe clay's.

CHAPTER 7 SUMMARY, CONCLUSIONS, AND FUTURE RESEARCH RECOMMENDATIONS

7.1 Summary and Conclusions

This dissertation's first goal was to adjust and evaluate optimization techniques as alternations for calibrating soil models developed for cyclic loading applications, while the second goal of this study was to develop a viscoplastic model for cyclic loading applications. In the present chapter, the work presented in this dissertation is summarized and concluded. Then, in the next section, recommendations for future works will be presented.

In the first part of this study, the application of the Gauss-Newton and Particle Swarm optimization algorithms was evaluated to calibrate soil constitutive models for cyclic loading application and cases in which models are to be calibrated against an extensive dataset. The algorithms were applied to calibrate the following three advanced constitutive models for cyclic loading applications against various types of clays and a low plasticity silt mixture; 1- the SANICLAY Bounding surface model by Seidalinov and Taiebat, 2014, 2- the SANICLAY Bounding surface with a Hybrid flow rule model by Shi et al., 2018, and 3- the Dafalias and Manzari, 2004 model.

In all cases, the optimization algorithms proved to be useful tools for calibrating advanced constitutive models under cyclic loading. Such algorithms could improve the speed of calibration, provide an efficient alternative tool to the conventional trial and error, and be applied to any constitutive model developed for cyclic loading applications. The optimization algorithms were also used to calibrate the viscoplastic model developed in this study. It should be underlined that in all cases, the optimization algorithms were only used to calibrate input parameters without physical meaning that cannot be extracted from laboratory or field test results directly. Users should ensure that their final values are in the range recommended by the model’s developers, and when available, model’s input parameters should be based on laboratory or field test data.

In the second part of this study, the formulation of a viscoplastic model for cyclic loading applications was discussed in both triaxial and multiaxial space. The new viscoplastic model was developed by anchoring and extending the plasticity concepts and theories necessary for simulating rate-dependent (and independent) response of clays under monotonic and cyclic loadings. Some features and abilities of the developed model could be summarized as:

1- It is an extended version of the *SANICLAY* model family with a distorted and rotated bounding surface and isotropic and rotational hardening rules that allow it to simulate the monotonic response of clays by considering soil consolidation states and anisotropy.

2- Employing bounding surface plasticity along with a moving projection center and proper relocations upon stress reversals allow it a realistic performance in simulating the soil response under cyclic loadings.

3- The decaying hardening variable applied to the plastic modulus formulation allows it to render a realistic plastic deformation response and hysteresis loops.

4- The application of a hybrid flow rule allows it to produce a realistic stress path response during a cyclic event, i.e., the butterfly-shaped loops could be simulated without the occurrence of the stress path lock-up.

5- The applied Perzyna's theory of viscoplasticity allows the model to consider loading rates and time effects under both monotonic and cyclic loadings.

The developed viscoplastic model in this study has sixteen input parameters, the physical meaning of which was discussed in chapter 5. Among these parameters, two are related to elasticity, three to a critical state, two to bounding surface plasticity, three to plastic modulus, two to rotational hardening rule, and two to the viscoplastic flow rule. As it was discussed, these parameters could be obtained by laboratory tests, closed-form solutions, the range suggested in the literature, or the PSO/GNO optimization techniques studied in the first part of this dissertation.

It was shown that the developed viscoplastic model was able to simulate the monotonic response of clays by considering consolidations state, anisotropy induced by soil stress history, and time or loading rates. Likewise, it was shown that the cyclic response of clays at different loading frequencies could be simulated decently in terms of the stress-strain loops and the stress path. Also, the application of the viscoplastic model to several experimental studies showed that it could simulate fairly the rate-independent cyclic behavior of the Glacio-Lacustrine clay, the loading rate effects on the monotonic and cyclic response of the Boston Blue and the Grande-Baleine clay, the effects of loading frequency on the modulus reduction and damping curves of the Kaolin clay, and

the influence of the loading frequency on the general trend of the peak normalized cyclic strength and the excess pore water pressure of the sensitive Saint-Adelphe clay.

7.2 Recommendations for Future Research

7.2.1 Model Implementation into *FLAC*

The developed viscoplastic model in this study was formulated first in terms of a triaxial stress space, then was generalized to a multiaxial stress space using a systematic approach suggested by Dafalias et al. (2006). Therefore, the model could be implemented in numerical tools to be used for solving real-world geotechnical problems. Among the existing options, *FLAC* (Fast Lagrangian Analysis of Continua) is one the most powerful tools for solving problems in earthquake geotechnical engineering applications that allow the users to implement their model as a user-defined model. Therefore, implementing the developed model into *FLAC* will give a powerful choice to practitioners to apply the viscoplastic model for clays for both cyclic and monotonic applications.

7.2.2 Model Validation Against an Experimental Program

Although the developed model was applied to experimental studies, it is of great interest and importance that the model is validated against further experiments. For this purpose, a comprehensive experimental program on clays should be performed consists of monotonic (isotopically and anisotropically consolidated tests, drained and undrained triaxial compression and extension tests with various loading rates, overconsolidation ratio, confining pressure, void ratios, etc.) and cyclic (triaxial and direct shear tests with different void ratios, frequencies, cyclic stress ratio, loading types, stress-controlled and/or strain-controlled). Once such a database is compiled, the developed model could be extensively validated and further improved. However, up until now, although there are a few extensive experimental studies on various soils, such as low plasticity silts, such a database has not been compiled for clays.

7.2.3 Pre-calibrating the Model

The viscoplastic model developed in this study has sixteen input parameters, the calibration of which, along with their physical meaning, was discussed in chapter 5. However, in some cases, the calibration of these parameters might be difficult for practicing engineers as understanding the constitution laws behind the internal equations requires advanced knowledge of both soil behavior and constitutive modeling. To make a model an easy to use tools for practitioners, it could be precalibrated so that it only works with a few well-known parameters in geotechnical practice, such as:

1- Overconsolidation ratio (*OCR*)

2- Initial void ratio

3- Plasticity Index (*PI*)

4- Cone penetration test (*CPT*)

5- Shear wave velocity (V_s)

7.2.4 Application of the Model to a Case History

It is also of great importance that the developed model be used to simulate a case history. The case history could be the fourth avenue landslide during the 1964 Alaskan earthquake (Somerville et al., 1990; Stark and Contreras, 1998). This case history has been well-studied and well-documented thorough laboratory and field testing. One of the limitations of this case history is that there are no ground motion recordings from this event. However, the ground motion prediction equation could be used to predict the response spectra of the earthquake, and ground motion recordings consistent with this event could be selected. Other case studies such as the landslides observed after the Saguenay earthquake on 25th November 1988 (Lefebvre et al., 1992) could also be simulated, albeit less information is available.

REFERENCES

Adachi, T., & Oka, F. (1982) Constitutive equations for normally consolidated clay based on elasto-viscoplasticity. *Soils Found*; 22(4), 57–70.

Antoniou, A., & Lu, W. S. (2007). Practical optimization: algorithms and engineering applications. Springer Science & Business Media.

Argyris, J. H., Faust, G., Szimmat, J., Warnke, E. P., & Willam, K. J. (1974). Recent developments in the finite element analysis of prestressed concrete reactor vessels. *Nuclear Engineering and Design*, 28(1), 42-75.

Aster, R. C., Borchers, B., & Thurber, C. H. (2011). Parameter estimation and inverse problems (Vol. 90). Academic Press.

Bai, Q. (2010). Analysis of particle swarm optimization algorithm. Computer and information science, 3(1), 180.

Beaty, M. H., & Byrne, P. M. (2011). UBCSAND constitutive model version 904aR. Itasca UDM Web Site, 69.

Been, K., & Jefferies, M. G. (1985). A state parameter for sands. *Geotechnique*, 35(2), 99-112.

Been, K., Jefferies, M. G., & Hachey, J. (1991). The critical state of sands. Geotechnique, 41(3), 365-381.

Biarez, J. & Hicher, P. Y. (1994). Elementary mechanics of soil behaviour: saturated remoulded soils. AA Balkema.

Bjerrum, L. (1967). Engineering geology of Norwegian normally consolidated marine clays as related to settlements of buildings. *Geotechnique*, 17(2), 83-118.

Bolton, M. D. (1986). The strength and dilatancy of sands. *Géotechnique*, 36(1), 65–78.

Bonin, M. D., Shaigetz, M. L., Pépin, N., Becker, D. E., & Karray, M. (2019). Geotechnical Characterization of a Glacio-Lacustrine Clay Deposit of the Abitibi Region – Case Study. Geo-St.John's, Newfoundland, Canada.

Boulanger, R. W. (2010). A sand plasticity model for earthquake engineering applications. Report No. UCD/CGM-10-01, Center for Geotechnical Modeling, Department of Civil and Environmental Engineering, University of California, Davis, CA, 77 pp.

Boulanger, R. W., & Idriss, I. M. (2006). Liquefaction susceptibility criteria for silts and clays. *Journal of geotechnical and geoenvironmental engineering*, *132*(11), 1413-1426.

Boulanger R. W., Idriss I. M. (2007). Evaluation of cyclic softening in silts and clays. *J Geotech Geoenviron Eng* ASCE, 133(6), 641–52.

Boulanger, R. W., & Truman, S. P. (1996). Void redistribution in sand under post-earthquake loading." *Can. Geotech. J.*, 33(5), 829–834.

Boulanger, R. W., & Ziotopoulou, K. (2015). PM4Sand (version 3): A sand plasticity model for earthquake engineering applications. Report No. UCD/CGM-15/01, Center for Geotechnical Modeling, Department of Civil and Environmental Engineering, University of California, Davis, CA.

Boulanger, R. W., & Ziotopoulou, K. (2017). PM4Sand (version 3.1): A sand plasticity model for earthquake engineering applications. Report No. UCD/CGM-17/01, Center for Geotechnical Modeling, Department of Civil and Environmental Engineering, University of California, Davis, CA.

Boulanger, R. W., & Ziotopoulou, K. (2018). PM4Silt (Version 1): A silt plasticity model for earthquake engineering applications. Report No. UCD/CGM-18/01, Center for Geotechnical Modeling, Department of Civil and Environmental Engineering, University of California, Davis, CA.

Bradley, B. A., & Cubrinovski, M. (2011). Near-source strong ground motions observed in the 22 February 2011 Christchurch earthquake. *Seismological Research Letters*, 82(6): 853-865.

Broyden, C.G. (1965). A Class of Methods for Solving Nonlinear Simultaneous Equations. *Mathematics of Computation*, American Mathematical Society, 19(92): 577–593. doi:10.1090/S0025-5718-1965-0198670-6. JSTOR 2003941.

Calvello, M., & Finno, R. J. (2004). Selecting parameters to optimize model calibration by inverse analysis. *Computers and Geotechnics*, 31(5), 410-424.

Campanella, R. G., & Mitchell, J. K. (1968). Influence of temperature variations on soil behavior. *Journal of Soil Mechanics & Foundations Div*.

Conn, A. R., Gould, N. I., & Toint, P. L. (2000). Trust Region Methods. *MPS/SIAM Series on Optimization*, SIAM, Philadelphia, PA.

Chekired, M., Lemire, R., Karray, M., & Hussien, M. N. (2015). Experiment setup for simple shear tests in a triaxial cell: TxSS. *Proceedings of the 68th Conference of the Canadian Geotechnical Society*, Quebec City.

Dafalias, Y. F., & Herrmann, L. R. (1986). Bounding surface plasticity. II: application to isotropic cohesive soils. *Journal of Engineering Mechanics*, ASCE, 112(12): 1263–1291.

Dafalias, Y. F., Manzari, M. T. (2004). Simple plasticity sand model accounting for fabric change effects. *Journal of Engineering Mechanics*, 130(6), 622–634.

Dafalias, Y. F., Manzari, M. T., & Papadimitriou, A. G. (2006). SANICLAY: simple anisotropic clay plasticity model. *International Journal for Numerical and Analytical Methods in Geomechanics*, 30(12), 1231-1257.

Dafalias, Y. F. Taiebat, M. (2013). Anatomy of rotational hardening in clay plasticity. Géotechnique, 63(16), 1406-1418.

Dafalias, Y. F. Taiebat, M. (2014). Rotational hardening with and without anisotropic fabric at critical state. Géotechnique, 64(6), 507–11.

Desai, C. S., & Chen, J. Y. (2006). Parameter optimization and sensitivity analysis for disturbed state constitutive model. *International Journal of Geomechanics*, 6(2), 75-88. https://doi.org/10.1061/(ASCE)1532-3641(2007)7:2(102)

Eberhart, R., & Kennedy, J. (1995). A new optimizer using particle swarm theory. In *Proceedings of the Sixth International Symposium on Micro Machine and Human Science*, pp. 39-43.

Eslami, M. M. (2017). Experimental mapping of elastoplastic surfaces for Sand and Cyclic Failure of low-plasticity fine-grained soils. *Ph.D. thesis*, Dept. of Civil and Environmental Engineering, Univ. of California, Los Angles, California.

Eslami, M. M. (2018). Evaluating post-cyclic monotonic undrained shear strength of young bay mud. Report No. UCLA/CEE-06/2018, Department of Civil and Environmental Engineering, University of California, LA.

Eslami, M., Zarrabi, M., & Yniesta, S. (2019). Evaluation of two constitutive models in predicting cyclic behavior of a natural clay. *In Eighth International Conference on Case Histories in Geotechnical Engineering*, Associazione Geotecnica Italiana, Rome, Italy, pp. 2275-2282.

Eslami, M., Zarrabi, M., & Yniesta, S. (2019). Performance of Bounding Surface Constitutive Models in Predicting Cyclic Behavior of Low-Plasticity Fine-Grained Soils. *In Geo-Congress 2019*: Geotechnical Materials, Modeling, and Testing, Reston, American Society of Civil Engineers, pp. 57-66.

Finno, R. J., & Calvello, M. (2005). Supported excavations: observational method and inverse modeling. *Journal of Geotechnical and Geoenvironmental Engineering*, 131(7), 826-836.

Fuentes, W., & Triantafyllidis, T. (2015). ISA model: a constitutive model for soils with yield surface in the intergranular strain space. *International Journal for Numerical and Analytical Methods in Geomechanics*, 39(11), 1235-1254.

Ghofrani, A., & Arduino, P. (2018). Prediction of LEAP centrifuge test results using a pressure-dependent bounding surface constitutive model. *Soil Dynamics and Earthquake Engineering*, *113*, 758-770.

Gnanendran, C. T., Manivannan, G., and Lo, S. C. R. (2006). Influence of using a creep, rate, or an elastoplastic model for predicting the behaviour of embankments on soft soils. *Can. Geotech. J.*, 43(2), 134–154.

Idriss, I. M., Dobry, R., & Sing, R. D. (1978). Nonlinear behavior of soft clays during cyclic loading. *Journal of geotechnical and geoenvironmental engineering*, 104 (ASCE 14265).

Isenhower, W. M., & Stokoe, K. H. (1981). Strain-rate dependent shear modulus of San Francisco Bay mud. *First international conference on recent advances in geotechnical earthquake engineering and soil dynamics*.

Kaliakin, V. N. Dafalias, Y. F. (1990). Theoretical aspects of the elastoplastic-viscoplastic bounding surface model for cohesive soils. *Soils and Foundations*, 30(3):11–24.

Karaboga, D., & Akay, B. (2009). A comparative study of artificial bee colony algorithm. *Applied mathematics and computation*, 214(1), 108-132.

Karim, M. R., & Gnanendran, C. T. (2014). Review of constitutive models for describing the time dependent behaviour of soft clays. *Geomechanics and Geoengineering*, *9*(1), 36-51.

Kong, L., Yao, Y., & Qi, J. (2020). Modeling the combined effect of time and temperature on normally consolidated and overconsolidated clays. *Acta Geotechnica*, 1-21.

Kutter, B., Manzari, M., Zeghal, M., & Zhou, Y. (2014). Armstrong R. Proposed outline for LEAP verification and validation processes. *In Proceedings of the geotechnics for catastrophic flooding events*. Informa UK Limited, pp. 99–108. http://dx.doi.org/10.1201/b17438-13.

Ladd, C. C. (1991). Stability evaluation during staged construction. *J. Geotech. Engrg.*, 117(4), 540–615.

Ladd, C. C., & Foott, R. (1974). New design procedure for stability of soft clays. *J. Geotech. Engrg. Div.*, 100(7), 763–786.

L'Ecuyer, N. (2000). Stabilité sismique des talus naturels argileux. Université de Sherbrooke.

LeBoeuf, D., Duguay-Blanchette, J., Lemelin, J. C., Péloquin, E., and Burckhardt, G. (2016). Cyclic softening and failure in sensitive clays and silts. *In 1st International Conference on Natural Hazards and Infrastructure*. Chania, Greece.

Lefebvre, G., LeBoeuf, D., & Demers, B. (1989). Stability threshold for cyclic loading of saturated clay. *Canadian Geotechnical Journal*, 26(1), 122-131.

Lefebvre, G., and Pfendler, P. (1996) Strain rate and preshear effects in cyclic resistance of soft clay. *J. Geotech. Engrg.*, 122(1), 21–26.

Lefebvre, G., Leboeuf, D., Hornych, P., & Tanguay, L. (1992). Slope failures associated with the 1988 Saguenay earthquake, Quebec, Canada. *Canadian Geotechnical Journal*, 29(1), 117-130.

Li, L. L. Dan, H. B., & Wang, L. Z. (2011). Undrained behavior of natural marine clay under cyclic loading, *Ocean Engineering*. 38(16): 1792–1805.

Liingaard, M., Augustesen, A., & Lade, P. V. (2004). Characterization of models for time-dependent behavior of soils. *International Journal of Geomechanics*, 4(3), 157-177.

Liu, Y., Sun, W., & Fish, J. (2016). Determining material parameters for critical state plasticity models based on multilevel extended digital database. *Journal of Applied Mechanics*, 83(1), 011003.

Lo Presti, D. C. F., Jamiolkowski, M., Pallara, O., & Cavallaro, A. (1996). Rate and creep effect on the stiffness of soils. *Measuring and Modeling Time Dependent Soil Behavior, Geotech. Special Publication*, 61, 166-180.

Lo Presti, D. C. F., Jamiolkowski, M., Pallara, O., Cavallaro, A., & Pedroni, S. (1997). Shear modulus and damping of soils. *Geotechnique*, 47(3), 603-617.

Manzari, M. T., El Ghoraiby, M., Kutter, B. L., Zeghal, M., Abdoun, T., Arduino, P., ... & Ghofrani, A. (2018). Liquefaction experiment and analysis projects (LEAP): Summary of observations from the planning phase. *Soil Dynamics and Earthquake Engineering*, 113, 714-743.

Martindale, H. Chakraborty, T. & Basu, B. A. (2013). strain-rate dependent clay constitutive model with parametric sensitivity and uncertainty quantification. *Geotechnical and Geological Engineering*, 31:229–48.

Manzari, M. T., & Dafalias, Y. F. (1997). A critical state two-surface plasticity model for sands. *Geotechnique*, 47(2), 255-272.

Manzari, M., Kutter, B., Zeghal, M., Iai, S., Tobita, T., & Madabhushi, S. (2014). LEAP projects: Concept and challenges. *In* Proceedings of the geotechnics for catastrophic flooding events. Informa UK Limited; pp. 109–16.

Marquardt, D. W. (1963). An algorithm for least-Squares estimation of nonlinear parameters. *J. Soc. Ind. Appl. Math*., 11(2), 431–441.

Moré, J. J. (1978). The Levenberg-Marquardt algorithm: implementation and theory. *In Numerical analysis* (105-116). Springer, Berlin, Heidelberg.

Mortezaie, A., & Vucetic, M. (2016). Threshold shear strains for cyclic degradation and cyclic pore water pressure generation in two clays. *Journal of Geotechnical and Geoenvironmental Engineering*, 142(5), 04016007.

Mousa, A. (2017). Revisiting the calibration philosophy of constitutive models in geomechanics. *International Journal of Geomechanics*, 17(8), 06017002. https://doi.org/10.1061/(ASCE)GM.1943-5622.0000895.

Muir wood D., (1990). *Soil behaviour and critical state soil* mechanics. Cambridge, Cambridge University Press.

Niemunis, A., & Herle, I. (1997). Hypoplastic model for cohesionless soils with elastic strain range. *Mechanics of Cohesive-frictional Materials: An International Journal on Experiments, Modelling and Computation of Materials and Structures*, 2(4), 279-299.

Ni, J. B., & Indraratna, X. Y. (2014). Model of soft soils under cyclic loading. *International Journal of Geomechanics*. 15 (4): 04014067.

Papadimitriou, A. G., Manzari, M. T., and Dafalias, Y. F. (2005). Calibration of a simple anisotropic plasticity model for soft clays. In Soil constitutive models: evaluation, selection, and calibration (pp. 415-424).

Perzyna, P. (1963). The constitutive equations for rate sensitive plastic materials. *Quarterly of Applied Mathematics*, 20(4), 321–332.

Qi, C., Fourie, A., & Chen, Q. (2018). Neural network and particle swarm optimization for predicting the unconfined compressive strength of cemented paste backfill. *Construction and Building Materials*, *159*, 473-478.

Ramdya, P., Thandiackal, R., Cherney, R., Asselborn, T., Benton, R., Ijspeert, A. J., and Floreano, D. (2017). Climbing favours the tripod gait over alternative faster insect gaits. *Nature communications*, 8(1), 1-11.

Rezania M., Taiebat M., Poletti E. (2016). A viscoplastic SANICLAY model for natural soft soil. *Computer and Geotechnics*, 73, 128-141.

Romero, S. (1995). The behavior of silt as clay content is increased. *MS thesis*, Univ. of California, Davis, Calif.

Roscoe, K. H., and Burland, J. B. (1968). On the generalized stress-strain behaviour of wet clay. *Engineering plasticity*, edited by J. Heyman and F. A. Leckie. 535–609. Cambridge, UK: Cambridge University Press.

Roscoe, K. H., Schofield, A., and Thurairajah, A. (1963). Yielding of clays in states wetter than critical. *Geotechnique*, *13*(3), 211-240.

Sadoghi Yazdi, J., Kalantary, F., & Sadoghi Yazdi, H. (2012). Calibration of soil model parameters using particle swarm optimization. *International Journal of Geomechanics*, 12(3), 229-238. https://doi.org/10.1061/(ASCE)GM.1943-5622.0000142.

Seed, H. B., & Idriss, I. M. (1971). Simplified procedure for evaluating soil liquefaction potential. *Journal of Geotechnical Engineering*, ASCE, 97(9): 1249–1273.

Seidalinov, G. (2012). A simple anisotropic bounding surface plasticity model for cyclic response of clays. *Ph.D. thesis*, Dept. of Civil Engineering, Univ. of British Columbia, Vancouver, British Columbia.

Seidalinov, G., & Taiebat, M. (2014). Bounding surface SANICLAY plasticity model for cyclic clay behavior. *Int. Journal for Numerical and Analytical Methods in Geomechanics*, 38(7), 702-724.

Simo, J. C., & Hughes, T. J. (2006). *Computational inelasticity* (Vol. 7). Springer Science and Business Media.

Shafiee, A., Stewart, J. P., Venugopal, R., and Brandenberg, S. J. (2017). Adaptation of broadband simple shear device for constant volume and stress-controlled testing. *Geotechnical Testing Journal*, Vol. 40, No. 1, pp. 15–28,

Shahrour, I., Meimon, Y. (1995). Calculation of marine foundations subjected to repeated loads by means of the homogenization method. *Comput Geotech*; 17(1), 93–106.

Soong, B., Yasuhara, K., & Murakami, S. (2004). Cyclic and postcyclic strength and stiffness of silty soils with initial static shear stress in direct simple shear tests. *Geotech. Test. J.*, 27(6), 607–613.

Somerville, P. G., McLaren, J. P., Saikia, C. K., & Helmberger, D. V. (1990). The 25 November 1988 Saguenay, Quebec, earthquake: Source parameters and the attenuation of strong ground motion. *Bulletin of the Seismological Society of America*, 80(5), 1118-1143.

Sheahan, T. C., Ladd, C. C., & Germaine, J. T. (1996). Rate-dependent undrained shear behavior of saturated clay. *Journal of Geotechnical Engineering*, *122*(2), 99-108.

Shi, Z. (2016). Numerical modelling of cyclic degradation of natural clay. *Ph.D. thesis*, Northwestern University.

Shi, Z., Hambleton, J., & Buscarnera, G. (2019). Bounding surface elasto-viscoplasticity: a general constitutive framework for rate-dependent geomaterials. *Journal of Engineering Mechanics*, 145(3): 04019002.

Shi, Z., Finno, R. J., & Buscarnera, G. (2018). A hybrid plastic flow rule for cyclically loaded clay. *Computers and Geotechnics, 101*, 65-79.

Stark, T. D., & Contreras, I. A. (1998). Fourth Avenue landslide during 1964 Alaskan earthquake. *Journal of geotechnical and geoenvironmental engineering*, 124(2), 99-109.

Taiebat, M., & Dafalias, Y. F. (2008). SANISAND: Simple anisotropic sand plasticity model. *International Journal for Numerical and Analytical Methods in Geomechanics*, 32(8), 915-948.

Taiebat, M., Dafalias, Y. F., & Peek, R. (2010). A destructuration theory and its application to SANICLAY model. *Int. J. for Numerical and Analytical Methods in Geomechanics*, 34(10), 1009-1040.

Tafili, M., Fuentes, W., & Triantafyllidis, T. (2020). A comparative study of different model families for the constitutive simulation of viscous clays. *International Journal for Numerical and Analytical Methods in Geomechanics*, 44(5), 633-667.

Tafili, M., & Triantafyllidis, T. (2020). AVISA: anisotropic visco-ISA model and its performance at cyclic loading. *Acta Geotechnica*, 1-19.

Tobita, T., Manzari, M., Ozutsumi, O., Ueda. K., Uzuoka, R., & Iai, S. (2014). Benchmark centrifuge tests and analyses of liquefaction-induced lateral spreading during earthquake. In Proceedings of the Geotechnics for catastrophic flooding events. Informa UK Limited, pp. 127–82. http://dx.doi.org/10.1201/b1743816.

Trelea, I. C. (2003). The particle swarm optimization algorithm: convergence analysis and parameter selection. *Information processing letters*, 85(6), 317-325.

Vasko, A., El Ghoraiby, M., & Manzari, M. (2018). LEAP-GWU-2015 Laboratory Tests. DesignSafe-CI, Dataset. doi:10.17603/DS2TH7Q. Available from "https://www.designsafe-ci.org/data/browser/public/designsafe.storage.published/PRJ-1780"

Vesterstrom, J., & Thomsen, R. (2004). A comparative study of differential evolution, particle swarm optimization, and evolutionary algorithms on numerical benchmark problems. *In Proceedings of the 2004 congress on evolutionary computation* (IEEE Cat. No. 04TH8753) (Vol. 2,1980-1987). IEEE.

Vucetic, M., & Dobry, R. (1989). Degradation of marine clays under cyclic loading. *Journal of Geotechnical Engineering*, 114(2), 133-149.

Vucetic, M. (1989). Normalized behavior of clay under irregular cyclic loading. Canadian Geotechnical Journal, 27(1), 29-46.

Verdugo, R., & Ishihara, K. (1996). The steady state of sandy soils. *Soils and foundations*, 36(2), 81-91.

Wilmott, P., Howison, S., & Dewynne, J. (1995). The mathematics of financial derivatives: a student introduction. Cambridge University Press.

Wood, D. M. (2014). Geotechnical *modelling*. CRC Press.

Yang, Z., & Elgamal, A. (2003). Application of unconstrained optimization and sensitivity analysis to calibration of a soil constitutive model. *International journal for numerical and analytical methods in geomechanics*, 27(15), 1277-1297.

Yin, Z. Y., & Hicher, P. Y. (2008). Identifying parameters controlling soil delayed behavior from laboratory and in situ pressuremeter testing. *International Journal for Numerical and Analytical Methods in Geomechanics*, 32: 1515–35.

Yang, Z., & Elgamal, A. (2008). Multi-surface cyclic plasticity sand model with Lode angle effect. *Geotechnical and Geological Engineering*, *26*(3), 335-348.

Yamashita, N., & Fukushima, M. (2001). On the rate of convergence of the Levenberg-Marquardt method. *Topics in numerical analysis* (239-249). Springer, Vienna.

Yao, Y. P., Hou, W., & Zhou, A. N. (2009). UH model: three-dimensional unified hardening model for overconsolidated clays. *Geotechnique*, 59(5), 451-469.

Yao, Y. P., & Zhou, A. N. (2013). Non-isothermal unified hardening model: a thermo-elasto-plastic model for clays. *Geotechnique*, 63(15), 1328-1345.

Yao, Y. P., Kong, L. M., Zhou, A. N., & Yin, J. H. (2015). Time-dependent unified hardening model: three-dimensional elastoviscoplastic constitutive model for clays. *Journal of Engineering Mechanics*, 141(6), 04014162.

Yniesta, S. (2016). Constitutive modeling of peat in dynamic simulations. *Ph.D. thesis*, Dept. of Civil and Environmental Engineering, Univ. of California, Los Angles, California.

Zarrabi, M., & Yniesta, S. (2019). Recent advanced constitutive models for liquefaction and cyclic softening Analysis. Geo-St.John's, Newfoundland, Canada.

Zarrabi, M., Shi, Z., Yniesta, S., and Buscarnera, G. (2020). Simulation of the cyclic response of anisotropic clay through bounding surface viscoplasticity. GeoVirtual2020, Canada.

Ziotopoulou, K., & Boulanger, R. W. (2012). Constitutive modeling of duration and overburden effects in liquefaction evaluations. *In Proc., 2nd Int. Conf. on Performance-Based Design in Earthquake Geotechnical Engineering*. Oakland, CA.

Zergoun. M. (1991). Effective stress response of clay to undrained cyclic loading. *Ph.D. thesis*, University of British Columbia.

Zergoun, M., & Vaid, Y.P. (1994). Effective stress response of clay to undrained cyclic loading. *Canadian Geotechnical Journal*, 31(5), 14-727.

Zhou, J., & Gong, X. (2001). Strain degradation of saturated clay under cyclic loading. Canadian Geotechnical Journal, 38(1), 208-212.

APPENDIX A – MODEL CALIBRATIONS AGAINST SBFW MIXTURES USING *PSO* AND *GNO*

Appendices A and shows the result of model calibrations discussed in Chapter 4 for all the tests.

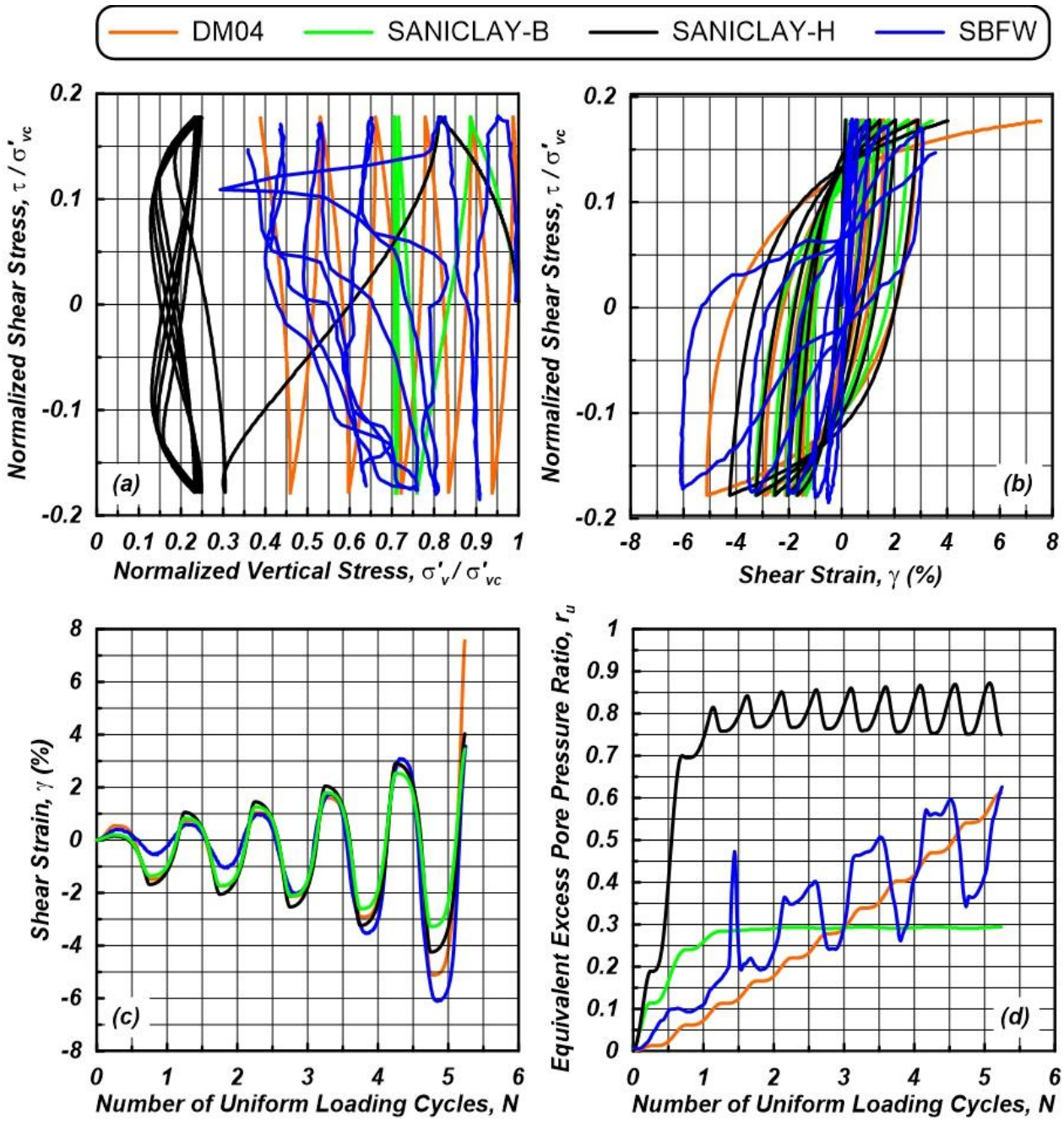

Figure A.1 Comparison between models' simulations calibrated using *PSO* and results of *DSS* laboratory cyclic shearing on *SBFW* (*CSR_0.178*)

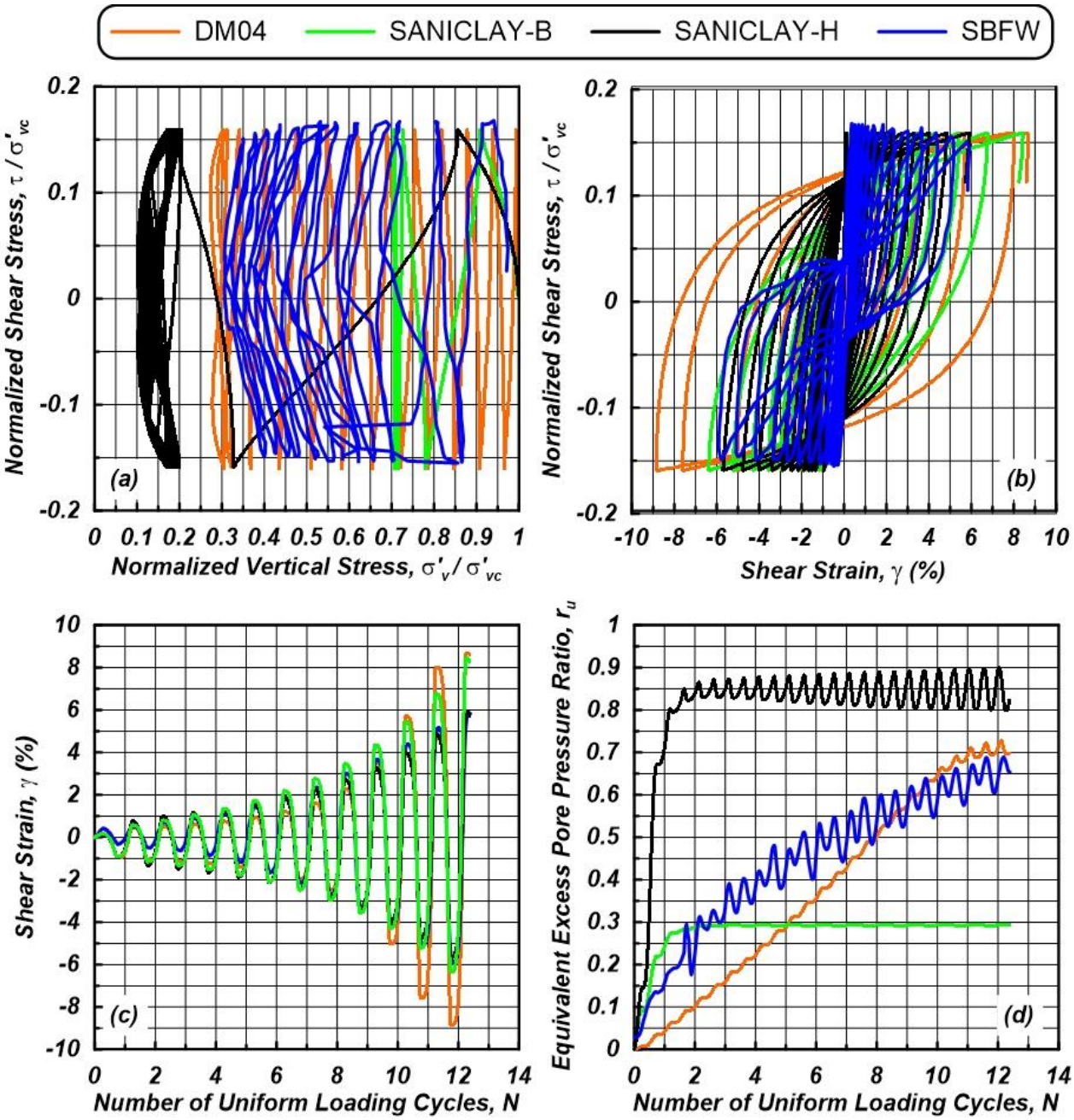

Figure A.2 Comparison between models' simulations calibrated using *PSO* and results of *DSS* laboratory cyclic shearing on *SBFW* (*CSR_0.161*)

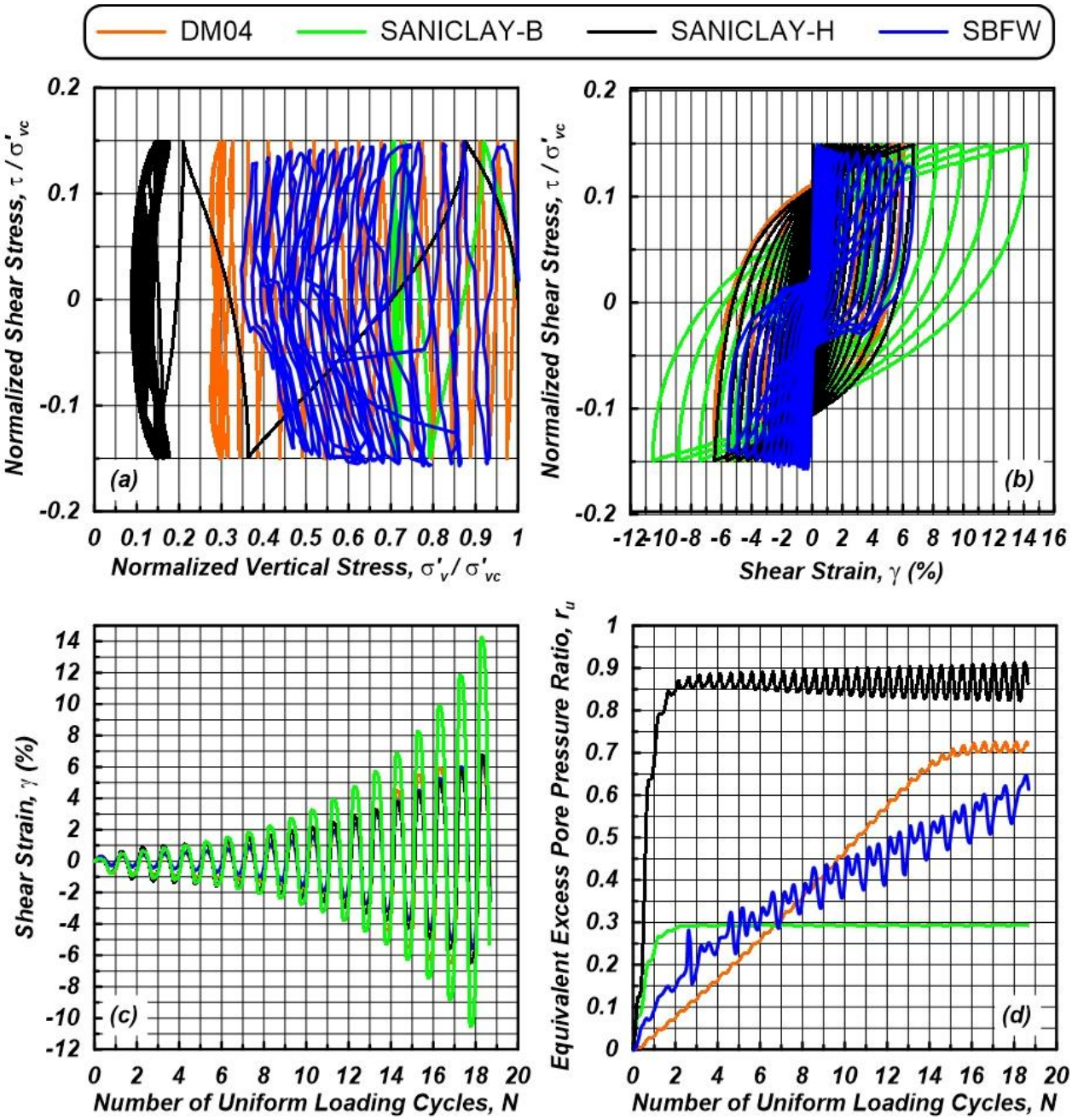

Figure A.3 Comparison between models' simulations calibrated using *PSO* and results of *DSS* laboratory cyclic shearing on *SBFW* (*CSR_0.149*)

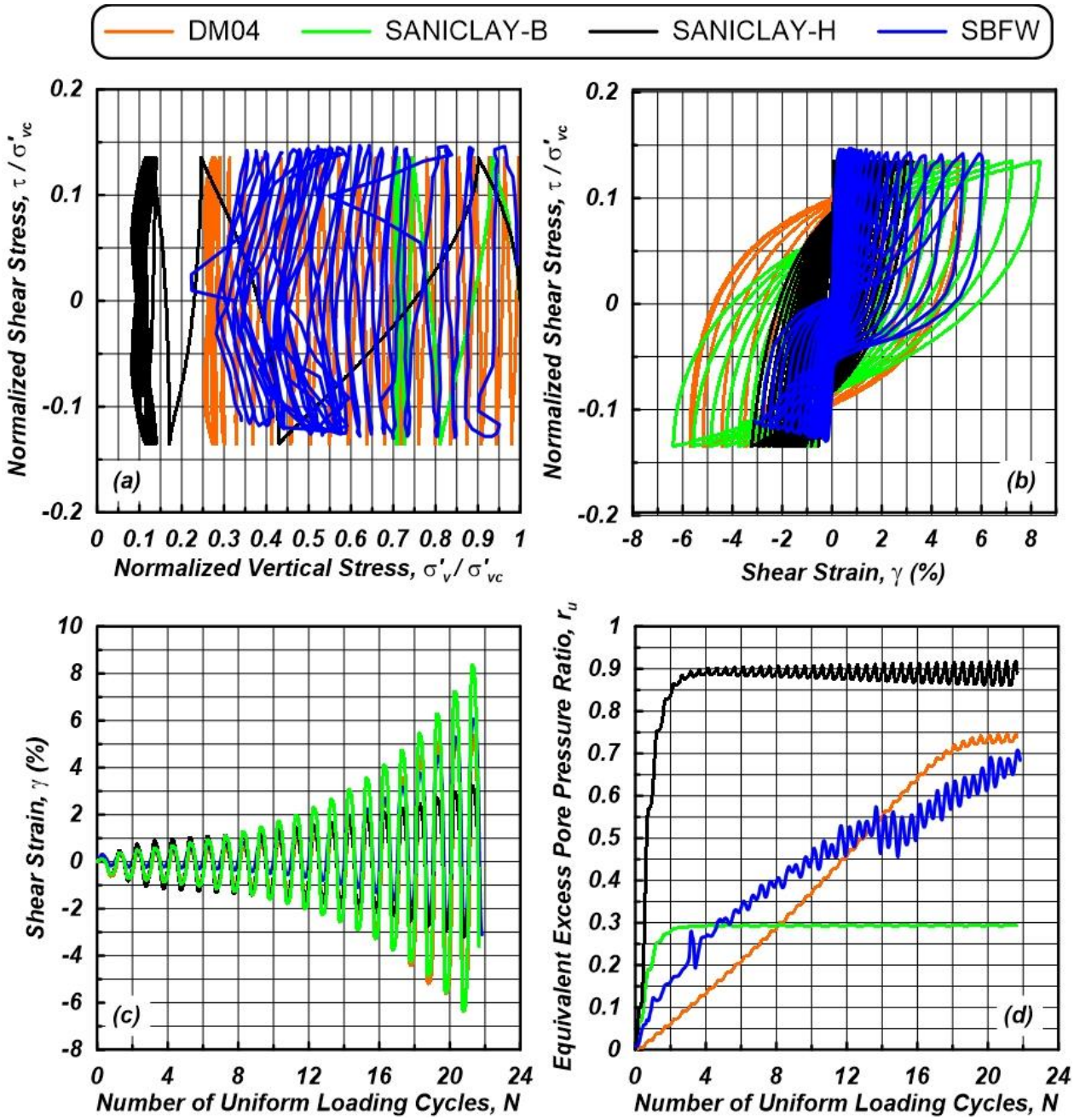

Figure A.4 Comparison between models' simulations calibrated using *PSO* and results of *DSS* laboratory cyclic shearing on *SBFW* (*CSR_0.137*)

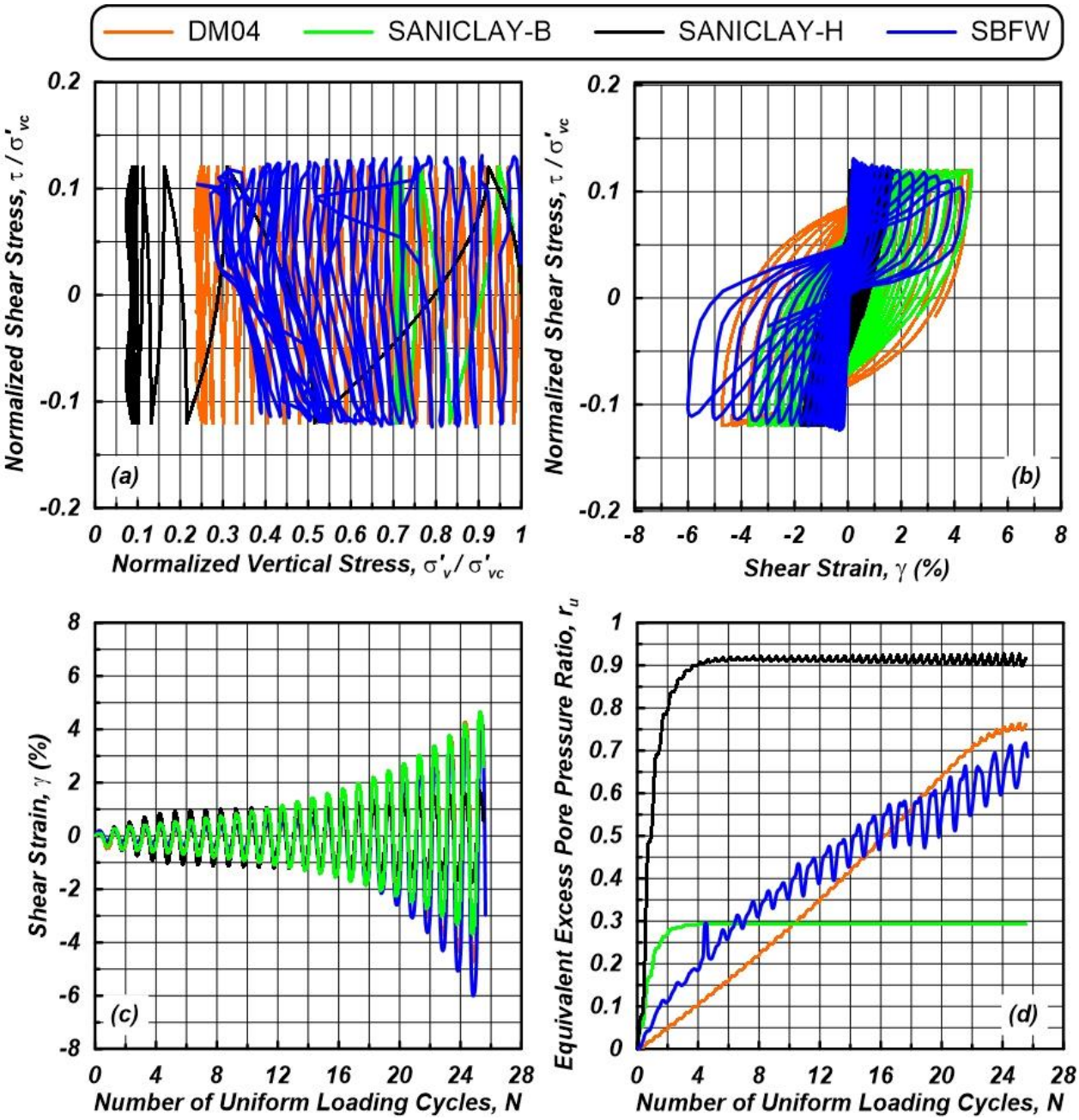

Figure A.5 Comparison between models' simulations calibrated using *PSO* and results of *DSS* laboratory cyclic shearing on *SBFW* (*CSR_0.126*)

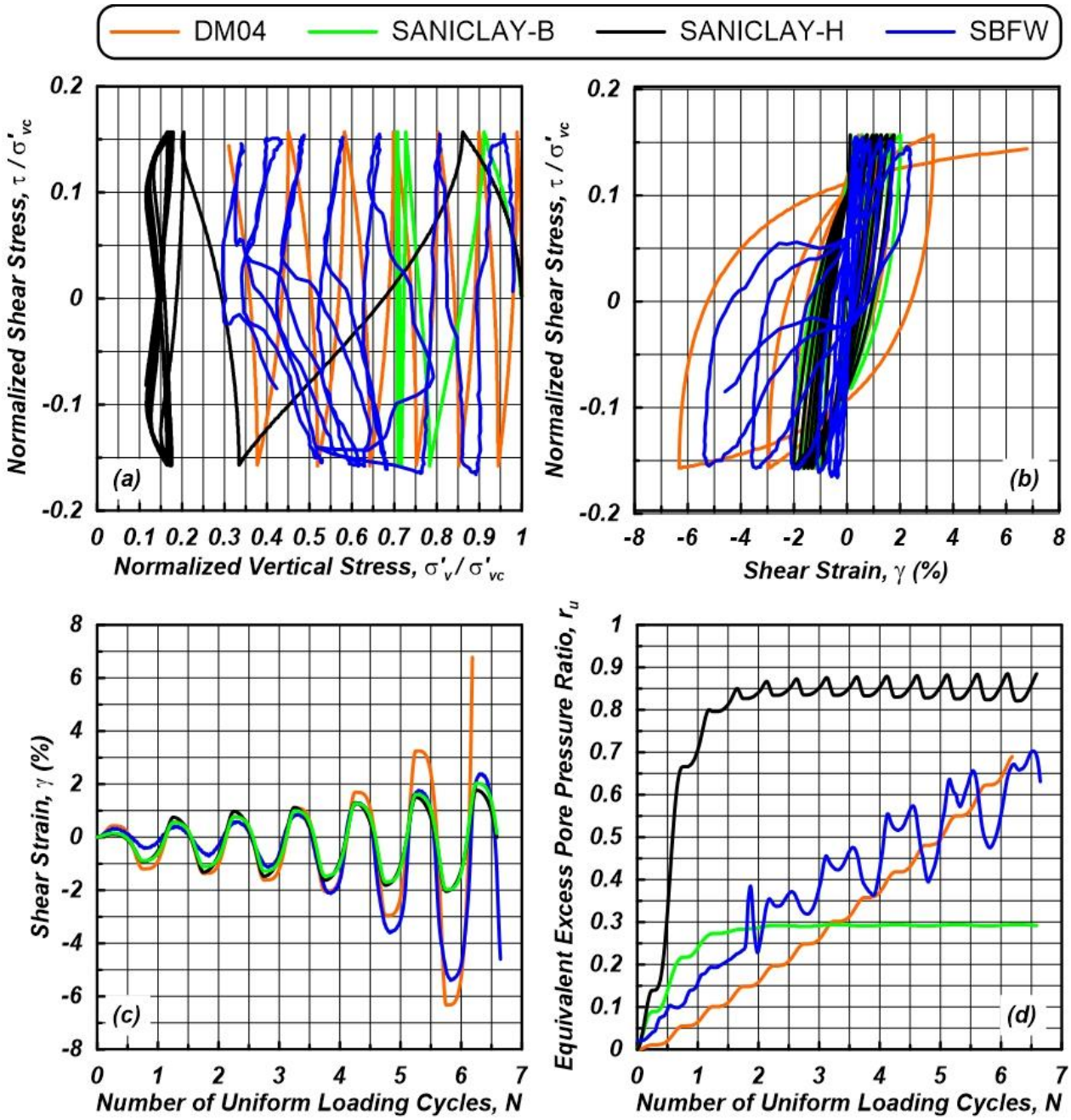

Figure A.6 Comparison between models' simulations calibrated using *PSO* and results of *DSS* laboratory cyclic shearing on *SBFW* (*CSR_0.161*)

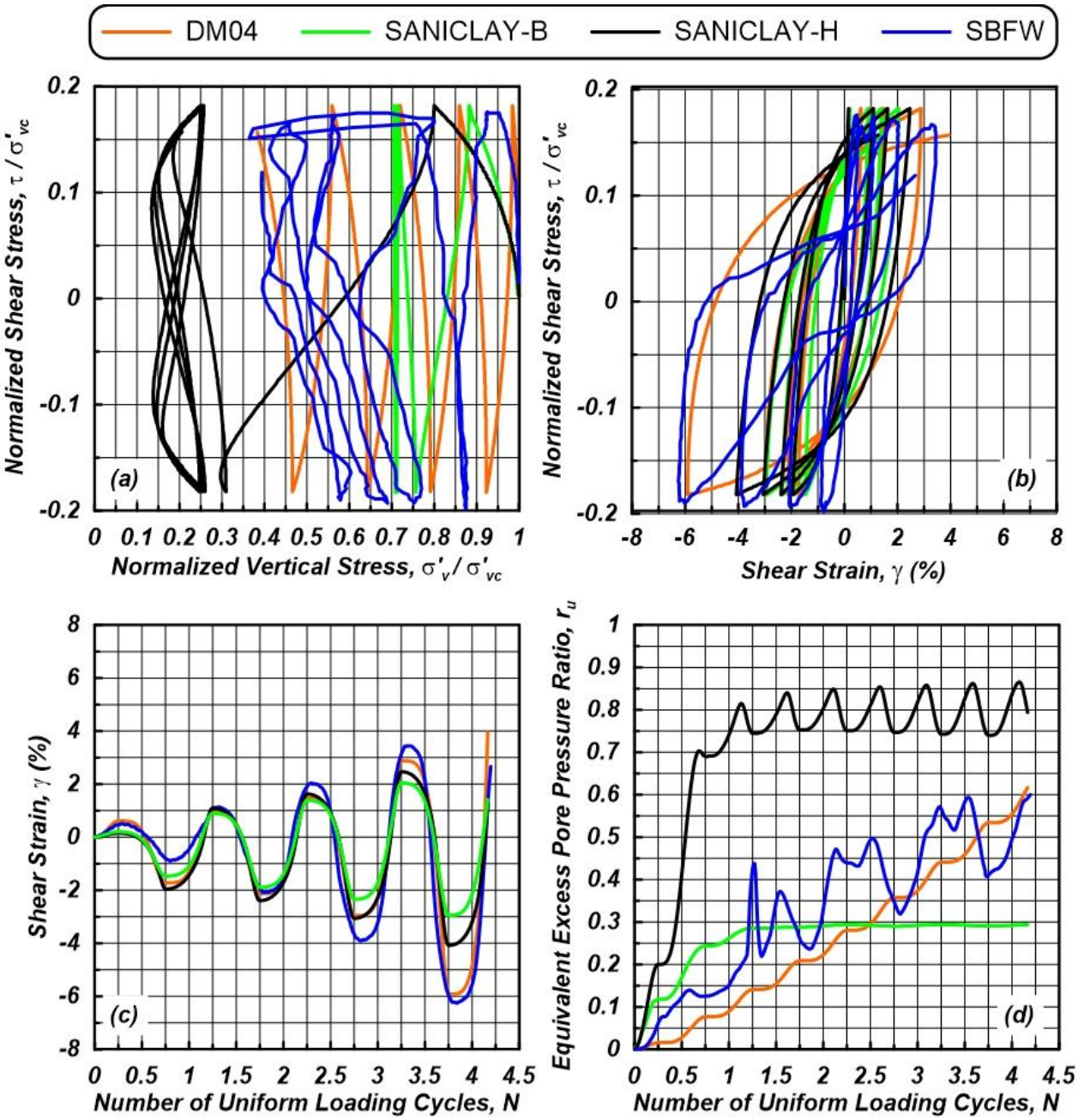

Figure A.7 Comparison between models' simulations calibrated using *PSO* and results of *DSS* laboratory cyclic shearing on *SBFW* (*CSR_0.186*).

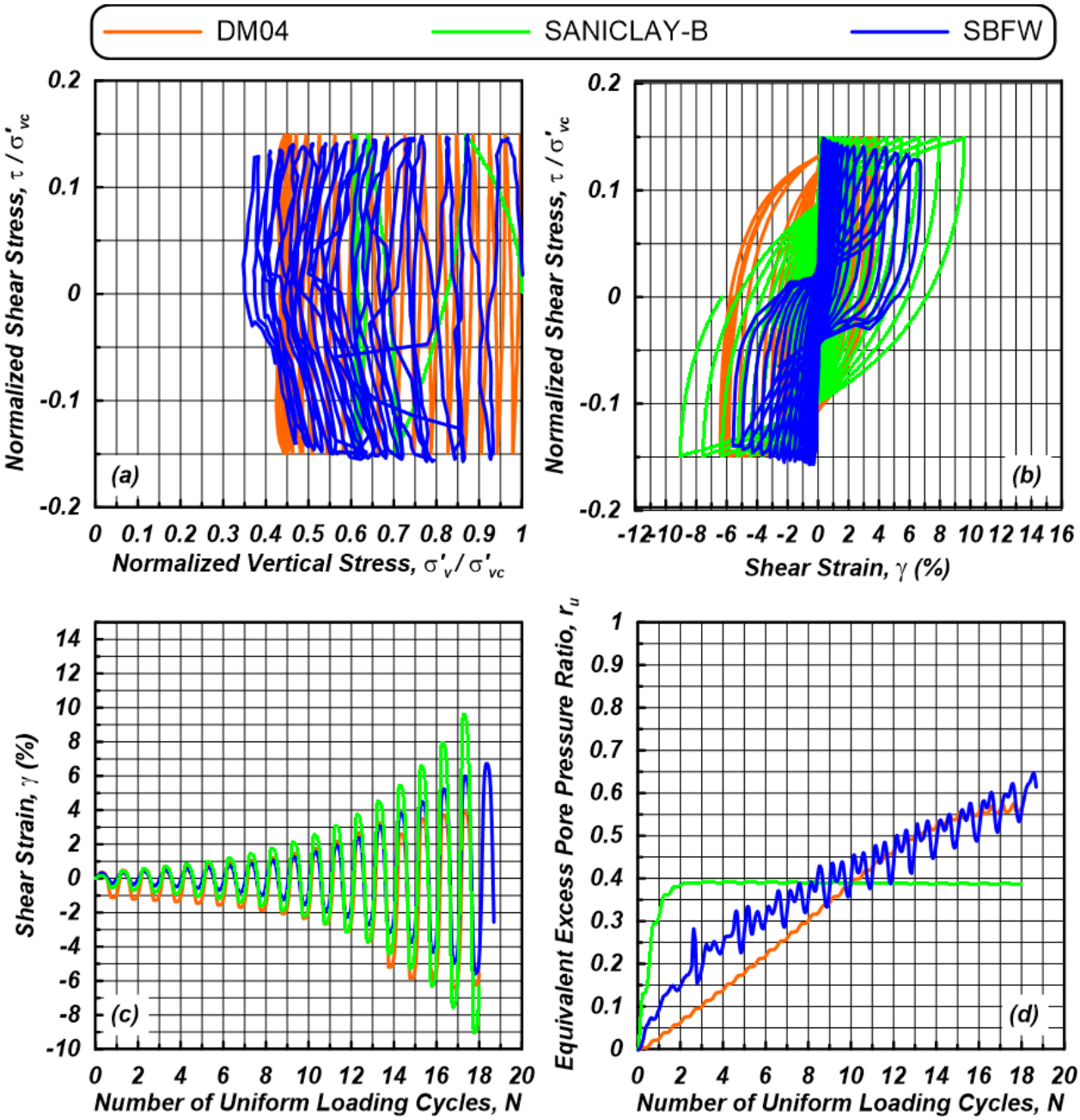

Figure A.8 Comparison between simulations of *DM04* and *SANICLAY-B* calibrated using GNO with results of *DSS* laboratory cyclic shearing (*CSR_0.149*).

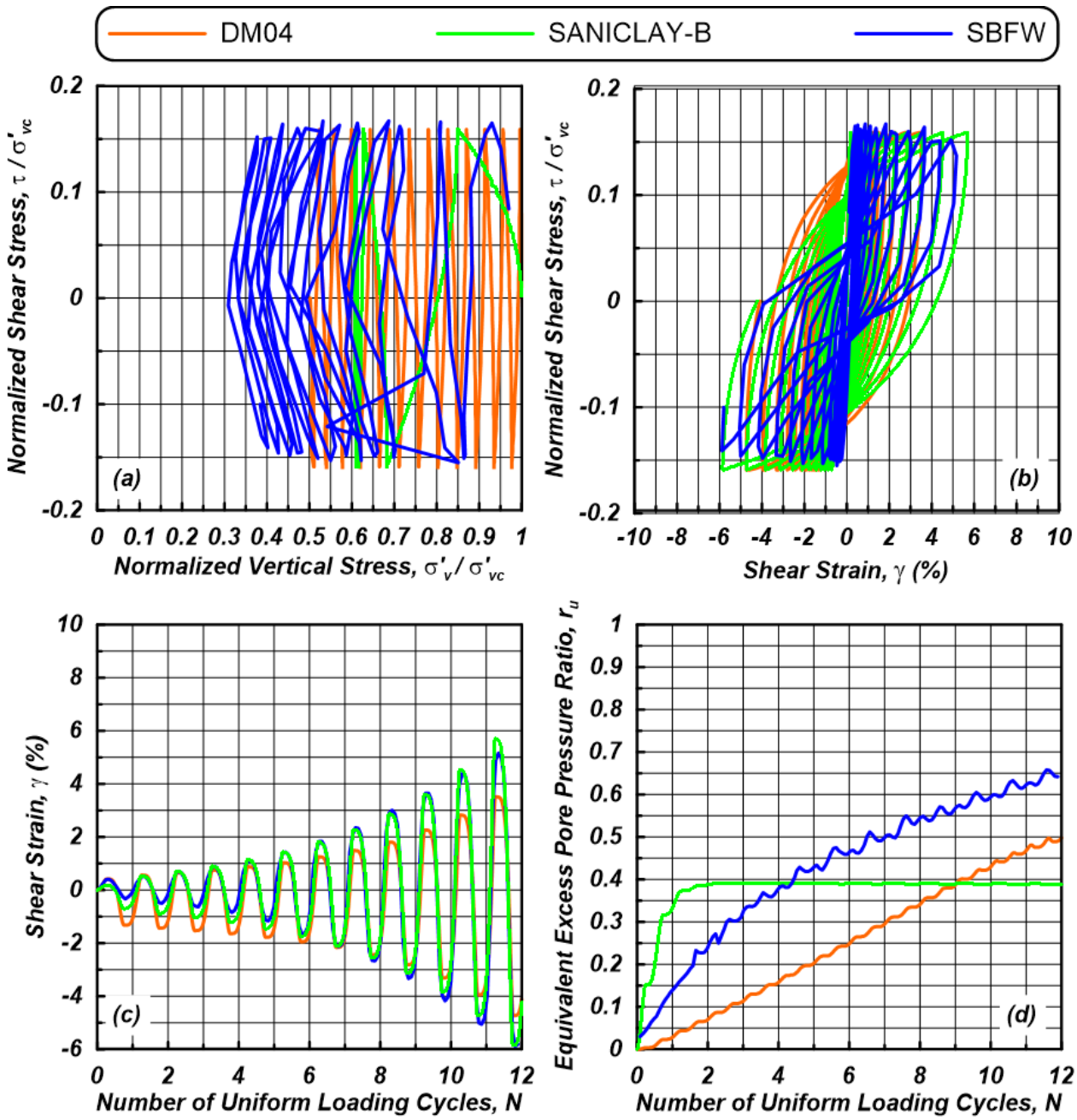

Figure A.9 Comparison between simulations of *DM04* and *SANICLAY-B* calibrated using GNO with results of *DSS* laboratory cyclic shearing (*CSR_0.161*).

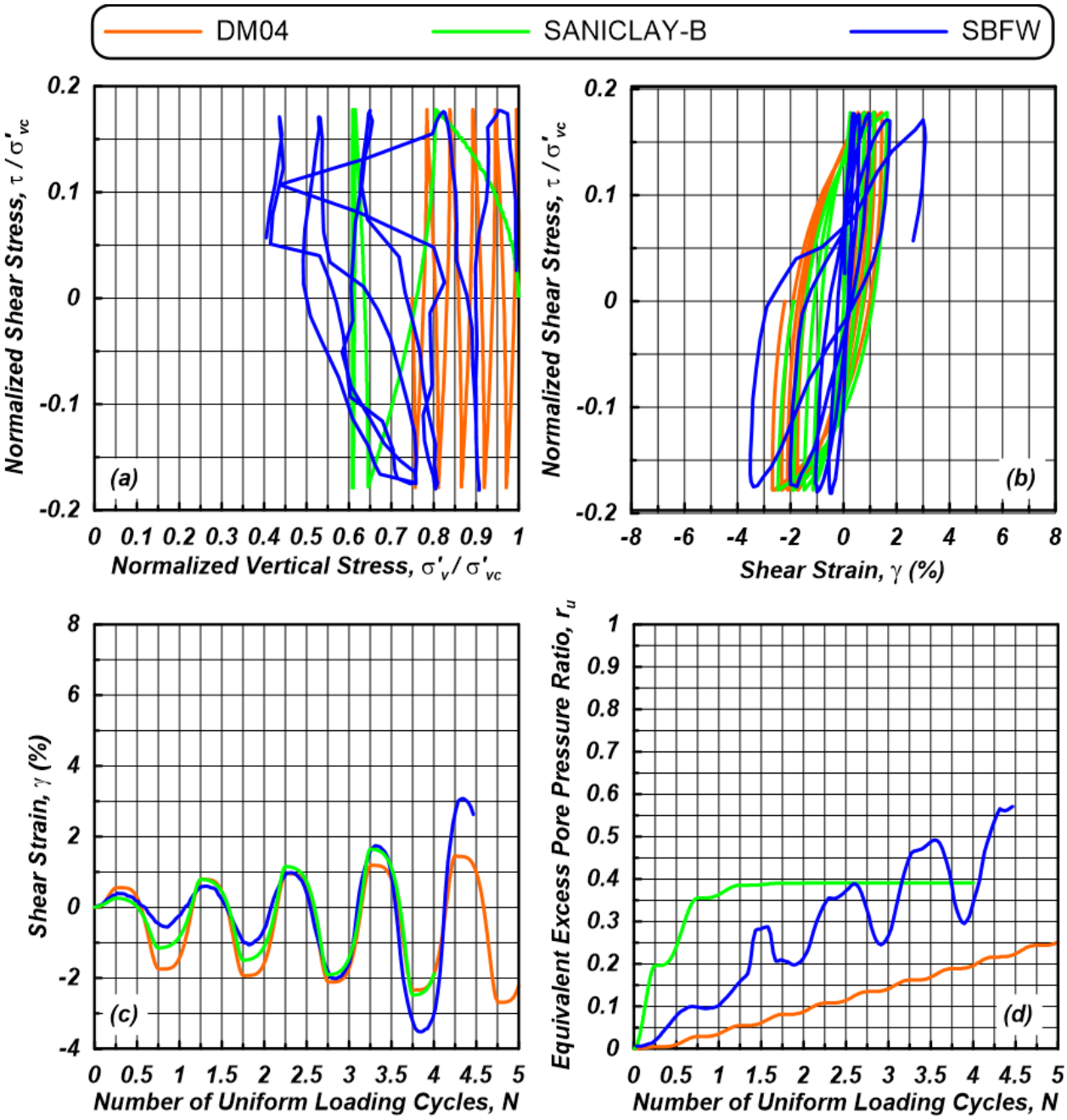

Figure A.10 Comparison between simulations of *DM04* and *SANICLAY*-B calibrated using GNO with results of *DSS* laboratory cyclic shearing (*CSR_0.180*).

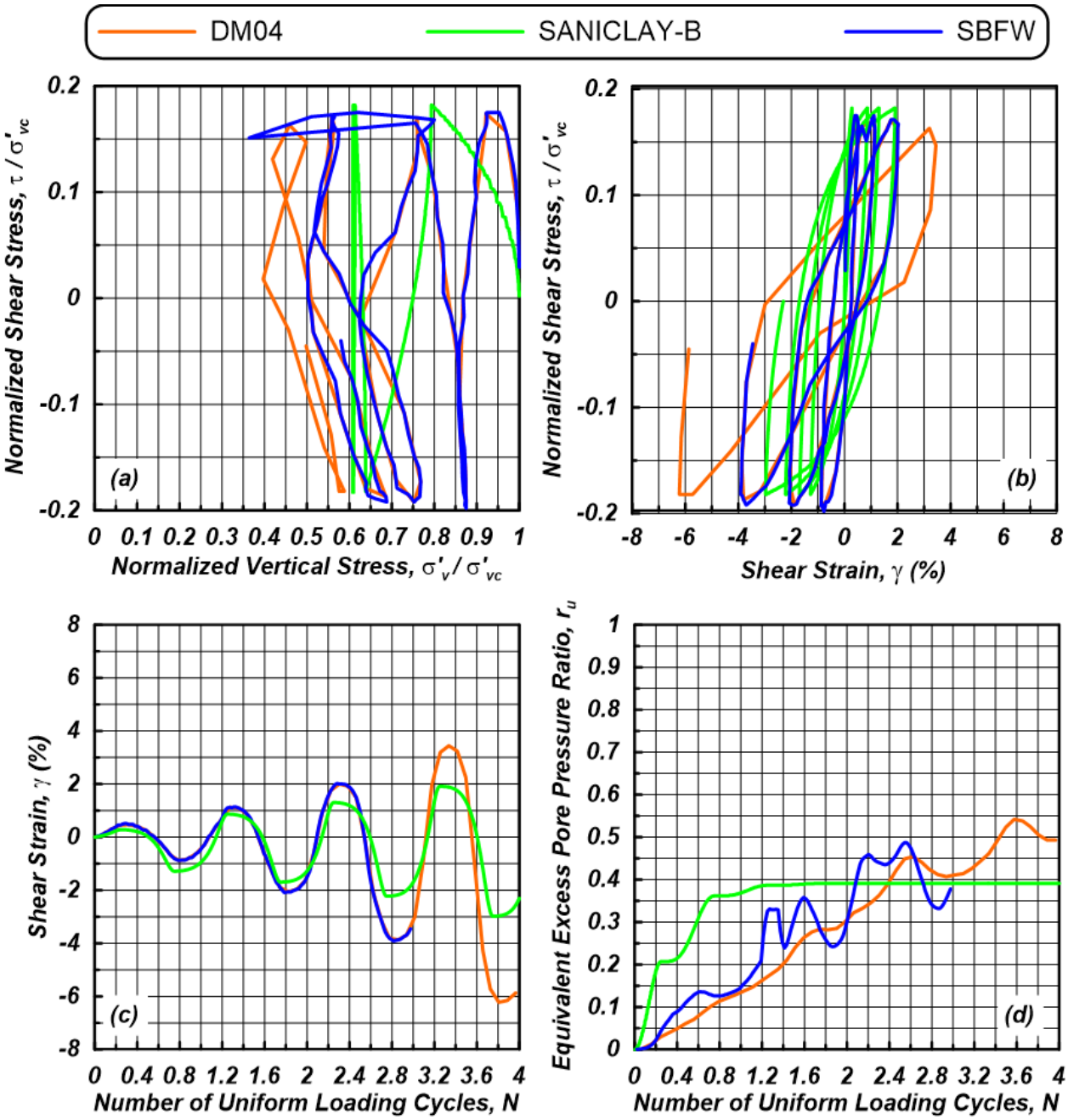

Figure A.11 Comparison between simulations of *DM04* and *SANICLAY-B* calibrated using GNO with results of *DSS* laboratory cyclic shearing (*CSR*_0.*186*).

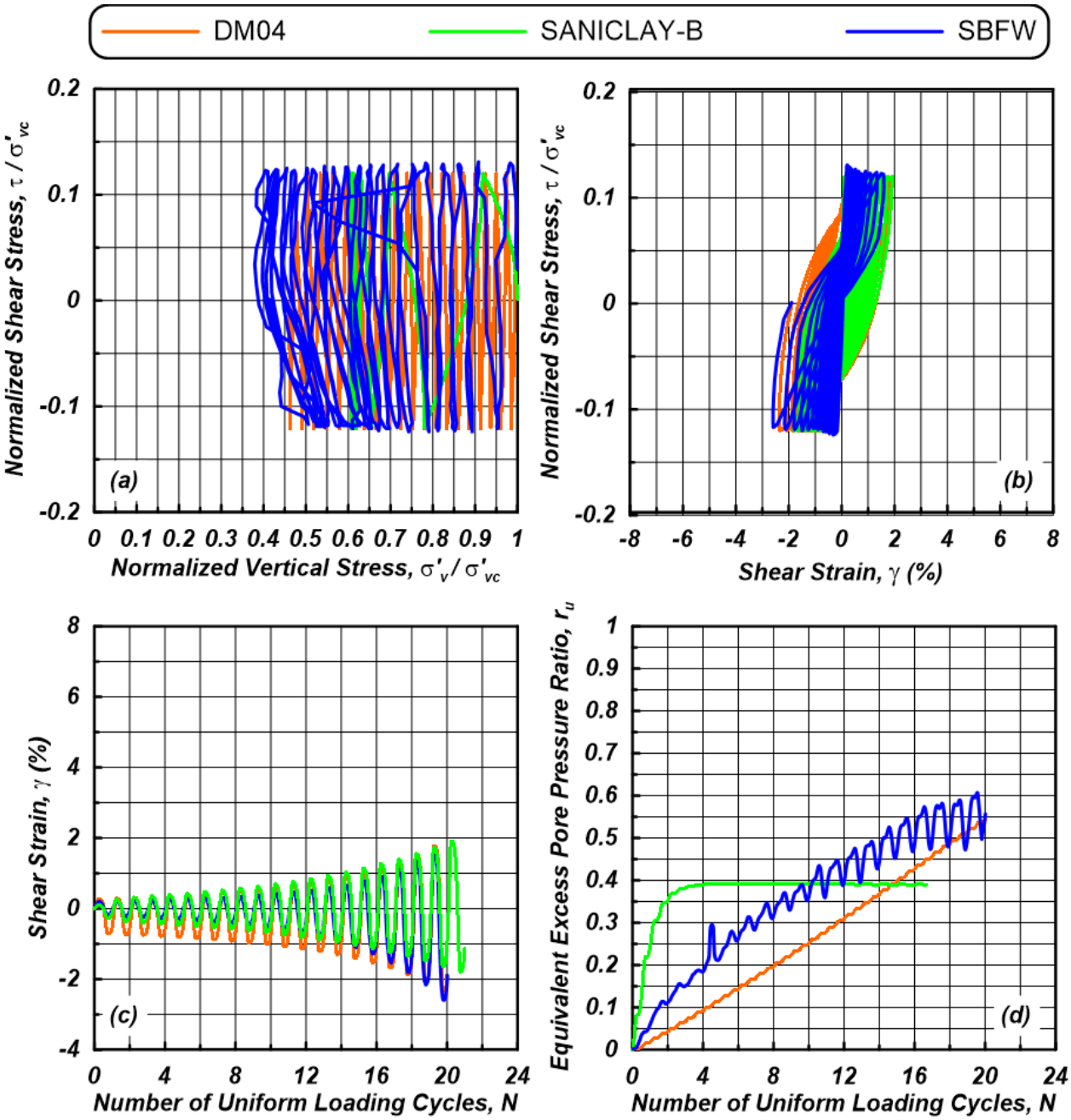

Figure A.12 Comparison between simulations of *DM04* and *SANICLAY-B* calibrated using GNO with results of *DSS* laboratory cyclic shearing (*CSR*_0.126).

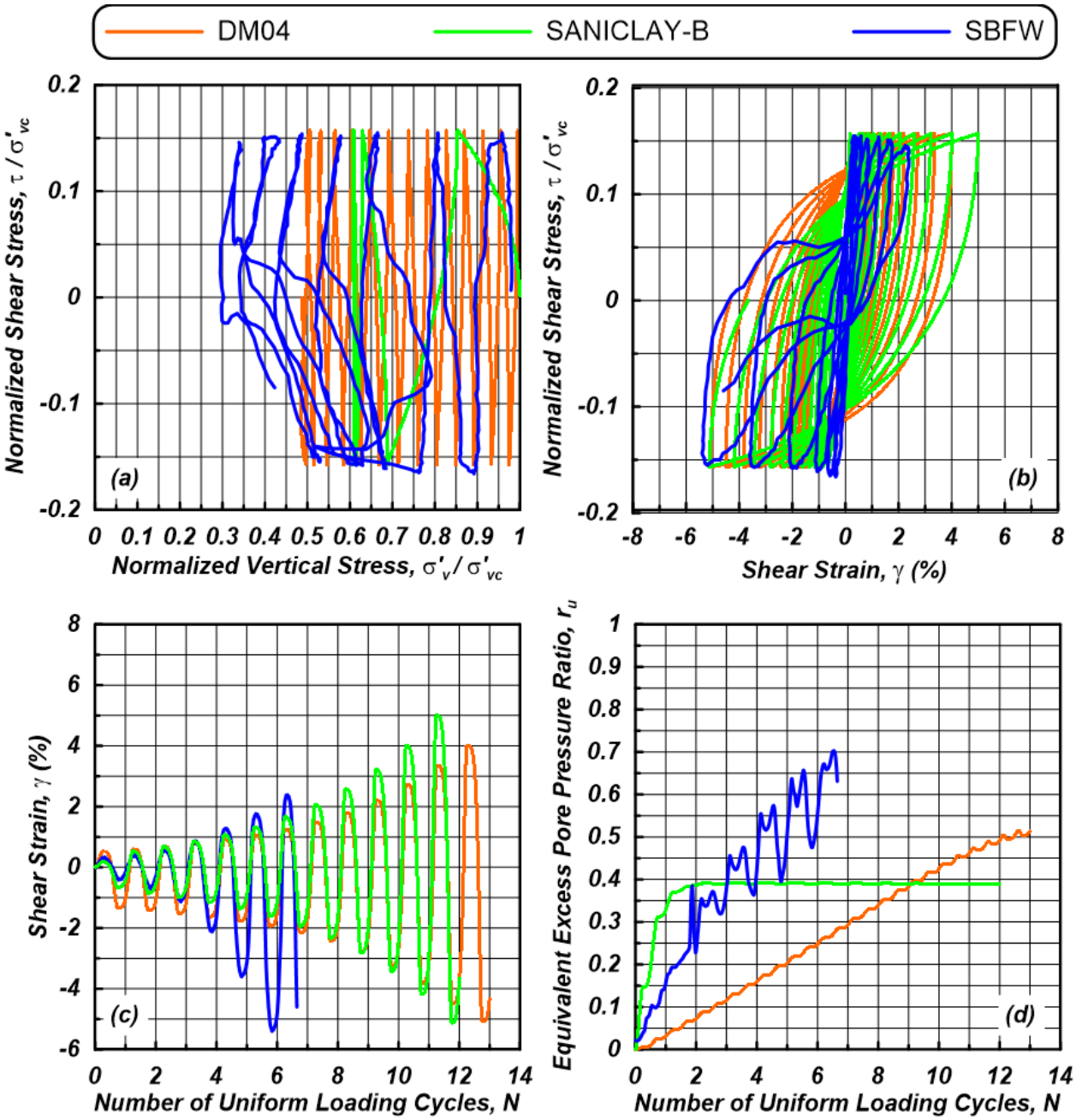

Figure A.13 Comparison between simulations of *DM04* and *SANICLAY-B* calibrated using GNO with results of *DSS* laboratory cyclic shearing (*CSR*_0.155).